Groundwater Quality Evaluation of Thessaly and Peloponnese: Data Analysis of 2019 year and Evidence of Degradation

Georgaki Maria-Nefeli[1], Georgakis Athanasios[2], Sarigiannis Dimosthenis[1], Kazakis Nerantzis[3]

[1]*Environmental Engineering Laboratory, Department of Chemical Engineering, Aristotle University of Thessaloniki, 54124, Thessaloniki, Greece, nefgeor@gmail.com*

[2]*Democritus Thrace University, Department of Civil Engineering, Section of Transportation, Kimmeria Campus, 67100 Xanthi, Greece*

[3]*Laboratory of Hydrogeology, Department of Geology, University of Patras, Rion, 26500, Patras, Greece*

Introduction / Background

Globally, groundwater is a primary source of water supply and irrigation, often with a balanced distribution (Wada et al., 2012). However, in Greece, water distribution is uneven, both temporally and regionally, with a significant portion of its main water resources being used for agricultural purposes. The chemical status of groundwater in mainland Greece is characterized as particularly degraded (Karavitis et al., 2024). The main sources of groundwater degradation are industrial and mining zones - heavy metal pollution, which is harmful even at low concentrations – the seawater intrusion, and the use of fertilizers and pesticides in areas of agricultural intensification (Dokou et al., 2015).

Objectives

Systematic groundwater monitoring ensures good water quality for water supply and agricultural irrigation in Greece, especially in Thessaly and Peloponnese, regions characterized by intense agricultural activity. The purpose of the study is to determine the distribution of groundwater parameters in the studied regions, the overall groundwater quality of these, and the identification of possible factors that influence groundwater system.

Methods

Based on the "National Water Monitoring System" (Ministry of Environment and Energy), this study aims to include all recently available data of 2019 on the hydrochemical characteristics of groundwater in Greece. This data includes measurements of physicochemical parameters, such as pH, temperature, electrical conductivity (EC), sulfate (SO_4), nitrate (NO_3), total chromium (Cr_{total}) and total phosphates (PO_4), from monitoring stations in the regions of East and West Peloponnese and Thessaly. The available groundwater variables were analyzed using statistical tools in SPSS software version 16.0 and RStudio Desktop (Dammi et al., 2021). Multivariate statistical methods (MSMs) were applied to identify trends and differences in groundwater quality in studied regions of Greece with increasing agricultural activity (Praus 2005; Belkhiri et. al. 2010). Varimax rotation approach and Kaiser normalization, combined with principal component analysis (PCA), which is included in factor analysis (R-mode FA), were applied as an exploratory tool to identify potential sources of groundwater pollution (Ma et al., 2014).

The limits of detection (LOD) and quantification (LOQ) are the most crucial data that researchers evaluate when assessing approach validity. The parameters LOD and LOQ define analyzed concentrations that may be accurately quantified. The LOQ indicates the lowest concentration that can be quantitatively determined with sufficient accuracy, whereas the LOD indicates the lowest detectable concentration (Taleuzzaman 2018). At chemical concentrations below the limit of quantification, half the value was assigned. References state that censored data are either removed or replaced with specified data, usually half of the LOQ (Cantoni et al., 2020).

Results

The chemical composition of groundwater samples, both from Peloponnese and Thessaly varies significantly (Table 1). Both a descriptive analysis and a test for normality to the data distribution were carried out. The pH, an important parameter for assessing water quality, ranges from slightly acidic to slightly alkaline in the studied regions, mainly within World Health Organization (WHO) limits. WHO recommends a pH of 6.5 to 8.5 (WHO 2008). Although pH does not directly affect human health, it is closely associated with the physicochemical properties of water. Electrical conductivity (EC) is frequently differentiated in water quality data in both the Peloponnese and the Thessaly, indicating moderate to high dissolved salt content. Water hardness is influenced by anions such as chloride and sulfate, as well as calcium and magnesium cations. The Peloponnese and Thessaly regions frequently have significant concentrations of both calcium and magnesium ions. Groundwater's chloride concentrations varied, with some samples having higher concentrations than the permissible limit of 250 mg/L (8062 mg/L). Significant concentrations of chloride in water are frequently used as an indicator of groundwater pollution (Panno et al., 2006). Nevertheless, geological factors, including seawater intrusion in coastal aquifers, or deep saline groundwater upwelling, may also cause naturally high

chloride concentrations in some areas. This could be related to high salt levels, marine pollution, and other activities (such as the use of chemicals in industry or agriculture. In both studied areas, some samples observed high nitrate (534 and 526 mg/L) and sulfate concentrations (2534 and 2423,4 mg/L), possibly due to the use of fertilizers in agriculture, indicating serious water pollution. In Thessaly, high concentrations of nitrite, ammonium and chromium total are observed in some samples, exceeding internationally accepted drinking water limits. In the Peloponnese, the values of these elements, although lower compared to Thessaly, exceed the permitted limits in some cases, especially for total chromium and ammonium samples.

The spatial distribution of trace element concentrations in the groundwater varied significantly. Despite a few exceptions, it was observed that most samples for trace elements (Cr total, Cr^{6+}, Pb, As, Cd, Ni) are either equal to or below the limit of quantification (LOQ or LOD); as a result, trace elements were not used in the factor analysis. This method provides a more accurate representation of the data and enables more accurate statistical analysis.

Table 1. Descriptive Statistics of Groundwater Quality Parameters in studied regions

Parameter	Peloponnese (n=235)				Thessaly (n=307)			
	Minimum	Maximum	Mean	Std. Deviation	Minimum	Maximum	Mean	Std. Deviation
pH	6,19	8,43	**7,45**	0,27	6,19	9,84	7,59	0,43
Temperature (°C)	9,5	31,6	18,3	2,59	9,5	31,6	18,06	2,55
Electrical Conductivity (EC, µS/cm)	230,5	**24900**	1223,65	2047,97	114	**24900**	1135,74	1815,65
Dissolved Oxygen (DO)	1	7,8	4,42	1,32	1	9,3	4,71	1,56
Calcium (Ca^{2+})	24,7	681,63	127,06	83,84	4,61	674,51	108,84	81,47
Magnesium (Mg^{2+})	0,66	290,81	27,22	38,56	0,66	290,81	30,08	36,61
Sodium (Na^+)	1,7	5163,2	96,95	401,07	0,9	5163,2	89,67	355,15
Potassium (K^+)	0,23	187,86	5,08	18,51	0,232	186,66	4,89	16,2
Bicarbonate (HCO_3^-)	47,28	486,93	301,25	70,88	23,19	851,84	306,46	101,92
Chloride (Cl^-)	3,51	**8062**	**205,58**	685,30	1,38	**8062**	**171,18**	602,55
Sulphate (SO_4^{2-})	2,57	**2534,5**	84,26	194,13	2,57	**2423,4**	79,06	176,47
Nitrate (NO_3^-)	0,06	**534**	33,38	61,47	0	**526**	32,29	57,22
Nitrite (NO_2^-)	0	0,26	0,02	0,03	0	**1,87**	0,05	0,17
Total Phosphates (PO_4^{3-})	0	0,46	0,01	0,04	0	0,364	0,02	0,04
Ammonium (NH_4^+)	0	**1,73**	0,02	0,12	0	**4,16**	0,04	0,27
Chromium dissolved (Cr)	0	**50,28**	2,91	4,94	0	**50,16**	3,13	4,96

According to Table 2, in the two studied regions, the porous aquifer is the most prevalent aquifer, with a percentage of 48.1% in the Peloponnese and 53.1% in Thessaly. For the supply and storage of groundwater, porous aquifers are frequently important, especially in urban or agricultural settings (Daskalaki & Voudouris, 2008). Porous aquifer's materials are characterized by high permeability, which facilitates the rapid movement of water within the aquifer. This fact creates ideal conditions for storing and pumping groundwater. Increased permeability also makes them more susceptible to contamination by industrial activities or fertilizers, as it makes them accessible quickly to water (Burri et al., 2019).

Table 2. Type of aquifer

	Peloponnese		Thessaly	
	Frequency	Percent (%)	Frequency	Percent (%)
Karst	98	41,7	106	34,5
Porous	**113**	48,1	**163**	53,1
Excavated rocks	24	10,2	38	12,4
Total	**235**	100	**307**	100

In total, there are 307 monitoring stations in Thessaly and 235 in Peloponnese. However, the sample size used in the Kaiser-Meyer-Olkin (KMO) test and Bartlett's Test of Sphericity is smaller due to a lack of measurements for certain groundwater quality parameters at specific monitoring stations. Degrees of freedom (df=120 and df=105, respectively) in Bartlett's test resulted from the factor analysis's inclusion of 16 variables for Peloponnese and 15 for Thessaly. Table 3 shows the KMO statistics values for each case that was studied. KMO statistics values for each region are 0,51 and 0,67, respectively, indicating marginal to moderate suitability for the method (Shrestha, 2021). At $p < 0,001$, Bartlett's test of sphericity is highly significant, indicating that at least some of the variables of the correlation matrix have significant correlations with one another. In this case, the test values are 4819,16 and 4699,34, and the corresponding significance level is less than 0,001 (Silva et al., 2014).

Table 3. Kaiser-Meyer-Olkin (KMO) and Bartlett's Test of Sphericity

		Peloponnese	Thessaly
KMO		**0,51**	**0,67**
Bartlett's Test of Sphericity	**Approx. Chi-Square**	4819,16	4699,34
	df	120	105
	Sig.	<0,001	<0,001

This study used principal component analysis (PCA) as the factor extraction method. PCA is often used to identify significant factors which influence groundwater quality, and it may minimize the number of variables without losing information (Bodrud-Doza et al., 2016). According to Table 3, the first four components explain 72,46% of the total variation in Peloponnese, while the other five frequent components account for 77,44% in Thessaly. These elements constitute the essential information of the initial data. The additional variables have an insignificant portion.

Table 3. Total Variance Explained in two regions

Component	Peloponnese						Thessaly					
	IE			RSSL			IE			RSSL		
	Total	%V	C%	Total	%V	C%	Total	%V	C%	Total	%V	C%
1	6,80	42,50	42,50	6,60	**41,23**	41,23	6,01	40,04	40,04	5,62	**37,47**	37,47
2	2,06	12,85	55,34	2,04	**12,77**	53,99	1,79	11,93	51,96	1,68	**11,22**	48,68
3	1,73	10,84	66,18	1,94	**12,13**	66,12	1,55	10,32	62,28	1,66	**11,06**	59,75
4	1,00	6,28	**72,46**	1,01	**6,34**	72,46	1,24	8,29	70,57	1,53	**10,20**	69,95
5							1,03	6,87	**77,44**	1,12	**7,49**	77,44

Extraction Method: Principal Component Analysis; IE:Initial Eigenvalues; %V: % of Variance; C%: Cumulative %;RSSL:Rotation Sums of Squared Loadings

Table 4 highlight the factor loadings after the rotation in each case. In Peloponnese, the first factor is responsible for 41.2% of the total dataset's variation. EC, sodium, chloride, sulfate, potassium, magnesium, and ammonia are the variables in this component with the highest loading coefficients. This factor reflects areas with elevated levels of inorganic salts and metals, which is strongly correlated with salinity. The salinity is primarily attributed to seawater intrusion into the aquifer, leading to an increased concentration of dissolved ions in the water (Han et al., 2015). While ammonia is present in this component with the intrusion ions, it is not a direct indicator of seawater intrusion. Instead, ammonia concentrations are monitored by processes such as organic matter decomposition, which is commonly increased in aquifers with a lack of oxygen (Moore & Joye, 2021). The second factor accounts for 12.8% of the total variation in the data, with high loadings on the nitrate and nitrite variables. This factor indicates agricultural contamination (agricultural runoff) since it contains nitrates, which are commonly found in fertilizers and organic sources, while nitrites are often associated with biogeochemical processes (Rivett et al., 2008; Khan et al., 2018). Their association usually reveals specific nitrogen cycle processes as well as the system's redox state. In oxygenated conditions, nitrite, an unstable intermediate, is frequently transformed to nitrate, indicating that nitrate dominance may be the last stage of oxidation (Nowka et al., 2015). A strong positive loading on the bicarbonate variables, which indicates their relationship to the geochemistry of carbonate rocks and the natural processes of CO_2 dissolution in the soil, characterizes the third component, which accounts for 12.1% of the total variation in the data. At the same time, it has a moderate negative loading on dissolved oxygen and pH, indicating the potential for inadequate oxygenation,

which can be linked with reductive environments or increased biological activity (Koch et al., 1985). The fourth factor expresses 6.3% of the total variation in the data and presents a high loading on the total phosphate's variable, indicating the use of phosphate fertilizers, and therefore potential pollution from fertilizer use and crops (Cheraghi e al., 2012).

Respectively in Thessaly, the first factor expresses 37.5% of the total variation in the data. Respectively in the Peloponnese, the first factor is characterized as a salinity factor, with high loadings on the variables EC, sodium, chloride, sulfate, potassium, and magnesium, describing the salinity and ionic concentration of the water. The second factor represents 11.2% of the total variation in the data and is characterized by a high positive moderate loading on the nitrate variable and a moderate positive loading on the calcium variable. Nitrates are related to the use of fertilizers in crops and to runoff from agricultural activities (Whang & Li, 2019). The existence of moderate calcium loading indicates that agricultural activities may occur in areas with a high geological presence of calcium or that calcium in rocks is dissolved from soils because of water inputs. The third factor is related to low oxygen or organic pollution environments, having a high positive loading on the variable's nitrite and ammonia. The simultaneous presence of both ions implies that reductive processes increase in low-dissolved oxygen environments, probably due to organic matter decomposition. The fourth factor is mainly related to physicochemical characteristics such as dissolved oxygen, temperature, and pH, reflecting the oxygenation processes in the aquatic environment. (Babatunde 2024). A high loading of dissolved oxygen (DO), a moderate negative loading for Temperature, and a moderate positive loading with pH are observed. The fifth factor expresses 7.5% of the total variation of the data and shows a high loading on the variable phosphate salts in water, which is related to agricultural (use of phosphate fertilizers) and biological sources. Phosphates are frequently indicators of eutrophication, or excessive nutrient enrichment of water, which can result in algae development and the degradation of quality of water (Cheraghi e al., 2012; Kundu et al., 2015).

Table 4. Rotated Component Matrix[a] in two regions

Parameter	Peloponnese				Thessaly				
	Component								
	1	**2**	**3**	**4**	**1**	**2**	**3**	**4**	**5**
pH	-0,13	-0,29	**-0,69**	-0,03	-0,04	-0,55	0,05	**0,54**	0,31
Water Temperature (°C)	0,39	-0,03	0,57	-0,07	0,34	0,14	-0,01	**-0,64**	0,23
Electrical Conductivity (EC)	**0,99**	0,09	0,07	-0,02	**0,98**	0,11	0,05	-0,10	-0,02
Dissolved Oxygen (DO)	-0,15	0,29	**-0,64**	-0,11	-0,11	0,10	0,01	**0,84**	-0,01
Calcium (Ca²⁺)	0,64	0,47	0,33	-0,04	0,57	**0,62**	0,00	-0,24	-0,21
Magnesium (Mg²⁺)	**0,80**	0,29	0,13	-0,05	**0,76**	0,30	0,18	-0,01	0,17
Sodium (Na⁺)	**0,99**	-0,05	0,00	0,00	**0,98**	-0,06	0,04	-0,07	-0,01
Potassium (K⁺)	**0,90**	-0,06	-0,03	-0,01	**0,92**	-0,07	0,02	-0,01	0,01
Bicarbonate (HCO₃⁻)	-0,15	0,04	**0,74**	-0,09					
Chloride (Cl⁻)	**0,99**	0,04	0,02	-0,02	**0,98**	0,06	0,01	-0,07	-0,05
Sulphate (SO₄²⁻)	**0,93**	0,07	0,11	0,01	**0,89**	0,09	0,11	-0,13	0,02
Nitrate (NO₃⁻)	0,02	**0,89**	0,10	-0,01	0,01	**0,87**	0,07	0,11	0,05
Nitrite (NO₂⁻)	0,05	**0,82**	-0,12	0,03	-0,04	0,08	**0,91**	0,08	0,15
Total Phosphates (PO₄³⁻)	-0,03	0,01	-0,01	**0,96**	-0,01	-0,04	0,06	-0,03	**0,92**
Ammonium (NH₄⁺)	**0,85**	-0,14	0,00	0,03	0,27	-0,04	**0,86**	-0,07	-0,08
Chromium dissolved (Cr)	-0,02	0,24	-0,02	-0,23	0,00	0,29	-0,19	0,09	0,10

Extraction Method: Principal Component Analysis.; Rotation Method: Varimax without Kaiser Normalization.; a. Rotation converged in 5 iterations (Peloponnese); Rotation converged in 6 iterations (Thessaly)

Conclusion

The degradation of groundwater quality makes agricultural production and public health difficult, as drinking water can be enriched with toxic metals. The analysis of hydro chemical data confirms the need for systematic monitoring of the region's stations and management of groundwater quality, especially in areas with high agricultural activity. This study identified significant relationship between anthropogenic variables and water quality parameter concentrations in groundwater wells. Overall, the type of aquifer has an important role in the creation of hydrogeological conditions and the vulnerability of areas to various environmental and anthropogenic stresses (Ashraf et al., 2017). The dominance of porous aquifers in the studied areas indicates increased water storage and transport capacity but at the same time

increased sensitivity to pollution from agricultural activities or other anthropogenic sources of pollution (Machiwal et al., 2018). The presence of sulfate (SO$_4$), nitrate (NO3), and chloride (Cl) indicates possible contamination due to anthropogenic activities affecting the quality of groundwater. The high concentration of nitrates and sulfates results from chemical pollution from agricultural (e.g. pesticides and fertilizers) and industrial activities, while the increased concentration of chlorides (Cl) is usually associated with excessive amounts of water in coastal areas (Akhtar et al., 2021).

Multivariate approaches like factor analysis can use and correlate numerous parameters. Factor analysis was performed to interpret the statistical methods according to the available data, proving to be a helpful tool for monitoring the groundwater quality. According to the results, this method provides the distribution and origin of water parameters. However, this study shows that additional data are required for the analysis of elements, including trace elements, with sufficient quantified values, so that the factor analysis does not overestimate or underestimate the influence of anthropogenic factors (e.g. industrial or agricultural activity). The estimation of the distribution and the improvement of the measurement methods of trace elements are necessary for the accurate analysis of hydrogeological processes and anthropogenic influences, as well as for enhancing the accuracy of statistical models, facilitating the identification of pollution sources. Furthermore, it is easier and more dependable to evaluate the results when they are presented utilizing Geographic Information Systems techniques (Mathenge et al., 2023; Xu & Zhan 2023). More extensive research can assist in developing a long-term groundwater management strategy for different objectives. Above all, it seems helpful to analyze geographical zones to identify high-pollution areas, the causes of pollution, particularly for heavy metals, and the agricultural applications that have an impact on nitrate levels.

Acknowledgements

References

Wada, Y., van Beek, L. P., & Bierkens, M. F. (2012). Non sustainable groundwater sustaining irrigation: A global assessment. *Water Resources Research*, *48*(6).

Karavitis, C. A., & Oikonomou, P. D. (2024). Water Resources Management and Policy in Greece: Challenges and Options. In *The Geography of Greece: Managing Crises and Building Resilience* (pp. 113-128). Cham: Springer International Publishing.

Dokou, Z., Kourgialas, N. N., & Karatzas, G. P. (2015). Assessing groundwater quality in Greece based on spatial and temporal analysis. *Environmental monitoring and assessment*, 187, 1-18.

Ministry of Environment and Energy. Retrieved from: http://nmwn.ypeka.gr/

Belkiri L and Mouni L (2012) "Hydrochemical analysis and evaluation of groundwater quality in El Eulma area, Algeria", Appl. Water Sci.: 2:127-133.

World Health Organization (WHO) (2011) Guidelines for drinking water quality, Geneva, World Health Organization. 515.

Mitchell, E. J., & Frisbie, S. H. (2023). A comprehensive survey and analysis of international drinking water regulations for inorganic chemicals with comparisons to the World Health Organization's drinking-water guidelines. *Plos one*, 18(11).

Praus, P. (2005). Water quality assessment using SVD-based principal component analysis of hydrological data. Water Sa, 31(4), 417-422.

Dammi Djimi, E. G., Abia, A. L. K., Belibi Belibi, P. D., Takam Soh, P., Che, R. N., Ghogomu, J. N., & Ketcha, J. M. (2021). Multivariate statistical and hydrochemical analysis of drinking water resources in Northern Cameroon watersheds. Water, 13(21), 3055.

Ma, R., Shi, J., Liu, J., & Gui, C. (2014). Combined use of multivariate statistical analysis and hydrochemical analysis for groundwater quality evolution: A case study in north chain plain. *Journal of Earth Science*, *25*, 587-597.

World Health Organization (WHO) (2008). *Guidelines for drinking-water quality: second addendum. Vol. 1, Recommendations*. World Health Organization.

Panno, S. V., Hackley, K. C., Hwang, H. H., Greenberg, S. E., Krapac, I. G., Landsberger, S., & O'kelly, D. J. (2006). Characterization and identification of Na-Cl sources in ground water. *Groundwater*, 44(2), 176-187.

Shrestha, N. (2021). Factor analysis as a tool for survey analysis. *American journal of Applied Mathematics and*

statistics, *9*(1), 4-11.

Silva, D. L., Sabino, L. D., Lanuza, D. M., Adina, E. M., Villaverde, B. S., & Pena, E. G. (2014, October). Silva's management competency theory: a factor-item analytic approach utilizing oblique rotation direct oblimin method under Kaiser-Bartlett's test of sphericity. In *Proceedings of the World Congress on Engineering and Computer Science* (Vol. 1).

Bodrud-Doza, M. D., Islam, A. T., Ahmed, F., Das, S., Saha, N., & Rahman, M. S. (2016). Characterization of groundwater quality using water evaluation indices, multivariate statistics and geostatistics in central Bangladesh. *Water science*, *30*(1), 19-40.

Babatunde, S. (2024). *Evaluating the Impact of Continuous Cover Cropping and Kernza on Nitrate and Orthophosphate Retention in Corn-Soybean Rotations: Implications for Drain Water Quality and Environmental Sustainability* (Doctoral dissertation, Western Illinois University).

Akhtar, N., Syakir Ishak, M. I., Bhawani, S. A., & Umar, K. (2021). Various natural and anthropogenic factors responsible for water quality degradation: A review. *Water*, *13*(19), 2660.

Xu, H., & Zhang, C. (2023). Development and applications of GIS-based spatial analysis in environmental geochemistry in the big data era. *Environmental Geochemistry and Health*, *45*(4), 1079-1090.

Mathenge, M., Sonneveld, B. G., & Broerse, J. E. (2022). Application of GIS in agriculture in promoting evidence-informed decision making for improving agriculture sustainability: a systematic review. *Sustainability*, *14*(16), 9974.

Taleuzzaman, M. (2018). Limit of blank (LOB), limit of detection (LOD), and limit of quantification (LOQ). *Org. Med. Chem. Int. J*, *7*(5).

Nowka, B., Daims, H., & Spieck, E. (2015). Comparison of oxidation kinetics of nitrite-oxidizing bacteria: nitrite availability as a key factor in niche differentiation. *Applied and environmental microbiology*, *81*(2), 745-753.

Daskalaki, P., & Voudouris, K. (2008). Groundwater quality of porous aquifers in Greece: a synoptic review. *Environmental Geology*, *54*, 505-513.

Burri, N. M., Weatherl, R., Moeck, C., & Schirmer, M. (2019). A review of threats to groundwater quality in the anthropocene. *Science of the Total Environment*, *684*, 136-154.

Han, D., Post, V. E., & Song, X. (2015). Groundwater salinization processes and reversibility of seawater intrusion in coastal carbonate aquifers. *Journal of Hydrology*, *531*, 1067-1080.

Moore, W. S., & Joye, S. B. (2021). Saltwater intrusion and submarine groundwater discharge: acceleration of biogeochemical reactions in changing coastal aquifers. *Frontiers in Earth Science*, *9*, 600710.

Khan, M. N., Mobin, M., Abbas, Z. K., & Alamri, S. A. (2018). Fertilizers and their contaminants in soils, surface and groundwater. *Encyclopedia of the Anthropocene*, *5*, 225-240.

Rivett, M. O., Buss, S. R., Morgan, P., Smith, J. W., & Bemment, C. D. (2008). Nitrate attenuation in groundwater: a review of biogeochemical controlling processes. *Water research*, *42*(16), 4215-4232.

Koch, F. A., & Oldham, W. K. (1985). Oxidation-reduction potential–a tool for monitoring, control and optimization of biological nutrient removal systems. *Water science and technology*, *17*(11-12), 259-281.

Cheraghi, M., Lorestani, B., & Merrikhpour, H. (2012). Investigation of the effects of phosphate fertilizer application on the heavy metal content in agricultural soils with different cultivation patterns. *Biological trace element research*, *145*, 87-92.

Wang, Z. H., & Li, S. X. (2019). Nitrate N loss by leaching and surface runoff in agricultural land: A global issue (a review). *Advances in agronomy*, *156*, 159-217.

Kundu, S., Coumar, M. V., Rajendiran, S., Rao, A., & Rao, A. S. (2015). Phosphates from detergents and eutrophication of surface water ecosystem in India. *Current science*, 1320-1325.

Machiwal, D., Jha, M. K., Singh, V. P., & Mohan, C. (2018). Assessment and mapping of groundwater vulnerability to pollution: Current status and challenges. *Earth-Science Reviews*, *185*, 901-927.

Ashraf, B., AghaKouchak, A., Alizadeh, A., Mousavi Baygi, M., R. Moftakhari, H., Mirchi, A., & Madani, K. (2017). Quantifying anthropogenic stress on groundwater resources. *Scientific reports*, *7*(1), 12910.

Automatic Detection and Extraction of Geological Lineaments on Amorgos Island Using Satellite Data and Open-Source Software

Georgios P. Georgalas[1], Polychronis Kolokoussis[1], Sofia Laskari[2], Konstantinos Soukis[2]

(1) National Technical University of Athens (NTUA), School of Rural, Surveying & Geoinformatics Engineering, Laboratory of Remote Sensing, Athens, Greece, gp.georgalas@gmail.com
(2) National and Kapodistrian University of Athens, Department of Geology and Geoenvironment, Dynamic, Tectonic and Applied Geology, Athens, Greece

Abstract

This study presents a methodology automatically detecting and extracting geological lineaments on Amorgos Island using satellite data and open-source software. The approach utilizes Landsat 8 satellite images and employs a newly developed Python-based algorithm, GeoLine, for automated lineament detection. The results demonstrate a dominant NE-SW orientation of lineaments, which aligns with previous geological studies of the region. The extracted lineaments show a 53% correlation with existing geological maps, confirming the reliability of the proposed approach.

Introduction

Geological lineaments represent structural discontinuities such as faults and fractures and play a crucial role in geoscientific studies. The ability to extract and analyze these features using remote sensing has been a growing research area. Various remote sensing techniques, including manual, semi-automated, and automated methods, have been employed for lineament detection (Tsilavo et al., 2006). The choice of techniques depends on the research objectives and available datasets, such as optical and radar imagery (Yathunanthan et al., 2014).

This study focuses on the automated extraction of geological lineaments using open-source software. By leveraging satellite data and computational techniques, it aims to develop an efficient and reproducible methodology for detecting geological structures, contributing to advancements in structural geological analysis.

Geological setting

Amorgos Island is located in the southeastern part of the Attic-Cycladic Crystalline Complex of Greece. This region formed as a result of the northward subduction of Gondwanan fragments beneath the Eurasian plate (Pe-Piper and Piper 2002; Papanikolaou 2021). The island's geology includes metamorphosed clastic sequences, carbonates, and flysch deposits, which are divided into three regions: northeastern, central, and southwestern (Figure 1, Laskari et al., 2022). The rocks of Amorgos have undergone multiple deformation events, particularly in the later stages, including alpine and neotectonic faults. The latter are associated with the 1956 offshore earthquakes (Papadopoulos and Pavlides 1992). Therefore, Amorgos provides an ideal setting for applying the automatic detection and extraction method of geological lineaments.
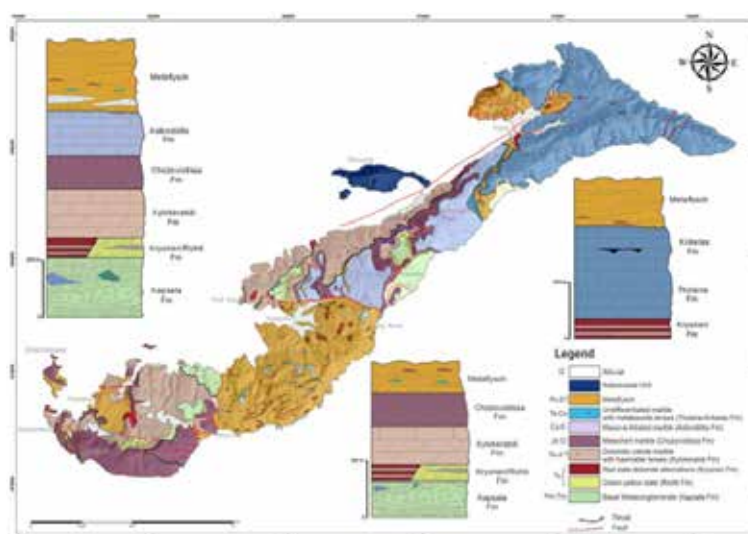

Figure 1. Geological map of Amorgos Island and lithostratigraphic columns of southwestern, central, and northeastern Amorgos (adapted from Laskari et al., 2022)
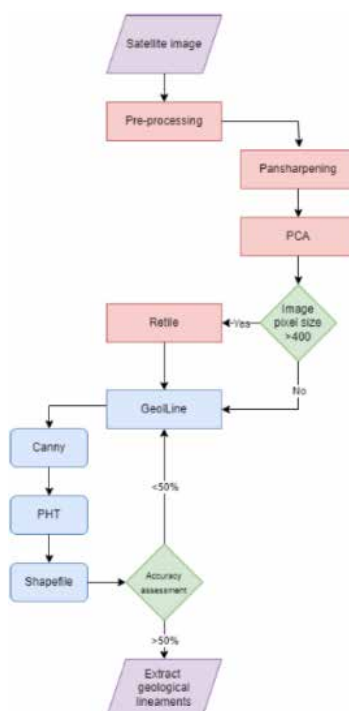
Data

For the objectives outlined, satellite imagery from the NASA Landsat 8/9 satellites was selected as the primary dataset source, based on accessibility, spatial resolution, spectral range, and enhancement capabilities even though Sentinel-2 imagery could have been used as well.

For this study, one Landsat 8 image acquired on May 27, 2022(Level 2 data product: "LC08_L2SP_181034_202 20527_20220603_02_T1"), has been used. This image included layers such as surface reflectance (SR), surface temperature (ST), intermediate ST bands, angle coefficient files, and quality assessment (QA) bands.

Method

Satellite data pre-processing was conducted in QGIS 3.22.1 using the Semi-Automatic Classification Plugin (SCP). Pansharpening was applied through the GDAL toolbox with Nearest Neighbor (NN) resampling. Dimensional reduction was performed using Principal Component Analysis (PCA) with PC1 selected for analysis. The final processed image had dimensions of 2067×1253 pixels, and a 15×15-meter pixel size. The image was segmented into 400×400-pixel tiles.

For automated tectonic lineament extraction, a Python-based algorithm called GeoLine was developed. Image import and georeferencing were handled using the GDAL library. Edge detection was performed with Canny algorithm. Vectorization was achieved through the Probabilistic Hough Transform (PHT), extracting edges as vector lines while refining parameters such as minimum length and angular tolerance (Fig. 2). The generating shapefiles were merged in QGIS, and a rose diagram was created using the Line Direction Histogram plugin.


Figure 2. Methodology's Flowchart.

Results And Discussion

This study evaluated the accuracy and relevance of the extracted geological lineaments by comparing them with published geological datasets. Five image sets were generated using different parameter configurations for the Canny and PHT algorithms.

Validation was conducted by comparing the extracted lineaments with datasets from Laskari et al. (2022) and the Hellenic Society of Geology and Mineral Exploration (H.S.G.M.E.) (Fig 3.). Additionally, the results were assessed against PCI Geomatica 9.1 software (Salui, 2018), where seven image sets were generated using different parameter configurations.
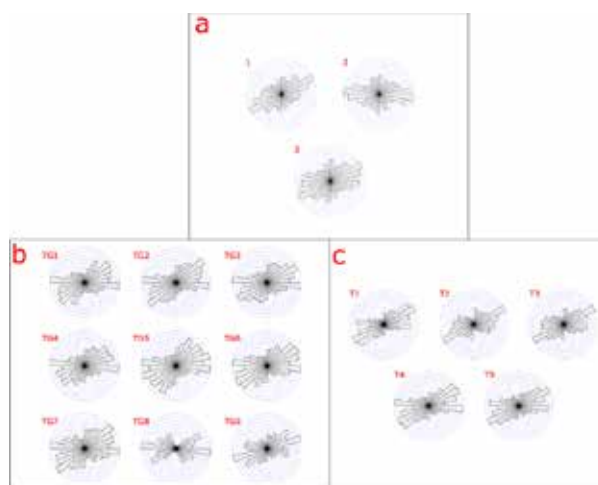
Figure 3. Rose diagrams of lineaments: (a) Ground truth data (1: Laskari et al., 2022; 2: H.S.G.M.E.; 3: combination of 1 & 2), (b) Geomatica Line algorithm, seven datasets with different parameters, (c) GeoLine algorithm, five datasets with different parameters.

Correlation analysis using the LineComparison plugin revealed an overall low correlation due to the limited distribution of control data. However, focused comparisons in specific regions around the control data consistently exceeded 33%. Notably, both Geomatica and GeoLine achieved correlation rates of up to 53%, with the T4 and TG7 datasets displaying the highest correlation percentages (Fig. 4).
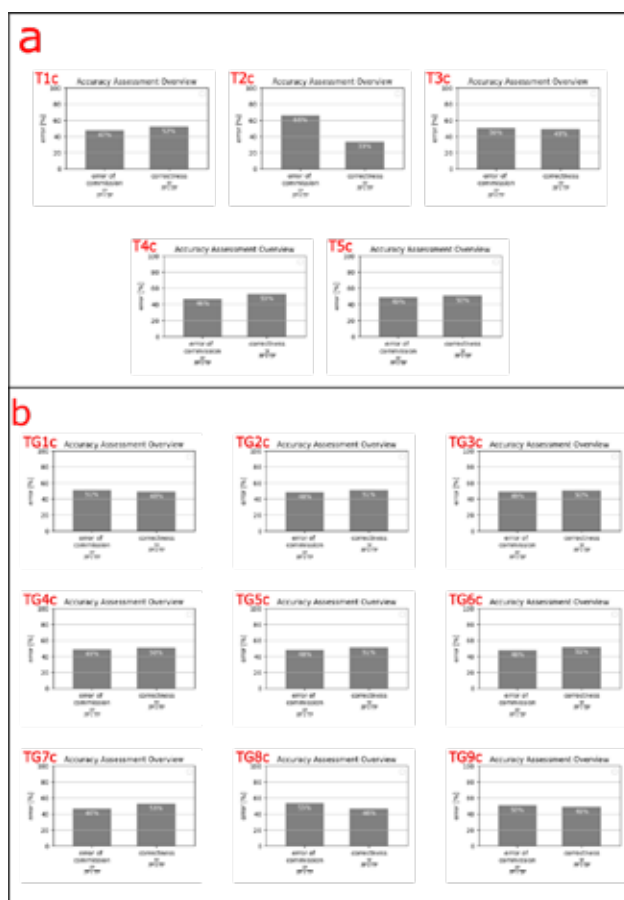
Figure 4. Accuracy assessment in demarcated zone with a) GeoLine dataset, and b) Geomatica dataset.

Although the results are promising, there is still room for improvement in terms of precision, accuracy, and usability. Future efforts will focus on two key areas.

First, enhancing result efficiency by refining GeoLine to improve post-lineament extraction capabilities. This includes achieving better correlation between detected lineaments and generating more accurate polygonal chains. Expanding the methodology to incorporate a wider range of satellite data sources, such as SAR images for terrain relief and high-resolution multispectral imagery like WorldView-3, would further improve accuracy and applicability.

Second, improving usability by automating procedural steps and integrating them into a user-friendly QGIS plugin. This would make the methodology more accessible to researchers with limited programming skills. Developing an open-source plugin would simplify data input and lineament extraction, streamlining workflows and broadening access for geoscientists.

These advancements would greatly enhance both the effectiveness and accessibility of the GeoLine algorithm, establishing it as a more valuable tool for geological research.

Conclusions

This study demonstrates the efficiency and accuracy of the developed methodology in extracting geological lineaments from satellite imagery, by showing a significant correlation with existing geological data. GeoLine shows strong potential for large-scale geological surveys, further refinement is needed to minimize noise and enhance accuracy in complex geological settings. By offering a reproducible and efficient methodology, this research contributes to the growing body of knowledge in the field of automated geological mapping.

References

Tsilavo Raharimahefa, Timothy M. Kusky, Structural and remote sensing studies of the southern Betsimisaraka Suture, Madagascar, Gondwana Research, Volume 10, Issues 1–2, 2006, Pages 186-197, ISSN 1342-937X, https://doi.org/10.1016/j.gr.2005.11.022.

Yathunanthan Vasuki, Eun-Jung Holden, Peter Kovesi, Steven Micklethwaite, Semi-automatic mapping of geological Structures using UAV-based photogrammetric data: An image analysis approach, Computers & Geosciences, Volume 69, 2014, Pages 22-32, ISSN 0098-3004, https://doi.org/10.1016/j.cageo.2014.04.012.

Ahmadi, H.; Pekkan, E. Fault-Based Geological Lineaments Extraction Using Remote Sensing and GIS—A Review. Geosciences 2021, 11, 183. https://doi.org/10.3390/geosciences11050183.

Sichugova L.V., Jamolov A.T., & Movlanov J.J. (2021). Statistical Analysis Of Lineaments Using Landsat 8 Data: A Case Study Of The Fergana Valley (East Uzbekistan). The American Journal of Applied Sciences, 3(3), 83–92. https://doi.org/10.37547/tajas/Volume03Issue03-14. .

Marzouki, A., Dridri, A. Lithological discrimination and structural lineaments extraction using Landsat 8 and ASTER data: a case study of Tiwit (Anti-Atlas, Morocco). Environ Earth Sci 82, 125 (2023). https://doi.org/10.1007/s12665-023-10831-4. El-Qassas, R.A.Y., Ahmed, S.B., Abd-Elsalam, H.F. and Abu-Donia, A.M. (2021) Integrating of Remote Sensing and Airborne Magnetic Data to Outline the Geologic Structural Lineaments That Controlled Mineralization Deposits for the Area around Gabal El-Niteishat, Central Eastern Desert, Egypt. Geomaterials, 11, 1-21. https://doi.org/10.4236/gm.2021.111001.

Papadopoulos, G., Pavlides, B.S., 1992. The large 1956 earthquake in the South Aegean: Macroseismic field configuration, faulting, and neotectonics of Amorgos Island. Earth Planet. Sci. Lett. 113 (3), 383–396. https://doi.org/10.1016/0012-821X(92)90140-Q.

Papanikolaou, D.I., 2021. Regional Geology Reviews The geology of Greece. Springer Nature pp. 345. https://doi.org/10.1007/978-3-030-60731-9.

Pe-Piper, G. and Piper, D.J.W., 2002. The igneous rocks of Greece. The anatomy of an orogen. –Gebrüder Borntraeger, Berlin, Stuttgart. G. Catsadorakis: Determinants of raptor abundance, 573.

Dürr, S., 1985. Geological Map of Greece, 1:50.000, Amorgos-Donousa Sheet.Institute of Geological and Mining Research, Athens.

Sofia Laskari, Konstantinos Soukis, Daniel F. Stockli, Stylianos Lozios, Alexandra Zambetakis-Lekkas, Reconstructing the southern Pelagonian domain in the Aegean Sea: Insights from U-Pb detrital zircon analysis, lithostratigraphic and structural study, and zircon (U-Th)/He thermochronology on Amorgos Island (SE Cyclades, Greece), Gondwana Research, Volume 106, 2022, Pages 329-350, ISSN 1342-937X, https://doi.org/10.1016/j.gr.2022.02.007.

Salui, C.L. Methodological Validation for Automated Lineament Extraction by LINE Method in PCI Geomatica and MATLAB based Hough Transformation. *J Geol Soc India* **92**, 321–328 (2018). https://doi.org/10.1007/s12594-018-1015-6

Major and trace element analysis on geological samples using WD-XRF on pressed pellets

I. Gerontidou[1], A. Koroneos [1]

(1) Department of Mineralogy-Petrology-Economic Geology, Faculty of Geology, Aristotle University of Thessaloniki, Thessaloniki, Greece, ioangero@geo.auth.gr.

The sample preparation protocol and the analytical method of elemental analysis using WD-XRF Supermini200 from Rigaku Holdings Corporation, are presented. The use of pressed pellets, traditionally employed for trace element analysis, is examined and proposed for major element analysis as well.

Introduction

Wavelength Dispersive X-ray Fluorescence (WD-XRF) spectrometry has been the cornerstone of elemental analysis for geological samples. It is a non-destructive analytical technique that provides high accuracy and precision, when measuring the composition of both light and heavy elements (Beckhoff et al., 2007; Rainer, 2016). Measuring major elements is quite a challenge because light elements emit weaker fluorescent energies. This problem was approached with the use of fused beads because they offer optimal homogeneity within the sample and a smooth surface for the primary X-ray to hit, minimizing energy scattering and absorption effects (Beckhoff et al., 2007). That's why major element XRF analysis has been, almost exclusively, done on fused glass beads. However, sample fusion is costly, requiring the purchase and maintenance of a fusion machine and Pt-Au ware. Moreover, it is time-intensive due to multiple stages of preheating, prefusion, fusion and air cooling.

In this study, the use of pressed pellets for major element analysis is examined, by creating and calibrating an empirical hybrid quantitative method using certified reference materials. The use of pressed pellets is the most cost effective and time saving sample preparation method. The core of this research is the comparison of certified reference material values with their obtained results using the proposed method. Along with the major elements, the commonly used trace elements in geological research are calibrated into the method, broadening its utility.

Sample preparation

The most important part of calibrating a new analytical method is to maintain a consistent sample preparation protocol (Marguí & Queralt, 2024). The reliability of the results is always dependent on proper sample handling. For this reason, thorough care is taken to keep the lab-ware clean and to work in a laboratory environment with limited dust, ensuring minimal contamination from the surroundings.

Geological samples, due to their inhomogeneity, cannot be analyzed directly as a solid. Instead, the rocks are first crushed using a steel jaw breaker, downsizing them to an approximately 2cm fracture size. The next and most crucial step is pulverizing the rocks to a fine powder. To evaluate the use of pressed pellets over fused beads, it is vital to achieve sample homogeneity. Pulverization is also the most prone step to contamination, which is the reason many researchers have investigated its effects (Thompson & Bankston, 1970; Hickson, 1986; Roser et al., 2003; Mojtahed et al., 2006; Saikia et al., 2009; Takamasa & Nakai, 2009; Morikawa, 2014; Yamasaki, 2018).

Among the available options, using tungsten carbide (WC) pulverizing mill bowl is the most time-efficient choice, and essential for quartz-bearing siliceous rocks. However, it can affect the elemental composition of the sample. Morikawa (2014) presents the contamination of a SiO_2 sample, with W, Cu, Co, Ni and Fe, Yamasaki (2018) and Saikia et al. (2009) confirm the Co and W contamination of volcanic rocks and a quartz sample respectively and Mojtahed et al. (2006) suggests the added impurity of W, Co, C, Ti, Ni, Ta. Those studies point out the drastic effects of the pulverization duration. Morikawa (2014) displays the impurities present at 3, 5 and 10 minutes, Saikia et al. (2009) at 5 minutes, whereas Yamasaki (2018) indicates Co (~10 ppm) and W (up to 100 ppm) contamination at 40 sec and lastly, Roser et al. (2003) confirm the Co and W contamination at 30sec pulverizing time using tungsten carbide mill.

To avoid any contamination mentioned above, the proposed protocol follows strictly the under 10 second duration time in WC pulverizer, preferably at 5 seconds. Another measure taken to ensure the purity of the sample is following the technique of prewash, where a small portion of the sample is grinded and discarded, before continuing with the rest of the sample. For the last step of pulverization, to ensure the fine grain size (smaller than 50μm), the sample is grinded on a manual agate mortar. The agate mortar has been proven to add limited contamination (Takamasa & Nakai, 2009).

The typical procedure for pelletizing geological samples is followed. The sample must be mixed with a reagent to behave

as a binder, guaranteeing the cohesion of the pressed solid disc. These reagents improve uniformity, durability, and increase the density of the pellet, creating a consistent surface to analyze. This study's protocol uses CEROX from FLUXANA GmbH & Co. KG, as a binder, which is known as Hoechst wax ($C_{38}H_{76}N_2O_2$). It is very low on impurities and resistant to X-rays. It is mixed with the sample on a 1:4 ratio (Rainer, 2016), more specifically 2 grams of the binder are mixed with 8 grams of the sample. In the case that the sample has very high relative density, the portions are increased accordingly to achieve infinite thickness (Marguí & Queralt, 2024) of the pressed pellet. X-rays can penetrate the sample up to a few millimeters that's why the pellet must be thick enough (>0.5 cm) for the penetration to not go further to the back of the pellet. The mixture of sample-binder is then inserted into the automatic Retsch 200 mixer mill for homogenization. After testing, the most optimal mixing is achieved at 15 minutes by fluctuating the speed of the mixer, turning it from low to high. This lets the particles mix more efficiently than letting the mixer work on high for the whole period. In the end, the palletization is completed with the Specac 15-ton Hydraulic press with the 40 mm pressing dies. XRF machines are sensitive to dust, so to make sure the pellet won't break inside the instrument, the durability of the pellets is tested with the drop test. The drop test involves the free fall of the pellet from 15 cm distance from a flat surface. The pellets that pass the fall test, show a homogeneous surface without colored spots that would indicate the differentiation within the solid, and have a smooth flat surface, are ready for analysis. The maintenance of the pressing dies is important to achieve the desired smooth flat surface.

Part of the sample preparation is also the calculation of loss on ignition (LOI). Geological samples contain volatiles like CO_2 (e.g. in calcite) and crystalline water (bound H_2O^+ found in OH-bearing minerals like amphiboles or micas). These elements cannot be analyzed with XRF. Modern XRF analytical methods can estimate the LOI without the need of pre-calculation. However, for better accuracy it is recommended to calculate LOI beforehand, by exposing the samples in high temperatures and measuring mass loss (Brouwer, 2003). Approximately 2 grams of the fully dried sample is inserted into a fully dried heat-resistant ceramic capsule and then placed in a high temperature furnace. This protocol suggests first heating the samples at 150°C for 15 minutes and then at 1050°C for 120 minutes, so that the temperature is gradually going up. At 1000°C there is complete removal of volatiles (Lechler & Desilets, 1987). After cooling down, the capsules are weighed to calculate the mass loss. The final goal of this procedure is to calculate the volatile content of the sample so that the LOI % value can be in the sample's final composition to be normalized to 100%. It is highlighted that the samples and crucibles are fully dried before the heating, so that moisture water (H_2O^-) is not confused with bound water (H_2O^+) at the LOI value.

Instrument specifications

The Superimini200 is a benchtop Wavelength Dispersive X-ray Fluorescence (WD-XRF) spectrometer from Rigaku. It is equipped with a Pd anode X-ray tube, operating at 200W power. The X-ray beam is filtered using a Zr filter. The system utilizes two primary crystals: LiF(200) and PET, coupled with two detectors: a flow proportional counter and a scintillation counter. It has a broad elemental detection range from O to U. For analysis on solids, the system operates under vacuum. The instrument requires a P10 gas mixture (10% Ar - 90% CH_4) as its primary consumable. To ensure optimal performance and consistent analytical results, the laboratory environment temperature must be kept below 28°C. The fluctuation in laboratory temperature has been observed to affect drastically the quality of the results, so the importance of maintaining a constant temperature of 20-25°C is highlighted.

Analytical method

The Supermini200 operates using the ZSX Guidance software, which is user-friendly and provides extensive control over the calibration and data analysis. For this study, the analytical method was developed using nineteen certified reference materials (CRMs) from FLUXANA. These standards were carefully selected to cover a wide compositional range, ensuring that the calculated results for unknown samples fall within the calibration range. Specifically, the analytical method achieves optimal precision when the unknown sample's composition lies between the highest standard composition (Point A) and the lowest standard composition (Point B) for each element. Since this analytical method was meant for geological samples, silica content is a useful indicator, so it was essential to cover a large range. The standards that were picked cover the silica range from 35.69% to 73.42%.

The method quantifies major elements in their oxide forms, including SiO_2, Al_2O_3, K_2O, Na_2O, MgO, CaO, TiO_2, MnO, Fe_2O_3, P_2O_5, and SO_3 in percent (%), as well as the trace elements Rb, Sr, Ba, Zr, V, Cr, Co, Ni, Cu, Zn, Pb, Sc, Y, Ga, and Nb in ppm.

The analytical method is classified as a standardized method, more specifically as an empirical analytical method. Its basis is the calibration curve, which is represented graphically from the relationship between the standards' certified analytical values (x axis) and their X-ray fluorescent intensities (y axis). This correlation then is used to obtain the content of the unknown sample by projecting the unknown sample's X-ray intensity on the graph (Brouwer, 2003).

The method includes the «optimizing measuring conditions» (OMC), which determines the measurement conditions for each element. This step is prior to the measurement of the standards and hence the calibration. It is critical because it affects all the next steps, and it would be very time-consuming to go back to adjusting this step after completing the method. For the OMC, standards are first measured with the highest and the lowest content for each element to take scans. The OMC is divided into four parts, determining the peak position, selecting background points position, setting counting time and adjusting the pulse height analyzer (PHA) window. The peak position (2-theta degrees) is unique for each element, there is a theoretical value, but this can vary depending on the laboratory conditions. Background noise from scattered X-rays was negligible for major elements, therefore background points weren't needed. Background points were selected for all the trace elements, with most requiring two points to form linear background (BG) coefficients, except from Co and Sc where three points were selected, forming quadratic BG coefficients. Effective management of measuring time is crucial so that accurate results are achieved without unnecessary delays. Insufficient measuring time can lead to poor precision, while excessive measurement can reduce the efficiency of the method. The measuring times allocated for each element were: 40 seconds (sec) for the peaks of major elements and 40-140 sec for the trace elements, depending on their complexity. For example, 139 sec were chosen for Ba, a challenging element to measure because of its overlap with Ti, whereas 40 sec were sufficient for Ni. Each background point is measured for 10 to 33 sec. The total analysis time is calculated to be 34 minutes per sample. PHA window was widened for all elements to include their entire signal.

Another important part of the analytical method creation is drift correction. Over time, instrument aging, temperature fluctuations and changes in environmental conditions affect the X-ray intensities. To overtake these variations and maintain result stability, drift correction materials are measured on the day the method is created, and the results are stored in the software for the instrument to use during subsequent measurements and adjust accordingly. It works as a monitor to bring the method back to its calibrated state. In this study, the Alpha-Beta drift correction method was applied, using high and low concentration standards for as many elements as possible. Specifically, BR SQ1N and BR SQ3N glass discs from Bruker Corporation were used for Si, Al, K, Na, Mg, Ca, Ti, Mn, Sr, Ba, Zr, Zn and Pb. It is essential to update the drift correction library, before and after any maintenance service of the instrument.

Three corrections were made. First, a mixing ratio correction (0.25) was applied for the binder, using a 1:4 binder-to-sample ratio to account for the dilution effect of the binder on the sample's X-ray fluorescent intensity. Lastly, overlap and matrix corrections were chosen for elements whose peaks overlap or show absorption/enhancement respectively. The analytical element lines with their correction lines are displayed on Table 1.

Table 1. Element lines with their correction line(s)

Element line	Si-KA	Al-KA	K -KA	Ca-KA	Mn-KA	Fe-KA	P -KA	S -KA
Correcting line(s)	Al-KA	Ca-KA Si-KA	Fe-KA	K -KA	Cr-KA	Mn-KA Co-KA Si-KA	Zr-KA Ca-KA	Ti-KA Pb-LA
Element line	Rb-KA	Sr-KA	Ba-LA	Zr-KA	V -KA	Cr-KA	Co-KA	Ni-KA
Correcting line(s)	Sr-KA Al-KA	Ca-KA Rb-KA	Sc-KA Cu-KA Ti-KA	Sr-KA Y -KA	Ti-KA Ba-LA Cr-KA	V -KA	Fe-KA Ni-KA	Y -KA Rb-KA
Element line	Cu-KA	Pb-LA	Sc-KA	Y -KA	Ga-KA	Nb-KA		
Correcting line(s)	Sr-KA	Si-KA Zr-KA	Ca-KA Ti-KA	Rb-KA	Al-KA	Zr-KA V -KA		

The empirical method was converted to Fundamental Parameters (FP) method to achieve greater accuracy (Rousseau, 2013). The empirical method, while effective for calibration, relies heavily on the standards and appears problematic when a sample shows heterogeneity in the matrix. This means that for samples that don't contain a high variety of elements, the empirical method is sufficient to quantify them, with the best accuracy. In the case of rocks where a lot of elements are present and there is a heterogeneous matrix (complex mineral assemblance) there is a misfit (Beckhoff et al., 2007). For a purely empirical method to work well for rocks, an extremely large number of standards would be needed, which is not possible to use. With the conversion of the empirical method to FP, theoretical equations are introduced to correct matrix effects (Rousseau, 2006; Kawai et al., 2019), rather than relying solely on empirical data, but still using them. This way, analysis of samples outside of the exact compositional range of the calibration standards is possible. This hybrid method proved to be more accurate than the purely empirical methods that were developed.

To ensure the ongoing validity of the analytical method, the software provides the ability to input a check sample. This

check sample is used as a consistent reference analyzed every time before a batch of unknown samples is analyzed. It has known composition and standard deviation values, which are predefined within the software. This way, the system automatically flags results that deviate beyond acceptable limits (high and low). It's best to also test the sample preparation process by making new pressed pellets occasionally of the same check sample's powder.

Validation – Accuracy and precision

The validation of an analytical method is a significant step after the calibration, this method was validated in-house (Boqué et al., 2002). For this study, six certified reference materials were used for the validation of the method to cover a wide range of silica content, from 42.38% to 73.42% (CRM values). This is so the validation covers a wide range of concentrations (Boqué et al., 2002) for geological samples. These samples are listed in Table 2 with their basic information.

Table 2. Certified reference materials used for the validation of the method.

No.	FX part number	Manufacturer	Manufacturer's code	Application
1	FI000042	GSJ	JP-1	peridotite
2	FI007834	GSJ	JB-2a	basalt
3	FI000048	GSJ	JSy-1	syenite
4	FI007152	GSJ	JA-1	andesite
5	FI000097	GSJ	DC71302	trachyte
6	FI007981	GSJ	GM	granite

Accuracy and precision are two key properties that determine the quality of the analytical method. Accuracy reflects how close the calculated result is to the true or correct value, while precision indicates the reproducibility of the results (Ragland, 1989).

To assess precision, Ragland (1989) proposes duplicate analyses on five samples, for each major element to calculate the percent deviation or coefficient of variation (V) from equation 1 (Tab. 3). V is perceived as a measure of error or precision. For this study triplicate analyses were carried out on six samples (Tab. 2). Before calculating V, the results per element must be standardized to be comparable. To do that, the average $\bar{x}$ (for each sample) and the grand mean $\bar{x}_G$ (average from all samples) are calculated to find the factor f from equation 2 (Tab. 3). Then, to standardize the results, each calculated value is multiplied with f, equation 3 (Tab. 3). Standard deviation (s) is calculated from the standardized results; hence V is calculated from the standardized results (equation 1 from Tab. 3).

Table 3. Equations used for precision and accuracy measures. Modified from Ragland (1989).

$V = 100s/\bar{x}_G$	equation 1
$f = \bar{x}_G / \bar{x}$	equation 2
f * element %	equation 3
$x^2 = \Sigma[(O-R)^2/R]$	equation 4

For the main major elements Al_2O_3, TiO_2, Fe_2O_3, MgO, CaO, Na_2O, K_2O, Ragland (1989) indicates that V should be < 3-4 % per oxide, whereas for SiO_2 V should be < 2 %. For this study, Al_2O_3, TiO_2, Fe_2O_3, MnO, MgO, CaO, Na_2O, K_2O have V ranging from 0.9 % to 3.9 % and SiO_2 has V = 0.068 %. For P_2O_5 and S_2O_3 V is 4.3 % and 4.9 % respectively, these elements are not approached by Ragland (1989), this V value is accepted because of the small content of P and S in these rocks and the difficulty of quantifying them.

To evaluate accuracy, Ragland (1989) describes the procedure of comparing the certified reference material value and the obtained concentrations for elements in one or more standards. He highlights the importance of these samples not being part of the regression calculations for the calibration curve. As an estimate of accuracy, he uses Chi-Squared (x^2) from equation 4 (Tab. 3), where "O" is the obtained value and "R" is the reference material value. The x^2 is calculated for each single comparison standard for the sum "Σ" of the major elements. This study's major elements had x^2 values ranging from 0.006 to 0.13. Ragland (1989) considers acceptable values for major elements with x^2 < 0.10-0.15.

For better presentation of the results, major and trace elements are projected with their obtained (y-axis) and certified reference material (x-axis) values in figures 1 and 2 respectively. On figures 1 and 2, the equations of the linear regression lines in the form of y = bx + a and the coefficient of determination R squared (R^2) are displayed. The quantity R^2 represents the variation of the data, a value near 1 indicates a good fit, whereas a value near 0 indicates a poor fit (Ross, 2010).
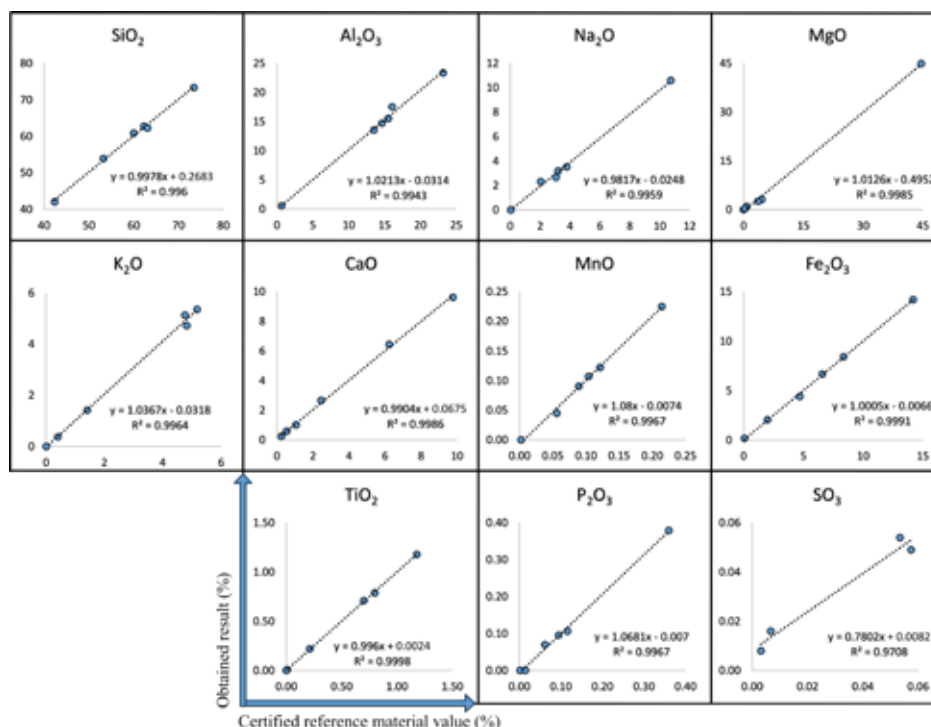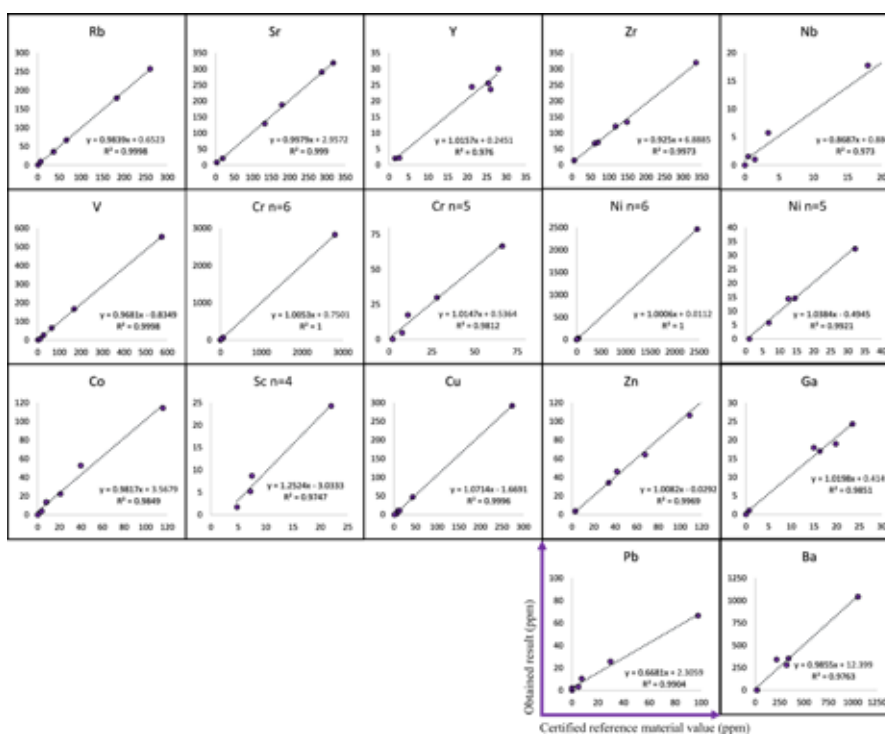
Figure 1. Certified reference material vs obtained result values for the major elements

The results for the major elements showed a coefficient of determination (R^2) higher than 0.99 for the major elements (Fig. 1), except for SO_3 yielding an $R^2=0.97$, which is considered a challenging element with very low content in the rocks studied. These results show excellent fit ($R^2 > 0.95$). This reflects a strong linear relationship between the obtained and the certified reference values.

Figure 2. Certified reference material vs obtained result values for the trace elements.

The results for trace elements (Fig. 2) showed a correlation factor $R^2 > 0.99$ for Rb, Sr, Zr, V, Ni, Cu, Zn, Pb and $R^2 > 0.97$ for Y, Nb, Cr, Co, Sc, Ga, Ba. For Cr and Ni, two diagrams are presented for 6 of the samples (n=6) and 5 samples (n=5), respectively, as one sample had an extremely high content that skewed the. To accurately test correlation between the samples, they must have comparable contents without extreme outliers. For Sc, 4 samples are plotted on the diagram (n=4) because the other two standards lacked certified values.

Limit of detection and limit of quantification for major elements.

Another important aspect of the analytical method set up is the determination of the limit of detection (LOD) and limit of quantification (LOQ). These values ensure the method's capability to reliably detect and quantify elements across the user's preferred concentration range (Shrivastava & Gupta, 2011). The LOD describes the lowest concentration of an element that can be detected but not necessarily quantified. The LOQ is the minimum concentration that can be quantified with acceptable precision and accuracy. For major elements the LOD and LOQ are calculated using equation i and equation ii respectively, with "s" as the standard deviation and "b" as the slope of the calibration curve (Tab. 4).

Table 4. Equations for LOD and LOQ calculation from Shrivastava & Gupta (2011)

LOD = 3s/b	equation i
LOQ = 10s/b	equation ii

For this study, the standard deviation (s) for each major element was calculated based on the average of the obtained results for the sample with the lowest concentration and its certified value (CRM). The slope (b) was derived from the equation $y=bx+a$, as determined from the regression lines presented in Fig. 1 and Fig. 2. The LOD and LOQ calculations, along with the obtained and CRM values, as well as the s and b for each oxide, are presented in Table 5.

The low LOD and LOQ values for major elements confirm the sensitivity of the method.

Table 5. LOD and LOQ values for major elements

Oxide	obtained value %	CRM value %	s	b	LOD %	LOQ %
SiO_2	42.30	42.38	0.0566	0.9978	0.170	0.567
Al_2O_3	0.59	0.66	0.0481	1.0213	0.141	0.471
K_2O	0.37	0.41	0.0276	1.0367	0.080	0.266
Na_2O	0.01	0.02	0.0078	0.9817	0.024	0.079
MgO	0.34	0.37	0.0240	1.0126	0.071	0.237
CaO	0.26	0.25	0.0057	0.9904	0.017	0.057
TiO_2	0.01	0.01	0.0007	0.9960	0.002	0.007
MnO	0.05	0.06	0.0078	1.0800	0.022	0.072
Fe_2O_3	0.10	0.08	0.0113	1.0005	0.034	0.113
P_2O_5	0.10	0.10	0.0007	1.0681	0.002	0.007
SO_3	0.02	0.01	0.0066	0.7802	0.025	0.084

Conclusions

Major element analysis has traditionally been done on fused glass beads, however in this study, major element analysis, in addition to trace elements, has been calibrated on pressed pellets. The accuracy and precision of the method were verified through multiple analyses on certified materials to ensure the reproducibility and results close to their true values. Major element analysis on pressed pellets has also been examined by Yamasaki et al., (2023) with a purely standardized method, who reported correlation results ranging from 0.9525 to 0.9989, thus proposing it for semi-quantitative analysis. The correlation results of the examined method range from 0.9943 to 0.9998 for the same ten main major elements (SiO_2, Al_2O_3, K_2O, Na_2O, MgO, CaO, TiO_2, MnO, Fe_2O_3, P_2O_5). The conversion of a purely empirical standardized method to a fundamental parameters method, could be the cause of the increased accuracy of this study's results. This quantitative analytical method was developed through the process of «trial and error», where adjustments were made based on observed errors until the desired accuracy was achieved. Important factors in creating such a method are sample preparation and corrections application. It is worth noting that this analytical method has been employed for two years at Aristotle University of Thessaloniki, in both undergraduate and postgraduate research. To ensure reliability, drift correction is conducted weekly, and the check sample is analyzed daily ensuring that any variations in instrument performance are corrected, and the results remain consistent and accurate over time.

References

Beckhoff, B., Kanngießer, B., Langhoff, N., Wedell, R., Wolff, H., 2007. Handbook of Practical X-Ray Fluorescence Analysis. Springer Berlin Heidelberg.

Boqué, R., Maroto, A., Riu, J., Xavier Rius, F., 2002. Validation of analytical methods. Grasas y Aceites, 53, 128–143.

Brouwer, P., 2003. Theory of XRF: getting acquainted with the principles. PANalytical BV.

Hickson, C., 1986. Sample contamination by grinding. The Canadian mineralogist, 24, 585–589.

Kawai, J., Yamasaki, K., Tanaka, R., 2019. Fundamental Parameter Method in X □Ray Fluorescence Analysis, in: Meyers, R.A. (Ed.), Encyclopedia of Analytical Chemistry. Wiley, 1–14.

Lechler, P.J., Desilets, M.O., 1987. A review of the use of loss on ignition as a measurement of total volatiles in whole-rock analysis. Chemical Geology, 63, 341–344.

Marguí, E., Queralt, I., 2024. Sample Preparation for X-Ray Fluorescence Analysis. In Encyclopedia of Analytical Chemistry, R.A. Meyers (Ed.), 1-29.

Mojtahed, S., Kohsary, A., Komuro, K., 2006. Investigation of contaminations resulted by tungsten carbide pulverizer and their spectra interference in xrf analysis method. Iranian journal of crystallography and mineralogy, 13, 177-188.

Morikawa, A., 2014. Sample preparation for X-ray fluorescence analysis II. Pulverizing methods of powder samples. Rigaku Journal, 30, 23-27.

Ragland, P.C., 1989. Basic Analytical Petrology. Oxford University Press.

Rainer, S., 2016. Use of X-ray Fluorescence Analysis for the Determination of Rare Earth Elements. Physical Sciences Reviews 1-17.

Roser, B., Kimura, J.-I., Sifeta, K., 2003. Tantalum and niobium contamination from tungsten carbide ring mills: much ado about nothing. Geoscience Report of Shimane University, 22, 107–110.

Ross, S.M., 2010. Linear Regression, in: Introductory Statistics. Academic Press, 537-604.

Rousseau, R.M., 2006. Corrections for matrix effects in X-ray fluorescence analysis—A tutorial. Spectrochimica Acta Part B: Atomic Spectroscopy, 61, 759–777.

Rousseau, R., 2013. How to Apply the Fundamental Parameters Method to the Quantitative X-ray Fluorescence Analysis of Geological Materials. Journal of Geosciences and Geomatics, 1, 1–7.

Saikia, G. C., Sinha, T. K., Kharshiing, F., 2009. Tungsten–cobalt contamination from pulverizing cup. Current Science, 1, 29–30.

Shrivastava, A., Gupta, V., 2011. Methods for the determination of limit of detection and limit of quantitation of the analytical methods. Chronicles of Young Scientists, 2, 21-25.

Takamasa, A., Nakai, S., 2009. Contamination introduced during rock sample powdering: Effects from different mill materials on trace element contamination. Geochemical Journal, 43, 389–394.

Thompson, G., Bankston, D.C., 1970. Sample Contamination from Grinding and Sieving Determined by Emission Spectrometry. Applied Spectroscopy, 24, 210–219.

Yamasaki, S.-I., Yamagishi, H., Tsuchiya, N., 2023. Major element analysis of geological samples with wavelength Dispersive X-ray Fluorescence (WDXRF) spectrometry using glass disks and pressed powder pellets. Sustainable Environment, 9, 1, 1-10.

Yamasaki, T., 2018. Contamination from mortars and mills during laboratory crushing and pulverizing. Bulletin of the Geological Survey of Japan, 69, 201–210.

The Art of Stone in Grevena-Kozani UGGp:
Community-led Conservation Efforts

Ghikas D.[1], Batsi A.[1]

(1) Grevena-Kozani UGGp, Kozani, Greece, geowonders@gmail.com

Introduction / Background

Grevena-Kozani UNESCO Global Geopark

Grevena-Kozani UGGp is located in West Macedonia and covers an area of 2.486km2. The territory joined the UNESCO Global Geoparks Network in 2021 and was the 6th geopark in Greece. UNESCO Global Geoparks (UGGp) are single, unified geographical areas where sites and landscapes of international geological significance are managed with a holistic concept of protection, education and sustainable development. A UNESCO Global Geopark uses its geological heritage, in connection with all other aspects of the area's natural and cultural heritage, to enhance awareness and understanding of key issues facing society, such as using our earth's resources sustainably, mitigating the effects of climate change and reducing natural hazard-related risks. At present, there are 213 UNESCO Global Geoparks in 48 countries (unesco.org).

Geologic Background

The territory boasts exceptional geodiversity, spanning the boundary between the internal and external structural zones of the Hellenides (Ferriere *et al.,* 2013). The geopark includes a large swathe of the Mesohellenic Basin (MHB), a Late-Eocene to Late-Miocene intermontane basin (Doutsos *et al*., 1994) filled with mostly siliciclastic turbidite sequences and shelf originally deposited in the Tethys Ocean, until thrusting of the Hellenide orogeny and post-orogenic extensional tectonics completed the structural evolution of this piggyback basin (Vamvaka, 2009 and references therein).

The MHB is a source of high-quality stone for construction, particularly within the Pentalophos and Eptahori formations which contain many sandstone and siltstone units which are well lithified, fine grained, minimally deformed and have low permeability (Tyrologou *et al.,* 2023). Communities living on or adjacent to outcrops of these rocks took advantage of this resource and developed an industry and culture based on stonework.

The Stone Masters of West Macedonia

Communities which were historical centers of stonework and building are collectively known as Mastorohoria (Master Villages). The craftsmen or masters would build structures out of locally available, high-quality stone and other natural materials. A building gang, or *boulouki,* composed of highly skilled masters, variously specialized technicians and artisans, and low-level workers, would depart from their village to a job site and remain there for many months, until the completion of the project (Poravos, 2023). Many mastorohoria are located within Grevena-Kozani UGGp, principally in the townships of Voio and Grevena, and many more communities and areas of the geopark feature stone architecture including homes, churches and bridges built by these masters.

The 20th century saw a precipitous decline of the Mastorohoria, as industrial building materials flooded the market and economic centers shifted elsewhere. Young males migrated away from the area, and remaining craftsmen did not document their knowledge. Today hardly any skilled workers exist, and many of the historic structures of this territory are in a state of decay, and their future is uncertain as their proper restoration depends on increasingly scarce qualifications. Improper or anachronistic renovations risk exacerbating the collapse of already fragile structures (Lianos, 2012) as well as obscuring their historic and aesthetic value.

In recent years, there has been a renewed interest in reviving the craft of stone building, as the region of West Macedonia has begun to invest in tourism and sustainability. For these efforts to be successful, the technical know-how of the original masters is of vital importance, and every means must be taken to preserve what knowledge remains. Additionally, the recognition of geoheritage, or the linking of geologic science with human society (Rassios and Grieco, 2021), is necessary for the region to be able to sustainably realize the touristic potential of its tangible and intangible cultural heritage.

Recent Community-led Conservation Efforts

In 2024, there were several developments in the revitilization of traditional stone architecture. Grevena-Kozani UGGp was able to contribute to these events and we are confident of long-term partnerships with the people and organizations who are working in this direction.

Announcement: School of Traditional Stoneworking, Pentalophos Voio

In May 2024, an assembly was held in the village of Pentalophos, Voio Township, at which the Minister of Culture, Ms. Lina Mendoni, together with professors from the National Metsovio Polytechnic University of Athens and Utah Valley University, announced the upcoming establishment of a School of Stone and Traditional Building Forms, to be based in the village of Pentalophos. From 21-27 October, these two schools held a field study course in Pentalophos, although the geopark was not able to participate in that event.

1st Traditional Stone Workshop, Kyparissi Grevenon

In August 2024, the 1st Workshop in Traditional Building, Art and Customs of the Craftsman Villages took place in the village of Kyparissi, the first workshop of its kind in the Township of Grevena. The 4-day event was a collaboration between the Community Association of Kyparissi, the Aristotelian University of Thessaloniki (AUTh), and a qualified stone master, Mr. Athanasios Poravos. Registered participants numbered about 30, coming from around the country, and had various backgrounds relating to architecture, engineering and history. Mr. Poravos guided the group through techniques for building a dry-stone wall, in the courtyard of the old stone schoolhouse of the village (now a museum). Participants received hands-on training in cutting, shaping and laying stones from Mr. Poravos, one of the few remaining First Masters in mainland Greece. In addition to the practical sessions, participants had lessons on various aspects of the stoneworking traditions of the region, including the history of vernacular architecture, as well as construction considerations including siting, framing, mortaring and repairing traditional stone structures. In the evenings, the group toured the villages of Kyparissi and Kalloni to examine their traditional building practices and current structural problems, and to learn the history of the area. Dr. Constantinos Katakalos (Dept. of Civil Engineering, AUTh) instructed participants on methods and materials for diagnosing, retrofitting and renovating traditional structures. Geopark staff guided the group through the geologic foundations of the Mastorohoria, with a tour of nearby outcrops and a classroom lesson and discussion on the geologic history of the territory.

Cultural practices related to stone working were also on display throughout the workshop, as local cultural societies, musicians, amateur artists and theater groups reenacted the emotional departure of workers from their communities and their arrival at seasonal building sites. Participants also learned words from *Koudaritika* (Stone Talk), the argo or secret language of the craftsmen, who wished not to be understood by their Ottoman rulers (Poravos, 2023). Events for the public included staged reenactments of some of the customs which marked both the annual departure of the workers from their villages, and the completion of a project. In the village of Sydendro, a village which was largely built by the craftsmen of the Mastorohoria, workshop participants and local authorities reenacted the tradition of *Bahcisia* (Tipping) whereby workers would climb onto the roof of a house which was nearly finished, erect a scaffolding and wooden cross, and pay hyperbolic (and somewhat   ironic) compliments to the owner of the building and his family, in exchange for gifts. This custom has been submitted to UNESCO for recognition as Intangible Cultural Heritage.

Figure 1. Left: historical photograph of a *boulouki*. Right: reenactment of the *Bachcisia*.

8th Workshop on Traditional Building, Pentalophos Voio

In September 2024, Dr. Constantinos Katakalos (Dept. of Civil Engineering, AUTh) led the 8th Workshop on Traditional Building in the village of Pentalophos. Geopark staff were invited speakers and field experts to give the participants, who numbered about 25, geologic and geoheritage context for their studies. They had the opportunity, for most participants their first, to examine outcrops of Pentalophos sandstone and learn about its formation, age, properties

and what criteria should be used in assessing the quality of the stone as building material. They also learned how the landscape and climate influenced the local environment and culture, and received general information about the geopark and its activities. Local stone craftsmen (masters) were also present as honored guests, and at the conclusion of the   workshop, participants received certificates of completion in a   ceremony, officiated by the Pentalophos stone masters.

Conclusions

   The distinctive vernacular architecture of the Mastorohoria, shaped by the local geologic history, is part of the unique character of the region. As West Macedonia strives to diversify its economy and stanch emigration, there is renewed and growing interest in reviving the craftsman traditions. This imperative will only grow as the stone structures of the territory will face continual need for maintenance. Grevena-Kozani UGGp is dedicated to the preservation of its historic stone structures, the continuance of its intangible cultural heritage, and the spread of knowledge about geoheritage—the indivisible bonds between geology and humanity.

Acknowledgements

References

Doutsos, T., Koukouvelas, I., Zelilidis, A., Kontopoulos, N., 1994. Introcontinental wedging and post-orogenic collapse in the Mesohellenic Trough. Geologische Rundschau 83, 257-275.

Ferrière, J., Chanier, F., Reynaud, J., Pavlopoulos, A., Ditbanjong, P. and Coutand, I. 2013. Evolution of the Mesohellenic Basin (Greece): a synthesis. In: (Ed.) Emmanuel Skourtsos, The Geology of Greece - Part II, Journal of the Virtual Explorer, Electronic Edition, ISSN 1441-8142, volume 45, paper 1.

Lianos, N. A., 2012. The Assumption of Mary Church at Dilofo of Kozani: a brief review of missed goals, documentation of the current condition and a restoration study. Πρακτικά 3ου Πανελλήνιου Συνεδρίου Αναστυλώσεων, Εταιρία Έρευνας και Προώθησης της Επιστημονικής Αναστύλωσης των Μνημείων (ΕΤΕΠΑΜ).

Poravos, A., 2023. Δεύτερο Ταξίδι στην Αιωνιότητα. Ατρειδών Κύκλος.

Rassios, A.E., and Grieco, G., 2021, Is geoheritage a "cutting-edge" science? Promotion of an extension to the definition of geoheritage with emphasis as a significant discipline in geosciences with cultural and societal relevance, in Wakabayashi, J., and Dilek, Y., eds., Plate Tectonics, Ophiolites, and Societal Significance of Geology: A Celebration of the Career of Eldridge Moores: Geological Society of America Special Paper 552, p. 37–53, https://doi.org/10.1130/2021.2552(03).

Tyrologou P., Vamvaka A., Koukouzas N. et al., 2023. Progress for carbon dioxide geological storage in West Macedonia: a field and laboratory-based survey. Open Res Europe, 3:85.   DOI: 10.12688/openreseurope.15847.2

Vamvaka, A., 2009. Geometry of deformation and kinematic analysis in Mesohellenic Trough. PhD Thesis, Dept. of Geology, Aristotle University of Thessaloniki, 220p.

www.unesco.org/en/iggp/geoparks/about

Paleoecological imprints of pteropod assemblages and their response to sapropel S1 conditions in the eastern Mediterranean Sea

Giamali C.[1], Kontakiotis G.[2], Antonarakou A.[2]

(1) The Goulandris Natural History Museum, Kifissia, Greece, ch.giamali@gnhm.gr, (2) National and Kapodistrian University of Athens, Faculty of Geology and Geoenvironment, Department of Historical Geology and Paleontology, Panepistimiopolis, Zografou, 15784, Athens, Greece

Research Highlights

Environmental factors during the sapropel S1 interval, affect pteropod assemblages in a way that the development of a precise eco-biostratigraphic scheme for the eastern Mediterranean Sea, seems feasible to accomplish.

Introduction

Pteropods are widespread and abundant in the global ocean and entirely adapted to a pelagic life cycle. They are considered valuable tool in paleoceanographic and paleoclimatic reconstructions due to their sensitivity in the environmental changes (Wall-Palmer *et al.*, 2014). Within the Mediterranean Sea, the preservation of pteropod shells is excellent because of the relatively shallow water, high bottom water temperatures, and the limited number of mud feeders (Herman, 1971). A considerable number of studies present the late Quaternary pteropod assemblages and their distribution pattern in the western and/or central Mediterranean basin (Buccheri *et al.*, 2002; Herman, 1971; Wall-Palmer *et al.*, 2014). In the eastern sector and particularly the Aegean Sea the only available data are that extracted from the gravity cores AEX-15, AEX-23, KIM-2A (Giamali *et al.*, 2019; 2020). These three cores constitute the only high-resolution records that depict their pattern during the deposition of the most recent sapropel S1. In the current work, we focus on understanding the response of the pteropod fauna in environmental changes during the sapropel S1 deposition. To do so, correlations with the distributional patterns of planktic foraminifera were also made. This preliminary attempt may lead to a future establishment of eco-biostratigraphic zonation based on pteropod assemblages.

Material & Methods

For the needs of our study, we used the data published by Giamali *et al.*, (2019; 2021), from two gravity cores, one in the north Aegean Sea, AEX-15, and one in the south Aegean Sea, KIM-2A (Fig. 1). In these cores, a total of 13 species of Euthecosomata (*Heliconoides inflatus, Limacina trochiformis, Limacina bulimoides, Limacina retroversa, Creseis acicula, Creseis sp., Boasia chierchiae, Hyalocyclis striata, Styliola subula, Clio pyramidata* s.l., *Clio cuspidata, Diacria trispinosa, Cavolinia* spp.) were identified. Here, we focus on the species that present a notable distributional pattern and were encountered in both cores in the interval from 10.0 ka to 5.0 ka. These are *H. inflatus, L. trochiformis, C. acicula, C. pyramidata,* and *D. trispinosa.* Furthermore, a correlation was made with planktonic foraminifera species that are common within the sapropel S1 (Cassford *et al.*, 2002; Kontakiotis, 2016). Sapropel layers in AEX-15 spans from 9.6 ka to 6.1 ka (with the interval between 7.0 ka and 6.1 ka being the oxidized part) and in KIM-2A from 9.4 ka to 6.4 ka with the sapropel interruption (S1i) placed at 7.8 ka to 6.8 ka. Comparison of these two cores is challenging and demanding as it includes two regions with different hydrographic characteristics and climate contrasts between more humid conditions in the north and semiarid conditions in the south and (Lykousis *et al.*, 2002). Moreover, data availability differs between the cores, due to higher resolution sampling of AEX-15 core. However, the downcore variation of the fauna enables an initial recognition of the imprints left by environmental changes on the pteropod distribution.
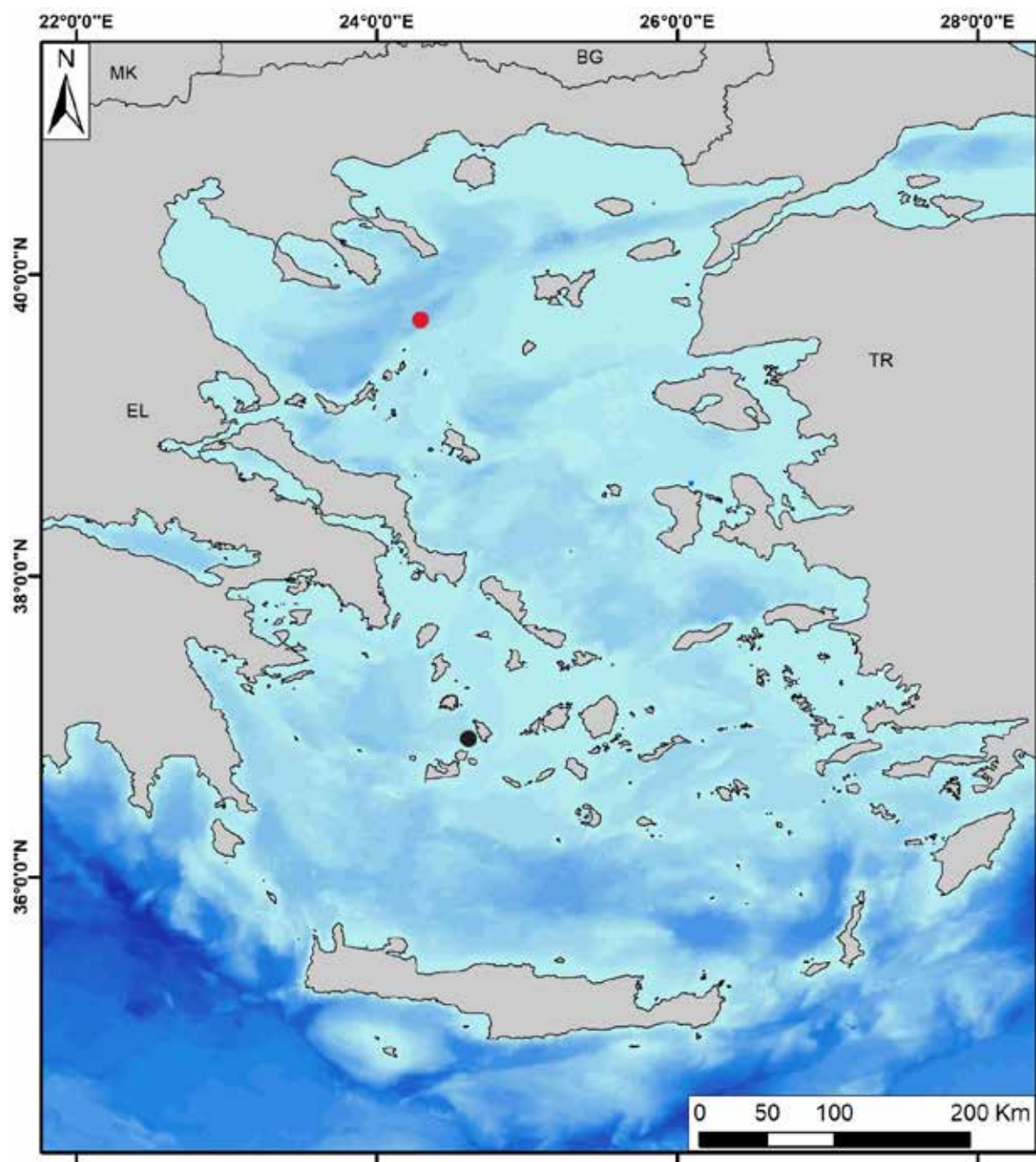
Figure 1. The Aegean Sea and the location of the two gravity cores; AEX-15 with red dot (39°39.900′N, 24°15.369′E; 1242 m water depth, length 178 cm) and KIM-2A with black dot (36°95.4640′N, 24°06.3540′E; 640 m water depth, length 200 cm). Map available via GIS, bathymetry is after (Ioc, 2003) country names are given by © EuroGeographics for the administrative boundaries (Eurostat).

Results & Discussion

As the distributional pattern of the plankton fauna is presented exhaustively in Giamali *et al*., (2019, 2020), herein we focus on the paleoecological aspects that are reflected in the downcore variation of specific pteropod species (Fig. 2). During the sapropel S1 deposition, an increase in temperature and humidity has been documented in all marine records in the eastern Mediterranean region (Giamali *et al*., 2019; Kontakiotis, 2016). This paleoclimate change coincides with the Holocene summer precession-related insolation maximum in the Northern Hemisphere (Laskar *et al*., 2004), and the monsoon intensification that resulted in a widespread increase in humidity over the entire Mediterranean region as well as the concomitant increase of freshwater inputs mainly to the eastern Mediterranean (Rohling, 1994; Rossignol-Strick, 1983).
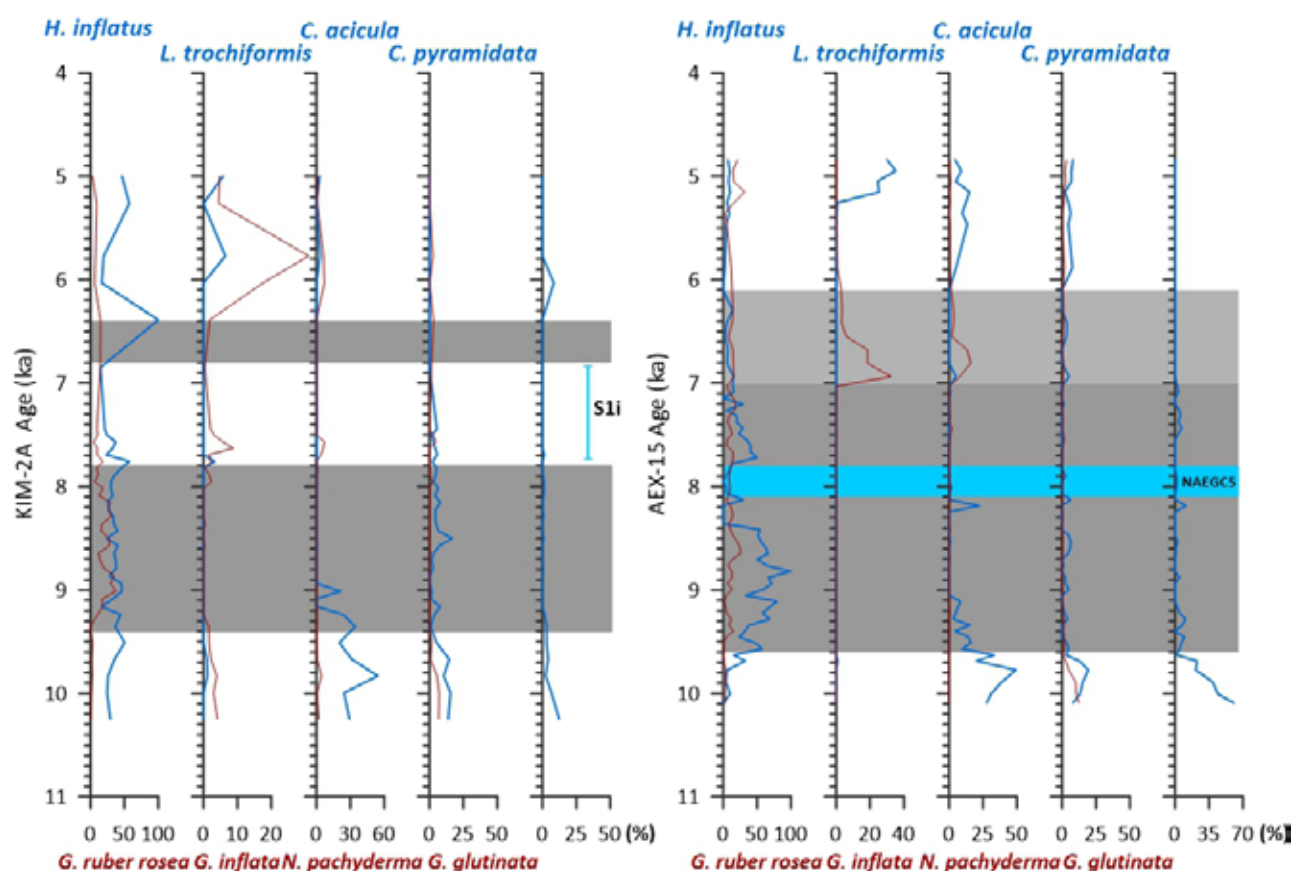
Figure 2. Downcore variations of selected pteropod and planktonic foraminifera species. Blue line corresponds to pteropods, dark red line to planktonic foraminifera. Gray bands correspond to the sapropel S1a and S1b in the core KIM-2A. Gray and light gray bands correspond to the sapropel S1 and its oxidized part in the core AEX-15. S1i interval is depicted in core KIM-2A, and the cooling event NAEGC5 in core AEX-15.

The warm-water mesopelagic *H. inflatus,* presents high percentages during the S1 deposition followed by a notable reduction during the S1i interval in core KIM-2A, and during the cooling event NAEGC5 (Giamali *et al.*, 2019). The distribution pattern of this species can be correlated well with that of the warm indicator *Globigerinoides ruber rosea*. Both species can provide a complete overview of the water column as the former lives at a depth ranging from 200-1000 m, whereas the latter is considered as indicative of warm surface waters (Pujol and Vergnaud-Grazzini, 1995). Though *H. inflatus*, seems to reflect better the temperature fluctuations. The epipelagic *L. trochiformis,* is associated with the mixed layer in the upper water column thriving in upwelling conditions (Bé and Gilmer, 1977). Such ecological preferences explain its absence from the S1 interval (Fig. 2). It can be correlated to *Globoconella inflata* which reflects deep seasonal mixing conditions (Hemleben *et al.*, 1989), such as those dominated during the S1i interval characterized by the breakdown of the stratification (Kontakiotis, 2016; Geraga *et al.,* 2010). It is notable that *L. trochiformis* bounds the S1a layer in the core KIM-2A and the termination of S1 layer in core AEX-15 (at 7.0 ka), suggesting the prevalence of homogenization/overturn conditions in the upper water column.

Creseis acicula is a warm-water, euryhaline species that has the shallowest depth habitat amongst all epipelagic pteropods (Liu *et al.*, 2022). This specific habitat most probably led to its outbreak as high percentages during the last 0.7 – 1.5 ka before the onset, and the first 0.3 ka of the sapropel S1 are observed (Fig. 2). This pattern may mark both the rising temperature and the increase of freshwater input in the Mediterranean Sea that may increase the ingestion and assimilation rates of the species for algal food (Liu *et al.,* 2022). Its reduction afterwards may mark the change in environmental conditions or an increase in competitors and/or predators (Dai *et al.*, 2020).

The mesopelagic species *C. pyramidata* and *D. trispinosa* on the contrary are less tolerant in high temperatures and in salinity fluctuations, and prefer a well-ventilated water column (Buccheri *et al.,* 2002; Giamali *et al.*, 2020), which explains their low percentages during the S1 interval. Their abrupt decline is correlated with the onset of S1 deposition in both cores. A similar downcore record can be seen through the distributional pattern of the planktonic foraminifera *Globigerinita glutinata*.

Conclusions

Based on the faunal distribution of two gravity cores of north and south Aegean Sea, the biotic response of specific pteropod species in environmental changes during the sapropel S1 deposition was made. In particular, temperature, salinity, stratification and food availability are the factors that affect the distribution of the examined species. The observed data if enhanced by new records within and beyond the Aegean basin, can give more insights for the establishment of a precise regional eco-biostratigraphic scheme.

Acknowledgements

References

Bé, A.W.H., Gilmer, R.W., 1977. A zoogeographic and taxonomic review of euthecosomatous Pteropoda. Oceanic Micropaleontology 1, 733-808.

Buccheri, G., Capretto, G., Di Donato, V., Esposito, P., Ferruzza, G., Pescatore, T., Russo Ermolli, E., Senatore, M.R., Sprovieri, M., Bertoldo, M., Carella, D., Madonia, G., 2002. A high resolution record of the last deglaciation in the southern Tyrrhenian Sea: environmental and climatic evolution. Marine Geology 186, 3, 447-470.

Casford, J.S.L., Rohling, E.J., Abu-Zied, R., Cooke, S., Fontanier, C., Leng, M., Lykousis, V., 2002. Circulation changes and nutrient concentrations in the late Quaternary Aegean Sea: A nonsteady state concept for sapropel formation. Paleoceanography 17, 2, 14-11-14-11.

Geraga, M., Ioakim, Chr., Lykousis, V., Tsaila Monopolis, St, Mylona, G., 2010. The high resolution palaeoclimatic and palaeoceanographic history of the last 24,000 years in the central Aegean Sea, Greece. Palaeogeography Palaeoclimatology Palaeoecology 287, 101e115.

Giamali, C., Kontakiotis, G., Koskeridou, E., Ioakim, C., Antonarakou, A., 2020. Key Environmental Factors Controlling Planktonic Foraminiferal and Pteropod Community's Response to Late Quaternary Hydroclimate Changes in the South Aegean Sea (Eastern Mediterranean). Journal of Marine Science and Engineering, 8, 9.

Giamali, C., Koskeridou, E., Antonarakou, A., Ioakim, C., Kontakiotis, G., Karageorgis, A. P., Roussakis, G., Karakitsios, V., 2019. Multiproxy ecosystem response of abrupt Holocene climatic changes in the northeastern Mediterranean sedimentary archive and hydrologic regime. Quaternary Research, 92, 3, 665-685.

Kontakiotis, G., 2016. Late Quaternary paleoenvironmental reconstruction and paleoclimatic implications of the Aegean Sea (eastern Mediterranean) based on paleoceanographic indexes and stable isotopes. Quaternary International 401, 28-42.

Laskar, J., Robutel, P., Joutel, F., Gastineau, M., Correia, A.C.M., Levrard, B., 2004. A long-term numerical solution for the insolation quantities of the Earth. A&A, 428, 1, 261-285.

Liu, O., Zhou, L., Zhang, W., Zhang, L., Tan, Y., Han, T., Dai, M., Liao, X., Huang, H., 2022. Rising temperature contributed to the outbreak of a macrozooplankton Creseis acicula by enhancing its feeding and assimilation for algal food nearby the coastal Daya Bay Nuclear Power Plant. Ecotoxicology and Environmental Safety 238, 113606.

Lykousis, V., Chronis, G., Tselepides, A., Price, N.B., Theocharis, A., Siokou-Fragou, I., van Wambeke, F., Danovaro, R., Stavrakakis, S., Duineveld, G., Georgopoulos, D., Ignatiades, L., Souvermezoglou, A., Voutsinou-Taliadouri, F., 2002. Major outputs of the recent multidisciplinary biogeochemical researches undertaken in the Aegean Sea. Journal of Marine Systems 33e34, 313e334.

Dai, M., Qi, Z., Zeng, L., Zhang, S., Wang, L., Qin, X., Liao, X., Yan, J., Huang, H., Shang, S., 2020. An unprecedented outbreak of pelagic molluscs Creseis acicula in Daya Bay, South China Sea. Authorea Prepr.

Hemleben, C., Spindler, M., Anderson, O.R., 1989. Modern planktonic Foraminifera. Springer.

Herman, Y., 1971. Vertical and horizontal distribution of pteropods in Quaternary sequences, in: Funnell, B. M., Reidel, W. R., (Eds.), The Micropalaeontology of Oceans, 463–486.

Pujol, C., Vergnaud-Grazzini, C., 1995. Distribution patterns of live planktic foraminifers as related to regional hydrology and productive systems of the Mediterranean Sea. Marine Micropaleontology 25, 187-217.

Rohling, E.J., 1994. Glacial conditions in the Red Sea. Paleoceanography, 9, 5, 653-660.

Rossignol-Strick, M., 1983. African monsoons, an immediate climate response to orbital insolation. Nature 304, 5921, 46-49.

Wall-Palmer, D., Smart, C. W., Hart, M. B., Leng, M. J., Borghini, M., Manini, E., Aliani, S., Conversi, A., 2014. Late Pleistocene pteropods, heteropods and planktonic foraminifera from the Caribbean Sea, Mediterranean Sea and Indian Ocean. Micropaleontology 60, 6, 557-578.

Correlation study of overland and marine aggregates capable to be used in various construction applications

Giannakopoulou, P.P.[1], Rogkala, A.[1], Lampropoulou, P.[1], Koutsovitis, P.[1], Kalpogiannaki M.[2], Giamas V.[1], Seikatis, O.[1], Islam I.[3], Petrounias, P.[1]

(1) Department of Geology, University of Patras, Patras, Greece, peny_giannakopoulou88@outlook.com (2) Section of Mineralogy and Petrology, Department of Geology and Geoenvironment, National and Kapodistrian University of Athens, Panepistimioupolis Zografou, 157 84 Athens, Greece (3) Department of Geology, Shaheed Benazir Bhutto University Sheringal, Dir Upper, 18030, Pakistan

Introduction

Ophiolitic rocks are used extensively as engineering materials in applications such as road construction, concrete and railway ballast (Rigopoulos *et al.*, 2010, Rigopoulos *et al.*, 2015, Petrounias *et al.*, 2016, Petrounias *et al.*, 2018, Giannakopoulou *et al.*, 2018). The suitability of aggregates for their applications is determined by evaluating their physical, physicochemical and mechanical properties, which are collectively known as engineering properties.

Nowadays, natural aggregate sources are depleting, and their mining impacts the environment adversely. In this direction, during the last decades, marine aggregates exploitation increases due to the high demand for material supply regarding construction industry (Velegrakis *et al.*, 2010). Also, marine aggregates play a crucial role in meeting the demand for construction materials, coastal protection, and beach replenishment. On average, in Europe, almost 60 million tonnes of marine aggregates are extracted from the sea used for construction and as a strategic material in supplying large scale coast defense and beach replenishment projects. The contribution of marine dredged sand and gravel resources as part of the wider portfolio of construction aggregate supply is growing in importance. Where local primary aggregates are constrained, either because resources are not geologically present or because existing resources have become depleted, alternative sources of supply have to be found. Economies of scale allow marine aggregate supplies to play an important role using a fleet of highly specialized dredgers to load sand and gravel from licensed areas located around the coast of England and Wales.

"The main use of marine aggregates is in the manufacture of concrete. Nearly 80% of the marine aggregates landed for construction purposes are used as concrete aggregate, increasing to nearly 90% in London and the south-east of England. By contrast 60% of land-won sand and gravel production and 16% of crushed rock is sold as concrete aggregate," says the organization. Indeed, while the largest use of marine aggregates is in construction, they are also widely used for the production of asphalt and coated products; masonry and paving blocks; drainage and fill materials; leisure facilities; sports pitches; golf courses; equestrian facilities; horticulture products; steel manufacture and beach replenishment. So, it is not surprising that worldwide production is on the increase. Therefore, it is necessary to optimize the river sand consumption while, at the same time, increasing the use of alternate sources to replace them. There is a wide use of marine sand as fine aggregate material in cement mortar and concrete (Limeira *et al.*, 2012, Xiao *et al.*, 2017, Ganesan *et al.*, 2022).

Marine aggregate extraction is closely regulated to protect the environment. Expert studies are undertaken to help inform license decisions and permission will be refused if there is any concern about impacts on the coastline or any other environmental or economic interests.

The aim of this study is, on the one hand, to evaluate the engineering properties of the tested aggregates, whether overland or marine, and on the other hand, to conduct a comparative study between them in order to identify whether the properties of aggregates change from the area where it is currently possible to locate them.

Materials and Methods Geological Setting of aggregate samples

Ten block samples of ultramafic rocks (five overland and five marine blocks) from Gerania ophiolite complex were collected according to the EN 932-1 standard to evaluate their suitability as aggregates for construction applications (Figure 1).

Figure 1. (a,b) overland ultramafic aggregate rock samples from Gerania ophiolite complex, (c,d) marine ultramafic aggregate rock samples from Gerania ophiolite complex.

The Gerania Ophiolite Complex belongs to the Pelagonian geotectonic zone of the internal Hellenides. They comprise a Permian sedimentary and volcanic succession overlain by a series of carbonate rocks and lesser radiolarites (Clément, B.,1971, Bornovas, J,. 1981, Vacondios, I., 1997, Giannakopoulou *et al*., 2018). This succession is tectonically overlain by an ophiolite sequence. The ophiolite is a NE-trending rhomb-shaped outcrop, with approximately 10 km in length and 5 km in width, representing an incomplete and dismembered ophiolite sequence. It is dominated by variably serpentinized and tectonized lherzolite, locally crosscut by thin pyroxenite dykes with subordinate harzburgite and dunite (Figure 2). These serpentinized peridotites are interrupted by gabbro dykes, some of which have been transformed into rodingites. An ophiolite mélange includes fragments of lavas, serpentinized peridotites, gabbros, oceanic sediments previously described as schist-chert formation, as well as an amphibolite metamorphic sole tectonically underlie the ophiolite.
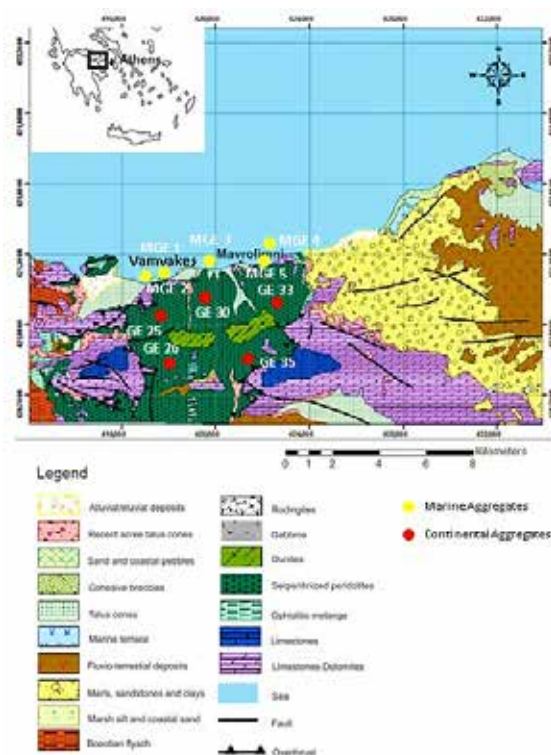
Figure 2. Geological map of the Gerania region (Giannakopoulou *et al.,* 2018), the rectangle in the inset shows the study area.

Analytical methods

All aggregate rock samples have petrographically been observed by variety of petrographic methods. The mineralogical and textural characteristics of the samples were studied in polished-thin sections using a polarizing optical microscope (Leitz Ortholux II POL-BK Ltd., Midland, ON, Canada), according to the EN-932-3 standard for the petrographic description of aggregates. The engineering properties of the tested aggregates were determined in the Research Laboratory of Minerals and Rocks, Department of Geology, University of Patras, Patra, Greece. Moisture content (w) was measured in accordance to the AASHTO T-255 standard, the Los Angeles (LA) test was carried out in accordance to the ASTM C-131 standard using the "B" gradation. The Uniaxial Compressive Strength (UCS) was determined from the average value of six cylindrical rock specimens for each sample with diameters ranging from 51 to 54 mm and their height/diameter ratios between two and three for each sample (ASTM D-2938). As for the geometrical properties of the tested aggregates, the flakiness index (I_F) and the elongation index (I_E) were performed according to the BS 812 Part 105.1 and 105.2 correspondingly.

Results and Discussion

Petrographic features

Peridotites from the Gerania ophiolite complex include lherzolite and harzburgite with low to moderate degrees of serpentinization and deformation even they are overland or marine. Lherzolite shows protogranular, porphyroclastic and locally cataclastic textures. Their primary minerals are olivine, orthopyroxene and clinopyroxene. Opaque minerals (mainly Al-spinel in light brown color) are present in small amounts. Porphyroclastic texture is characterized by large orthopyroxene, clinopyroxene and olivine clasts in a finegrained matrix made up of recrystallized olivine neoblasts. Serpentine is the main secondary mineral, which shows mostly mesh and locally ribbon textures. The effect of serpentinization also leads to the replacement of orthopyroxene from bastite. The secondary assemblage is completed by chlorite and actinolite. Also, a dense network of microcracks is observed. The harzburgite presents mainly porphyroclastic and locally cataclastic textures. Its primary assemblage includes olivine, orthopyroxene and rare clinopyroxene. Olivine appears as porphyroclasts, which present strong deformation, as well as small-sized unstrained neoblasts. Frequent replacement of orthopyroxene from olivine neoblasts is also observed. Al-spinel in light brown color and Cr-spinel characterized in red-brown color are present in small amounts, some of which display embayed margins and rims altered to secondary magnetite. A dense network of microcracks also occurs in the harzburgite. The serpentine comprises the most common secondary phase presenting ribbon texture; minor chlorite occurs as well. Regarding the tested aggregate samples (overland and marine), the only remarkable variation that appears is the degree of oxidation of the metallic minerals, which is likely due to the entry of seawater into the intercrystalline cracks, where it creates conditions for their extensive oxidation. The remaining secondary minerals do not appear to show any change in any environment they have been exposed to.
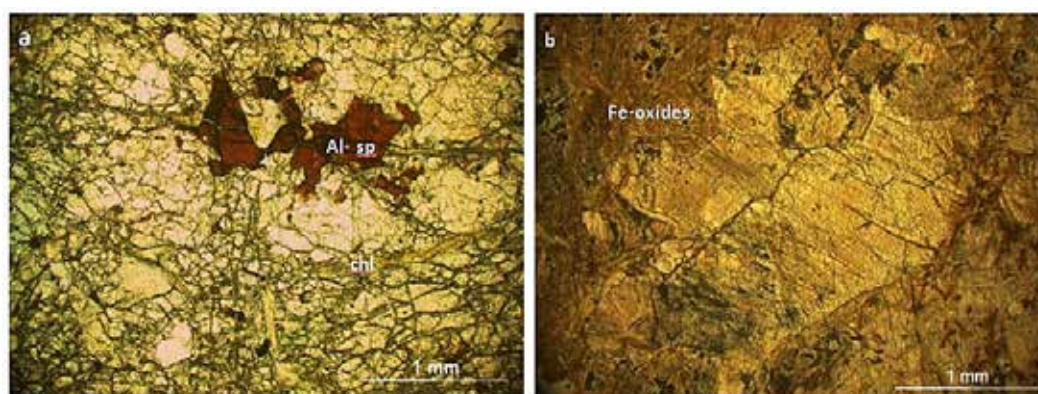
Figure 3. Photomicrographs of (a) overland lherzolite where chlorite is occurred and Al-spinel, (b) marine lherzolite which present high oxidation.

Engineering properties

The values of the engineering properties are summarized below in Table 1. In general, the results show that the overland and marine aggregates present similar physicomechanical characteristics. A small decrease in the mechanical strength of the marine lherzolites is observed compared to the overland ones. More specifically, it seems that the physical properties present a similar variation which may be attributed to the different degree of alteration.

This fact regarding the physical properties is also confirmed by the petrographic study which did not reveal significant differences. The same conclusion has also been conducted by the results of the geometric properties, where the more serpentinized are the aggregates the more elongated grains present. There is no significant difference among them depending on their origin (overland or marine).

Table 1. Engineering properties of the tested aggregate rocks (*GE: overland aggregates, MGE: marine aggregates, w: moisture content, I_F: Flakiness Index, I_E: Elongation Index, LA: Los Angeles, UCS: Uniaxial Compressive Strength).

Samples	Engineering Properties				
	W (%)	I_F (%)	I_E (%)	LA (%)	UCS (MPa)
GE25	0.78	22.54	34.17	15.90	79.0
GE26	0.91	33.90	32.33	19.6	66.0
GE30	0.92	26.84	34.16	16.60	75.0
GE33	0.08	16.25	30.16	20.90	69.1
GE35	0.69	25.15	24.51	23.90	76.0
MGE1	2.60	28.53	27.67	25.60	42.0
MGE2	2.30	29.56	31.25	24.35	49.0
MGE3	2.10	27.84	32.89	26.48	48.0
MGE4	0.90	29.95	34.52	27.00	54.0
MGE5	2.80	31.00	36.01	26.68	39.0

Regarding the mechanical properties UCS and L.A, a small reduction of the properties is shown in marine aggregates, which is probably due to the extensive oxidation of the secondary minerals where they can result in extensive intercrystalline microcracks that can act as surfaces of weakness and cause fractures. Several scientists have conducted similar conclusions when investigated the mechanical behavior of mafic rocks (Petrounias *et al.,* 2018). Giannakopoulou et al. 2018 considered that the increase of alteration such as serpentinization in ultramafic rocks strong influences the physical and mechanical properties of rocks. This happens because the soft and platy nature of serpentine constitutes a critical factor for the development of extensive porous areas, which are weak. The above result, although presented in all the examined samples, it should not be generalized because the mentioned variation may be result of the degree of serpentinization. However, the results of the present study are particularly encouraging as marine aggregates appear to be a quite valuable alternative way to replace overland aggregates.

Conclusions

The engineering characteristics of the tested marine peridotites are generally identical to the tested overland peridotites used as aggregates and hence these results are particularly encouraging for the replacement of the overland aggregates with the corresponding marine. However, it should be mentioned that a study like this in order to conduct a safer conclusion must combine the research results of many scientific fields such as engineering geology, applied petrography and marine geology.

Acknowledgements

References

AASHTO T255 (American Association of State Highway and Transportation Officials). Standard Method of Test for Total Evaporable Moisture Content of Aggregate by Drying; AASHTO: Washington, DC, USA, 2000.

ASTM C-131. Resistance to Abrasion of Small-Size Coarse Aggregate by Use of the Los Angeles Machine; American Society for Testing and Materials: Philadelphia, PA, USA, 1989.

ASTM D-2938. Standard Test Method of Unconfined Compressive Strength of Intact Rock Core Specimens; Annual Book of Standards, 4.08; American Society for Testing and Materials: Philadelphia, PA, USA, 1986.

Bornovas, J. 1981. Geological map of Greece, Kapareli Sheet, 1:50.000; IGME: Athens, Greece.

BS 812, Testing Aggregates, Part 105: Methods for Determination of Particle Shape. Section: 105.1: Flakiness Index; British Standards Institution: London, UK, 1989.

BS 812, Testing Aggregates, Part 105: Methods for determination of particle Shape. Section: 105.2: Elongation Index; British Standards Institution: London, UK, 1990.

Clément, B. 1971. Découverte d'un flysch éocrétacé en Béotie (Grèce overlande). C. R. Acad. Sci., 272, 791–792.

EN 932. Part 3: Procedure and Terminology for Simplified Petrographic Description; European Standard: Pilsen, Czech Republic, 1996.

EN 932-1. Part 1: Composition, Specifications and Conformity Criteria for Common Cements; European standard: Pilsen, Czech Republic, 2011.

Giannakopoulou, P. P., Petrounias, P., Rogkala, A., Tsikouras, B., Stamatis, P. M., Pomonis, P., Hatzipanagiotou, K. 2018. "The Influence of the Mineralogical Composition of Ultramafic Rocks on Their Engineering Performance: A Case Study from the Veria-Naousa and Gerania Ophiolite Complexes (Greece)" Geosciences 8, no. 7: 251. https://doi.org/10.3390/geosciences8070251

Limeira, J., Agulló, L., Etxeberria, M. 2012. Dredged marine sand as construction material European Journal of Environmental and Civil Engineering 16 906–18.

Petrounias, P., Giannakopoulou, P.P., Rogkala, A., Stamatis, P.M., Tsikouras, B., Papoulis, D., Lampropoulou, P., Hatzipanagiotou, K. 2018. The Influence of Alteration of Aggregates on the Quality of the Concrete: A Case Study from Serpentinites and Andesites from Central Macedonia (North Greece). Geosciences, 8, 115.

Petrounias, P., Rogkala, A., Kalpogiannaki, M., Tsikouras, B., Hatzipanagiotou, K. 2016. Comparative study of physico-mechanical properties of ultrabasic rocks (Veria-Naousa ophiolite) and andesites from central Macedonia (Greece). Bull. Geol. Soc. Gr. 50, 1989–1998.

Petrounias, Petros, Panagiota P. Giannakopoulou, Aikaterini Rogkala, Panagiotis M. Stamatis, Paraskevi Lampropoulou, Basilios Tsikouras, and Konstantin Hatzipanagiotou. 2018. "The Effect of Petrographic Characteristics and Physico-Mechanical Properties of Aggregates on the Quality of Concrete" Minerals 8, no. 12: 577. https://doi.org/10.3390/min8120577.

Rigopoulos, I., Tsikouras, B., Pomonis, P., Hatzipanagiotou, K. 2010. The influence of alteration on the engineering properties of dolerites: The example from the Pindos and Vourinos ophiolites (northern Greece). Int. J. Rock Mech. Min. Sci. 47, 69–80.

Rigopoulos, I., Tsikouras, B., Pomonis, P., Hatzipanagiotou, K. 2015. Assessment of the engineering behavior of ultramafic and mafic rocks using chemical indices. Eng. Geol. 196, 222–237.

Vacondios, I. 1997. Etude Metallogenique des Chromites Liees aux Ophiolites de Type Mediterranee Occdentale ou orientale: Le chromites de Tinos et des Gerannees. Ph.D. Thesis, University of Patras, Patras, Greece, Volume 98.

Velegrakis, A., Ballay, A., Poulos, S., Radzevicius, R., Bellec, V., Manso, F. 2010. European marine aggregate resources: Origins, usage, prospecting and dredging techniques. Journal of Coastal Research, S151.

Xiao, J., Qiang, C., Nanni, A., Zhang, K. 2017. Use of sea-sand and seawater in concrete construction: current status and future opportunities Constr. Build. Mater. 155 1101–11.

17th INTERNATIONAL CONGRESS of the Geological Society of Greece

Estimation of an empirical relationship for calculating quantities of demolished materials through three-dimensional visualization of buildings affected by the earthquake of June 12, 2017, in Vrisa, Lesvos.

Giannakou A., Soulakellis N., Zouros N., Kavroudakis D.
Affiliation : University of the Aegean, Department of Geography

Intoduction

Natural disasters, particularly earthquakes, can cause severe social, economic, and environmental disruptions. These include fatalities, injuries, infrastructure failures, and challenges related to waste management. Post-disaster debris management is critical due to its implications for public health, environmental preservation, and the efficiency of relief operations. Accurate estimation of the volume and composition of building debris is essential for effective waste management planning.

Objectives

This study aims to develop a rapid methodology for estimating construction and demolition waste C&DW quantities generated after natural disasters using geospatial data. Initially, an attempt will be made to estimate C&DW production rates based on footprint measurements for different building categories. These estimates can be used both for calculating the quantities of various waste streams according to the European Waste Catalogue classification system and for determining total waste quantities at both the building and area levels. Subsequently, using empirical data from demolished buildings, an effort will be made to construct a mathematical formula that calculates the quantities of construction waste in volume and weight units, utilizing independent variables (building characteristics).

Methods

Specifically, the study will investigate the impact of the number of floors and footprint area of buildings on the estimation of waste quantities resulting from collapses or demolitions of buildings severely affected by a natural disaster. These variables are chosen because empirical data for them can be easily and quickly collected with high accuracy through the use of geoinformatics systems, either before or after the occurrence of the disaster. The estimation of the mathematical model will be performed using the method of multiple linear regression, a widely used and powerful statistical tool for estimation based on empirical data. In this analysis, for the first time, detailed data are available at the building level for 182 structures following a catastrophic event, specifically the Vrisa earthquake of June 12, 2017 (6.3 Mw) analyzed at three different scales: area scale, street scale and building scale.
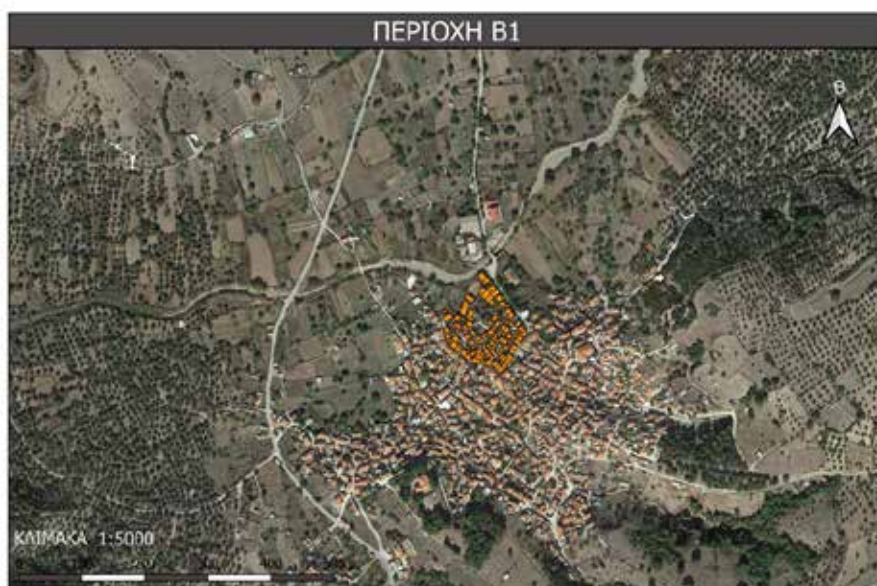
Map 1: Map of Area B1, Vrisa Settlement

Using 140 point clouds and 240 3D models obtained from terrestrial laser scanners and terrestrial photogrammetry, along with two orthophotos, two digital terrain models and a digital surface model generated by UAVs, a wealth of empirical data has been gathered at both area and building levels. This data facilitates the development of a model to calculate C&DW quantities following a disaster.

Figure 1. A section of the 3D model from July 25, 2017, generated from high-resolution images taken by unmanned aerialvehicles (UAVs), N. Soulakellis, S. Chatzistamatis, C. Vasilakos, G. Tataris, A. Papakonstantinou, D. Kavroudakis, K. Topouzelis, O. Roussou, Ch. Kalloniatis, E. E. Papadopoulou, K. Chaidas, P. Kalaitzis, (2018)

Results

As part of this study, an initial attempt was made to estimate the rates of demolition waste production in volume and weight per square meter of floor plan for various categories of buildings. In the study area, the most prevalent use of buildings consists of residences and warehouses, which is logical for a small traditional village on an island, such as Vrisa. Thus, it was deemed necessary to create a separate categorization of the buildings in these two uses based on the number of floors, the type of exterior masonry, and the method of roofing. These data can easily be derived using GIS, as well as through on-site visits to an affected area after a natural disaster. Four tables of weight and volume values of waste per square meter of floor area were compiled in total for different types and codes of construction waste, in accordance with the European Waste Catalogue, as well as overall for each building category. These values can be used for a quick calculation of potential quantities of waste from collapses and demolitions of buildings that may be damaged after a catastrophic event, as well as the total quantities of waste in an affected area. To summarize, buildings with storage use have an average of 2,470 kg/m² and 1.47 m³/m² of generated construction waste, while buildings with residential use have an average of 4,170 kg/m² and 2.40 m³/m² of generated construction waste.

In addition, using the processed data for 182 buildings in the B1 sector of Vrisa, four mathematical formulas were calculated for estimating construction waste and are presented below in a table format.

Table 1: Consolidated table of the four mathematical formulas with their variables and weights.

|	Y	β_0	β_1	x_1	β_2	x_2
				Equation of the form $Y = \beta_0 + \beta_1 \cdot x_1 + \beta_2 \cdot x_2$		
1.	Weight (kg)	-130242.6	48903.4	Building Height (m)	1332.6	Building floor area (m^2)
2.	Volume (m^3)	-58.85607	22.78869	Building Height (m)	0.74388	Building floor area (m^2)
3.	Weight (kg)	-147134.0	154491.7	Number of floors	1734.2	Building floor area (m^2)
4.	Volume (m^3)	-64.66171	70.11125	Number of floors	0.94282	Building floor area (m^2)

To examine the relationship between the variables, four multiple linear regression analyses were conducted, where the dependent variables were waste weight (kg) and waste volume (m³), while the independent variables included building height (m), floor area (m²), and the number of floors.

The results indicated that the fitted models were statistically significant, explaining a substantial proportion of the variance in the dependent variables.

1. Waste weight (kg) as the dependent variable with building height and floor area as independent variables
   - $F_{(2,179)} = 320.30$, $R^2 = 0.782$, $p < 0.001$
   - Building height: $\beta = 48{,}903.4$, $t = 18.092$, $p < 0.001$
   - Floor area: $\beta = 1{,}332.6$, $t = 7.809$, $p < 0.001$
2. Waste volume (m³) as the dependent variable with building height and floor area as independent variables
   - $F_{(2,179)} = 528.5$, $R^2 = 0.8552$, $p < 0.001$
   - Building height: $\beta = 22.79$, $t = 22.16$, $p < 0.001$
   - Floor area: $\beta = 0.74$, $t = 11.46$, $p < 0.001$
3. Waste weight (kg) as the dependent variable with the number of floors and floor area as independent variables
   - $F_{(2,179)} = 262.40$, $R^2 = 0.7457$, $p < 0.001$
   - Number of floors: $\beta = 154{,}491.7$, $t = 15.992$, $p < 0.001$
   - Floor area: $\beta = 1{,}734.2$, $t = 9.866$, $p < 0.001$
4. Waste volume (m³) as the dependent variable with the number of floors and floor area as independent variables
   - $F_{(2,179)} = 359.70$, $R^2 = 0.8008$, $p < 0.001$
   - Number of floors: $\beta = 70.11$, $t = 17.55$, $p < 0.001$
   - Floor area: $\beta = 0.94$, $t = 12.97$, $p < 0.001$.
   -

These findings confirm that building height, floor area, and the number of floors are strong predictive factors of waste volume and weight, with all β coefficients being statistically significant.

Subsequently, we created the necessary diagnostic plots to check the assumptions of the linear model regarding the residuals. From the first plot, we observe that the red line partially follows the horizontal dashed line, indicating that there do not appear to be issues with linearity. In the second plot, since the points follow the dashed line, the assumption of normality of the residuals is satisfied. In the third plot, the red line is almost flat, thus fulfilling the assumption of homoscedasticity. In the fourth plot, the solid red line remains close to the grey horizontal dashed line, and none of the points exhibit a Cook's distance greater than 0.5, indicating that there are no influential observations."
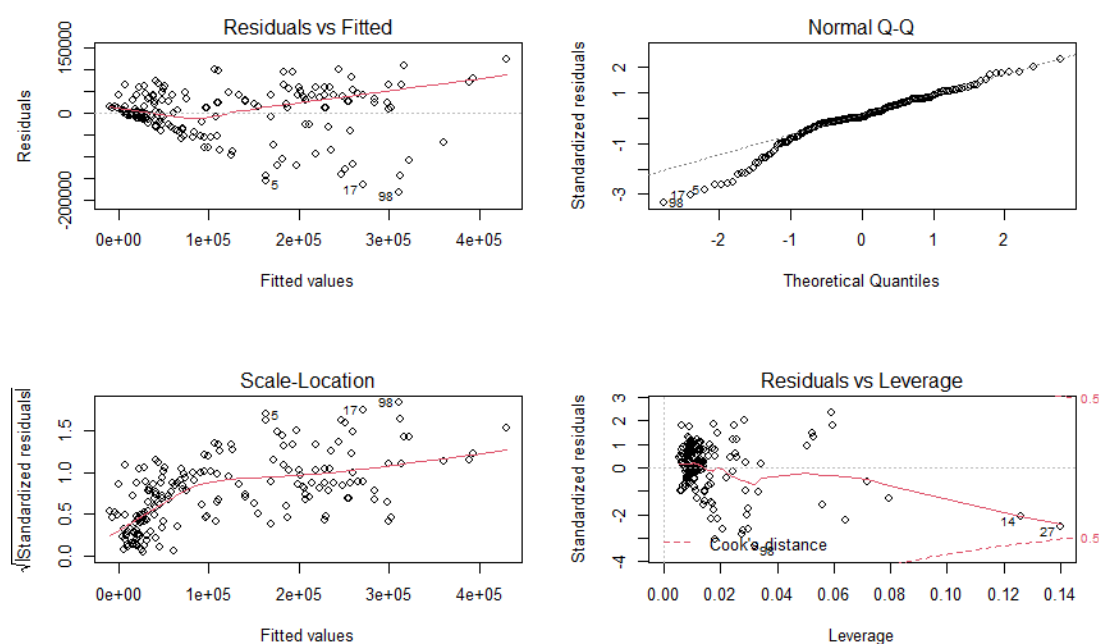
Figure 2. Linear model diagnostic plots

Additionally, an effort was made to study the impact of the number of floors of the buildings in sector B1 of the settlement of Vrisa for three different categories of floor area. Specifically, the study examines how the quantities of

waste in kg, m³, as well as in kg/m² and m³/m², vary on average in the cases of single-story buildings with a floor area ≤ 50 m², two-story buildings with a floor area ≤ 50 m², and three-story buildings with a floor area ≤ 50 m². A similar process is applied for floor areas E > 50 m² and E ≤ 100 m², as well as for E > 100 m². The results are based both on the initial data derived from geographic information systems [Chrysafis, 2018] and on the application of the empirical relationships developed within the framework of this thesis analysis.

Table 2: Comparison of results with the application of empirical relationships

	SINGLE-STORY ≤ 50 m²	TWO-STORY ≤ 50 m² T	THREE-STORY ≤ 50 m²
KG	41289,16	181945,4	0
KG/M2	2741,83	15651,09	0
M3	23,36	88,5	0
M3/M2	1,56	7,6	0
	SINGLE-STORY > 50 AND ≤ 100 m²	TWO-STORY > 50 AND ≤ 100 m²	THREE-STORY > 50 AND ≤ 100 m²
KG	143774,5	226939,3	0
KG/M2	2287,66	5371,12	0
M3	76,79	112,78	0
M3/M2	1,22	2,67	0
	SINGLE-STORY > 100 m²	TWO-STORY > 100 m²	THREE-STORY > 100 m²
KG	214902,8	259520,4	390750,2
KG/M2	1790,6	4277,62	6442,24
M3	116,9	130,29	191,38
M3/M2	0,97	2,15	3,16

Finally, comparison of the results was conducted between the use of the formula developed by the NTUA Chemical Engineering School which has been widely used since 2005 for the preparation of all Regional Solid Waste Management Plans in Greece and the empirical relationships of this thesis. Specifically, the estimation of waste weight using the NTUA formula shows a deviation of approximately 50% upwards compared to empirical relationships and the estimation of waste volume shows a deviation of approximately 60% upwards. This confirms the need for a model to calculate demolition waste quantities that take into account the unique morphological characteristics of an area (e.g., traditional settlements, stone-built structures, etc.) rather than relying solely on statistical data from the Hellenic Statistical Authority (ELSTAT) regarding the number of demolitions.

Conclusions
In conclusion, the availability and collection of empirical data is the most important and necessary step in establishing standardized methods for estimating construction waste, both at the local level and at the building level. The collection of data can precede a disaster and, therefore, facilitate political leadership in organizing immediate and effective recovery plans for areas threatened by various types of natural phenomena. According to the EU Protocol for the management of construction and demolition waste [European Commission, 2016], an inspection must be conducted prior to demolition projects for any material to be reused or recycled, as well as for any hazardous waste. The methodology developed in this study for determining waste generation rates per EWC category can significantly contribute to this inspection and aid in the systematic utilization of materials from debris for subsequent building reconstruction processes. The proposed models from our study can be used for future estimates of waste that may result from a potential natural disaster in various other areas that morphologically resemble the area of our study. Specifically, they can be applied to traditional settlements whose basic morphological characteristics include stone-built walls, wooden internal and external openings, internal partition walls made of bagdati (a type of traditional construction technique), wooden floors, etc. It is understood that they can also be used for predictions and estimates of other traditional settlements on the island of Lesbos, as well as settlements in the Aegean island complex with similar architecture. Our analysis was based on estimates from the available building stock rather than field measurements taken after the disaster occurred. Estimating quantities based on available building stock almost always provides a consistent amount of waste, whereas methods relying on field measurement data after an event can yield significantly fluctuating values.

The need to find a standardized empirical relationship for calculating construction waste with broad application in traditional settlements of Greece, with vulnerable building stock and unauthorized structural interventions, necessitates further research using more empirical data. One attempt is to use existing data for the entire area of Vrisa, so that our mathematical models can be reassessed and adjusted. Additionally, data could be obtained for other areas of the island of Lesbos using GIS methods, so that by knowing the available building stock, we can automatically estimate potential disaster waste quantities, as various natural hazards (earthquakes, floods, fires, etc.) threaten the existence of the island. Furthermore, measurements of construction waste quantities should be made after necessary demolitions by the waste management authorities (AEKK) within their environmental responsibility framework, so that a comparison and verification of the results from the application of the empirical relationships can be made. Finally, other or different variables could be used in the mathematical model so that, using the method of multiple linear regression, it can be determined whether they contribute and to what extent to the correct estimation of quantities, as well as to identify their interdependencies. Such variables could, for example, include the building coefficient, or even categorical variables, such as floor type, roof type etc.

References
Chrysafis N., 2018. Investigation of geoinformatics methods in the management modeling of C&DW (Construction and Demolition Waste) after a destructive earthquake: The case of Vrisa, Lesvos. Master's thesis, Department of Geography, University of the Aegean.

N. Soulakellis, et al., 2018. Synergistic exploitation of geoinformation methods for post-earthquake 3D mapping of Vrisa traditional settlement, Lesvos island, Greece. Int. Arch. Photogramm. Remote Sens. Spatial Inf. Sci., XLII-3/W4, 491–498**.**

D. Fatta, et al., 2003. Generation and management of construction and demolition waste in Greece- an existing challenge. Resources Conservation and Recycling 40(1):81-91.

Samy García-Torres et al., 2017. Methodology to characterize and quantify debris generation in residential buildings after seismic events. Resources, Conservation and Recycling, Volume 117, Part B, Pages 151-159**.**

Askarizadeh A. et al., 2015. Management of post-earthquake construction debris in Tehran Metropolitan. International Journal of Environmental Science and Technology volume 13, pages 639–648.

Koutsoudaki E., 2016. Linear and Non-Linear Regression with Applications in R. Master's thesis, Department of Engineering and Informatics, University of Patras**.**

Preliminary results on the toxic elemental accumulation in the Fe-oxides of the stream sediments from Palea Kavala, Northern Greece

Giouri K.[1], Stergiou C.L.[1,2], Melfos V.[1], Papadopoulou L.[1], Kantiranis N.[1], Peytcheva I.[3], Stefanova E.[3]

(1) School of Geology, Aristotle University of Thessaloniki (AUTH), 54124, Thessaloniki, Greece (2) Chemical Process & Energy Resources Institute (CPERI), Centre for Research and Technology Hellas (CERTH), 50200, Ptolemaida, Greece (3) Geological Institute, Bulgarian Academy of Sciences, 241113, Sofia, Bulgaria

Introduction

The origin of metals in the environment can be both attributed to natural or to anthropogenic sources. The occurrence of mineralization in an area can affect the metals concentration in the geological background. Wastes from past or current mining and metallurgical activities can contribute to these concentrations through natural processes or through the disposal of the wastes encountered during these activities (Kabata-Pendias, 2011; Alloway, 2013). The research area of Palea Kavala in Northern Greece, is distinguished by the presence of diverse mineralizations rich in Pb, Zn, Fe, Mn, As, Cu, Au, and Ag. Mining and metallurgical activities have been conducted in the region in the antiquity and in the beginning of the 20th century, resulting in the disposal of large quantities of mining waste. The presence of Fe-oxides has been identified in the geological background of the Palea Kavala area. Although they can accumulate inorganic pollutants, no detailed study has been carried out concerning the composition of these oxides in the broader district. The main analytical technique applied for the detailed determination of elements accumulated in the oxides was the application of LA-ICP-MS. The advantage of this method in relation with other analytical techniques, is that it does not require the dissolution of the material to be analyzed and is fast. Additionally, its detection limits are very low and no loss of elements concentration could result, since it does not include many steps, which could cause contamination of the samples (Günther et al. 2000, Huelin et al. 2006). This ongoing study is considered as environmentally significant, since it will reveal locations with high concentrations of chemical elements that are often characterized as harmful for the local community.

Geological Setting

The study area belongs to the Pangeon unit, part of the Southern Rhodope Core Complex. The latter represents a large metamorphic core complex, which was exhumed along the Strymon detachment fault between upper Oligocene and middle Miocene. The lithology of the Pangeon unit includes Paleozoic-Mesozoic gneisses overlain by marbles with schist intercalations (Krohe and Mposkos, 2002; Brun and Sokoutis, 2007). These rocks were intruded by the Kavala (or Symvolon) pluton of Miocene age (22-21 Ma) (Kydonakis *et al.*, 2014). This pluton is an I-type intrusion and mainly consists of amphibole-biotite granodiorite with subordinate amounts of tonalite, diorite, monzogranite, and monzodiorite. Alluvial sediments of a Quaternary age consisting of clays, sands and gravels overlie the crystalline rocks in the western part of the studied area and form the Philippi basin (Figure 1).

Approximately 150 major and minor base- and precious metal occurrences, mostly weathered and oxidized, are spread in an area of about 100 km^2. These metal occurrences have a magmatic-hydrothermal origin and are found within the Kavala pluton, as well as in the surrounding metamorphic rocks. Five different metal assemblages, including Fe-Mn-(Pb-Zn-Ag), Fe-Mn-Au, Fe-As-Au, Fe-Cu-Au and Bi-Te-(Pb-Sb-Au), exhibit a zonal distribution around the magmatic intrusion and contain complicated primary and secondary metallic mineral paragenesis. Primary minerals consist of pyrite, arsenopyrite, chalcopyrite, galena, sphalerite, tetrahedrite-tennantite, with subordinate pyrrhotite, bismuthinite, petzite, lillianite, proustite, pyrargyrite, argentite, cosalite, tetradymite, jalpaite, stephanite and native gold and silver. The secondary minerals comprise mainly goethite, lepidocrocite, hematite, covellite, chalcocite, malachite, smithsonite, cerussite, mimetite, siderite, arseniosiderite, scorodite, jarosite, pyrolusite, manganite, manganosite, cryptomelane, todorocite, nsutite (Vavelidis *et al.*, 1997; Fornadel *et al.*, 2011).

Considerable underground and surface mining activities took place during Classical to Roman periods for gold or lead–silver, and during the 20th century (1904-1914) for iron, manganese, zinc and lead. In the vicinity of the mines, large piles of mining wastes, mainly from the recent activities, are spread along the rivers and the streams. The wastes are eroded and significant quantities of the metals are diffused in the aquatic environment of the river drainage systems and are transported downhill, in the Phlippi basin (Giouri et al. 2013, 2016a,b, 2018; Giouri, 2020).
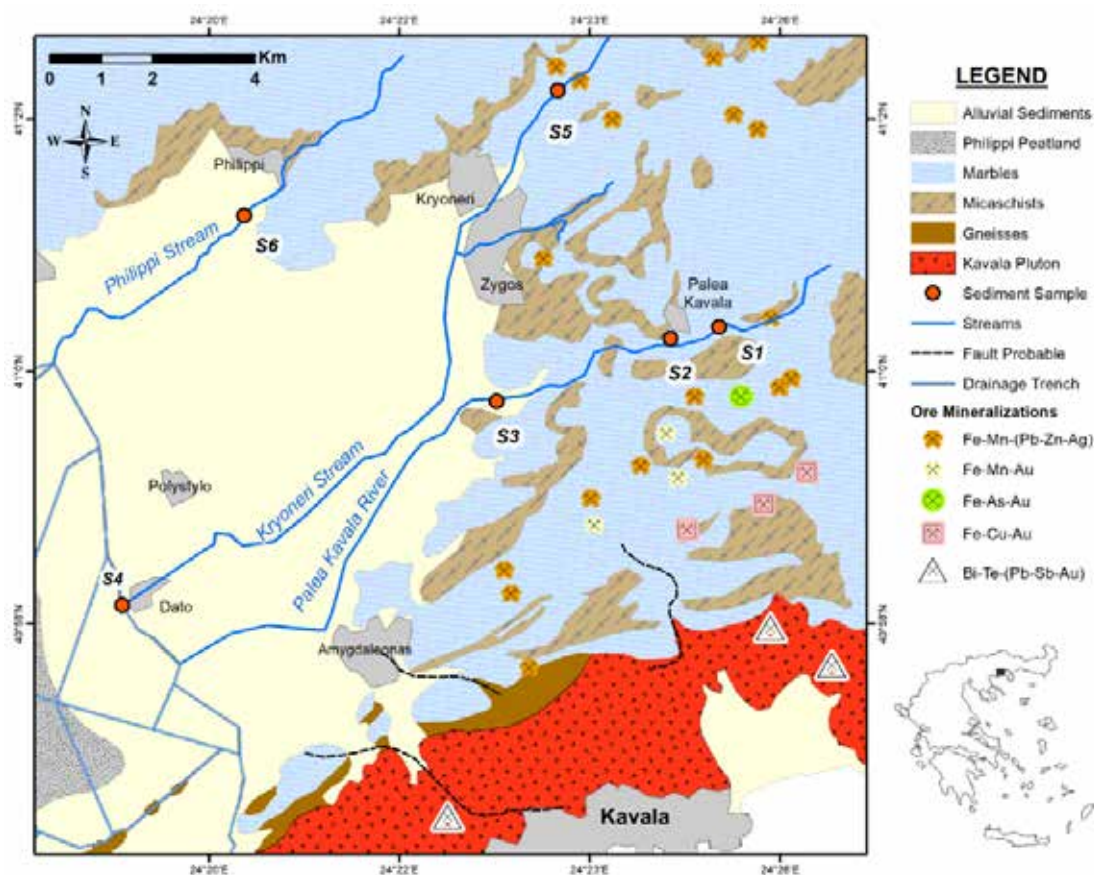
Figure 1. Geological map of the Kavala-Philippi area (modified after Kronberg, 1970 & Kronberg, Melidonis
1970), including the Palea Kavala river and the Kryoneri and Philippi streams. The sampling sites of the stream sediments are
also shown.

Methods

Samples collection

Six sampling sites were strategically chosen for sediment collection, distributed across three branches of the main drainage system that traverse areas of ore mineralization and historic mining waste deposits. The site selection considered the expectation that closely situated locations would not exhibit significant variations in geochemical background. Despite the presence of numerous metal occurrences in the study area, their exact dimensions are undefined, and they lack a discernible geometric distribution. Consequently, metal dispersion throughout the region is irregular. Sediments were collected from the following locations: samples S1, S2, and S3 were obtained downstream of the Palea Kavala River, samples S4 and S5 from the Kryoneri Stream, and sample S6 from the Philippi Stream (Figure 1). The collection process involved using an acid-washed plastic shovel to minimize contamination, after which the samples were transferred into clean polyethylene bags. These bags were sealed immediately to preserve sample integrity and transported to the laboratory for further processing and analysis.

Samples preparation

The collected samples were dried at 60 ˚C in an oven, at the Department of Mineralogy-Petrology-Economic Geology of the School of Geology, Aristotle University of Thessaloniki (AUTH), in order to remove the adsorbed moisture. Then they were gently ground in an agate mortar, in order to be disaggregated. The dried and disaggregated samples were sieved through a 0.5 mm and a 0.18 mm sieve in order to obtain the in-between fraction of each sample for the polished sections. Samples were also sieved through a 0.063 mm sieve in order to obtain the fine grained fractions for further chemical analyses.

Samples analysis

In the present study, the fine grained fraction (<0.063 mm) was used for the determination of the mineralogical composition of sediments by the application of X-ray diffraction (XRD), at the Department of Mineralogy-Petrology-Economic Geology, AUTH, using a PHILIPS PW1820/00 X-ray diffractometer, which carry a PW1710 microprocessor. The operating conditions were 35 kV and 25 mA using Ni-filtered CuK radiation. The 2θ scanning range was between 3 and 63 degrees and the scanning speed was 1.2 deg/min. The sediments fraction between 0.5 and 0.18 mm of each sample has been studied under a stereoscopic

microscope in order to separate the Fe-oxide fraction. Subsequently, polished-thin sections were prepared and an initial identification of minerals was carried out by the use of a reflected-transmitted light polarizing microscope. The determination of both composition and morphology of the Fe-oxides, was conducted by the use of scanning electron microscopy (SEM) at the Faculty of Sciences, Aristotle University of Thessaloniki, by the use of a JEOL JSM-840A SEM equipped with an ISIS 300 OXFORD energy-dispersive spectrometer (EDS). The LA-ICP-MS was applied for the determination of the Fe-oxides chemical composition in ultra-trace level. The analyses were conducted at the Geological Institute of the Bulgarian Academy of Sciences in Sofia. Trace elements were measured using a PerkinElmer ELAN DRC-e ICP mass spectrometer coupled with a New Wave UP193-FX excimer laser ablation system, with ablation conducted in a helium medium. The system was optimized daily to ensure sensitivity, using a 35 μm spot size and an energy density of 5.0–5.2 J/cm². The analysis included a 100-second cycle (40 seconds for background, 60 seconds laser-on). Predefined areas in the sections avoided mineral inclusions, and repeated external standardization was performed with NIST SRM 610, USGS GSD-1G, and USGS Mass 1 standards. Data reduction utilized SILLS software (Guillong *et. al,* 2008), with Fe and contents determined by SEM-EDS as internal standards. Fluctuations in isotope intensity were evaluated to exclude contamination by other minerals.

Results

The mineralogical composition of the samples consists mostly of quartz, plagioclase, K-feldspar, mica, calcite, with minor amphiboles. Clay minerals such as chlorite, smectite and kaolinite were also determined (Figure 2a). By the use of a stereoscopic microscope, grains of ore minerals were separated out of the sediments, and randomly oriented samples were analyzed with XRD. These enriched samples consisted of hematite and goethite, along with mica, K-feldspar, quartz and clay minerals (Figure 2b).

The application of optical and scanning electron microscopy on the studied samples revealed that the sediments of the research area comprise ore minerals which are mainly Fe-oxides (Figures 3a,b, 4a,b, 5a,b). According to the results of the scanning electron microscopy (SEM-EDS) these Fe-oxides are mainly hematite and magnetite which are rich in As, Pb and/or Zn. Other identified minerals were goethite, pyrite, galena and titanite. This comes in agreement with the results revealed by Giouri *et al.* (2013, 2016a,b, 2018) and Giouri (2020) according to which most of the sediments in the studied area are enriched in metal(loids), which among others include As, Pb and Zn. More specifically, by the comparison of the mean elements concentrations in the sediments with the corresponding mean concentrations in the rocks of the studied area, it is demonstrated that the sediments are enriched 1.3 times in Fe, 8.7 times in As, 34.9 times in Pb and 4.4 times in Zn (Giouri, 2020). Hence, as concluded by both the bulk sediments geochemistry and the statistical analysis of the results, the enrichment of sediments in As, Pb and Zn is mainly attributed to the neighboring ore deposits.

The LA-ICP-MS further proved As, Pb and Zn accumulation and revealed specific groups of trace elements participating in the studied Fe-oxides (Figures 3c, 4c, 5c). The Fe-oxide from sample S6 contains the highest accumulation of trace elements, while sample S3 is the most depleted one. Based on the chemical composition of the analyzed oxides main accumulations of elements included As (<16,971.57 μg/g in S5), Cd (<10.90 μg/g in S5), Cr (<7,932.26 μg/g in S5), Co (<69.83 μg/g in S6), Cu (<342.02 μg/g in S5), Ni (<716.41 μg/g in S5), Pb (<4,314.55 μg/g in S5) and Zn (<4,180.71 μg/g in S5), as well as the critical and rare metals Ag (<197.30 μg/g in S5), Ce (<211.42 μg/g in S6), La (<440.91 μg/g in S5), Lu (<3.36 μg/g in S6), Th (<16.92 μg/g in S5), and U (<3.29 μg/g in S5, Figures 3c, 4c, 5c).
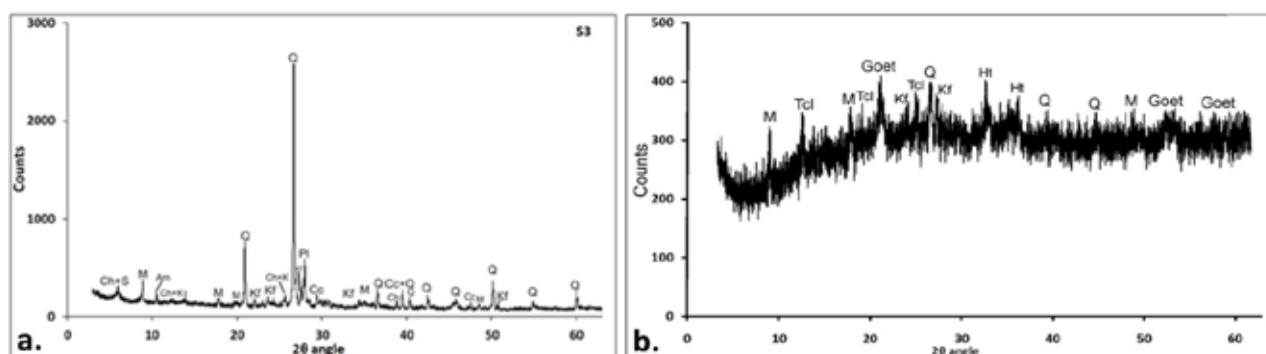
Figure 2. a. XRD pattern of the representative sample S3 (fraction < 0.063 mm). b. XRD pattern of the sample that was enriched in ore minerals. Abbreviations: amphibole (Am), calcite (Cc), chlorite (Ch), goethite-limonite (Goet), hematite (Ht), kaolinite (K), K-feldspars (Kf), micas (M), plagioclase (Pl), smectite (S), quartz (Q), and total clays (Tcl).

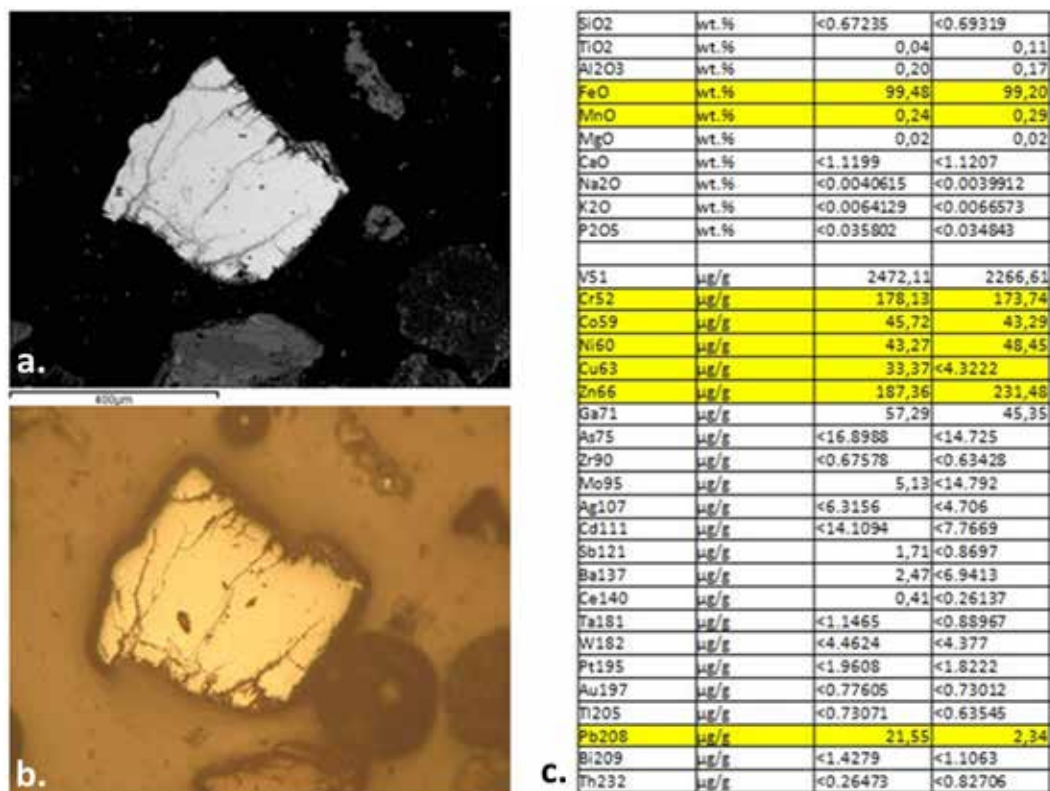| SiO2	wt.%	<0.67235	<0.69319
TiO2	wt.%	0,04	0,11
Al2O3	wt.%	0,20	0,17
FeO	wt.%	99,48	99,20
MnO	wt.%	0,24	0,29
MgO	wt.%	0,02	0,02
CaO	wt.%	<1.1199	<1.1207
Na2O	wt.%	<0.0040615	<0.0039912
K2O	wt.%	<0.0064129	<0.0066573
P2O5	wt.%	<0.035802	<0.034843
V51	µg/g	2472,11	2266,61
Cr52	µg/g	178,13	173,74
Co59	µg/g	45,72	43,29
Ni60	µg/g	43,27	48,45
Cu63	µg/g	33,37	<4.3222
Zn66	µg/g	187,36	231,48
Ga71	µg/g	57,29	45,35
As75	µg/g	<16.8988	<14.725
Zr90	µg/g	<0.67578	<0.63428
Mo95	µg/g	5,13	<14.792
Ag107	µg/g	<6.3156	<4.706
Cd111	µg/g	<14.1094	<7.7669
Sb121	µg/g	1,71	<0.8697
Ba137	µg/g	2,47	<6.9413
Ce140	µg/g	0,41	<0.26137
Ta181	µg/g	<1.1465	<0.88967
W182	µg/g	<4.4624	<4.377
Pt195	µg/g	<1.9608	<1.8222
Au197	µg/g	<0.77605	<0.73012
Tl205	µg/g	<0.73071	<0.63545
Pb208	µg/g	21,55	2,34
Bi209	µg/g	<1.4279	<1.1063
Th232	µg/g	<0.26473	<0.82706

Figure 3. a. SEM back-scattered electron image of a Fe-oxide grain from sample S3. b. The same grain as seen under reflected light. c. Representative chemical analyses by means of LA-ICP-MS.
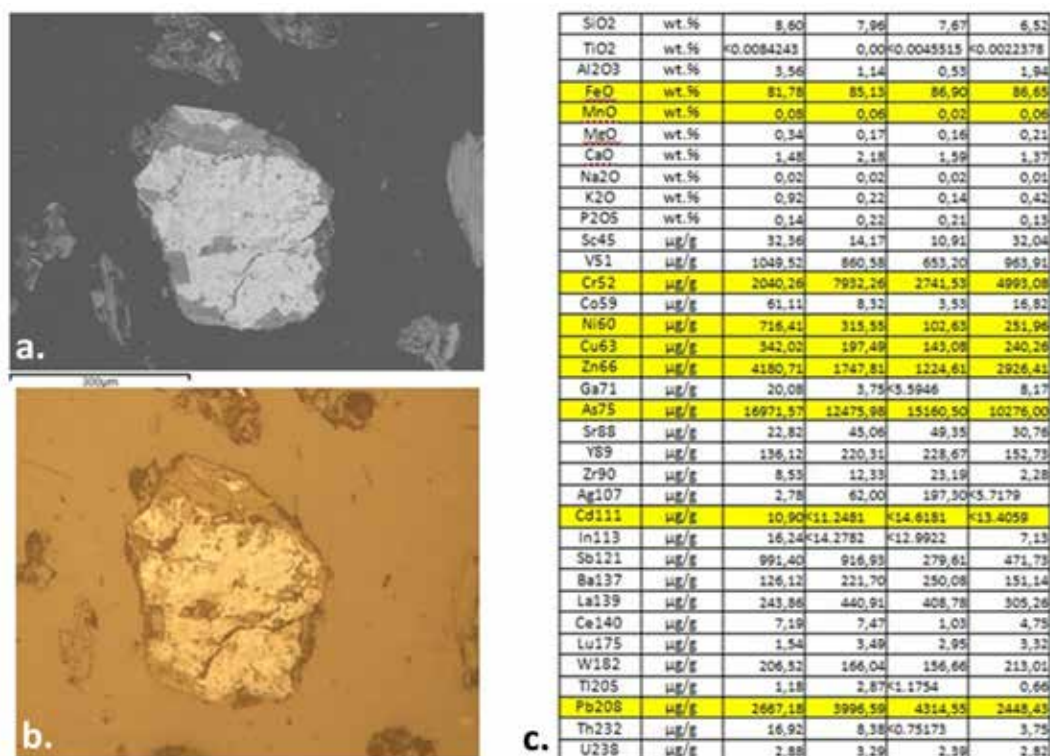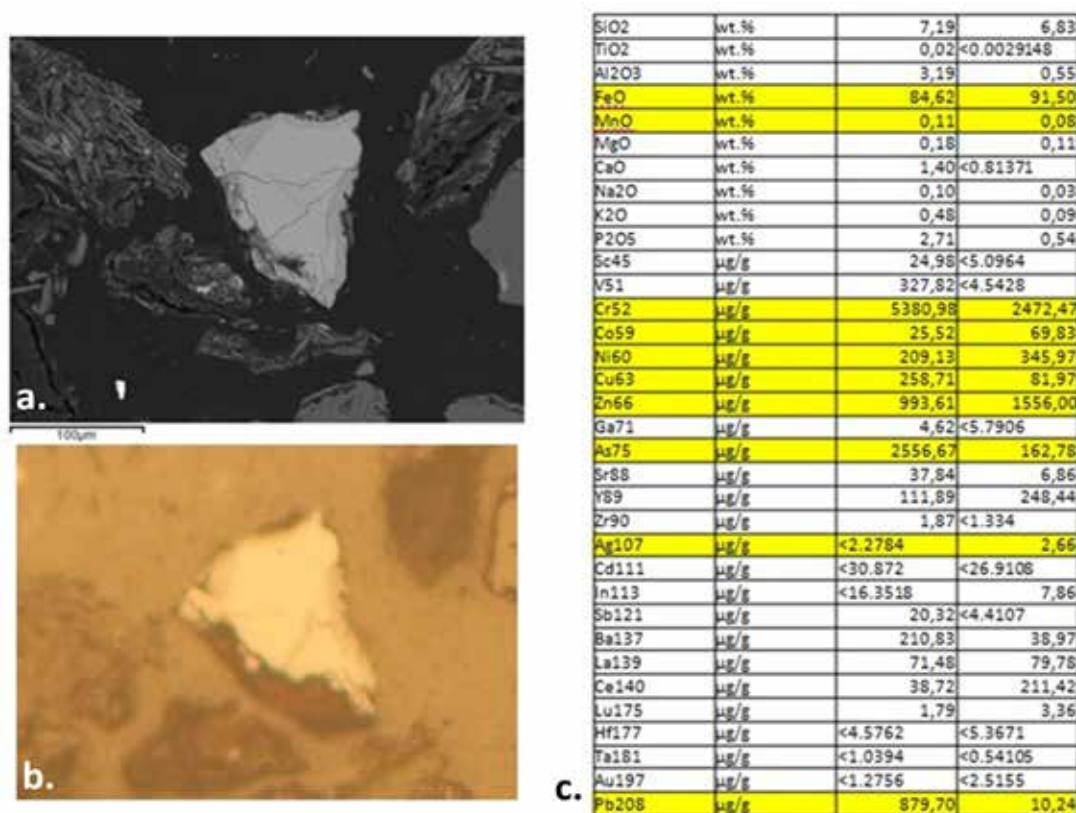

SiO2	wt.%	8,60	7,96	7,67	6,52
TiO2	wt.%	<0.0084243	0,00	<0.0045515	<0.0022378
Al2O3	wt.%	3,56	1,14	0,53	1,94
FeO	wt.%	81,78	85,13	86,90	86,65
MnO	wt.%	0,05	0,06	0,02	0,06
MgO	wt.%	0,34	0,17	0,17	0,21
CaO	wt.%	1,48	2,18	1,59	1,37
Na2O	wt.%	0,02	0,02	0,02	0,01
K2O	wt.%	0,92	0,22	0,14	0,42
P2O5	wt.%	0,14	0,23	0,21	0,13
Sc45	µg/g	32,36	14,17	10,91	32,04
V51	µg/g	1049,52	860,58	653,20	963,91
Cr52	µg/g	2040,26	7932,26	2741,53	4993,08
Co59	µg/g	61,11	8,32	3,53	16,82
Ni60	µg/g	716,41	315,55	102,63	251,96
Cu63	µg/g	342,02	197,49	143,08	240,26
Zn66	µg/g	4180,71	1747,81	1224,61	2926,41
Ga71	µg/g	20,08	3,75	<5.5946	8,17
As75	µg/g	16971,57	12475,98	15160,50	10276,00
Sr88	µg/g	22,82	45,06	49,35	30,76
Y89	µg/g	136,12	220,31	228,67	152,73
Zr90	µg/g	8,53	12,33	23,19	2,28
Ag107	µg/g	2,78	62,00	197,50	<5.7179
Cd111	µg/g	10,90	<11.2481	<14.6181	<13.4059
In113	µg/g	16,24	<14.2782	<12.9922	7,13
Sb121	µg/g	991,40	916,93	279,61	471,73
Ba137	µg/g	126,12	221,70	250,08	151,14
La139	µg/g	243,86	440,91	408,78	305,26
Ce140	µg/g	7,19	7,47	1,03	4,75
Lu175	µg/g	1,54	3,49	2,95	3,32
W182	µg/g	206,52	166,04	156,66	213,01
Tl205	µg/g	1,18	2,87	<1.1754	0,66
Pb208	µg/g	2667,18	3996,59	4314,55	2448,43
Th232	µg/g	16,92	8,38	<0.75173	3,75
U238	µg/g	2,88	3,29	2,36	2,82

Figure 4. a. SEM back-scattered electron image of a Fe-oxide grain from sample S5. b. The same grain as seen under reflected light. c. Representative chemical analyses by means of LA-ICP-MS.

SiO2	wt.%	7,19	6,83
TiO2	wt.%	0,02	<0.0029148
Al2O3	wt.%	3,19	0,55
FeO	wt.%	84,62	91,50
MnO	wt.%	0,11	0,08
MgO	wt.%	0,18	0,11
CaO	wt.%	1,40	<0.81371
Na2O	wt.%	0,10	0,03
K2O	wt.%	0,48	0,09
P2O5	wt.%	2,71	0,54
Sc45	µg/g	24,98	<5.0964
V51	µg/g	327,82	<4.5428
Cr52	µg/g	5380,98	2472,47
Co59	µg/g	25,52	69,83
Ni60	µg/g	209,13	345,97
Cu63	µg/g	258,71	81,97
Zn66	µg/g	993,61	1556,00
Ga71	µg/g	4,62	<5.7906
As75	µg/g	2556,67	162,78
Sr88	µg/g	37,84	6,86
Y89	µg/g	111,89	248,44
Zr90	µg/g	1,87	<1.334
Ag107	µg/g	<2.2784	2,66
Cd111	µg/g	<30.872	<26.9108
In113	µg/g	<16.3518	7,86
Sb121	µg/g	20,32	<4,4107
Ba137	µg/g	210,83	38,97
La139	µg/g	71,48	79,78
Ce140	µg/g	38,72	211,42
Lu175	µg/g	1,79	3,36
Hf177	µg/g	<4.5762	<5.3671
Ta181	µg/g	<1.0394	<0.54105
Au197	µg/g	<1.2756	<2.5155
Pb208	µg/g	879,70	10,24

Figure 5. a. SEM back-scattered electron image of a Fe-oxide grain from sample S6. b. The same grain as seen under reflected light. c. Representative chemical analyses by means of LA-ICP-MS.

Although the mineralogical composition of the studied samples mainly consists of silicate minerals, the presence of chlorite, smectite, and kaolinite among the clay minerals indicates a complex sedimentary matrix (Figure 2a). In addition, the co-occurrence of pyrite and galena with Fe-oxides as indicated by SEM-EDS analysis suggests secondary oxidation processes, leading to the incorporation of trace elements such as As, Pb, and Zn within the oxide matrix.

The trace element contents revealed by LA-ICP-MS, especially for the elements As, Pb, Zn, Cr, and Cd, exceed common environmental thresholds, highlighting potential geochemical hazards (Kabata-Pendias, 2011). The ongoing research includes the co-evaluation of the semi-quantitative mineralogical compositions by XRD and the statistical analysis of LA-ICP-MS results in an effort to estimate the spatial distribution of potentially hazardous concentrations. For example, a 10% Fe-oxide content in contaminated sediment suggests a significant geochemical reservoir of toxic elements, that could be related to a maximum of ~1.7 g in As per kg of sediment (as of <16,971.57 µg/g in S5, Table 4). These advanced mineralogical and geochemical approach, if coupled with leaching studies may help determine whether these elements remain immobilized or may constitute an environmental risk, under natural or disturbed conditions.

Conclusions

The study highlights the significant influence of ore deposits on the geochemical background of the Palea Kavala area, emphasizing the role of Fe-oxides in stream sediments as environmental monitors due to their capacity to accumulate inorganic pollutants. Mineralogical analysis revealed the presence of major components like quartz, K-feldspar, mica, calcite, and clay minerals, with minor presence of amphibole, hematite, and goethite. Analytical techniques such as SEM-EDS, LA-ICP-MS, and XRD identified Fe-oxides as primary carriers of toxic metals, including As, Cd, Cr, Mn, Ni, Pb, Zn, and U. The geochemical variability among samples suggests that local redox conditions, mineralogical composition, and post-depositional alterations have played key roles in element mobility and retention. The strong association of As, Pb, and Zn with Fe-oxides raises concerns about their potential release into the environment under varying physicochemical conditions, emphasizing the need for further geochemical and environmental assessments. The findings underscore the environmental significance of Fe-oxides in tracing pollutant

pathways and their role in geochemical cycling. This comprehensive approach demonstrates how integrating multiple analytical methods provides robust insights into sediment composition and metal distribution. Future research could focus on the mobility and bioavailability of these metals to better assess their environmental impact.

Acknowledgements

References

Alloway B.J., 2013. Bioavailability of Elements in Soil. In: Selinus O. (eds) Essentials of Medical Geology. Springer, Dordrecht.

Brun, J.P., Sokoutis, D. 2007. Kinematics of the Southern Rhodope Core Complex (North Greece). International Journal of Earth Sciences 96, 1079-1099.

Fornadel, A.P., Spry, P.G., Melfos, V., Vavelidis, M.,Voudouris, P., 2011. Is the Palea Kavala Bi–Te–Pb–Sb±Au district, northeastern Greece, an intrusion-related system? Ore Geology Reviews 39, 119–133.

Giouri K., Melfos V., Papadopoulou L., Vavelidis M., Alifragkis D. (2016a). Correlation of selected metals and their binding behaviour with sediment fractions in Philippoi area, NE Macedonia, northern Greece. Scientific Annals of the Faculty of Geology, University of Thessaloniki (Honorary Publication in Memory of Professor A. Kasoli-Fournaraki), 105, 1-7.

Giouri A., Melfos V., Papadopoulou L., Vavelidis M., Alifragkis D. (2018). Selected Metal Content and Binding Behaviour in Riverbed Sediments of the Kavala-Philippi Area (Northern Greece). Geosciences, 8, 187, 1-17.

Giouri A., Vavelidis M., Melfos V. (2013). Occurrence of Arsenic in waters and sediments of the Palea Kavala river, NE Macedonia, Northern Greece. Bull Geol Soc Greece, XLVII, 8 p.

Giouri K., Vavelidis M., Melfos V., Papadopoulou L. (2016b). Assessment of selected metals enrichment in sediments from Palea Kavala river, NE Macedonia, Northern Greece. Bull Geol Soc Greece, L, 2137-2144.

Giouri K. (2020). Mineralogical and geochemical environmental research in the wider area of Philippoi, Kavala Prefec. Ph.D. Thesis, School of Geology, Aristotle University of Thessaloniki, Annex Number of Scientific Annals of the School of Geology No 209, 206 pp.

Guillong, M.; Meier, D.L.; Allan, M.M.; Heinrich, C.A.; Yardley, B.W.D. Appendix A6: SILLS: A MATLAB-based program for the reduction of laser ablation ICP-MS data of homogeneous materials and inclusions. In Laser Ablation ICP-MS in the Earth Sciences: Current Practices and Outstanding Issues; Sylvester, P., Ed.; Mineralogical Association of Canada Short Course 40: Vancouver, BC, Canada, 2008; pp. 328-333.

Günther, D., Horn, I., Hattendorf, B., 2000. Recent trends and developments in laser ablation-ICP-mass spectrometry. Journal of Analytical Chemistry, 678, 4–14.

Huelin, S., Longerich, H., Wilton, D., Fryer, B. 2006. The determination of trace elements in Fe–oxide coatings on pebbles using LA-ICP-MS. Journal of Geochemical Exploration, 91, 110–124.

Kabata-Pendias, A., 2011. Trace elements in soils and plants, 4th ed., CRC Press, 548 p.

Krohe, A., Mposkos, E., 2002. Multiple generations of extensional detachments in the Rhodope Mountains (northern Greece): evidence of episodic exhumation of high-pressure rocks, in: Blundell, D.J., Neubauer, F., von Quadt, A. (Eds), The timing and location of major ore deposits in an evolving orogen, Geological Society, London, UK, (204), 151–178.

Kronberg, P. Kavala Sheet, 1970. In Geological map of Greece, Scale 1:50.000. Institute of Geology and Mineral Exploration (IGME), Athens, Greece.

Kronberg, P.; Melidonis, 1970, N. Krinidhes Sheet. In Geological map of Greece, Scale 1:50.000. Institute of Geology and Mineral Exploration (IGME), Athens, Greece.

Kydonakis, K., Gallagher, K., Brun, J.P., Jolivet, M., Gueydan, F., Kostopoulos, D. 2014. Upper Cretaceous exhumation of the western Rhodope Metamorphic Province (Chalkidiki Peninsula, northern Greece). Tectonics 33, 1113–1132.

Melfos, V., Voudouris, P., Vavelidis, M., Spry, P.G., 2008. Microthermometric results and formation conditions of a new intrusion-related Bi–Te–Pb–Sb±Au mineralization in the Kavala Pluton, Greece. Proceedings of the 13th All-Russian Conference on Thermobarogeochemistry in conjuction with the 4th Asian and Pacific International Fluid Inclusion Society Symposium, Moscow, Russia, volume 2, 165-168.

Vavelidis, M., Melfos, V., Eleftheriadis, G., 1997. Mineralogy and microthermometric investigations in the Au-bearing sulphide mineralization of Palea Kavala (Macedonia, Greece), in: Papunen, H. (Eds.), Mineral Deposits: Research and Exploration — Where do They Meet?, Balkema, Rotterdam, NL, 343–346.

Investigating the interseismic coupling degree of the northern Apennines external Arc in Emilia Romagna region, (northern Italy).

S. Giuffrida[1-6], L. Anderlini[2], S. Graham[3], F. Carnemolla[1-6], F. Brighenti[4-6], G. de Guidi[1-6], F. Cannavò[5], R. Caputo[4-6]

(1) Department of Biological, Geological and Environmental Sciences (University of Catania, Italy) (2) National Institute of geophysics and Volcanology (INGV, Bologna, Italy) (3) Physics Department (The College of New Jersey-TCNJ, NJ) (4) Department of Physic and Earth Sciences (University of Ferrara, Italy) (5) National Institute of Geophysics and Volcanology-Etnean Observatory (INGV-OE, Italy) (6) CRUST - Interuniversity Center for 3D Seismotectonics with territorial applications, Italy

The Emilia Romagna region, hosts part of the outermost sector of the northern Apennines. This domain is affected by a contractional stress dynamic results from the westward subduction of the Adriatic lithosphere and its flexural retreat. This process leads the formation of a thrusts and fold belt system, migrating toward east and north-east (Malinverno and Ryan, 1986; Fig. 1 a - b). The above-mentioned regional dynamics, determine a shortening deformation pattern, in the interseismic period, probably accommodated by various faults hidden below the Po-Plain, which represents the nowadays foredeep of the northern Apennines. In this work, we apply a kinematic Block Modeling approach (McCaffrey, 2002), to investigate which faults, striking across the Po Plain, is actively accommodating the recognized geodetic velocity field. We use several GNSS data available in these areas (Serpelloni et al., 2022), and exploit all the available fault parameters (e.g., position, strike, dip angle and locking depth) from previous studies and database, to verify the role of major fault segments in accommodating the given velocity field. Our solution shows that the outermost sector of the Northern Apennines, which includes the Mirandola fault and Ferrara Thrusts System, is characterized by contractional slip rates, at most equal to 1.5 mm/yr (dip-slip component), that reproduce the observed velocity field in the long-term (Fig. 2 a). These two above mentioned faults have been widely studied during the last years because of their capability of generating high magnitude earthquakes. An example is the 2012 seismic sequence, characterized by two mainshocks occurred on 20 May (Mw ~ 6) and 29 May (Mw ~ 5.8), (Lavecchia et al., 2012; Fig. 1 b).

Due to the complex seismotectonic history of the studied domain, we discretise the northern Apennines external Arc by means of a Triangular Dislocation Elements (TDEs) mesh to resolve the variability of the slip-deficit rate pattern on fault planes. (Fig. 2 a) According to Meade and Loveless (2009), we calculate the interseismic coupling degree as the ratio of the slip deficit and the long term slip derived from the relative motion of the bounding blocks (Fig 2 b). We therefore investigate each fraction of coupling increment to discern portions of fault planes characterized by a complex behaviour (e.g., aseismic creep vs elastic responses). Finaly, we detect at least three locked asperities, with which we propose a set of possible rupture scenarios and calculate the amount of seismic moment rate that the Emilia Romagna region is accumulating. The obtained seismic moment accumulation rate (3.21×10^{16} Nm/yr) is higher than the rate of the released seismic moment (2.2×10^{16} Nm/yr) in the last ~35 years. Assuming that all this energy (1.01×10^{16} Nm/yr) is released elastically, it would be the equivalent of an earthquake of Mw ~ 4.4, each year.**.**
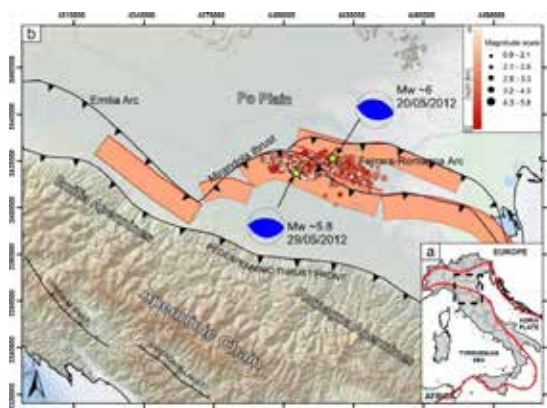
Figure 1. – a) Europe-Africa relative convergence in the context of the Central mediterranean area, (red line represent the front of the collisional domain. – b) Simplified seimotectonic map of the Emilia region (modified after: Toscani et al., 2009; Martelli et al., 2017). Seismogenic sources in orange are from DISS (Database of individual Seismogenic Sources). The microseismicity associated to the 2012 seismic event is from La Torre et al., 2023 (CLASS Database). Focal mechanisms of the May 2012 mainshocks are from INGV (https://terremoti.ingv.it/en). Digital Elevation Model from emodnet (https://emodnet.ec.europa.eu/).
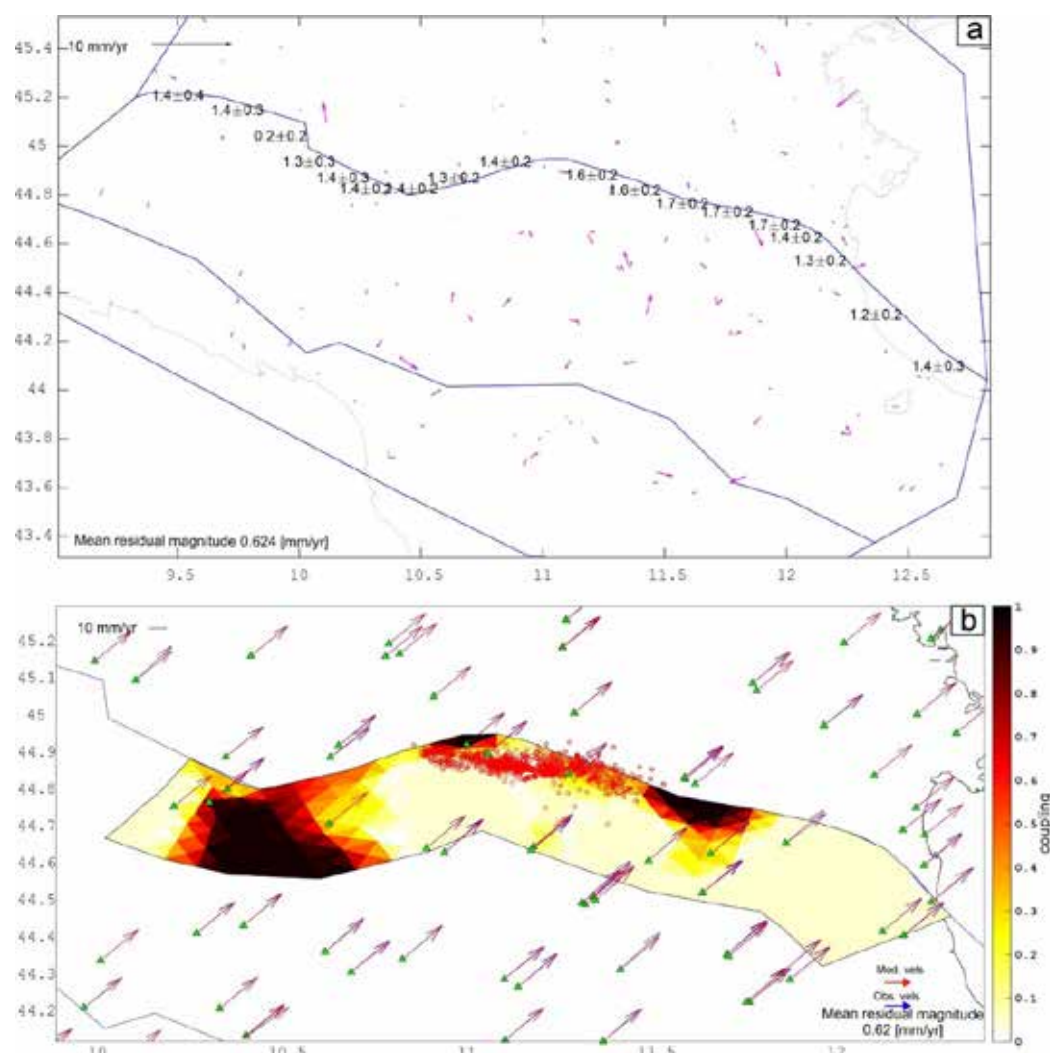
Figure 1. – a) long-term slip rate values (dip slip components) of the northern Apennines external Arc. – b) view of the triangular patches mesh coloured as function of the interseismic coupling distribution, red circles indicate the instrumental seismicity from CLASS database (La Torre et al., 2023), blue and red arrows indicate the observed and the modelled velocity field respectively, green triangles are the permanent GNSS stations of Serpelloni et al., 2022 (in ITRF 2014 reference frame).

References

DISS Working Group (2023). Database of Individual Seismogenic Sources (DISS), Version 3.3.0: A compilation of potential sources for earthquakes larger than M 5.5 in Italy and surrounding areas. Istituto Nazionale di Geofisica e Vulcanologia (INGV). https://doi.org/10.13127/diss3.3.0

Latorre, D. et al. (2023) 'An updated view of the Italian seismicity from probabilistic location in 3D velocity models: The 1981–2018 Italian catalog of absolute earthquake locations (CLASS)', Tectonophysics, 846. Available at: https://doi.org/10.1016/j.tecto.2022.229664.

Lavecchia, G. et al. (2012) 'The May-June 2012 Ferrara Arc earthquakes (northern Italy): Structural control of the spatial evolution of the seismic sequence and of the surface pattern of coseismic fractures', Annals of Geophysics, 55(4), pp. 533–540. Available at: https://doi.org/10.4401/ag-6173.

Malinverno A, Ryan W (1986) Extension in the Tyrrhenian Sea and shortening in the Apennines as result of arc migration driven by sinking of the lithosphere. Tectonics 3:227–245

Martelli, L. et al. (2017) 'Seismic hazard of the Northern Apennines based on 3D seismic sources', Journal of Seismology, 21(5), pp. 1251–1275. Available at: https://doi.org/10.1007/s10950-017-9665-1.

Meade, B.J. and Loveless, J.P. (2009) 'Block modeling with connected fault-network geometries and a linear

elastic coupling estimator in spherical coordinates', Bulletin of the Seismological Society of America, 99(6), pp. 3124–3139. Available at: https://doi.org/10.1785/0120090088.

Mccaffrey, R. (2002) 'Crustal Block Rotations and Plate Coupling', AGU Monograph, pp. 1–40.

Serpelloni, E. et al. (2022) 'Surface Velocities and Strain-Rates in the Euro-Mediterranean Region From Massive GPS Data Processing', Frontiers in Earth Science, 10. Available at: https://doi.org/10.3389/feart.2022.907897.

Toscani, G. et al. (2009) 'Plio-Quaternary tectonic evolution of the Northern Apennines thrust fronts (Bologna-Ferrara section, Italy): Seismotectonic implications', Bollettino della Societa Geologica Italiana, 128(2), pp. 605–613. Available at: https://doi.org/10.3301/IJG.2009.128.2.605.

Geochemical and Mineralogical Study of the Antimony (Sb)-mineralization at the north Pelion region, Magnesia, Greece.

Gjika A.[1], Stouraiti C.[1], Voudouris P.[1], Laskaridis K.[2], Anastasatou M.[2], Mavrogonatos C.[3], Strauss H.[4]
(1) Faculty of Geology and Geoenvironment, National and Kapodistrian University of Athens, Athens, Greece, antonelag@geol.uoa.gr; chstouraiti@geol.uoa.gr; voudouris@geol.uoa.gr; (2) Hellenic Survey of Geology and Mineral Exploration (HSGME), Athens, Greece, klaskaridis@eagme.gr; manastasatou@eagme.gr; (3) Department of Earth Sciences, University of Pisa, Pisa, Italy, konstantinos.mavrogonatos@unipi.it; (4) Institut für Geologie und Paläontologie, Westfälische Wilhelms-Universität Münster, Münster, Germany, hstrauss@uni-muenster.de.

Introduction

Antimony (Sb) is consistently included in the European Union's (EU) list of Critical Raw Materials (CRM) since its establishment in 2011, due to its economic importance and the EU's supply reliance on imports from third countries (European Commission, 2023). Greece is one of the EU member states that host a significant number of antimony mineralization (both occurrences and deposits that were exploited in the past), located in central-eastern Macedonia, western Thrace, the eastern Aegean Sea, and the Pelion peninsula (Stergiou *et al.*, 2022,2023; Kanellopoulos *et al.*, 2024). Antimony mineralization at Pelion has never been the subject of systematic research, especially compared to other Greek antimony mineralization. The aim of this study is to determine the mineralogical and geochemical characteristics of the antimony mineralization at the Mantemia and Moni Panagias sites, North Pelion, in an attempt to determine the conditions of ore deposition.

Regional Geology

The Pelion peninsula consists of a HP-LT metasedimentary sequence (e.g., mica schists) of Permian-Cretaceous age, which can be subdivided into two units (i.e. the North Pelion unit and the South Pelion unit) based on dissimilarities regarding their lithology, stratigraphy and provenance (Hinshaw *et al.*, 2024). The metamorphic rocks of North Pelion overlie the Permo-Carboniferous and Neoproterozoic Pelagonian basement and exhibit similar provenance history to the Cycladic Blueschist Unit (CBU) (Hinshaw *et al.*, 2024). Magmatic intrusions of Tertiary age and porphyritic texture occur throughout the North Pelion unit, crosscutting the metamorphic rocks (IGME, 1987). Antimony mineralization occurs in the "Alikopetra" area of N. Pelion, in proximity to the contact of the HP-LT metamorphic rocks of the North Pelion unit and the marbles of the Pelagonian basement.

Methods

Sixteen (16) samples were collected from two Sb-mineralization sites, namely the "Mantemia" and "Moni Panagias", in the broad "Alikopetra" area. The mineralogical content of the samples was determined using optical microscopy, X-ray Diffraction analysis (XRD), and Scanning Electron Microscopy combined with Energy-dispersive X-ray Spectroscopy (SEM-EDS). Geochemical analyses included X-ray Fluorescence Spectroscopy (XRF) and Inductively Coupled Plasma Mass Spectrometry (ICP-MS). The analyses were conducted at the laboratories of the Hellenic Survey of Geology and Mineral Exploration (HSGME).

Results and Discussion

The antimony mineralization at the "Mantemia" site occurs in the form of stibnite lenses within the marble, ranging in size between 2-15 cm (Fig. 2A). The ore assemblage consists of stibnite, pyrite, sphalerite and Sb-Pb sulfosalts, accompanied by the secondary Sb minerals valentinite, a mineral of the roméite group, stibiconite and senarmontite (Fig. 2B, C). Five different species of Sb-Pb sulfosalts were identified, namely zinkenite, fülöppite, plagionite, robinsonite and boulangerite (Fig. 3). Sphalerite exhibits low Fe concentrations (up to 1.65 wt.%). Pyrite has a high As content, reaching up to 10 wt% and being mostly incorporated in the rims of the crystals. Geochemical analysis yielded concentrations up to 29 wt.% Sb, 6.13 wt.% Fe, 6100 ppm Zn, 3550 ppm As, 2400 ppm Pb, 300 ppm Cu, 40 ppm Sn, 167 ppm Ga, 67 ppm Ta, 3 ppm Te and 2 ppm Ag in the ore. The hydrothermal alteration of the host-rock consists of quartz, carbonate minerals (calcite, dolomite), and muscovite.

The antimony ore at "Moni Panagias" occurs in thin and discontinuous quartz veins (Fig. 2D). The ore assemblage at this site appears more diverse, consisting of stibnite, pyrite, sphalerite, arsenopyrite, cinnabar, Bi-Pb-Cu±Ag sulfosalts, (Bi-tennantite, coloradoite and tetradymite, accompanied by the same secondary Sb minerals as in "Mantemia" (Fig. 2E, F). Iron content in sphalerite reaches 2.32 wt.%, while As content in arsenic pyrite reaches 4.98 wt.%. The geochemical composition of the "Moni Panagias" ore consists of 9.10 wt.% Sb, 2.41 wt.% Fe, 7200 ppm Zn, 2240 ppm As, 160 ppm Cu, 2 ppm Ag and 2 ppm Te. The "Moni Panagias" mineralization exhibits a depletion in Pb (up to 210 ppm), Sn (up to 10

ppm), Ga (up to 7 ppm) and Ta (up to 6 ppm), and an enrichment in Bi (up to 30 ppm) compared to the "Mantemia ore". The mineral composition of the hydrothermal alteration remains similar to "Mantemia"; however, the quartz participation is significantly higher in this location.
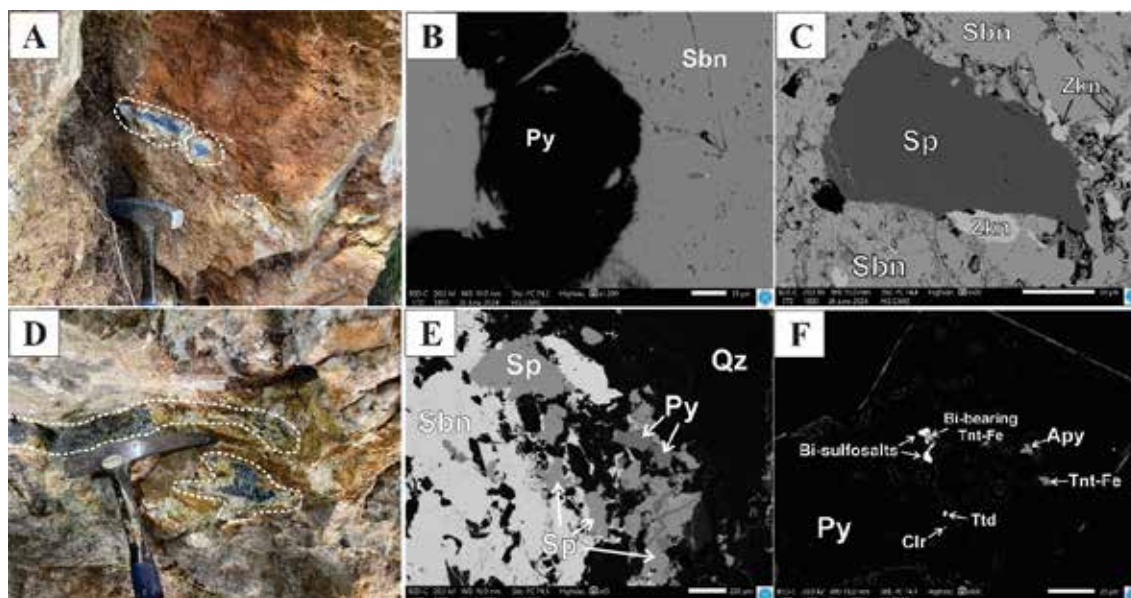

Fig. 2. (A) In-situ antimony mineralization at the "Mantemia" site, (B) Backscattered electron image (BSE) of pyrite and stibnite crystals from the "Mantemia" ore, (C) BSE of sphalerite, zinkenite and stibnite crystals from the "Mantemia" ore, (D) In-situ antimony mineralization at the "Moni Panagias" site, (E) BSE of stibnite, sphalerite, pyrite and quartz from the "Moni Panagias" ore (F) BSE of mineral inclusions inside a pyrite crystal, consisting of Bi-Pb-Cu±Ag sulfosalts, (Bi-)tennantite, arsenopyrite, coloradoite and tetradymite. Abbreviations (according to IMA–CNMNC 2021): Py=pyrite, Sbn=stibnite, Sp=sphalerite, Zkn=zinkenite, Qz=quartz, Tnt=tennantite, Apy=arsenopyrite, Clr=coloradoite, Ttd=tetradymite.
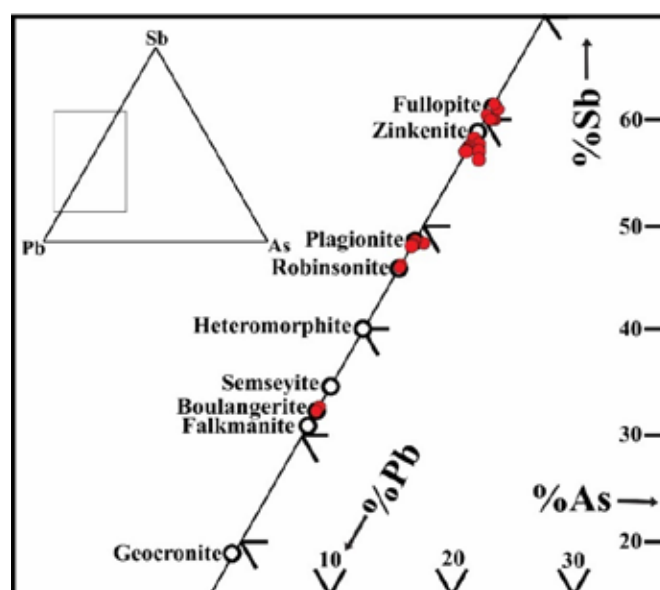
Fig. 3. Composition of Sb-Pb sulfosalts from "Mantemia" plotted on a Sb-Pb-As ternary diagram.

Conclusions

The antimony mineralization in Pelion exhibits characteristics of an epithermal mineralization, formed due to hydrothermal activity, under relatively low temperatures and intermediate to low-sulfidation fluid states. The differences

identified between the two mineralization sites can be attributed to variations of physicochemical conditions during the precipitation of the ore, such as lower fluid sulfidation states and temperatures during the precipitation of the "Moni Panagias" ore (probably due to increased neutralization and/or sulfur consumption), compared to those at "Mantemia" ores.

Acknowledgements

References

European Commission, Study on the Critical Raw Materials for the EU 2023 – Final Report. https://data.europa.eu/doi/10.2873/725585

Hinshaw, E.R., Stockli, D.F., and Soukis, K., 2024. Coherent underplating of HP-LT blueschist packages and basement during the Hellenic subduction recorded by zircon U-Pb data, Pelion, Greece. Journal of the Geological Society, vol. 181 (2).

IGME, 1987. *Geological Map of Greece, Scale 1.50,000, "Zagora-Syki" Sheet*. Institute of Geology and Mineral Exploration in Athens.

Kanellopoulos, C., Sboras, S., Voudouris, P., Soukis, K., Moritz, R., 2024. Antimony's significance as a Critical Metal: The global perspective and the Greek Deposits. Minerals, 14, 121, https://doi.org/10.3390/min14020121

Stergiou, C.L., Melfos, V., Voudouris, P., Papadopoulou, L., Spry, P.G., Peytcheva, I., Dimitrova, D., Stefanova, E. 2022. A Fluid Inclusion and Critical/Rare Metal Study of epithermal Quartz-Stibnite Veins associated with the Gerakario Porphyry Deposit, northern Greece. Applied Sciences 12, 909, https://doi.org/10.3390/app12020909

Stergiou, C.L., Sakellaris, G-A., Melfos, V., Voudouris, P., Papadopoulou, L., Kantiranis, N., Skoupras, E., 2023. Mineralogy, Geochemistry and Fluid Inclusion Study of the Stibnite Vein-Type Mineralization at Rizana, Northern Greece. Geosciences, 13, 61. https://doi.org/10.3390/geosciences13020061

SantoArray: Densifying station coverage in Santorini amidst the Amorgos-Anydros earthquake swarm crisis

Gkogkas K.[1], Papazachos C.[2], Chatzis N.[2], Vamvakaris D.[2], Karagianni E.[2], Ventouzi C.[2], Vellis A.[2], Anterriotis-Kalpakidis N.[2], Madelis D.[2], Paradisopoulou P.[2], Aidona E.[2], Pikridas Ch.[2]
(1) Institute of Geophysics, Polish Academy of Sciences, Warsaw, Poland, konstantinos.gkogkas@igf.edu.pl
(2) Aristotle University of Thessaloniki, Thessaloniki, Greece, kpapaza@geo.auth.gr

Introduction

During February-March 2025, a seismic swarm occurred near the Santorini-Anydros-Amorgos area, with thousands of earthquakes being recorded with a maximum magnitude of **M**5.2. Hundreds of earthquakes with magnitudes larger than 3 were recorded and felt by inhabitants of Santorini and neighboring islands, to a tentative self-evacuation of Santorini and the declaration of emergency state by the Hellenic government. In light of these events, we rapidly responded to the ongoing crisis by designing and deploying a new seismic array in Santorini (SantoArray). The collaboration between the Aristotle University of Thessaloniki (Greece) and the Institute of Geophysics, Polish Academy of Sciences (Poland) facilitated the preparation, shipment, deployment, maintenance, and data analysis of 7 SmartSolo units and 117 DATA-CUBE instruments. The network operated continuously for approximately 3 weeks (28 February – 23 March 2025) without instrumentation losses, resulting in a plethora of data recorded by the deployed large-N network. We present detailed information on this newly deployed temporary seismic network along with a preliminary example of data analysis.

Over the last decades, the proliferation of equipment for large-N seismic experiments has provided unique opportunities for extensive investigations aiming at resolving the Earth's finer structure and towards a better understanding of seismicity. In the case of Santorini, numerous nodal experiments (e.g., PROTEUS; Hooft et al., 2019; Chatzis et al., 2022) have provided local and fine-scale tomographic images of the crust and uppermost mantle (e.g., Dimitriadis et al., 2010, Hooft et al., 2019; Heath et al., 2019; McVey et al., 2022; Autumn et al., 2025; Huftstetler et al., 2025) with the aim of improving our understanding of the deeper structure of the volcanic plumbing system, as well as the geophysical and geological characteristics of the near-surface structure. The presented SantoArray experiment expands over Santorini, Kammeni and Thirasia islands, providing a unique opportunity to better resolve the islands' shallow structure using land stations.
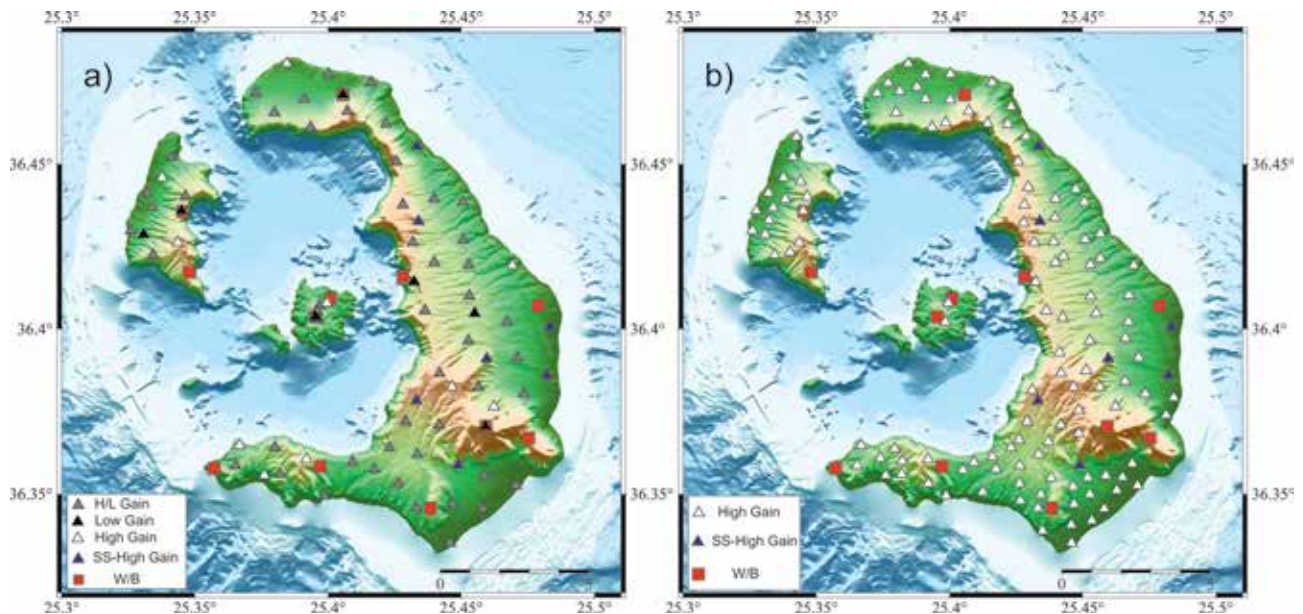
SantoArray

The SantoArray comprises of continuous records from all permanent (broadband and wide-band; red squares in Figure 1) stations in Santorini operating under the Hellenic Unified Seismic Network (H.U.S.N., Evangelidis et al., 2021), augmented with temporarily deployed nodal stations (117 DATA-CUBE 3-C & 7 SmartSolo 3-C instruments) in two deployment phases (I and II), with distinct instrument configurations and geometries. Phase I (28 February – 11 March, Figure 1a) involved the installation of 7 SmartSolo 5Hz IGU-16HR-3C sensors (blue triangles in Figure 1a) and 117 DATA-CUBE digitizers equipped with 4.5Hz 3-component sensors, set in two different instrument gain configurations (minimum-"low" and maximum-"high" possible) deployed as follows: 50 co-located low- and high-gain sensor sites (grey triangles in Figure 1a), 10 high-gain sensors (white triangles in Figure 1a) and 7 low-gain sensors (black triangles in Figure 1a), with a ~1.3 km average inter-station spacing. Phase II (11-23 March; Figure 1b) was initiated due to instrument battery replacing needs and comprises of the same total instrument number. However, during Phase II we have set all sensors configuration to the maximum possible gain (white triangles in Figure 1b), while sensors co-located at "double" (low- and high-gain) sites and near permanent station locations (grey and several black triangles of Figure 1a) were relocated and distributed throughout Santorini to improve the inter-station spacing to about ~600m. We successfully retrieved all stations and downloaded above 95% of the expected continuous time series for future analyses.

Data examples

Figure 2 presents a preliminary analysis of two local earthquakes that occurred in the vicinity of Anydros (08/03/2025 **M**3.7, Figure 2a) and Kyparissia (09/03/2025 **M**4.7, Figure 2b) recorded during first phase of the SantoArray experiment operation (Phase I). For both events, P- and S-wave phases were manually picked, and P-wave arrival times were calculated relative to the origin time of each event. Then, a simple topographic correction was applied to account for the rapidly changing topography in Santorini, incorporating the mean P and S velocities presented by

Chatzis et al. (2022). A smooth 2D kriging interpolation was applied to the observations to enhance the visualization of spatial wave propagation. The preliminary observations verify the adequate data quality for earthquakes occurring in both near (Anydros sequence example), and large distances (Kiparissia earthquake) from Santorini, and highlight areas of loose formations (sparse time contours in Figure 2b) and near the bedrock (dense time contours in Figure 2b).


Figure 1. Sensor distribution of the newly deployed SantoArray temporary network. Red squares show permanent Wide-band and Broadband stations from the Hellenic Unified Seismic Network. Blue triangles show deployment locations of the 7 SmartSolo sensors and otherwise colored triangles show the 117 DATA-CUBE sensors. a) SantoArray Phase I, b) SantoArray Phase II.
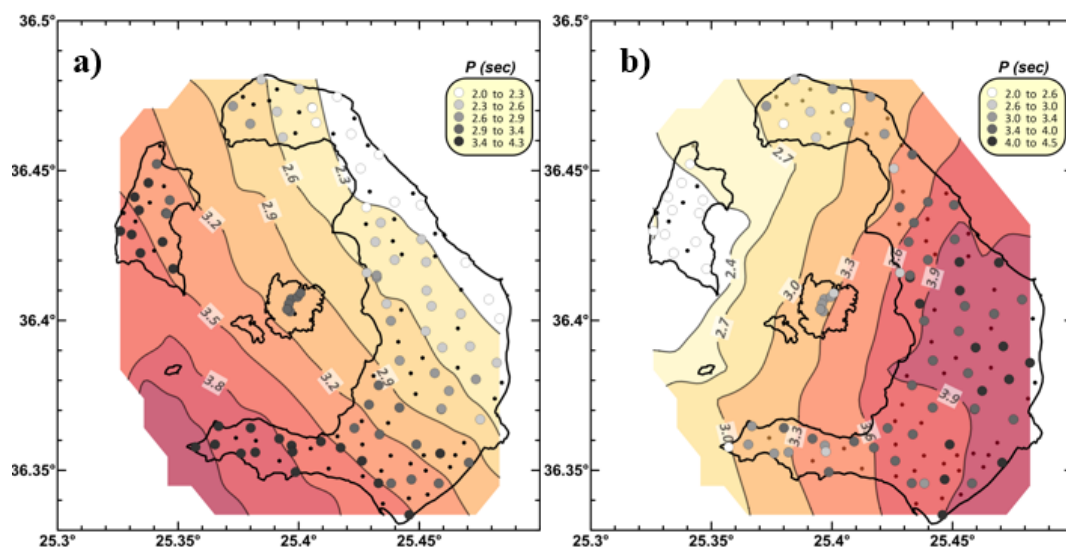
Figure 2. Example of P-wave arrivals from two local earthquakes recorded by SantoArray. Travel-times (colored circles) were calculated for the vertical component measured from the earthquake origin time and corrected for topography. Black dots show locations of SantoArray Phase II stations that were asynchronously deployed and did not record the earthquakes presented here. Smoothed 2-D kriging traveltime contours are plotted in the background. a) the 08/03/2025 M3.7 Anydros earthquake the 08/03/2025 M4.7 Kiparissia earthquake. Traveltimes presented are relative to arbitrary times [00:13:55 for (a) and 20:56:00 for (b)].
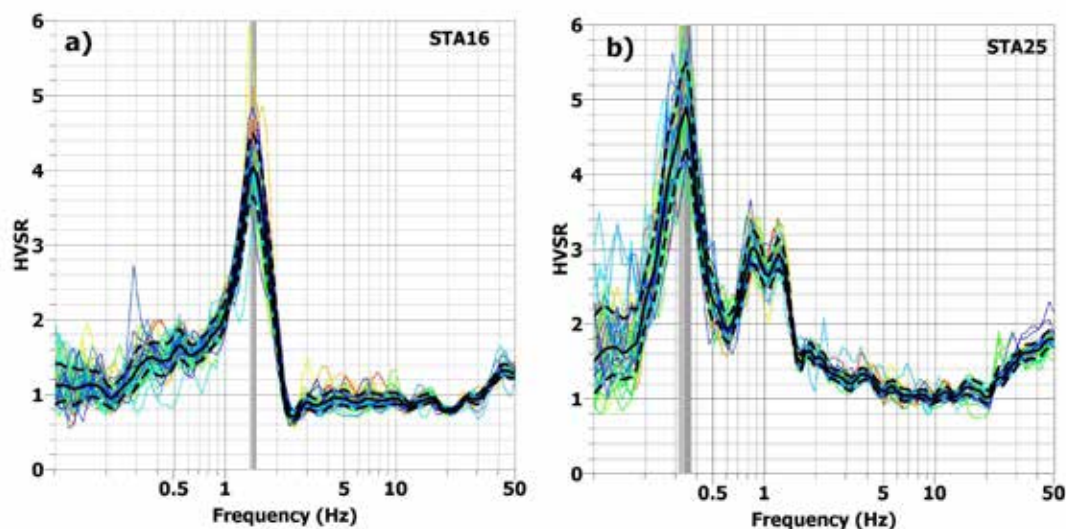
Figure 3. Typical examples of HVSR curves. a) HVSR curve from a site close to the outcrop basement, where a prominent peak is observed at the f_0=1.5 Hz due to impedance contrast between pyroclastic deposits and the underlying metamorphic basement. b) HVSR curve from a site with a very low frequency peak at f_0=0.35 Hz, indicating very deep volcanics above the basement, as well as a secondary frequency peak at f_1~1 Hz, due to shallower impedance contrast within the volcanic layers. The frequency peak is presented in vertical grey line.

In Figure 3, we present two examples of HVSR (Nakamura 1989) curves obtained from single-station 3-component ambient noise measurement at two sites located closer (Fig.3a) and farther (Fig.3b) from the basement outcrop. A sharp fundamental frequency peak is observed in both plot, in agreement with earlier findings (e.g. Chatzis et al., 2022). Moreover, the fundamental frequency, f_0, shifts from ~1.5Hz to 0.35Hz as we move further away from the basement, verifying that the HVSR dataset can be employed to identify the presence of shallow and deep volcanic layers above the metamorphic basement, based on existing and future calibrations of the bedrock depth against the fundamental frequency.

Conclusions

The deployment and operation of SantoArray was completed successfully. The rapid emergency response to the earthquake swarm crisis and the instrument and data retrieval rates underscores the ability of future large-N seismic experiments of similar nature in Greece. The recorded earthquakes presented here provide high quality data encouraging future analysis for several purposes, e.g. earthquake relocation, body-wave tomography, sire-response analysis, etc. Moreover, the hybrid geometry of the network will also allow us to use the recorded ambient noise records for several purposes, such as HVSR and noise autocorrelation, or to compute and use thousands of inter-station pairs for ambient noise cross-correlation tomography, yielding tomographic images of Santorini with unprecedented resolution. Additional inter-disciplinary and collaborative approaches are planned to be realized with the SantoArray data, towards a better understanding of Santorini's seismic structure, the earthquake swarm and the volcano structure and behavior.

Acknowledgement

References

Aristotle University of Thessaloniki. Aristotle University of Thessaloniki Seismological Network, 1981. doi: 10.7914/SN/HT.

Autumn, K. R., Hooft, E. E., & Toomey, D. R. (2025). Exploring Mid-to-Lower Crustal Magma Plumbing of Santorini and Kolumbo Volcanoes using PmP Tomography. Authorea Preprints.

Chatzis, N., Papazachos, C., Theodoulidis, N., Hatzidimitriou, P., Vougioukalakis, G., Paulatto, M., ... & Ventouzi,

C. (2022). Metamorphic bedrock geometry of Santorini using HVSR information and geophysical modeling of ambient noise and active-source surface-wave data. Journal of Volcanology and Geothermal Research, 432, 107692.

Dimitriadis, I., Papazachos, C., Panagiotopoulos, D., Hatzidimitriou, P., Bohnhoff, M., Rische, M., & Meier, T. (2010). P and S velocity structures of the Santorini–Coloumbo volcanic system (Aegean Sea, Greece) obtained by non-linear inversion of travel times and its tectonic implications. Journal of Volcanology and Geothermal Research, 195(1), 13-30.

Evangelidis, C. P., Triantafyllis, N., Samios, M., Boukouras, K., Kontakos, K., Ktenidou, O. J., ... & Tselentis, G. A. (2021). Seismic waveform data from Greece and Cyprus: Integration, archival, and open access. Seismological Society of America, 92(3), 1672-1684.

Heath, B. A., Hooft, E. E. E., Toomey, D. R., Papazachos, C. B., Nomikou, P., Paulatto, M., ... & Warner, M. R. (2019). Tectonism and its relation to magmatism around Santorini Volcano from upper crustal P wave velocity. Journal of Geophysical Research: Solid Earth, 124(10), 10610-10629.

Hooft, E. E. E., Heath, B. A., Toomey, D. R., Paulatto, M., Papazachos, C. B., Nomikou, P., ... & Warner, M. R. (2019). Seismic imaging of Santorini: Subsurface constraints on caldera collapse and present-day magma recharge. Earth and Planetary Science Letters, 514, 48-61.

Hufstetler, R. S., Hooft, E. E., Toomey, D. R., VanderBeek, B. P., Papazachos, C., & Chatzis, N. (2025). Seismic Structure of the Mid to Upper Crust at the Santorini-Kolumbo Magma System from Joint Earthquake and Active Source Vp-Vs Tomography. Authorea Preprints.

Nakamura, Y. (1989). A method for dynamic characteristics estimation of subsurface using microtremor on the ground surface. *Railway Technical Research Institute, Quarterly Reports*, *30*(1).

McVey, B. G., Hooft, E. E. E., Heath, B. A., Toomey, D. R., Paulatto, M., Morgan, J. V., ... & Papazachos, C. B. (2020). Magma accumulation beneath Santorini volcano, Greece, from P-wave tomography. Geology, 48(3), 231-235.

National Observatory of Athens, Institute of Geodynamics, Athens. National Observatory of Athens Seismic Network, 1975. doi: 10.7914/SN/HL.

University of Athens. Hellenic Seismological Network, University of Athens, Seismological Laboratory, 2008. doi: 10.7914/SN/HA.

17th INTERNATIONAL CONGRESS
of the Geological Society of Greece

Assessment of assembly point suitability in tsunami-prone South Aegean coasts after the 2025 Santorini-Amorgos earthquake swarm and related risk reduction measures

Gogou M.[1], Spyrou N.I.[1], Mavroulis S.[1], Evelpidou N.[2], Mavrouli, M.[3], Lekkas E.[1,4], Antonarakou A.[5]

(1) Department of Dynamic Tectonic and Applied Geology, Faculty of Geology and Geoenvironment, School of Sciences, National and Kapodistrian University of Athens, Athens, Greece, mgogou@geol.uoa.gr
(2) Department of Geography and Climatology, Faculty of Geology and Geoenvironment, School of Sciences, National and Kapodistrian University of Athens, Athens, Greece
(3) Department of Microbiology, Medical School, National and Kapodistrian University of Athens, Athens, Greece
(4) Earthquake Planning and Protection Organization, Athens, Greece
(5) Department of Historical Geology and Palaeontology, Faculty of Geology and Geoenvironment, School of Sciences, National and Kapodistrian University of Athens, Athens, Greece

Introduction

The early 2025 earthquake swarm between Santorini and Amorgos, in the southern part of the Aegean Sea, triggered an immediate mobilization of the authorities and operational structures of the Civil Protection system in Greece, with a primary focus on increased preparedness actions for an imminent strong earthquake. Among other significant actions, a specially developed web platform was made available for all users (mysafetyplan.gov.gr), for locating designated assembly points in case of an earthquake. These locations were selected by the Independent Department of Civil Protection of the Municipalities, though the methodology used for their selection and the factors considered in the decision-making process were not explicitly defined.

The Aegean Sea, like the broader Eastern Mediterranean region, is characterized by high tsunami hazard (Shaw *et al.* 2008; Sørensen *et al.*, 2012; Papadopoulos and Fokaefs, 2005; Karkani *et al.*, 2022; Gogou *et al.*, 2023). In addition to historical records, three seismic events in the past 70 years have triggered tsunamis with considerable impact on the coastal areas, including those triggered by the 1956 Amorgos earthquake (Galanopoulos, 1956; Ambraseys, 1960; Papadopoulos and Pavlides, 1992; Okal *et al.*, 2009; Leclerc F. *et al.*, 2024), the 2017 Kos earthquake (Lekkas *et al.*, 2018) and the 2020 Samos earthquake (Triantafyllou *et al.*, 2021; Dogan *et al.*, 2021). Furthermore, the study area belongs to the tsunamigenic zone of Cyclades, which is characterized by moderate tsunamigenic potential (Papadopoulos and Fokaefs, 2005; Gogou *et al.*, 2023).

The high tsunami exposure in the region is related to the increasing urbanization on the islands over the past few decades and, most notably, to the continuous expansion of tourism in coastal zones. Moreover, the ongoing climate crisis, which has led to steadily rising temperatures throughout the year (Copernicus Climate Change Service, 2025), has enabled the tourism development in coastal areas even during winter season (Bank of Greece, 2025). This fact has resulted in the extension of the tourist season in Greece, consequently increasing exposure and vulnerability to several natural hazards, including tsunami.

The present study assesses the suitability of designated assembly points in case of an event triggers a tsunami in the southern part of the Aegean Sea. The research methodology was applied to the coastal areas of islands within the Cyclades complex, located close to the activated area surrounding Anydros Islet.

Methodology

Mapping and quantifying tsunami hazard remains a significant challenge, as predicting the occurrence, magnitude, and extent of damage from a tsunami is inherently complex and difficult to model. The wide array of potential causes, combined with the numerous possible source areas, renders it nearly impossible to provide a fully accurate and deterministic risk assessment.

Even in regions with rich tsunami inventory, the potential for a larger, more impactful event persists, despite the exclusion of certain combinations of source and magnitude through prior analysis. This is especially true for areas that are susceptible to tsunamis triggered by any of the primary tsunami-triggering mechanisms (earthquakes, volcanic eruptions, and coastal and offshore landslides) or by their combination, as applicable to the study area.

Based on the literature on tsunami impacts in coastal areas, both within the study area and globally, along with the unique morphological features of the southern part of the Aegean Sea and the exposure and vulnerability of the coasts to potential tsunamis, the delineation of tsunami risk zones of the studied coastal areas was implemented.

When the run-up increases, the tsunami risk usually increases as well, since the inundation covers a larger area. However, there are certain factors that can reduce the risk, even when the run-up is high. These factors include urban and morphological characteristics of the affected area, including natural barriers (such as coastlines with steep slopes, sandy beaches, or wetlands), as well as constructions and infrastructure that avoid contact with sea level.

The used run-up values were obtained from a combination of data from past events (Gogou *et al.*, 2018) and contributed to the effective tsunami risk zoning, which comprises the following six zones characterized by different run-up values (Table 1):

*   **Zone 1 with run-up up to 3 m**: These run-up values have been reported during tsunami generation in the southern part of the Aegean Sea, based on the available historical data. They represent the minimum recorded values in the area. However, they are characterized by high occurrence probability. Furthermore, this zone is the most vulnerable and exposed to tsunami impact as it lies along the coastal front. Considering that this zone is where most of the constructions, infrastructure, and the most intense human activity are developed, the Zone 1 is defined as the direct-high risk zone, presented with red colour in Table 1 and Figure 1.
*   **Zone 2 with run-up ranging from 3 to 5 m**: This zone is located farther inland compared to the previous zone, making it more distant from the coastal front. It includes run-up values recorded and reported from the majority of the islands of the central and southern part of the Aegean Sea, which were affected by the 1956 Amorgos tsunami. This area is also considered highly vulnerable to tsunami inundation and impact. The Zone 2 is defined as the high risk zone, presented with orange colour in Table 1 and Figure 1.
*   **Zone 3 with run-up ranging from 5 to 10 m**: This zone also includes run-up values from the 1956 tsunami. At least five areas in Amorgos, Folegandros and Astypalaea Islands experienced such inundation or larger based on Okal *et al*. (2009). The Zone 3 is defined as the moderate risk zone, presented with yellow colour in Table 1 and Figure 1.
*   **Zone 4 with run-up ranging from 10 to 20 m**: In the 1956 tsunami, the highest recorded run-up reached 20 m along the southern coastline of Amorgos Island (Okal et al., 2009). The Zone 4 is defined as the low risk zone presented with light green colour in Table 1 and Figure 1.
*   **Zone 5 with run-up ranging from 20 to 30 m**: . This zone includes run-up values that exceed the maximum identified and published run-up in the southern Aegean islands from the 1956 tsunami, which is 20 meters in the southern part of Amorgos. The Zone 5 is defined as the very low risk zone presented with dark green colour in Table 1 and Figure 1.
*   Zone **6 with run-up larger than 30 m**: This zone is considered to have a low probability of tsunami impact due to volcanic eruptions along the South Aegean Volcanic Arc based on historical evidence. However, extreme events cannot be entirely ruled out. Similar tsunami events caused by volcanic activity, such as the 1883 Krakatau eruption, have produced run-ups of up to 42 meters (Charles W. et al., 1994). This zone can be considered safe under most scenarios due to the rarity of the phenomenon. This zone is located farther inland compared to the previous zone and has no colour indication in Table 1 and Figure 1.

The proposed zoning for the coastal areas of the southern Aegean islands is presented in Table 1.

Table 1. The Tsunami Risk Zones for the Central Aegean area.

Zone	Max Run-Up (m)	Past events	Tsunami Risk
1	< 3 m	Common events (tsunamis with lowest run-up)	Direct-high
2	3-5	Recorded values from 1956 Amorgos tsunami	High
3	5-10	Recorded values from 1956 Amorgos tsunami	Moderate
4	10-20	Maximum run-up from 1956 Amorgos tsunami	Low
5	20-30	Seabed deformation or largest landslide	Very low
6	> 30	Rare extreme events (volcanic eruptions)	Considered safe under most scenarios

Using a Geographic Information System (GIS), the delineation of tsunami risk zones was conducted based on the local contours of selected islands in the south Aegean and subsequently overlaid with recent satellite imagery. Then,

the thematic layer of the assembly points for earthquake-related emergencies were also added and evaluated based on the tsunami risk zones. This methodological approach enabled the identification of (i) the specific tsunami risk zones in which the designated assembly points are located, and (ii) the corresponding level of tsunami hazard exposure associated with each site.

The aforementioned methodology was applied along the entire coastline of Ios, Folegandros, Naxos, Irakleia, Schoinousa, Ano Koufonisi, Kato Koufonisi, Amorgos, Santorini, and Anafi Islands. These islands were selected due to their short distance from the seismically activated area in early 2025 and the increased probability of being affected by a potential tsunami, which could be triggered in the case of a larger seismic event either by sea-bed displacement or by coastal and submarine landslides.

Results

This section comprises the results of the applied methodology to four locations within the study area: Perissa area in Santorini, Katapola settlement in Amorgos, Chora town in Naxos, and the Ios port (Figure 1). These sites were selected because they are characterized by significant population densities, comprising both residents and visitors, as well as the presence of critical infrastructure essential during emergencies triggered by natural hazards, particularly earthquakes and related geohazards.

In Santorini, the designated assembly points are situated at considerable distances from the coastline. For example, the southeastern assembly point is located approximately 3,100 meters from the coastal settlement of Perivolos and 3,200 meters from Perissa. While such locations may be suitable for seismic safety, they are impractical as immediate, pedestrian-accessible assembly points in the event of a tsunami. In Naxos, many of the designated assembly points fall within the direct-high risk zone (red zone). In Ios, the sole designated assembly point for the port area is located within the inundation zone, even under 0–3 m run-up. This renders the location unsuitable for tsunami evacuation.
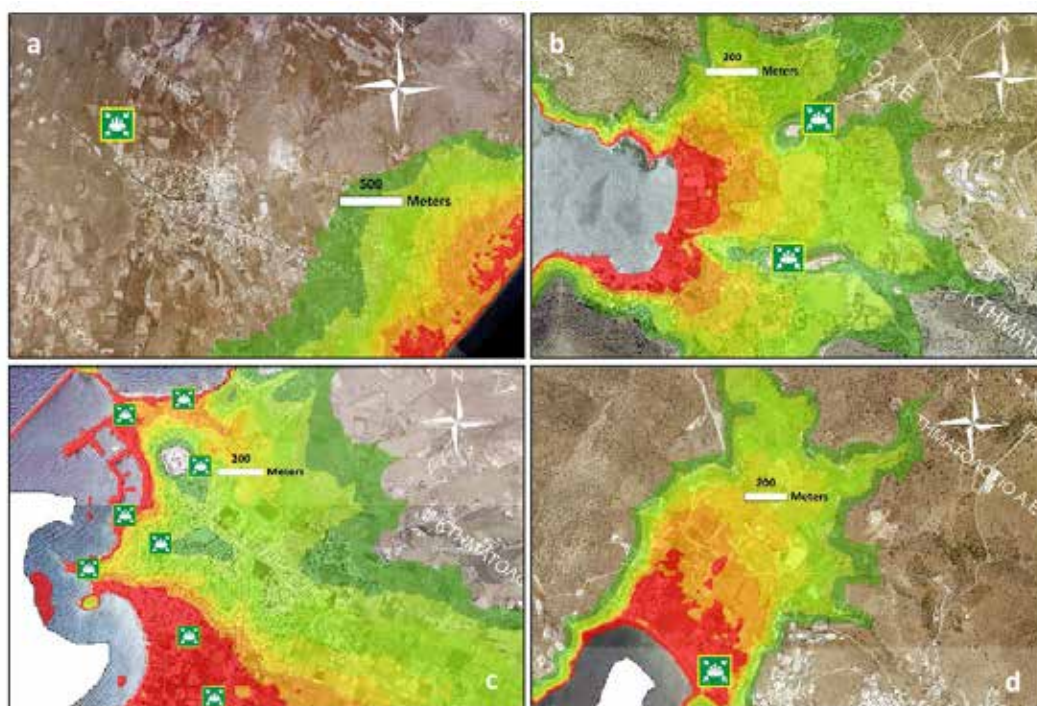
Figure 1. Maps illustrating the results of the applied methodology in selected coastal areas of the Cyclades island complex: (a) Perivolos – Perissa in Santorini. This assembly point is located at a considerable distance from the coastal zone, making it safe from the adverse effects of a potential tsunami, but unsuitable for immediate sheltering of the affected people, who will have to cover many kilometers to reach the site. (b) Katapola in Amorgos. The assembly points have been correctly selected, as they are located both in the safe zone and close to the residential area. (c) Chora town in Naxos. Most of the selected assembly points are considered unsuitable, as the majority is located either along the coastal front or within the direct-high and high risk zones. (d) Ios Port. The designated assembly point is considered unsuitable due to its location within the direct-high risk zone.

This approach enables the integration of additional thematic layers, such as key urban planning characteristics, including land use, road network, and public spaces, into the assessment process. Such integration supports the development of targeted actions aimed at enhancing safety and accessibility, including the updating and optimization of assembly points and the delineation of safe evacuation routes.

A representative application of the aforementioned methodology was conducted within the present study in the area of the port of Ios. The assembly point proposed in the frame of this study (indicated by the blue symbol in Figure 2), is situated on a hillside between the port facilities and Gialos beach and selected to serve the eastern shoreline of the port bay. The site is positioned approximately 15 m above sea level and lies just 130 m from the coastline. Based on the aforementioned zoning, it is classified within a low tsunami risk zone. As such, it may be considered a safe location in the event of tsunami scenarios of equal or lesser intensity than the 1956 Amorgos tsunami, compared to the rejected assembly point located within the port area and in the direct-high risk zone (Figure 2).

Figure 2. (a) View of the area showing both the rejected assembly point included in the web platform and the new assembly point proposed in the frame of the present study. (b) The old point is located within the direct-high risk zone, while the new point lies within the low risk zone. (c) Delineation of evacuation routes from three important locations to the proposed assembly point in case of an emergency.

The primary accessibility characteristics of the newly designated assembly point in Ios Port (indicated by the blue symbol in Figure 2) are summarized as follows:

- From a representative location within the coastal settlement (Coordinates: 36.726458, 25.274483): approximately 400 meters, with an estimated average arrival time of 6 minutes.
- From Gialos Beach (point 1 in Figure 2): approximately 240 meters, with an estimated average arrival time of 4 minutes.
- From the main port pier (point 2 in Figure 2), the location used for large passenger vessel docking and embarkation/disembarkation: approximately 250 meters, with an average arrival time of 3 minutes.
- From the central area of the marina pier (point 3 in Figure 2): approximately 200 meters, with an estimated average arrival time of 2 minutes.

These distances and times reflect the site's high accessibility from key coastal activity zones, supporting its suitability as an emergency evacuation point.

Conclusions

With the exception of a few cases (e.g., Amorgos), where designated assembly points have been appropriately selected and offer sufficient protection in the event of a tsunami, the majority of sites proposed by local municipalities and currently listed on the aforementioned web platform of assembly points are assessed as inadequate for tsunami response and require urgent reassessment.

In Santorini, additional strategically positioned assembly points should be designated specifically for vulnerable coastal zones. In Naxos, due to the high density of the urban fabric in Chora town, it is essential to reassess current assembly points and develop accessible, well-defined evacuation routes that can be safely followed during emergencies.

With particular focus to the area of the bay where the port of the Ios island is located, , the present study proposes a more appropriate emergency assembly point. Based on calculated distances and estimated pedestrian travel times, the newly proposed site demonstrates an adequate level of protection from tsunami inundation. However, for these evacuation routes to function effectively, targeted urban planning interventions are necessary, such as creating direct, unobstructed paths to safe zones, avoiding bottlenecks, low-lying flood zones, and congested areas, as well as selecting designated multi-modal paths, walkable for pedestrians, accessible for vehicles and people with disabilities, among other actions. Additionally, at least two more assembly points should be established: one for the western section of the bay and another for the southeastern zone.

To mitigate tsunami risk in the study area, several key actions are recommended. These include the systematic reassessment and, where necessary, revision of designated evacuation and assembly points, as well as the clear delineation of tsunami evacuation zones. It is essential to design and mark evacuation routes that are both accessible and efficient, ensuring they can be safely used by all individuals, including individuals with disabilities. Regular operational exercises should be conducted with the active participation of residents and authorities at the central, regional, and local levels, to ensure preparedness and coordination in the event of a tsunami. Furthermore, continuous scientific monitoring of regional seismic and volcanic activity is necessary, as well as the submarine mapping, alongside enhancements to the tsunami early warning system and the supporting sensor network. Finally, public awareness and education initiatives should be implemented, targeting local populations, visitors, and vulnerable groups, in order to foster a culture of preparedness and resilience.

Acknowledgements

References

Ambraseys, N.N., 1960. The seismic sea wave of July 9th 1956, in the Greek Archipelago, Journal of Geophysical Research, 65, 4, 1257-1265, https://doi.org/10.1029/JZ065i004p01257

Mandeville, C.W., Carey, S., Sigurdsson, H, King, J., 1994. Paleomagnetic evidence for high-temperature emplacement of the 1883 subaqueous pyroclastic flows from Krakatau Volcano, Indonesia. Journal of Geophysical Research, 99 (B5), 9487-9504. https://doi.org/10.1029/94JB00239

Copernicus Climate Change Service. Surface Air Temperature Maps. Available online: https://climate.copernicus.eu/surface-air-temperature-maps (accessed on 5 April 2025).

Dogan, G.G., Yalciner, A.C., Yuksel, Y., Ulutaş, E., Polat, O., Güler, I., Şahin, C., Tarih, A., Kânoğlu, U., 2021. The 30 October 2020 Aegean Sea Tsunami: Post-Event Field Survey along Turkish Coast. Pure and Applied Geophysics, 178, 785-812. https://doi.org/10.1007/s00024-021-02693-3

Galanopoulos, A.G., 1956. The seismic sea-wave of July 9, 1956. Proceedings of the Academy of Athens, 82, 90-101.

Gogou, M., Andreadakis, E., Nomikou, P., Lekkas, E., 2018. Previewing (and prioritization) tsunami risk in coastal zone of southern Aegean Sea, 9th International INQUA Meeting on Paleoseismology, Active Tectonics and Archeoseismology (PATA).

Gogou, M., Mavroulis, S., Evelpidou, N., Lekkas, E., 2023. Earthquakes and Tsunamis: Natural Hazards over the Aegean Archipelago. In: The Handbook of Environmental Chemistry. Springer, Berlin, Heidelberg. https://doi.org/10.1007/698_2022_941

Gogou, M., Mavroulis, S., Evelpidou, N., Stagonas, D., Lekkas, E., 2024. Effective estimation of Tsunami Coastal Impacts based on Tsunami Inventories, Satellite Imagery and Inundation Zoning, 18th Plinius Conference on Mediterranean Risks, Chania, Greece, 30 Sep–3 Oct 2024, Plinius18-102, https://doi.org/10.5194/egusphere-plinius18-102

Gogou, M., Triantafyllou, I., Mavroulis, S., Lekkas, E., A. Papadopoulos, G., 2021. The October 30, 2020 tsunami in the eastern Aegean Sea: Intensity mapping on Samos Island based on the Integrated Tsunami Intensity Scale (ITIS 2012). EGU General Assembly 2021, 19–30 Apr 2021, EGU21-5006, https://doi.org/10.5194/egusphere-egu21-5006

Karkani, A.; Evelpidou, N.;Tzouxanioti, M.; Petropoulos, A.; Gogou, M.; Mloukie, E., 2022. Tsunamis in the Greek Region: An Overview of Geological and Geomorphological Evidence. Geosciences, 12, 4. https://doi.org/10.3390/geosciences12010004

Leclerc, F., Palagonia, S., Feuillet, N., Nomikou, P., Lampridou, D., Barrière, P., Dano, A., Ochoa, E., Gracias, N., Escartin, J., 2024. Large seafloor rupture caused by the 1956 Amorgos tsunamigenic earthquake, Greece. Communications Earth & Environment, 5, 663. https://doi.org/10.1038/s43247-024-01839-0

Lekkas, E., Carydis, P., Mavroulis, S., Gogou, M., Andreadakis, Emm., Katsetsiadou, K.-N., Skourtsos, Emm., Minos-Minopoulos, D., Bardouli, P., Voulgaris, N., Papadimitriou, P., Kaviris, G., Tselentis, G.-A., Karakonstantis, A., Parcharidis, I., Papastergios, A., Tsironi, V., Lalechos, S., Avramea, Kleanthi, M., Papaioannou, C., Salonikios, T., Adam, N., Sakellariou, D., 2017. The Mw 6.6, July 21, 2017 Kos Earthquake, Scientific Report (Version 2.0). Newsletter of Environmental, Disaster, and Crises Management Strategies, 1, ISSN 2653-9454.

Okal, E.A., Synolakis, C.E., Uslu, B., Kalligeris, N., Voukouvalas, E., 2009. The 1956 earthquake and tsunami in Amorgos, Greece. Geophysical Journal International, 178: 1533-1554. https://doi.org/10.1111/j.1365-246X.2009.04237.x

Papadopoulos, G.A., Fokaefs, A., 2005. Strong tsunamis in the Mediterranean Sea: a reevaluation. ISET Journal of Earthquake Technology, 42, 159-170.

Papadopoulos, G.A., Pavlides, S.B., 1992. The large 1956 earthquake in the South Aegean: Macroseismic field configuration, faulting, and neotectonics of Amorgos Island, Earth and Planetary Science Letters, 113, 3, 1992, 383-396, https://doi.org/10.1016/0012-821X(92)90140-Q

Shaw, B., Ambraseys, N.N., England, P.C., Floyd, M.A., Gorman, G.J., Higham, T.F.G., Jackson, J.A., Nocquet, J.-M., Pain, C.C., Piggott, M.D., 2008. Eastern Mediterranean tectonics and tsunami hazard inferred from the AD 365 earthquake. Nature Geoscience, 1, 268-276, https://doi.org/10.1038/ngeo151

Sørensen M.B., Spada M., Babeyko A., Wiemer S., Grünthal G., 2012. Probabilistic tsunami hazard in the Mediterranean Sea. Journal of Geophysical Research, 117, B01305, http://dx.doi.org/10.1029/2010JB008169

Triantafyllou, I., Gogou, M., Mavroulis, S., Lekkas, E. Papadopoulos, G.A.; Thravalos, M., 2021. The Tsunami Caused by the30 October 2020 Samos (Aegean Sea) Mw 7.0 Earthquake: Hydrodynamic Features, Source Properties and Impact Assessment from Post-Event Field Survey and Video Records. Journal of Marine Science and Engineering, 9, 68. https://doi.org/10.3390/jmse9010068

Palaeoenvironmental Interpretation and Soft Sediment Deformation of the Ionian Basin Lower Jurassic Formations in Astakos (Western Greece)

Golfinopoulos V.[1], Piper J.W.D.[2], Zelilidis A.[1], Pe-Piper G.[3], Papadopoulou P.[1], Bourli N.[1], Iliopoulos G.[1]

(1) University of Patras, Department of Geology, Patras, Greece, gkolfinopoulosv@ac.upatras.gr (2) Dalhousie University, Department of Oceanography Halifax, Canada (3) Saint Mary's University, Department of Geology, Halifax, Canada

Introduction

The Ammonitico Rosso (AR) Formation (Fm) is one of the best-known lithofacies of the Tethys Ocean's history due to its peculiar lithological features (Cecca et al. 1992). During the Early Jurassic, the opening of the Tethys Ocean begun, influenced by intense faulting which led to the development of both shallow marine platforms and deep-sea basins (Bernoulli and Renz, 1970). Extensional stress led to the development of the Ionian Basin (Bernoulli and Renz, 1970; Zelilidis et al., 2015). Intrabasinal differentiations resulted in submarine highs with minimal sediment deposition and continuous deposition in local depressions (Bernoulli and Renz, 1970).

Benthic foraminifera and ostracods are valuable tools for palaeoenvironmental reconstructions (Ansari et al., 2022 and reference therein;). Especially for the Jurassic, they could be useful for the age determinations of the studied formations as well. Thus, a variety of studies on Lower – Middle Jurassic ostracods and benthic foraminifera have been conducted in the Neo-Tethys region. Despite extensive research on Jurassic foraminifera and ostracods in the Tethys Ocean, there is a notable absence of such studies in Greece, except for a few studies on Jurassic benthic foraminifera using thin sections. Nevertheless, the systematic study of ostracods through the study of thin sections is not possible.

Landslides that produce mass-transport deposits occur in loosely consolidated soft sediments in both subaerial and submarine environments (Ferrill et al. 2023). Synsedimentary deformation structures (synsedimentary faults, folds, slide planes, dewatering structures, etc.) are widely distributed in the syn-rift formations of the Ionian Basin of Greece (Golfinopoulos et al. 2025 and reference therein).

The study area is located in the region of Western Greece, in the regional district of Aitoloakarnania, approximately 8 km northwest of Astakos town and 10 km southeast of Mytikas village. In this area, Jurassic and Cretaceous formations of the External Ionian Basin are exposed in coastal sections, road cuts, and sparsely vegetated mountain slopes.

Objectives

The main objectives of this study are: i) to document the first stereoscopic record of Jurassic benthic foraminifera and ostracods in Greece, ii) to reconstruct the palaeoenvironment and determine the age of the AR and Posidonia beds Fms in the Ionian Basin, iii) to unravel the internal structure of AR Fm, which includes several horizons of synsedimentary deformation and iv) to present the revised geological map of the studied area as part of this project.

Methods

In the field, detailed bed-by-bed logs were measured, and then the corresponding lithostratigraphic columns were produced. Fieldwork also included measurements, descriptions, and reconstruction of the studied stratigraphy, bearing in mind the local tectonic activity. A total of 52 rock samples and 8 sediment samples were collected from eight sequences. Thirty of the most characteristic rock samples were thin sectioned for microfacies analysis. Microfacies analysis was conducted using Folk's (Folk, 1959) and Dunham's (Dunham, 1962) classifications. Additionally, the revised Wilson model (Wilson, 1975), which defines 26 standard microfacies (SMF) types that are associated with 10 standard facies zones (FZ), was employed. For all sediments samples, micropalaeontological analysis was carried out. The strongly deformed horizons were recorded in detail, including their thickness, deformation axis, their relation to the underlying and overlying horizons, and the bedding planes' dip and direction. Additionally, the characteristics and kinematics of the faults were recorded and analyzed in relation to the depositional processes.

Results

The Jurassic to Cretaceous formations of the External Ionian sub-basin were studied, focusing on the AR Fm, as it appears fully developed in the study area. Specifically, in this area, the following formations are exposed (from the

base to the top): Pantokrator limestones, Sinies limestones, Lower Posidonia beds, AR, limestones with filaments, and Vigla limestones Fms. The base of the succession consists of massive- to thick-bedded white limestones (Pantokrator Fm, Sequence 1). These are overlain by thin- to medium-bedded siliceous limestones (Sinies Fm) which locally contain ichnofossils, stylolites, and occasional chert nodules (Sequences 2-5). Conformably, on the latter, alternations of laminated green-brown pelites with laminated marly limestones were recognized (possible Posidonia beds, Sequence 6, the beginning of Sequence 7). Above them, alternations of red pelites and calcilutites with grey and red nodular limestones were observed (AR Fm, Sequence 7). In the red pelites, grey nodular limestones, and red nodular limestones, ammonites and ichnofossils were observed. The upper stratigraphic part of this formation consists of pink-beige limestones (Limestones with filaments Fm, the beginning of Sequence 8). These strata are laminated to medium-bedded. In the upper part of the studied section, thin- to thick-bedded beige siliceous limestones with chert nodules and chert bands (Vigla limestone Fm, Sequence 8) are present. Notably, within this upper formation, brown shales containing very small polymetallic nodules were recorded (Golfinopoulos et al. 2025, Figure 1).
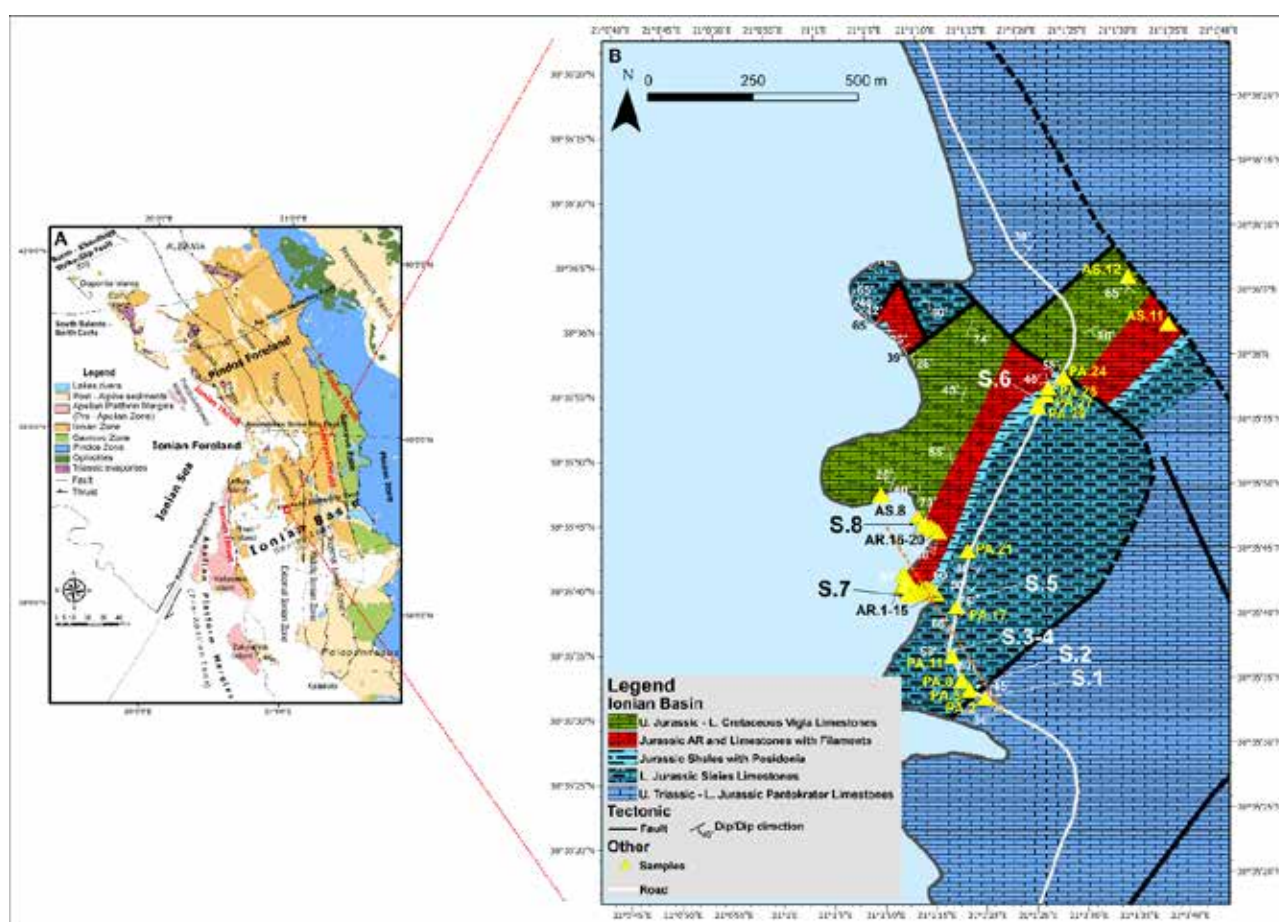
Figure 1: A) Simplified geological map of the External Hellenides in NW Greece, modified from (Zelilidis et al. 2015), where the red box indicates the study area. B) Geological map of the study area. Codes with letter "S" represent the locations of the sequences referred to in the text (modified from Golfinopoulos et al. 2025).

The microfacies analysis of 30 studied thin sections from Sequences 1 - 8 showed two different depositional environments, toe of slope (FZ 3) and platform-margin reefs (FZ 5), corresponding to two different standard microfacies types. Each MF corresponds to a different SMF type. Specifically, MF 1 is classified as biosparite/ boundstone (SMF 7), while MF 2 includes micrites, fossiliferous micrites, and both sparse and packed biomicrites/ wackestones and packstones (SMF 3, SMF 3-RAD, SMF 3-CALP, SMF 3-FIL). The biofacies analysis revealed among others (radiolaria, filaments, benthic and planktonic foraminifera), the existence of planktonic foraminifera of the genus *Globuligerina* in Sequences 5, 6, 7 and 8. The samples of Sequence 5 belong to the upper part of Sinies limestone Fm, based on their lithological features and their relationship to the overlying formations, they appear to have been deposited during the Late Pliensbachian. If verified, this claim would shift the first appearance of

planktonic foraminifera from the Toarcian to the Pliensbachian (Golfinopoulos et al. 2025).

In total 8 sediment samples from Sequences 6-7 were micropalaeontologically studied as well. Two of the samples were barren, while all the other samples contained sufficient numbers of benthic foraminifera tests and ostracod valves. A few fish teeth and sea urchin spines were recorded as well. In total, 15 benthic foraminifera species belonging to 7 families, namely Ichthyolariidae, Vaginulinidae, Lagenidae, Nodosariidae, Polymorphinidae, Spirillinidae and Saccamminidae, were determined. Regarding the ostracod assemblages, at least 10 species belonging to 3 families (Polycopidae, Healdiidae and Bairdiidae), were determined as well. Most of the studied material is moderately to very badly preserved, thus making some of the determinations difficult. Ostracod molds of oval to ellipsoidal shape have been retrieved. Their shape points to a suborder other than Metacopina and Podocopina, whose shape is more sub-triangular. A significant number of the determined in this study benthic foraminifera (Ichthyolariidae, Vaginulinidae, Polymorphinidae and Saccamminidae) and ostracods (Polycopidae and Healdiidae) are characteristic for the Lower Jurassic (Pliensbachian – Toarcian) assemblages of the Tethys Ocean.

In Sequence 7 synsedimentary deformation structures have been developed. The succession of this Sequence begins with greenish-grey shales, quite distinct from the overlying red and white limestones and shales of the AR Fm. The base of the unit is not exposed, whereas at beach level, the top is marked by a few centimetres of greenish deformed fissile shale, conformably overlain by AR-type limestone. Along the strike, in the cliff face, the contact appears rather irregular. As the internal details of this unit are not well exposed, it is simply termed the Lower Unit. It is probably either a complex slide or a debris-flow deposit with rafted blocks of bedded limestone, but the possibility that the unit is in situ and suffered some internal deformation from the overlying slide cannot be excluded. The base of the AR Fm shows considerable synsedimentary deformation. The lowest shale unit has a recumbent fold closure. It is overlain by discontinuous decimeter-scale boudins of micritic limestone enclosed in rubbly AR limestones and shale, with a ghost stratigraphy about 1 m thick. This is overlain by 30 cm of apparently undeformed reddish marl and several meters of alternating nodular limestones and reddish shales with discontinuities between packets of limestone beds, thus creating a series of oblique, bedding-parallel slabs of alternating limestone and shale. In places, limestone beds terminate or are boudinaged, and shales are deformed. The proportion of limestone increases upward. This limestone is overlain by a 2 m thick, polymictic limestone, matrix-supported conglomerate interpreted as a debris-flow deposit, termed debrite 1. Debrite 1 is overlain by about 1 m of reddish shales with discontinuous thin limestone beds. Overlying bedded limestones show brittle deformation into metre-scale tilted blocks, apparently as part of the slide mass. Interbedded with the AR limestones is at least one graded calcirudite to calcarenite turbidite. Debrite 2 overlies the tilted blocks and is about 1 m thick. It is redder in colour than debrites 1 and 3 and is also matrix-supported. Debrite 3 is poorly sorted, with large subangular blocks, supported by a matrix of sand-sized limestone clasts and red mud. The top of debrite 3 is overlain by 30 cm of seemingly undeformed red shale and then an AR limestone section that in its upper part is deformed into a large open fold (Figure 2). The fold is unconformably overlain by about 1 m of bedded limestones with rapid lateral thinning, suggesting that it is also a block within the overall slide. These bedded limestones are overlain by an 1 m bed of sorted conglomerate with an erosional contact with the underlying limestones. The conglomerate consists of rounded limestone pebbles, with the upper part of the bed comprising fine pebbles and granules. Above this conglomerate is a succession of red-grey bedded calcarenites (Golfinopoulos et al. 2025).

Figure 2: Representative view of sequence 7, where the three debrites (1-3) are developing.

Conclusions

During this study, 8 sedimentary sequences in the Astakos area have been studied. Detailed sedimentological, tectonic, and biostratigraphic analyses of both carbonate and clastic sediments have been conducted. Therefore, the following findings have been reported:

- This work presents the first stereoscopic record of Jurassic ostracods and benthic foraminifera in Greece.
- There are indications that some *Globuligerina* tests occurred earlier than previously known; their first appearance probably occurred during the Pliensbachian.
- Lower Posidonia Beds and Ammonitico Rosso Formations were deposited in the shelf and transported in deeper environments during the Pliensbachian to Toarcian.
- The studied sedimentary sequence, though, comprises an allochthonous submarine slide deposit, consisting of four imbricate slices capped by debrites (except the upper one) rather than four discrete slides. Upwards, a conglomerate with reworked limestone clasts has been deposited as a result of a single turbidite. The sequence closes with sediments of the limestone with filaments and Lower Posidonia bed Fms.
- The autochthonous AR Fm depositional setting fits well with a carbonate ramp, on which turbidity currents with a transport distance of several kilometres would have developed from a watery debris flow formed by headwall collapse
- The discovery of the AR Fm slide has a profound effect on the reported sedimentation rates for the area, which until now have not taken under consideration the duplication of the layers, and which thus must be significantly lower.
-

Acknowledgements

References

Ansari, A.H., Talib, A., Kumar, A., 2022. Tracing ecological fluctuations during the Middle to Late Jurassic of Jhura, Kutch, India, using foraminifera. Marine Micropaleontology, 177, 102183.

Bernoulli, D., Renz, O., 1970. Jurassic Carbonate Facies and New Ammonite Faunas from Western Greece. Eclogae Geologicae Helvetiae, 63, 573–607.

Cecca, F., Fourcade, E., Azéma, J., 1992. The Disappearance of the "Ammonitico Rosso". Palaeogeography Palaeoclimatology Palaeoecology, 99, 55–70.

Danelian, T., De Wever, P., Azéma, J., 1997. Palaeoceanographic Significance of New and Revised Palaeontological Datings for the Onset of Vigla Limestone Sedimentation in the Ionian Zone of Greece. Geological Magazine, 134, 869–872.

Dunham, R.J., 1962. Spectral Subdivision of Limestone Type. In Classification of Carbonate Rocks. American Association of Petroleum Geologists: Tulsa, OK, USA, Volume 1, pp. 62–84.

Ferrill, D.A., Smart, K.J., Lehrmann, D.J., Morris, A.P., McGinnis, R.N., 2023. Synsedimentary Slump Folding: Examples and Consequences of an under-Recognized Process in Epicratonic Basins. Marine and Petroleum Geology, 152, 106274.

Folk, R.L., 1959. Practical Petrographic Classification of Limestones. American Association of Petroleum Geologists Bulletin, 43, 1–38.

Golfinopoulos, V., Piper, D.J.W., Zelilidis, A., Pe-Piper, G., Papadopoulou, P., Bourli, N., Iliopoulos, G., 2025. Depositional Environments and Soft Sediment Deformation in the Early Jurassic Ammonitico Rosso Formation of Western Greece. Geosciences, 15, 10.

Wilson, J.L., 1975. Carbonate Facies in Geologic History. Springer: New York, NY, USA, 1-471.

Zelilidis, A., Maravelis, A.G., Tserolas, P., Konstantopoulos, P.A., 2015. An Overview of the Petroleum Systems in the Ionian Zone, Onshore NW Greece and Albania. Journal of Petroleum Geology, 38, 331–348.

17th INTERNATIONAL CONGRESS of the Geological Society of Greece

A decade of data: Updating the Hellenic Macroseismic Database for historical earthquakes

Goutsos, G.[1], Sakkas, G.[1,2], Sakellariou, N.[3], Kouskouna, V.[1]

[1]*National and Kapodistrian University of Athens, Athens, Greece, goutsos2002@yahoo.com, [2]Center for Security Studies, Athens, Greece, [3]Museo Nacional de Ciencias Naturales, Madrid, Spain*

Introduction

The Hellenic Macroseismic Database for historical earthquakes (HMDB.UoA, Kouskouna and Sakkas 2013) was developed at the Laboratory of Seismology of the University of Athens in 2013 within the framework of NERIES and SHARE projects, as a contributor to the Archive of Historical Earthquake Data inventory of Europe. Since then, new studies presenting additional macroseismic intensities from historical earthquakes have been published. Our aim is to update this database with the new Macroseismic Data Points (MDPs) and present its latest version. In addition, amendments regarding the parameters PlaceID, PlaceName and coordinates were introduced in order to better constrain the identity of localities and their multiple names within the centuries. Thus, a separate column containing the latest name of the locality is added, as well as one for comments related to the amendments. We anticipate enhancing the database with earthquakes from the early 20th century in the near future.

Before the update

The first version of HMDB.UoA consists of four tables (Kouskouna and Sakkas, 2013):

The *Earthquake Catalogue table* containing the core information on the available earthquakes such as origin time and date, focal depth, epicentral area, geographical coordinates of the epicentre, maximum observed intensity and epicentral intensity, equivalent moment magnitude, number of available macroseismic data points as well as additional data on methods for estimating magnitude, preferred epicentre and magnitude and errors (Table 1).

Table 1. Example of the Earthquake catalogue table in Excel sheet format.

id_UoA	Date	Year	Mo	Da	Ho	Mi	Se	Comments	Ax	StudyCode	Study	NMDP	Ix	IxNum	EpLat	EpLon	Io	IoNum	Ms	Mw	Mark
1	1040 02 02	1040	02	02					Izmir (TURKEY)	TAXE003	Taxeidis, 2003	1	9	9	38.417	27.150			6.7		IN AHEAD
2	1296 07 17 21	1296	07	17	21				Bergama (TURKEY)	TAXE003	Taxeidis, 2003	3	10	10	39.117	27.183			7.2		IN AHEAD
3	1383 08 06	1383	08	06				Dawn	Mytilene (LESVOS)	TAXE003	Taxeidis, 2003	1	10	10	39.100	26.550			7.2		IN AHEAD
4	1389 03 20 14 30	1389	03	20	14	30		Ho: 14-15	Chios (CHIOS)	KOUS2013	Kouna & Sakkas,	4	10	10	38.255	26.573			7.2		IN AHEAD
5	1396 00	1396							Chios (CHIOS)	TAXE003	Taxeidis, 2003	1	7	7	38.367	26.133			5.6		IN AHEAD
6	1471 00	1471						Year: before 1472	Lemnos (LEMNOS)	KOUS2013	Kouna & Sakkas,	2	8	8	39.950	25.300			6.2		IN AHEAD
7	1528 00	1528						Year: before 1528	Mytilene (LESVOS)	KOUS2013	Kouna & Sakkas,	1	10	10	39.100	26.550			7.2		IN AHEAD
8	1546 00	1546							Mastichochoria (CHIOS)	KOUS2013	Kouna & Sakkas,	1	7	7	38.230	26.030			5.6		IN AHEAD
9	1565 00	1565							Chios (CHIOS)	TAXE003	Taxeidis, 2003	1	6-7	6.5	38.367	26.133			5.4		IN AHEAD
10	1577 09 21	1577	09	21				Day: before 21	Balikesir (TURKEY)	KOUS2013	Kouna & Sakkas,	1	8	8	39.650	27.883			6.2		IN AHEAD
11	1580 00	1580							Mynia (PHOKIS)	KOUS2013	Kouna & Sakkas,	10	8	8							IN AHEAD
12	1595 09 22	1595	09	22					Manisa (TURKEY)	KOUS2013	Kouna & Sakkas,	12	7	7	38.657	27.643	6-7	6.5	5.6	6.1	IN AHEAD
13	1611 00	1611						1611-1612	Manisa (TURKEY)	KOUS2013	Kouna & Sakkas,	1	6-7	6.5	38.614	27.426			5.4		IN AHEAD
14	1636 02 27 22	1636	02	27	22				Kalloni (LESVOS)	TAXE003	Taxeidis, 2003	1	6-7	6.5	39.233	26.207			5.4		IN AHEAD
15	1646 00	1646							Nazilli (TURKEY)	TAXE003	Taxeidis, 2003	4	8-9	8.5	37.913	28.322			6.4		IN AHEAD
16	1648 10 18	1648	10	18				Night	Chios (CHIOS)	TAXE003	Taxeidis, 2003	1	3-4	3.5	38.367	26.133					NOT IN AHEA
17	1653 02 22	1653	02	22					Aydin (TURKEY)	TAXE003	Taxeidis, 2003	9	9-10	9.5	37.927	28.033	9	9	7.0		IN AHEAD
18	1654 05 20	1654	05	20					Izmir (TURKEY)	TAXE003	Taxeidis, 2003	1	7-8	7.5	38.417	27.150			5.9		IN AHEAD
19	1664 06 02	1664	06	02				night	Izmir (TURKEY)	TAXE003	Taxeidis, 2003	1	6-7	6.5	38.417	27.150			5.4		IN AHEAD
20	1667 11	1667	11						Izmir (TURKEY)	TAXE003	Taxeidis, 2003	1	5	5	38.417	27.150			4.8		IN AHEAD

The *Macroseismic Intensity Data Points* table (Kouskouna and Sakkas, 2013, Tables 2, 4) is the catalogue of available macroseismic data per earthquake. It contains available information on macroseismic data points (MDPs) such as the various available names of the localities, place identifier for seismic history (Locati and Cassera, 2010), locality geographical coordinates, assigned macroseismic intensities, reliability of data, source of data and is directly connected to the earthquake catalogue as well as the sources table (*Studies* table).

The *Reference Places table* (Table 3) containing reference places used as basic input for the online map. It is an independent table, not related to the other tables. Information of this table include the name of locality and the geographical coordinates, country, geographical area that the reference location belongs, availability of the reference location to shown on the map depending on the zoom level.

The *Studies* table (Table 4) contains the necessary information of the sources (original macroseismic studies) of the database. This information includes name of authors, editors, title of the study, original language of the study and links to the studies.

Table 2. Example of the *Macroseismic Intensity Data Points* table in Excel sheet format

id_UoA	EqDate	MDPidUoA	PlaceID	PlaceNameGreek	PlaceNameText	PlaceNameWeb	PlaceNameEng	PlaceNameEngGr	PlaceSc	PlaceLat	PlaceLon	PlaceLatTE	PlaceLonTE	Int	IntNum	MdpCount	Mark	Country
1	1040 02 02	1	TR-00052	Σμύρνη	Izmir	Σμύρνη (Izmir)	Izmir	Izmir Σμύρνη		38.417	27.150			9	9	1	IN AHEAD	TR
2	1296 07 17 21	2	TR-00051	Κωνσταντινούπολη	Istanbul	Κωνσταντινούπολη (Istanbul)	Istanbul	Istanbul Κωνσταντινούπολη		41.008	28.980			6	6	3	IN AHEAD	TR
2	1296 07 17 21	3	TR-00016	Πέργαμος	Bergama	Πέργαμος (Bergama)	Bergama	Bergama Πέργαμος		39.117	27.183			10	10	3	IN AHEAD	TR
2	1296 07 17 21	4	TR-00057	Χλιαρά	Kirkagac	Kirkagac	Kirkagac	Kirkagac Χλιαρά		39.060	27.680			10	10	3	IN AHEAD	TR
3	1383 08 06	5	GR-00132	Μυτιλήνη	Mytilini	Μυτιλήνη (Mytilini)	Mytilini	Mytilini Μυτιλήνη		39.100	26.550			10	10	1	IN AHEAD	GR
4	1389 03 20 14 30	6	GR-00232	Άγιος Κήρυκος Ικαρί	Agios Kirykos, Ikaria	Άγιος Κήρυκος Ικαρίας (Ayios Kirykos, Ikaria)	Agios Kirykos Ikaria	Agios Kirykos Ikaria Άγιος Κήρυκος Ικαρίας	MS	37.583	26.233			9	9	4	IN AHEAD	GR
4	1389 03 20 14 30	7	TR-00124	Νέα Φώκαια	New Foça/YeniFoça	Νέα Φώκαια (New Foça/YeniFoça)	New Foça/YeniFoça	New Foça/YeniFoça Νέα Φώκαια	SS	38.740	26.840			9	9	4	IN AHEAD	TR
4	1389 03 20 14 30	8	TR-00052	Σμύρνη	Izmir	Σμύρνη (Izmir)	Izmir	Izmir Σμύρνη		38.417	27.150			7-8	7.5	4	IN AHEAD	TR
4	1389 03 20 14 30	9	GR-00041	Χίος	Chios	Χίος (Chios)	Chios	Chios Χίος		38.367	26.133			10	10	4	IN AHEAD	GR
5	1396 00	10	GR-00041	Χίος	Chios	Χίος (Chios)	Chios	Chios Χίος		38.367	26.133			7	7	1	IN AHEAD	GR
6	1471 00	11	GR-00095	Κάστρο Κότζινο	Kotzinos castle	Κάστρο Κότζινο (Kotzinos castle)	Kotzinos castle	Kotzinos castle Κάστρο Κότζινο	SS	39.941	25.284			8	8	2	IN AHEAD	GR
6	1471 00	12	GR-00125	Παλαιόκαστρο/Μύρ	Palaiokastro/Mirina	Παλαιόκαστρο/Μύρινα (Palaiokastro/Mirina)	Palaiokastro/Mirina	Palaiokastro/Mirina Παλαιόκαστρο/Μύρινα	SS	39.867	25.067			7	7	2	IN AHEAD	GR
7	1528 00	13	GR-00132	Μυτιλήνη	Mytilini	Μυτιλήνη (Mytilini)	Mytilini	Mytilini Μυτιλήνη		39.100	26.550			10	10	1	IN AHEAD	GR
8	1546 00	14	GR-00116	Μαστιχοχώρια	Mastichochoria	Μαστιχοχώρια (Mastichochoria)	Mastichochoria	Mastichochoria Μαστιχοχώρια	MS	38.230	26.030			7	7	1	IN AHEAD	GR
9	1565 00	15	GR-00041	Χίος	Chios	Χίος (Chios)	Chios	Chios Χίος		38.367	26.133			6-7	6.5	1	IN AHEAD	GR
10	1577 09 21	16	TR-00011	Μπαλικεσίρ	Balikesir	Balikesir	Balikesir	Balikesir Μπαλικεσίρ		39.650	27.883			8	8	1	IN AHEAD	TR
11	1580 00	17	GR-00003	Αγία Ευθυμία	Ayia Efthymia/Mynia	Αγία Ευθυμία/Μυνιά (Ayia Efthymia/Mynia)	Ayia Efthymia/Mynia	Ayia Efthymia/Mynia Αγία Ευθυμία		38.483	22.367			8	8	10	IN AHEAD	GR
11	1580 00	18	GR-00016	Άμφισα	Amfisa	Άμφισα (Amfisa)	Amfisa	Amfisa Άμφισα		38.533	22.383			7	7	10	IN AHEAD	GR
11	1580 00	19	GR-00219	Βουνιχώρα	Vounikhora	Βουνιχώρα (Vounikhora)	Vounikhora	Vounikhora Βουνιχώρα		38.450	22.300			6	6	10	IN AHEAD	GR
11	1580 00	20	GR-00057	Γαλαξείδι	Galaxidi	Γαλαξείδι (Galaxidi)	Galaxidi	Galaxidi Γαλαξείδι		38.377	22.384			7	7	10	IN AHEAD	GR
11	1580 00	21	GR-00225	Ζάκυνθος	Zakinthos	Ζάκυνθος (Zakynthos)	Zakinthos	Zakinthos Ζάκυνθος		37.782	20.896			F	3.9	10	IN AHEAD	GR
11	1580 00	22	GR-00103	Λιδωρίκι	Lidhorikion	Λιδωρίκι (Lidhorikion)	Lidhorikion	Lidhorikion Λιδωρίκι		38.533	22.200			7	7	10	IN AHEAD	GR
11	1580 00	23	GR-00129	Μονή Σωτήρος	Moni Sotiros	Μονή Σωτήρος (Moni Sotiros)	Moni Sotiros	Moni Sotiros Μονή Σωτήρος	IB	38.483	22.367			8	8	10	IN AHEAD	GR
11	1580 00	24	GR-00052	Ναύπακτος	Naupaktos	Ναύπακτος (Nafpaktos)	Naupaktos	Naupaktos Ναύπακτος		38.395	21.833			7	7	10	IN AHEAD	GR
11	1580 00	25	GR-00153	Πεντεόρια	Pendeoria	Πεντεόρια (Pendeoria)	Pendeoria	Pendeoria Πεντεόρια		38.417	22.317			6	6	10	IN AHEAD	GR
11	1580 00	26	GR-00067	Τριταία/Καλοπετινίτ	Tritaia/Kalopetinitsa	Τριταία/Καλοπετινίτσα (Tritaia/Kalopetinitsa)	Tritaia/Kalopetinitsa	Tritaia/Kalopetinitsa Τριταία/Καλοπετινίτσα		38.450	22.367			6	6	10	IN AHEAD	GR

Table 3. Example of the ref_places (reference areas) table in Excel sheet format

RecordID	PlaceNameGreek	PlaceNameText	PlaceNameWeb	PlaceLat	PlaceLon	Country	ZoomLevel	GeographicalArea
GR-00001	Οθωνοί	Othonoi	Οθωνοί (Othonoi)	39.844	19.403	GR	detail	aegean
GR-00002	Ερεικούσσα	Erikoussa	Ερεικούσσα (Erikoussa)	39.883	19.583	GR	detail	aegean
GR-00003	Κέρκυρα	Corfu	Κέρκυρα (Kerkyra)	39.624	19.920	GR	medium	aegean
GR-00004	Παξοί	Paxoi	Παξοί (Paxoi)	39.198	20.170	GR	medium	aegean
GR-00005	Αντίπαξοι	Antipaxoi	Αντίπαξοι (Antipaxoi)	39.152	20.226	GR	medium	aegean
GR-00006	Λευκάδα	Leukada	Λευκάδα (Leukada)	38.836	20.707	GR	medium	aegean
GR-00007	Μεγανήσι	Meganisi	Μεγανήσι (Meganisi)	38.656	20.775	GR	medium	aegean
GR-00008	Αργοστόλι	Argostoli	Αργοστόλι (Argostoli)	38.179	20.487	GR	medium	aegean
GR-00009	Ιθάκη	Ithaki	Ιθάκη (Ithaki)	38.363	20.718	GR	medium	aegean
GR-00010	Ζάκυνθος	Zante (Zakinthos)	Ζάκυνθος (Zakinthos)	37.783	20.900	GR	medium	aegean
GR-00011	Αγρίνιο	Agrinion	Αγρίνιο (Agrinion)	38.633	21.417	GR	large	aegean
GR-00012	Βόνιτσα	Vonitsa	Βόνιτσα (Vonitsa)	38.917	20.833	GR	detail	aegean
GR-00013	Αμφιλοχία	Amfilokhia	Αμφιλοχία (Amfilochia)	38.862	21.166	GR	medium	aegean
GR-00014	Θέρμο	Thermon	Θέρμο (Thermon)	38.583	21.667	GR	detail	aegean
GR-00015	Μεσολόγγι	Messolongi	Μεσολόγγι (Messolongi)	38.367	21.433	GR	medium	aegean
GR-00016	Αστακός	Astakos	Αστακός (Astakos)	38.535	21.081	GR	detail	aegean
GR-00017	Ναύπακτος	Naupaktos	Ναύπακτος (Nafpaktos)	38.395	21.833	GR	medium	aegean
GR-00018	Αίγιο	Aiyion	Αίγιο (Aiyion)	38.250	22.083	GR	medium	aegean

Table 4. Example of the *Studies* table

StudyCode	Study	Authors	Editors	TitleOriginal	CitationOriginal	TitleEnglish	CitationEnglish	PublicationYear	ExtLink	ExtPdfLink	Language
KOUAL998	Kouskouna et al., 1998	Kouskouna V.; Karnassopoulou A.; Makropoulos K.; Taxeidis K.; Tzanis A.		Investigation of earthquakes (1400-1899) in Greece.	Kouskouna V., Karnassopoulou A., Makropoulos K., Taxeidis K. and Tzanis A., 1998. Investigation of earthquakes (1400-1899) in Greece. Internal report for the BEECD project, Department of Geophysics, University of Athens, Athina, 112 pp.	Investigation of earthquakes (1400-1899) in Greece.	Kouskouna V., Karnassopoulou A., Makropoulos K., Taxeidis K. and Tzanis A., 1998. Investigation of earthquakes (1400-1899) in Greece. Internal report for the BEECD project, Department of Geophysics, University of Athens, Athina, 112 pp.	1998		http://macroseismology.geol.uoa.gr/studies/KOUAL998.pdf	English
KOUS001	Kouskouna, 2001	Kouskouna V.	Ελληνική Γεωλογική Εταιρεία	Ο σεισμός της (28ης Δεκεμβρίου 1891) 9ης Ιανουαρίου 1892 στη Λάρισα.	Κουσκουνά Β., 2001. Ο σεισμός της (28ης Δεκεμβρίου 1891) 9ης Ιανουαρίου 1892. Δελτίο της Ελληνικής Γεωλογικής Εταιρείας, τομ. XXXIV/4, 1425-1432, 2001. Πρακτικά 9ου Διεθνούς Συνεδρίου, Αθήνα, Σεπτέμβριος, 2001.	The (December 28th, 1891) January 9th, 1892 Larisa (Central Greece) earthquake.	Kouskouna V., 2001. The (December 28th, 1891) January 9th, 1892 Larisa (Central Greece) earthquake. Bulletin of the Geological Society of Greece, Vol. XXXIV/4, 1425-1432. Proceedings of the 9th International Congress, Athens, September 2001 (in Greek).	2001		http://macroseismology.geol.uoa.gr/studies/KOUS001.pdf	Greek
MAKKO994a	Makrop. & Kous., 1994a	Makropoulos K.C.; Kouskouna V.	Albini P.; Moroni A.	The Ionian Islands earthquakes of 1767 and 1769: seismological aspects. Contribution of historical information to a realistic seismicity and hazard assessment of an area.	Makropoulos K.C. and Kouskouna V., 1994a. The Ionian Islands earthquakes of 1767 and 1769: seismological aspects. Contribution of historical information to a realistic seismicity and hazard assessment of an area. In: P. Albini and A. Moroni (eds.), Materials of the EC Project "Review of Historical Seismicity in Europe", vol. 2, 27-36.	The Ionian Islands earthquakes of 1767 and 1769: seismological aspects. Contribution of historical information to a realistic seismicity and hazard assessment of an area.	Makropoulos K.C. and Kouskouna V., 1994a. The Ionian Islands earthquakes of 1767 and 1769: seismological aspects. Contribution of historical information to a realistic seismicity and hazard assessment of an area. In: P. Albini and A. Moroni (eds.), Materials of the EC Project "Review of Historical Seismicity in Europe", vol. 2, 27-36.	1994		http://macroseismology.geol.uoa.gr/studies/MAKKO994a.pdf	English

Inspections to detect problems

Checks were made to investigate whether the existing MDPs in the respective table needed to be improved. This was achieved by introducing appropriate functions (if, ifand), which identify any points which need amendment, such as:

- localities with the same name (PlaceName) but different identification key (PlaceID)
- localities with the same PlaceID for different PlaceSc (Place Special case: isolated building, multiple settlement…)
- localities with the different name (PlaceName) but same geographical coordinates
- localities with the same identification key (PlaceID) for different localities
- localities with the same identification key (PlaceID) for different coordinates

These points were marked with different colors (Figure 5). It was observed that certain cells present more than one color. All appropriate corrections were made to these cells

Steps followed

Five new columns were added to the mdp_cat table

- OldPlaceNamesEn (containing the old names in English)
- OldPlaceNamesGr (containing the old names in Greek)
- LatestPlaceNameGr (containing the latest names in Greek)
- LatestPlaceNameEn (containing the latest names in English)
- Comments (containing the comments for any changes made to this mdp)

The format of StudyCode column was changed from 5 letters and 3 digits to 4 letters and 4 digits.

Finally, all coordinates were checked on all coordinates and adjustments were made, where necessary (Tables 5, 6 and Figure 1).

Table 5. Examples of points to be amended

PlaceID	PlaceNameGreek	PlaceNameText	PlaceNameEng	PlaceLat	PlaceLon
TR-00076	Ρεϊσντερέ	Reis-dere (Reisdere)	Reis-dere (Reisdere)	38.317	26.417
TR-00076	Τσεσμέκιοϊ	Tcheshmekioi (Reisdere)	Tcheshmekioi (Reisdere)	38.317	26.417
PlaceID	**PlaceNameGreek**	**PlaceNameText**	**PlaceSc**	**PlaceLat**	**PlaceLon**
GR-00003	Αγία Ευθυμία	Ayia Efthymia/Mynia		38.483	22.367
GR-00129	Μονή Σωτήρος	Moni Sotiros	IB	38.483	22.367
PlaceID	**PlaceNameGreek**	**PlaceNameEng**	**PlaceSc**	**PlaceLat**	**PlaceLon**
TR-00088	Τροία	Truva		39.956	26.240
TR-00088	Τροία	Truva	MS	39.956	26.240
PlaceID	**PlaceNameGreek**	**PlaceNameText**	**PlaceNameWeb**	**PlaceLat**	**PlaceLon**
TR-00053	Καραμπουρούν	Karaburun	Karaburun	38.617	26.517
TR-00107	Καραμπουρούν	Karaburun	Karaburun	38.617	26.517

Color	Meaning
	Same PlaceID for dif. region
	DIF PlaceNameText same COORDIN.
	DIF PlaceNameText same COORDIN2
	Same PlaceID Dif. COORDIN
	Dif. PlaceSc same COORDIN
	same coord dif place id
	Dif. PlaceID, same PlaceName
	Dif. PlaceID, same PlaceName
	Dif. PlaceID, same PlaceName
	Dif. PlaceID, same PlaceName
	Dif. PlaceID, same PlaceName
	Dif. PlaceID, same PlaceName
	Same PlaceID Dif PlaceSc

Corrections and inserting new data can be performed manually, or by using functions such as *vlookup* and *countif*. These functions automatically fill in the necessary parameters.
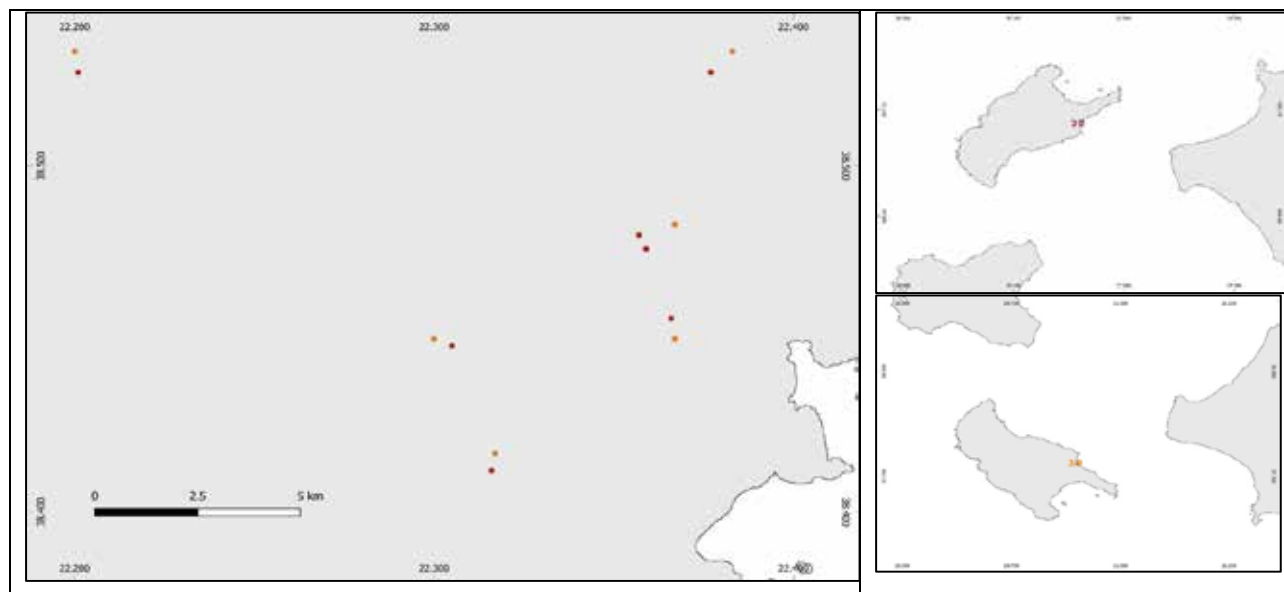
Figure 1. Two examples before (orange) and after (red) adjustments for the 1580 Mynia (PHOKIS) earthquake. Coordinates have been relocated and one intensity value was corrected from 3.9 to 3.5.

Table 6. Two examples before and after adjustments

	PlaceID	PlaceNameGreek	PlaceNameText	PlaceNameWeb	PlaceNameEng	PlaceNameEngGr	PlaceLat	PlaceLon
EXAMPLE	GR-00206	Τσουκαλοχώρι	Tsoukalokhorion	Τσουκαλοχώρι (Tsoukalokhorion)	Tsoukalokhorion	Tsoukalokhorion Τσουκαλοχώρι	39.267	26.067
1 BEFORE	GR-00185	Σκαλοχώρι	Skalokhorion	Σκαλοχώρι (Skalokhorion)	Skalokhorion	Skalokhorion Σκαλοχώρι	39.267	26.067
EXAMPLE	GR-00358	Μηλίτσα (εδώθε)	Militsa (Edhothe)	Μηλίτσα (εδώθε) (Militsa)	Militsa	Militsa Μηλίτσα (εδώθε)	36.867	21.833
2 BEFORE	GR-00359	Μηλίτσα (πέρα)	Militsa (Pera)	Μηλίτσα (πέρα) (Militsa)	Militsa	Militsa Μηλίτσα (πέρα)	36.867	21.833
EXAMPLE	PlaceID	Comments	OldPlaceNamesEn	OlderPlaceNamesGr	LatestPlaceNameGr	LatestPlaceNameEn	PlaceLat	PlaceLon
1 AFTER	GR-00206	PlaceNames and coordinates have been corrected	Tsoukalokhorion	Τσουκαλοχώρι	Σκαλοχώρι	Skalokhorion	39.260	26.075
EXAMPLE	PlaceID	Comments	OldPlaceNamesEn	OlderPlaceNamesGr	LatestPlaceNameGr	LatestPlaceNameEn	PlaceLat	PlaceLon
2 AFTER	GR-00358	I, PlaceNames and coordinates have been corrected			Μηλίτσα (εδώθε)	Militsa (Edhothe)	36.875	21.839
	GR-00359	I, PlaceNames and coordinates have been corrected			Μηλίτσα (πέρα)	Militsa (Pera)	36.870	21.846

Updating / adding "new" earthquakes

After the automation procedure, the existing database may be considered enriched and corrected. Moreover, we started to enrich this database with new data, either adding MDPs from recent studies in existing earthquakes, or introducing new earthquakes (Tables 7,8 and Figure 2). Thanks to the automation, this process was achieved without difficulty.

Table 7. The re-assessed Intensities and additional MDPs

Place	Date	NMDPs	Studies used for the update
Filiatra	1886 08 27	344	Sakellariou, N., Kouskouna, V. (2014)

Atalanti	1894 04 27	96	Albini, P., Pantosti D. (2004) / Sakellariou, N., Kouskouna, V. (2014)
Atalanti	1894 04 20	65	Albini, P., Pantosti D. (2004) / Sakellariou, N., Kouskouna, V. (2014)
Messini	1885 03 28	40	Sakellariou, N., Kouskouna, V. (2014)
Kyparissia	1899 01 22	109	Sakellariou, N., Kouskouna, V. (2014)

Table 8. "New" earthquakes and their MDPs from recent studies added in the database

Place	Date	NMDPs	Study
Lefkada	1704 11 22	12	Kouskouna et al. 2020
Negreponte	1708 04	3	Kouskouna et al. 2020
Lamia	1740 10 05	6	Kouskouna et al. 2020
Kefallinia	1741 06 23	6	Kouskouna et al. 2020
Corinthia	1742 02 21	11	Kouskouna et al. 2020
Aigio	1748 05 25	5	Kouskouna et al. 2020
Thiva	1853 08 18	41	Kaviris et al. 2022
Thiva	1853 09 29	14	Kaviris et al. 2022
Thiva	1893 05 23	13	Kaviris et al. 2022
Thiva	1893 05 22	3	Kaviris et al. 2022
Thiva	1872 09 26	1	Kaviris et al. 2022
Thiva	1833 12 13	1	Kaviris et al. 2022
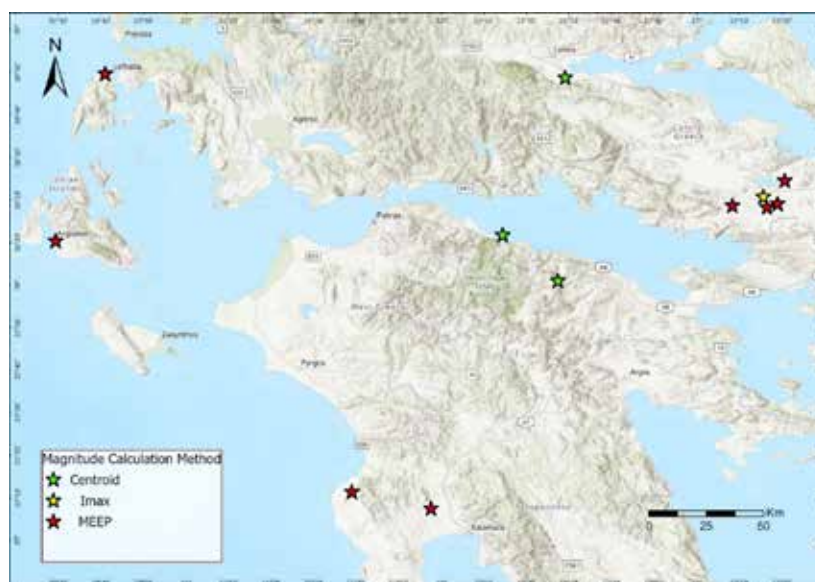
Figure 2. The epicentral areas of the "new" earthquakes (from Table 8)

Future objectives

New data inserted in the database, need previous thorough checks in terms of compatibility with the database format. More importantly, for each earthquake a macroseismic review is necessary to identify the most accurate and reliable source, as well as to double-check the available information from multiple sources in both terms of localities naming, geographical coordinates and avoid duplications that may lead to false data and, consequently, to unreliable results. On the other hand, newer earthquakes may include more data and be easier to calculate reliable equivalent moment magnitudes and epicentral

areas.

We aim to upload the updated database file at the webpage http://macroseismology.geol.uoa.gr/, as described by (Kouskouna and Sakkas 2013) using MIDOP (Locati and Cassera 2010) and also to incorporate early 20th century earthquakes and their MDPs, as it is common knowledge that the parameters determination of earthquakes continued to be based on macroseismic data for a few decades after the turn of the century. However, instrumental data begin to be more and more available and offer an opportunity to apply calibration methods using both macroseismic and instrumental data for improved parameters determination.

Acknowledgements

Bibliography

Albini, P. & Pantosti. D., 2004. The 20 and 27 April 1894 (Locris, Central Greece) Earthquake Sources through Coeval Records on Macroseismic Effects Bulletin of the Seismological Society of America, Vol. 94, No. 4, pp. 1305–1326

Kaviris, G., Kapetanidis, V., Spingos, I., Sakellariou, N., Karakonstantis, A., Kouskouna, V., Elias, P., Karavias, A., Sakkas, V., Gatsios, T., Kassaras, I., Alexopoulos, D.J., Papadimitriou, P., Voulgaris, N., Parcharidis, I., 2022. Investigation of the Thiva 2020–2021 Earthquake Sequence Using Seismological Data and Space Techniques. Appl. Sci. 2022, 12, 2630. https://doi.org/10.3390/app12052630

Kouskouna, V. & Sakkas, G., 2013. The University of Athens Hellenic Macroseismic Database (HMDB.UoA): historical earthquakes DOI 10.1007/s10950-013-9390-3

Kouskouna, V., 2001. The (December 28th, 1891) January 9th, 1892 Larisa (Central Greece) earthquake. Bulletin of the Geological Society of Greece, Vol. XXXIV/4, 1425-1432. Proceedings of the 9th International Congress, Athens, September 2001 (in Greek).

Kouskouna, V., Kaperdas, V., Sakellariou, N., 2020. Comparing calibration coefficients constrained from early to recent macroseismic and instrumental earthquake data in Greece and applied to eighteenth century earthquakes Volume 24, pages 293–317,

Kouskouna, V., Karnassopoulou A., Makropoulos K., Taxeidis K. & Tzanis A., 1998., Investigation of earthquakes (1400-1899) in Greece. Internal report for the BEECD project, Department of Geophysics, University of Athens, Athina, 112 pp.

Kouskouna, V., Makropoulos, K.C. & Tsiknakis, T., 1992. Contribution of historical information to a realistic seismicity and hazard assessment of an area. The Ionian Islands earthquakes of 1767 and 1769: historical investigation. In: P. Albini and A. Moroni (eds.), Materials of the EC Project "Review of Historical Seismicity in Europe", vol. 1, 195-206.

Kouskouna, V., Makropoulos, K.C. & Tsiknakis, K., 1992. Contribution of historical information to a realistic seismicity and hazard assessment of an area. The Ionian Islands earthquakes of 1767 and 1769: historical investigation. In: P. Albini and A. Moroni (eds.), Materials of the EC Project "Review of Historical Seismicity in Europe", vol. 1, 195-206.

Makropoulos, K.C. & Kouskouna, V., 1994a. The Ionian Islands earthquakes of 1767 and 1769: seismological aspects. Contribution of historical information to a realistic seismicity and hazard assessment of an area. In: P. Albini and A. Moroni (eds.), Materials of the EC Project "Review of Historical Seismicity in Europe", vol. 2, 27-36.

Makropoulos, K.C. & Kouskouna, V., 1994b. The 1894 April 20 and 27 Atalanti earthquakes: 100 years after - lessons learnt. Proc. XXIV ESC Gen. Ass., Athens, 19-24 Sept. 1994, vol. 1, 61-71.

Locati, M. & Cassera, A., 2010. MIDOP: Macroseismic Intensity Data Online Publisher. Rapporti Tecnici INGV, 123, 92 pp.

Sakellariou, N., Kouskouna, V. & Makropoulos, K.C., 2010. Macroseismic Intensities in Central-Southern Peloponnese during the 19th century. Laboratory of Seismology, Internal Report, 2010.

Sakelariou, N., & Kouskouna, V., 2014. Assigning Macroseismic Intensities of Historical Earthquakes from late 19th century in SW Peloponnese (Greece). Second European Conference on Earthquake Engineering and Seismology, Istanbul, Aug. 25-29.

Stucchi, M., A. Rovida, A., Gomez Capera, A.A, Alexandre, P., Camelbeeck, T., Demircioglu, M.B., Gasperini, P., Kouskouna, V., Musson, R.M.W., Radulian, M., Sesetyan, K., Vilanova, S., Baumont, D., Bungum, H., Fäh D., Lenhardt, W., Makropoulos, K., Martinez Solares, J.M., Scotti, O., Živčić, M., Albini, P., Batllo J., Papaioannou, C., Tatevossian, R., Locati, M., Meletti C., Viganò, D., Giardini, D., 2013. The SHARE European Earthquake Catalogue (SHEEC) 1000–1899. DOI 10.1007/s10950-012-9335-2.

Taxeidis K., 2003. Study of Historical Seismicity of the Eastern Aegean Islands. PhD thesis, N&K University of Athens, Greece, 301 pp.

17th INTERNATIONAL CONGRESS of the Geological Society of Greece

Seeking for dependencies of the high frequency "kappa" parameter of earthquake spectrum on weather/climate conditions

Grendas I.[1], Roumelioti Z.[1]

(1) Department of Geology, University of Patras, Patras, Greece, grendasioannis@gmail.com

Abstract

We investigate the seasonal variability of the κ_0 parameter, which describes the near-surface high-frequency attenuation of seismic waves. We analyze data from the ARGONET vertical array of accelerometers in Cephalonia, Greece, focusing on comparisons of high-frequency spectral decay between the surface station CK0 and the borehole bedrock station CK83. The study uses the ARGONET database records from July 2015 to October 2022. Results using two different approaches agree on a significant variation of κ_0 at CK0, with lower values in summer (dry period for Cephalonia) and higher values in winter (rainy period). This suggests that weather/climate related factors, such as soil moisture and temperature, influence near-surface attenuation, at least as expressed through the value of κ_0. This result challenges the assumption of a static value for κ_0 often made in site characterization for seismic hazard assessment.

Background

Kappa, κ, is used to quantify the attenuation of high-frequency seismic waves as they travel through the Earth's crust and near-surface materials. First introduced by Anderson and Hough (1984), it is determined from the slope of the high-frequency decay in the Fourier Amplitude Spectrum (FAS) of acceleration, typically using earthquake ground motion records. It is often analyzed in one component that reflects the attenuation occurring along the seismic ray path due to anelastic and scattering processes in the crust and one that quantifies the near-surface attenuation due to the shallow geological conditions, particularly in sedimentary layers.

The component of κ related to site-specific near-surface attenuation, widely called the kappa-zero, κ_0, is a crucial parameter in engineering seismology (e.g., Boore and Joyner, 1997; Ktenidou et al., 2014; Douglas et al., 2020). It enhances the accuracy of ground motion models in predicting high-frequency spectral amplitudes and is directly utilized in developing design spectra and ground motion simulations. By incorporating κ_0, engineers can better estimate seismic demands on structures, especially those sensitive to high-frequency vibrations. That is why it has been considered vital for critical facilities, such as nuclear power plants, where accurate characterization of high-frequency ground motion components is essential.

While κ has been widely adopted by both the seismological and civil engineering communities, several challenges and criticisms have emerged regarding its application. Estimating κ involves subjective decisions, such as selecting the frequency range for analysis and assuming linearity in the spectral decay. This can lead to variability and inconsistencies, which are further amplified by a lack of standardized methodologies in the parameter's computation and data with insufficient high-frequency content (e.g., Ktenidou et al., 2014). Furthermore, κ reflects a combination of attenuation processes, including scattering, anelastic absorption, site amplification effects and even soil-structure interaction and similar effects emerging from sensor installation practices (e.g., Parolai and Bindi, 2004; Hollender et al., 2020). Disentangling these contributions can be difficult and complicates the interpretation of the parameter under discussion. Another recently proposed process that may affect the spectral region where κ is measured is soil-atmosphere interaction, which suggests a seasonal variation in κ (e.g., Roumelioti et al., 2020; Grendas et al., 2025).

Objectives

This study aims to investigate the seasonal variability of κ_0 using data from the ARGONET vertical array, a special infrastructure for site effect studies on Cephalonia Island, Greece. The objective is to use this well-studied site to extract valuable insights about the possible contribution of weather/climate into the complex nature of near-surface, high-frequency attenuation.

Data and Initial Processing

The ARGONET infrastructure includes, among other components, a vertical array of accelerometers located in the sedimentary valley of Koutavos, south-southeast of Argostoli, the capital of the island of Cephalonia in western Greece. Details of the infrastructure can be found in Theodoulidis et al. (2018). In this study, we only use data from the surface and deepest sensor of the vertical array, code-named CK0 and CK83, respectively. CK0 is installed inside a light wooden construction on a relatively soft site. Average shear-wave velocity, V_s, for the upper 30 m depth (VS_{30}) according to the V_s values from different methods (cross-hole, down-hole, seismic interferometry) reported in Cushing et al., (2020), is in the range 201-262 m/s. CK83, on the other hand, installed at a depth of 83 m, is reported to be in the limestone bedrock (Theodoulidis et al., 2018). For the purposes of this study, this station is used as a "reference" station, both in the classical sense of engineering seismology (i.e., absence of

significant site effects), but also in the sense that it is very unlikely to be significantly affected by short-term ground-atmosphere interactions (Roumelioti et al., 2020; Grendas et al., 2025).

Since its launch in 2015, ARGONET has been in continuous recording mode. Earthquake records that include CK83 acceleration time histories with a Peak Ground Acceleration (PGA) ³2mg are processed and organized in the ARGONET database, which is openly available online (https://argonet-kefalonia.org/data/argonet_data/). In this work, we process the horizontal records at CK0 and CK83 stations of 964 earthquakes epicentered in the wider area of Western Greece and occurring from July 2015 to October 2022.

The horizontal acceleration waveforms were first processed for standard corrections and S-wave window selection. The various steps of this processing are not presented here for reasons of space, but are described in detail in Grendas et al. (2021). Briefly, we selected S-wave windows of variable duration, depending on the earthquake-receiver distance and the earthquake magnitude. These S-wave windows were Fast Fourier Transformed (FFT) and smoothed following Konno and Ohmachi (1998) (with the parameter b of the method set to 50). Spectra were first generated for each horizontal component separately, and then combined (square root of the sum of squares) to compute a single horizontal spectrum per station and earthquake.

Computation of κ and κ_0

Kappa values were computed for each horizontal FAS, A(f), based on a linear fit of its amplitudes in the high-frequency spectral region in between user-defined frequencies f_e and f_{end}, following the original work of Anderson and Hough (1984) and the equation:

$$A(f)=A_0 \exp^{(-\pi \cdot \kappa \cdot f)} \qquad (f>f_e) \qquad\qquad [1]$$

in which A_0 corresponds to the plateau of spectral amplitudes at $f<f_e$. Figure 1 shows the computation of κ schematically. In addition to the examined earthquake spectrum (in blue), the corresponding Fourier spectrum of a noise window preceding the earthquake signal is shown (in red). The part of the earthquake spectrum used in the analysis is required to be above a certain multiple of the noise spectrum. Figure 1 shows an example of a multiple of 3. In this work, we set a stricter minimum signal-to-noise level of 5.
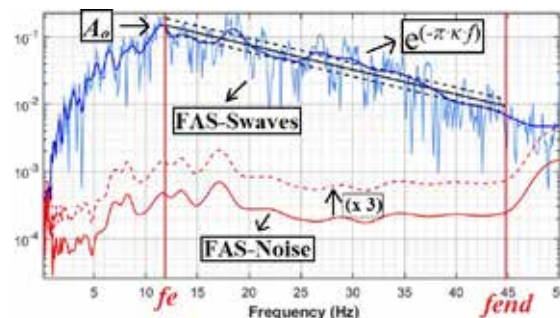
Figure 1. The Fourier Amplitude Spectra (FAS) of the S-wave earthquake motion (light blue line), its smoothed version (bold blue line), and the corresponding smoothed FAS of the noise before the arrival of the P-wave (bold red line). The red dashed line marks the 3-fold noise FAS level as an example of the minimum threshold for the earthquake signal to be considered reliable (Signal-to-Noise Ratio, SNR³3). Black lines show the least-squares regression of log(FAS) values in the frequency range from f_e to f_{end}, ±1 standard deviation (STD) of the mean.

We computed κ values for four different fixed frequency ranges, i.e., 6-25 Hz, 6-35 Hz, 10-25 Hz, and 10-35 Hz. The results for each of the two stations and each frequency range studied are plotted against epicentral distance in Figure 2. By linear regression of the distributions in Figure 2, it is possible to separate the "path" and the epicentral distance independent ("site" or/and "source" considered) terms of kappa. The mean values for the second term of kappa or κ_0, i.e., the values of κ corresponding to zero epicentral distance are reported in Figure 2 and Table 1. We restricted the linear regressions to data corresponding to epicentral distances £60 km, partly because data points were sparse at larger distances and partly because around 60 km there is an obvious change in the regional attenuation that could not be fit by a single line. We also kept the slope of the linear fit, based on the regression of the entire set of ARGONET data (i.e., all stations of the vertical array, not shown in this paper), fixed so as to reasonably assume exactly the same path attenuation factor for the two stations studied, since they are both located at the same epicentral distance.

Results in both Figure 2 and Table 1 show a larger variability of κ values at CK0 compared to CK83. They also highlight that mean κ_0 values are, as expected, larger at the "soft" CK0 stations and much smaller in the "soft rock" CK83 station. Another rather expected result is the dependence of κ and consequently of the κ_0 values on the frequency range used in the analysis, further highlighting the problem in understanding κ in the absence of standardized analysis practices.

Computation of Δκ$_0$

The exclusive site-specific character of κ$_0$ has been a subject of debate (e.g., Ktenidou et al., 2014 and references therein). Most studies support it (e.g., Cotton et al., 2006; Drouet et al., 2010; Ktenidou et al., 2013; Ktenidou et al., 2015). However, others also argue for a dependence on the seismic source (e.g., Tsai and Chen, 2000; Purvance and Anderson, 2003; Kilb et al., 2012), a component that would be difficult to isolate based on classical linear regression analysis on the κ measurements of a single site. To overcome this difficulty and secure that we have effectively removed any possible source effects, instead of using κ or κ$_0$ we used one site as target and one as reference and we computed their κ differences, Δκ. Δκ is equivalent to Δκ$_0$ under the realistic assumption that the wavefield at both examined stations experiences the same along-path attenuation.
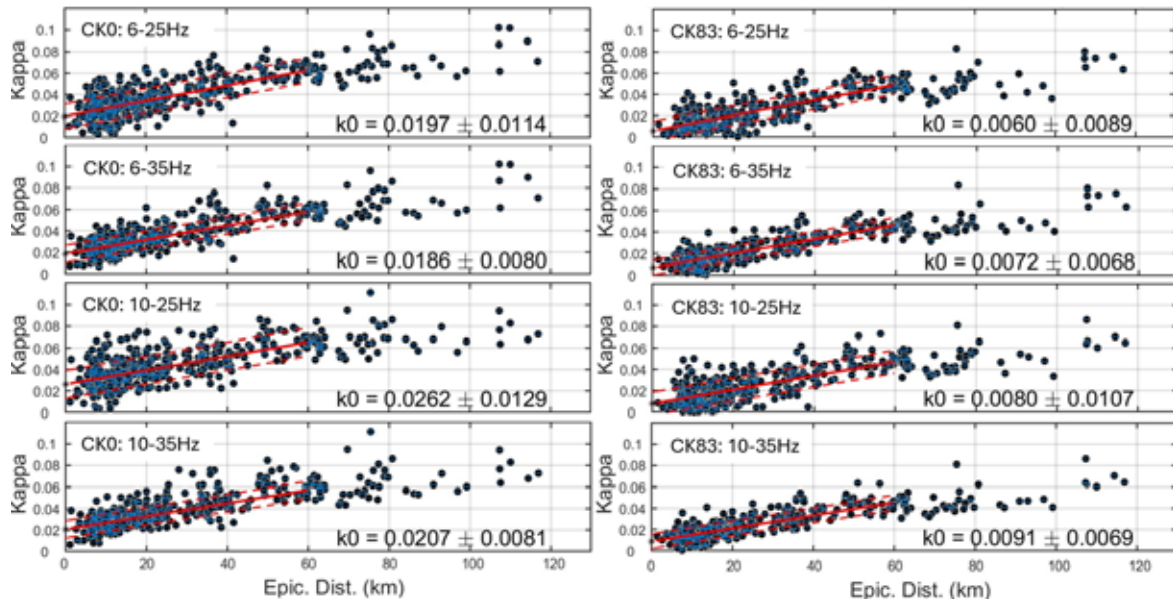
Figure 2. κ values computed from the earthquake records at stations CK0 (left) and CK83(right) considering four different frequency ranges (noted on top left of each subplot). The slope of the linear regression has been kept constant considering all ARGONET data. Mean κ$_0$ values (κ at zero distance) and the ± 1 STD are also noted in each subplot.

Table 1. Computed κ$_0$ and Δκ$_0$ mean values and their standard deviations (σ) for four examined frequency ranges. Δκ$_0$ results are shown for both applied methods described in the text. Columns named "SV model range" list the quantity "maximum seasonal model amplitude - minimum seasonal model amplitude" for each examined case.

f$_e$-f$_{end}$ (Hz)	CK0		CK83		Δκ$_0$ Method1			Δκ$_0$ Method2		
	κ$_0$ (ms)	σκ$_0$ κ$_0$ (ms)	κ$_0$ (ms)	σκ$_0$ κ$_0$ (ms)	Δκ$_0$ (ms)	σΔκ$_0$ Δκ$_0$ (ms)	SV model range	Δκ$_0$ (ms)	σΔκ$_0$ Δκ$_0$ (ms)	Sv model range
6-25	19.7	11.4	6.0	8.9	18	6	7	17.4	0.8	6.5
6-35	18.6	8.0	7.2	6.8	14	6	5	14.4	0.5	4.3
10-25	26.2	12.9	8.0	10.7	20	10	10	20.6	1.1	9.6
10-35	20.7	8.1	9.1	6.9	15	10	6	14.4	0.7	4.5

In our case, CK0 is the target site and we examine its high-frequency shaking characteristics with respect to the borehole station CK83 using two different methods: In "Method 1", we used pairs of κ values from CK0 and CK83 stations to estimate Δκ=κ$_{(CK0)}$-κ$_{(CK83)}$ and equivalently Δκ$_0$. In "Method 2", we measured Δκ$_0$ directly on Standard Spectral Ratios (SSRs) of CK0 with respect to CK83. The two approaches will be presented in more detail in the following.

The computation of Δκ$_0$ from the κ values of CK0 and CK83 is straightforward and resulting values are plotted in Figures 3a and 4. For examining possible variations of Δκ$_0$ with seasons (Seasonal Variation, SV), we considered a "pseudo-waveform" Δκ$_0$(day), where "day" is derived from date considering as starting point the 1st of January of each year. We analyzed this pseudo-waveform for its frequency content via FFT. We computed FAS only for periods T_{SV}^h, corresponding to 365/h for h=1 and h=2, seeking for possible variations with a return period of the order of a year or half a year and aiming to a smooth model of the phenomenon, if proven significant. The seasonal variation of Δκ$_0$ ($\Delta \kappa_h (SV)$), was finally modeled as the sum of the 2,

discrete period (T_{SV}^h) cosine wavelets, based on the corresponding scaled FAS Amplitude, $\Upsilon(T_{SV}^h)$, and adopted phase, $\varphi(T_{SV}^h)$ (in degrees),as in:

$$\Delta\kappa_h(SV) = \Upsilon(T_{SV}^h) \cdot \cos\left\{\left(2 \cdot \pi / T_{SV}^h\right) \cdot [\text{Date} - \varphi(T_{SV}^h)]\right\} \tag{2}$$

Figure 3a shows as an example the starting data and resulting model (red dots and cyan lines in Figure 3a) for the frequency range 6-25Hz and the corresponding result of the FFT analysis (Figure 3b). The starting data and final models for the seasonal variation of $\Delta\kappa_0$ for all four tested frequency ranges are presented in Figure 4. If there is a time pattern in $\Delta\kappa_0$, a clear peak is expected to be observed in plots like the example plot in Figure 3b. In the specific example of Figure 3b, a prominent peak is seen at the examined period of 1 year, suggesting a yearly repeating change in $\Delta\kappa_0$.

In general, Figure 3 shows a clear time variation of $\Delta\kappa_0$ measurements, with lower $\Delta\kappa_0$ during summer and highest during winter. The proposed model for this variation also predicts the lowest $\Delta\kappa_0$ values during the first third of July and the highest values during the first third of January of each year. These results were consistent for all four examined frequency ranges and any differences were restricted to the order of a few days.

The modelled seasonal variation of the high-frequency ground motion amplitudes at CK0 with respect to those in CK83 can be characterized as significant, since its range (maximum seasonal model amplitude - minimum seasonal model amplitude) is of the order of 1 standard deviation of the mean $\Delta\kappa_0$ from data (Table 1, $\sigma\Delta\kappa_0\Delta\kappa_0$, Columns 7, 8). This means that the proposed model, if used to "correct" the observed data examined in this study, could lower the variability in κ_0 or $\Delta\kappa_0$ measurements and lead to more robust computations of the mean κ_0. The performance of the seasonal variation model of $\Delta\kappa_0$ shows some dependence on the frequency interval adopted in the analysis, but in all cases explains much of the variability of the examined parameter (Table 1).
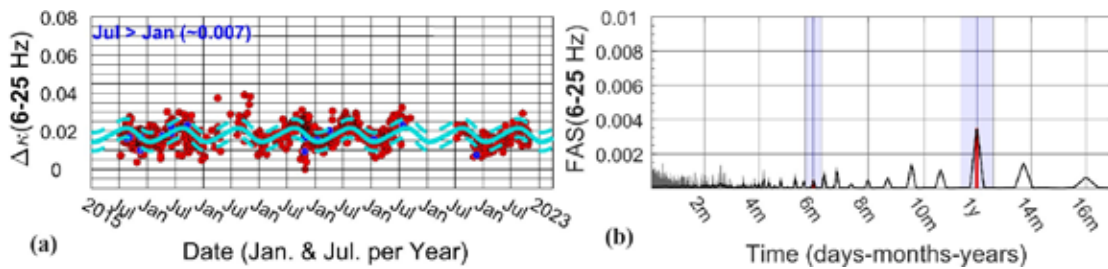
Figure 3. Variation of $\Delta\kappa_0$ with date a) data points of individual $\Delta\kappa_0$ measurements for the frequency range 6-25Hz and superimposed model of the seasonal variation of $\Delta\kappa_0$ ± 1 standard deviation (STD) of the mean model (cyan curves), b) Fourier Amplitude Spectrum (FAS) of the pseudo-waveform $\Delta\kappa_0$(day) considered. Shaded areas mark the areas of the investigated return periods of the phenomenon (i.e, at 1 year and 6 months). The difference between the lower and higher $\Delta\kappa_0$ values predicted by the proposed model are noted in the top left of a).
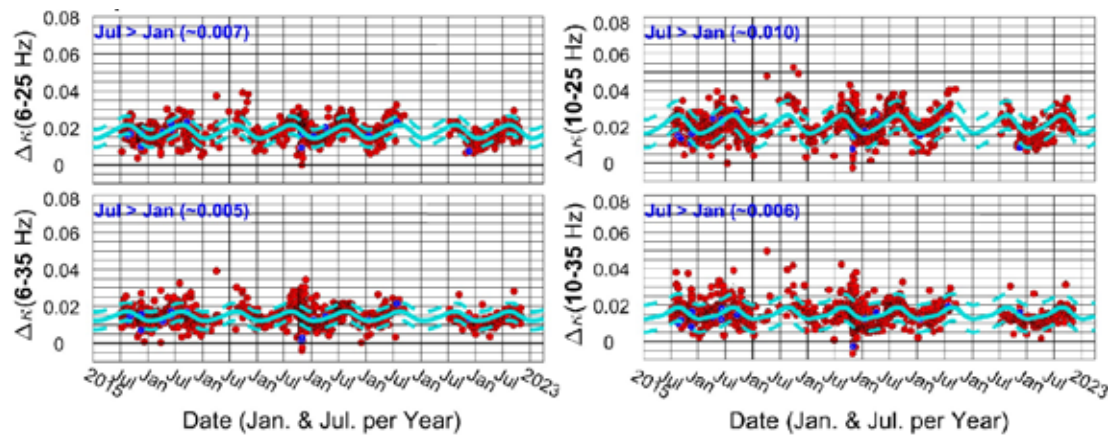
Figure 4. $\Delta\kappa_0$ values based on the κ_0 measurements at CK0 and CK83 stations ($\kappa_{(CK0)}$-$\kappa_{(CK83)}$) for the 4 examined frequency ranges. The modeled seasonal variation of $\Delta\kappa_0$ and its Standard Deviation (STD), are shown in cyan solid and dashed lines, respectively. The highest value of the seasonal $\Delta\kappa_0$ model is predicted to occur in July and the lowest in January of each year. The difference between the lowest and highest predicted $\Delta\kappa_0$, is written in the top left of each subplot.

The alternative approach to compute $\Delta\kappa_0$ (our "Method 2") is to measure it directly on Standard Spectral Ratios (SSRs) of CK0 with respect to CK83. By dividing the FAS of CK0 to those of CK83 and considering that the interstation distance is much smaller compared to any epicentral distance in the examined dataset, we assume that source and path effects are effectively removed (Borcherdt, 1970), including the path-dependent component of κ. In the high-frequency part of the SSR, the spectral division mainly includes the division of the factors $\exp(-\pi\kappa_{(CK0)}f)/\exp(-\pi\kappa_{(CK83)}f)$. The path-dependent component of κ is considered the same for both the surface and borehole station and is eliminated and what remains is the difference $\kappa_{0(CK0)}-\kappa_{0(CK83)}$, i.e., the quantity under study.

SSRs for the horizontal component of the ARGONET dataset have already been computed by Grendas et al. (2025). Herein, we use these published seasonal varying ratios to perform linear regression on their high-frequency parts and more specifically within the same four frequency ranges examined earlier ("Method 2"). The resulting $\Delta\kappa_0$ values are depicted in Figure 5, along with SSRs colored according to the date of their occurrence. Warm colors correspond to dry, summer months and cold colors to winter months and it is evident that the differences in the high-frequency signal of CK0 with respect to CK83 increases during winter and diminishes during the summer.

Linear regressions to compute the mean $\Delta\kappa_0$ and its values during the identified "extreme" seasonal variation periods (i.e., July-August and January-February) have been performed directly on the SSRs of Figure 5. Pertinent results are shown in each subplot, considering the four examined frequency ranges. The linear fits for the two extreme seasonal variation periods are also shown. $\Delta\kappa_0$ values and their STDs are also listed in Table 1, under "Method 2".

By comparing the linear fits in Figure 5, it becomes evident how the seasonal variation can largely affect the computation of $\Delta\kappa_0$ (and directly of κ and κ_0), at least at the specific site examined in this study. Datasets with a biased concentration of summer recordings would provide much larger values of κ_0 compared to non-biased or inversely biased datasets. The effect seems to be more significant when the examined frequency range terminates at frequencies largely affected by seasonal variations. In Figure 5, for example, the left subplots including analysis up to 25Hz present much larger discrepancies between the two "extremes" with respect to subplots to the right where the analysis is extended well beyond the frequency range mostly affected by seasonal variation. All these observations raise another "red flag" when the engineering and seismological communities face the necessity to harmonize κ measurements for comparisons.

Overall, the results of the two methods for computing $\Delta\kappa_0$ are similar and this is demonstrated by the comparison of values reported in Table 1.
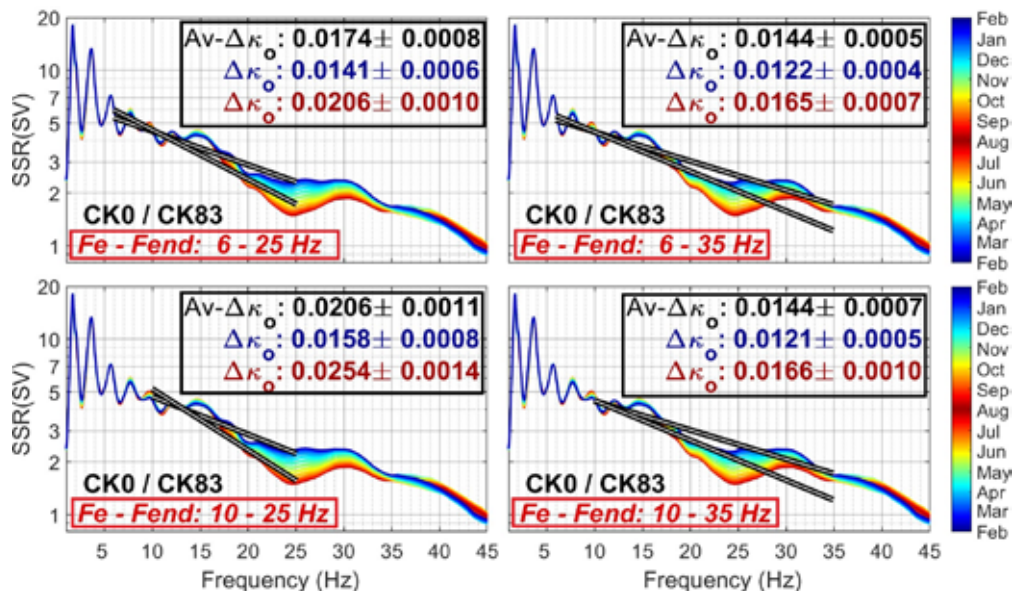
Figure 5. Mean Standard Spectral Ratios (SSRs) (for the 1st day of each month) between CK0 and CK83 stations colored according to the date of occurrence of. Subplots differentiate in the frequency range used for the linear regression. Double lines mark the regression results for the two extreme $\Delta\kappa_0$ cases (summer vs winter). On the top right of each subplot, the mean $\Delta\kappa_0$ and $\Delta\kappa_0$ values corresponding to the two extremes of the modelled seasonal variation are noted.

Conclusions/Discussion

Despite its limitations, kappa remains a valuable parameter for understanding high-frequency attenuation and

conducting site-specific hazard analyses. Its practical utility has made it a significant parameter of engineering seismology, but ongoing research aims to refine its estimation techniques and improve its integration into seismic hazard models. By addressing its limitations and standardizing methodologies, the role of kappa in seismic hazard analysis can be further enhanced.

In this work we addressed an additional process that may add to the lumped character of this single-number descriptor of high-frequency attenuation, i.e., the soil-atmosphere interaction. We specifically examined if the high-frequency part of the earthquake spectrum, i.e., the part commonly used for the computation of kappa, changes with a seasonal periodicity. To do so, we comparatively examined kappa values at one surface and one borehole, bedrock station.

Our results demonstrate that the difference in κ_0 values of the two examined stations exhibit considerable variability due to seasonal weather conditions, the frequency range used in the computation of the parameter, and potentially source processes. The pronounced seasonal variation observed at the surface soft soil site CK0 highlights the influence of rainfall-induced changes in ground humidity on near-surface attenuation. This finding challenges the common assumption of a static, site-specific κ_0 value and requests further research on the possible need to consider seasonal variability of high-frequency ground motion in seismic hazard assessments.

The frequency-dependent behavior of κ_0, evident in the variations observed across different tested frequency ranges, suggests that attenuation slopes might not be uniform across the entire high-frequency spectrum at a given site. This observation warrants further investigation to understand the underlying mechanisms driving these frequency-specific variations. It also adds to previous discussions in the published literature about the need to standardize the methods for computing kappa to be able to compare kappa values from different regions and studies and limit its broader applicability in seismic hazard models (e.g., Ktenidou et al., 2014).

This study also confirms the effectiveness of using SSR(f) for more robust κ_0 estimation, providing lower standard deviations compared to traditional methods based on individual kappa factor differences.

Overall, this research provides additional insights into the complex nature of κ_0 and its potential variability. Further research is needed to investigate seasonal variations of kappa at a statistically significant number of sites, quantify dependencies and develop improved predictive models that incorporate these sources of variability for enhanced accuracy and reliability.

Acknowledgements

References

Anderson, J.G., Hough, S.E., 1984. A model for the shape of the Fourier Amplitude Spectrum of acceleration at high frequencies. Bull. Seismol. Soc. Am. 74, 1969–1993.

Boore, D. M., Joyner, W. B., 1997. Site amplifications for generic rock sites. Bull. Seism. Soc. Am., 87(2), 327-341.

Borcherdt, R., 1970. Effects of Local Geology on Ground Motion Near San Francisco Rbay. Bull. Seismol. Soc. Am. 60, 29–61.

Cotton, F., Scherbaum, F., Bommer, J.J., Bungum, H., 2006. Criteria for selecting and adjusting ground-motion models for specific target regions: Application to central Europe and rock sites. J. Seismol. 10, 137–156.

Cushing, E.M., Hollender, F., Moiriat, D., Guyonnet-Benaize, C., Theodoulidis, N., Pons-Branchu, E., Sépulcre, S., Bard, P.Y., Cornou, C., Dechamp, A., Mariscal, A., Roumelioti, Z., 2020. Building a three dimensional model of the active Plio-Quaternary basin of Argostoli (Cephalonia Island, Greece): An integrated geophysical and geological approach. Eng. Geol. 265, 105441.

Douglas, J., Edwards, B., Convertito, V., Sharma, N., Tramelli, A., Kotha, S. R., Bora, S. S., 2020. Predicting site-specific kappa (κ) to improve ground-motion models for seismic hazard assessment. Earth-Science Reviews, 203, 103142.

Drouet, S., Cotton, F., Guéguen, P., 2010. VS_{30}, κ, regional attenuation and M_w from accelerograms: Application to magnitude 3-5 French earthquakes. Geophys. J. Int. 182, 880–898.

Grendas, I., Theodoulidis, N., Hollender, F., Hatzidimitriou, P., 2021. Effects of the S-wave time-window selection on Standard Spectral Ratio (SSR): Application to the ARGONET vertical array, Greece. 6th Int. Conf. Earthq. Eng. Seismol., Gebze Turkey.

Grendas, I., Roumelioti, Z., Theodoulidis, N., Hollender, F., 2025. Ground motion dependency on seasonal variations: Observations at the ARGONET array (Cephalonia, Greece). Bull. Seism. Soc. Am., (accepted).

Hollender, F., Roumelioti, Z., Maufroy, E., Traversa, P., Mariscal, A., 2020. Can we trust high-frequency content

in strong-motion database signals? Impact of housing, coupling, and installation depth of seismic sensors. Seismol. Res. Lett. 91, 2192–2205.

Kilb, D., Biasi, G., Anderson, J., Brune, J., Peng, Z., Vernon, F.L., 2012. A comparison of spectral parameter kappa from small and moderate earthquakes using southern california ANZA seismic network data. Bull. Seismol. Soc. Am. 102, 284–300.

Konno, K., Ohmachi, T., 1998. Ground-motion characteristics estimated from spectral ratio between horizontal and vertical components of microtremor. Bull. Seismol. Soc. Am. 88, 228–241.

Ktenidou, O.J., Gélis, C., Bonilla, L.F., 2013. A study on the variability of Kappa (κ) in a Borehole: Implications of the computation process. Bull. Seismol. Soc. Am. 103, 1048–1068.

Ktenidou, O.-J., Abrahamson, N. A., Drouet, S., Cotton, F., 2014. Understanding the physics of kappa (κ): Insights from a global dataset of high-quality ground motion recordings. Bull. Seism. Soc. Am., 104(5), 2313-2332.

Ktenidou, O.J., Abrahamson, N.A., Drouet, S., Cotton, F., 2015. Understanding the physics of kappa (κ): Insights from a downhole array. Geophys. J. Int. 203, 678–691.

Parolai, S., Bindi, D., 2004. Influence of Soil-Layer Properties on k Evaluation. Bull. Seism. Soc. Am., 94(1), 349–356.

Purvance, M.D., Anderson, J.G., 2003. A comprehensive study of the observed spectral decay in strong-motion accelerations recorded in Guerrero, Mexico. Bull. Seism. Soc. Am. 93, 600–611.

Roumelioti, Z., Hollender, F., Guéguen, P., 2020. Rainfall-induced variation of seismic waves velocity in soil and implications for soil response: What the ARGONET (Cephalonia, Greece) vertical array data reveal. Bull. Seism. Soc. Am. 110, 441–451.

Theodoulidis, N., Hollender, F., Mariscal, A., Moiriat, D., Bard, P.Y., Konidaris, A., Cushing, M., Konstantinidou, K., Roumelioti, Z., 2018. The ARGONET (Greece) seismic observatory: An accelerometric vertical array and its data. Seismol. Res. Lett. 89, 1555–156.

Tsai, C.-C.P., Chen, K.-C., 2000. A model for the high-cut process of strong motion accelerations in terms of distance, magnitude, and site condition: an example from the SMART 1 array, Lotung, Taiwan. Bull. Seism. Soc. Am 90, 1535–1542.

Digital model of Hydrological components, Mean annual Temperature, Precipitation and Evapotranspiration in Macedonia, Greece

Grimpylakos, Georgios[1]
(1) Department of Geography, University of the Aegean, Mytilene, Greece

Introduction / Background

River hydrology and morphology provide a relationship between flowing water and the physical environment of rivers. The hydromorphological regime (C11) is one of the hydromorphological quality elements of the WFD and is defined by the water flow's characteristics regarding quantity and dynamics hence to each connection to ground waters (Rinaldi et al. 2013b, Belletti et al. 2015, and Kilinc & Kay 2018). In recent years, 2009-2025, the classification of a river's hydromorphology is directly correlated with the classification and characterization of a river's morphology and hydrology which are recognized as fundamental intergrading components for studying, analysing and understanding it's behavior in order to adapt and suggest appropriate river management applications (e.g., Sear et al. 1995, Gilvear 1999, Kondolf et al. 2003, Downs and Gregory 2004, Brierley and Fryirs 2005, Brierley and Fryirs 2008; Meitzen et al. 2013, Tadaki et al. 2014, Belletti et al. 2015). The increased concern of quality, regarding river water and its habitats, combined with their correlation with the river's degradation have become important elements of hydromorphological assessment (Kilinc & Kay 2018). Furthermore, floods are common in certain areas of the world, and there have been more than 400 major floods during 2000-2024 with more than 70 billion Euros (EM-DAT, 2024).

Objectives

This study aims to create digital maps of hydrological components, such as Mean Annual Temperature, Precipitation and Evapotranspiration, which are recognized as essential components for the study and modeling of hydrological cycle, river management and hydrological natural hazards and point out the need for high spatial resolution.

Study area

Macedonia is a district of North Greece as shown at Figure 1. Studying area is a polygon that includes all the watersheds of Macedonia's torrents and rivers, resulting in a polygon the boundaries of which differ from the boundaries of Macedonia's political district and define it as an area of North Greece. The boundaries of each watershed were determined by the Ministry of Rural Development and Food in collaboration with the Institute of Geology and Mineral Exploration and always according to the WFD guidelines for water bodies. The study area is 36.290 km^2, has a perimeter of 2.163 km and includes 77 different torrents in which main rivers are divided according to WFD, and their watersheds area is of 2,9-4.775 km^2.

Data and Methodology

To study the climatic parameters for a given area, a 30-year period with good spatial and temporal distribution is needed.

For our study area, 85 meteorological – climatological stations (mentioned as MCS) from the Ministry of Rural Development and Food (82) and Hellas Gold (3) provided data which correspond to different time periods during an eighty-year period (1930-2010) and include daily, monthly and annual measurements of precipitation, while 43 of them included also daily monthly and annual measurements of temperature. After sorting the data from all 85 MCS the best period corresponded to 1974-2004, as the number of stations with daily and continuous data was higher (Grimpylakos 2020).

Specifically, to estimate the mean annual precipitation, 163.254 measurements belonging respectively to 40 MCS were used (Figure 1,3) and a subset of 20 MCS (figure 2,4). The second map of Precipitation was created using a subset of 20 MCS which also had adequate Temperature data for the creation of the Temperature and Evaporation map.

To estimate the mean annual temperature, approximately 800.000 measurements of daily minimum and maximum temperature, obtained from 43 MCS, during 1930-2010 were examined. The same thirty-year period 1974-2004 with

consistent daily data of 255.326 measurements were used, belonging respectively to the same 20 stations of the second map of precipitation (Figure 2,4).

The average initial MCS spatial distribution was $1/38,7km^2$. After sorting and evaluating data, the overall spatial distribution of MCS for the precipitation map at figure 3 is $1/82.25km^2$ and for temperature (figure 5), precipitation (figure 4) and corresponding evapotranspiration map (figure 6) is $1/164.5km^2$. However, there are areas with lower density of approximately $1/300km^2$ for maps at figures 4,5,6 and of $1/180km^2$ at figure 3.

A very basic problem in spatial analysis is interpolating a spatially continuous variable from point samples. There are many different spatial interpolation techniques. Some of the most used interpolation methods to model spatially distribution from point data are: Inverse Distance Weighting (IDW), spline and ordinary kriging. Overall, anomalies of local scale can be adjusted without affecting the values derived from interpolation at other points on the surface (Burrough and McDonnell 1998).

Inverse distance weighted (IDW) is a method of interpolation that estimates cell values by averaging the values of nearby measured data points. This technique weighs the points closer to the prediction location greater than those farther away, hence the name inverse distance weighted (Watson and Philip 1985). However, the main problem with this technique is that it assumes that maximum and minimum values are measured at the sampled points and all other points have values between those values.

Spline is an interpolation method in which cell values are estimated using a mathematical function that minimizes overall surface curvature, resulting in a smooth surface that passes exactly through the input points. It is a deterministic, locally stochastic interpolation technique, which represents two-dimensional curves on three-dimensional surfaces (Eckstein 1989; Hutchinson and Gessler 1994).

These methods are known as deterministic interpolation methods because they are directly based on the surrounding measured values and use specified mathematical formulas that determine the smoothness of the resulting surface. On the other hand, kriging uses statistical models that include autocorrelation among measured points, to predict the values at unknown points. The most applied form uses "semivariogram" among pairs of sampled points. The Kriging interpolation method was developed by Matheron (1970).

All data were divided into 2 groups. The first group was named "training" and content 90% of sample points while the second group was named "test" and content 10% of the sample points. Training group's measurements were used for predicting the values of the examined variable at whole Macedonia by using the aforementioned interpolation methods. Test's group was used to validate the results of each method as shown at table 1.

The correlation between elevation and mean annual temperature, precipitation and evapotranspiration was checked with SPSS program and the results are shown at table 2.

Table 1. Root mean square error of each applied technique was calculated and IDW shows significant higher accuracy.

| Interpolation techniques	IDW	Kriging	Spline	Polynomial
Root Mean Square Error	0,091	0,133	0,159	0,134

Figure 1. Map projecting the spatial distribution of the 20 meteorological – climatological stations with continuous temperature data during period 1974-2004, at North Greece.

Results and Discussion

Mean monthly precipitation was estimated for each month at all 20 (that have also good spatial-temporal distribution of temperature data) and 40 (with no adequate distribution of temperature data) MCS and then the mean annual precipitation was calculated for all of them. The highest possible correlation between Precipitation and elevation was not significant $R^2<0,29$ (Table 2) and so an equation for the estimation of the mean annual precipitation for each cell of Macedonia could not be used. Four different interpolation techniques were examined, and the root mean square error was estimated for each technique (Table 1). The IDW method was found to be the most accurate one and two thematic maps were created showing the mean annual precipitation in Macedonia North Greece. The spatial distribution of the mean annual precipitation that derived from the 40 MCS during 1974-2004 is projected at Figure 3. The spatial distribution of the mean annual precipitation that derived from the data of 20 MCS, a subset of 40, during 1974-2004 is projected at Figure 4.

The thematic map that derived from the 20 stations at Figure 4 did not include 20 stations of Figure 3, so it was missing mean annual precipitation values between 417,0 – 417,3 and 853,8 – 999,8 as these data did not exist at the 20 stations. The data distribution of the 20 stations at West, Central and South Macedonia is very sparse, resulting in much less precipitation zones. The map of 40 stations has much better spatial distribution and is more accurate than that of 20 stations and is suggested for analysis purposes). Precipitation increases with elevation, but as there is lack of MCS at elevation above 1250m, there are also no values above 1000mm at the produced map for precipitation (figure 6), Koumaria has the highest mean annual precipitation of 1020,4mm at 700m elevation.

Figure 2. Map projecting the spatial distribution of the 40 meteorological – climatological stations with continuous precipitation data during period 1974-2004, at North Greece.

Figure 3. Thematic map projecting the spatial distribution of mean annual precipitation (mm) at Macedonia of North Greece. The data derived from 40 meteorological – climatological stations during period 1974-2004 and the cell size is 750m.
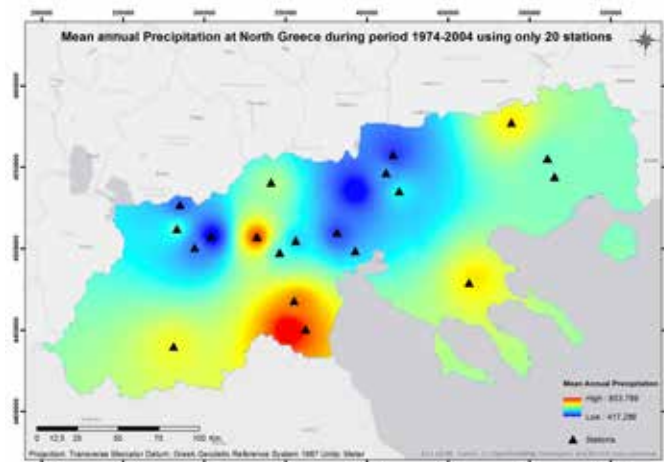
Figure 4. Spatial distribution of mean annual precipitation at Macedonia Greece derived from 20 meteorological stations during period 1974-2004
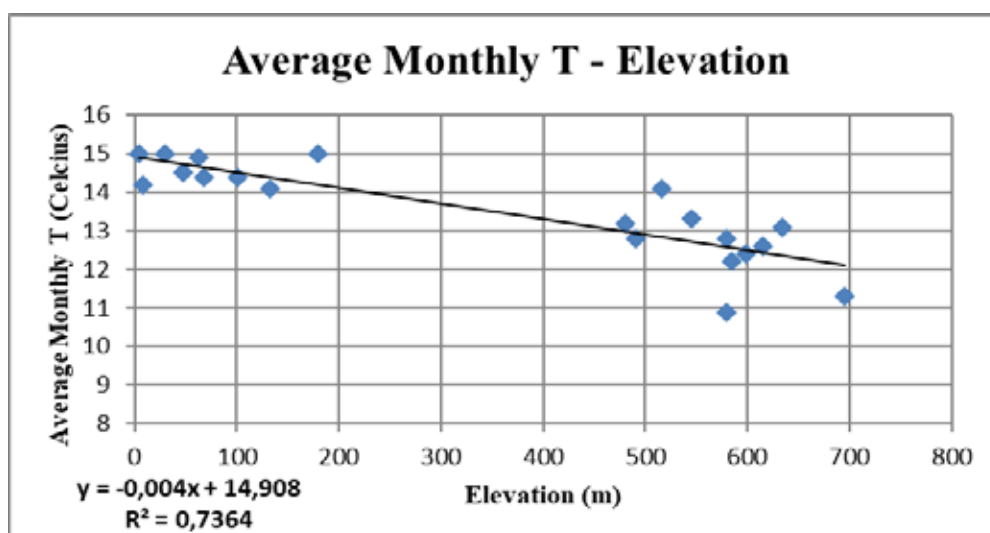
Chart 1. Correlation of mean annual temperature with elevation using linear equation.

The mean monthly temperature for each of the 20 MCS was calculated and then, the mean of these values gave the mean annual temperature for each station. There is a significant correlation between Mean annual Temperature and elevation as shown at (Chart 1), with R^2 = 0,7364, and the corresponding equation shows that the temperature declines as the elevation rises. This equation was applied using the raster calculator of ArcMap 10.3 and high-resolution Digital elevation model (DEM) with 28.3mx28.3m cell size, which was constructed from the Advanced Space borne Thermal Emission and Reflection Radiometer (ASTER) of NASA Terra satellite. The corresponding map was created (Figure 5).

Table 2. Correlation of Variables Temperature, Precipitation and evapotranspiration of each method of Thornthwaite, Turc and Coutagne with Elevation.

Elevation	Examined Variable				
	T (°C)	P(mm)	Thornthwaite	Turc	Coutagne
Pearson	-0,851	0,306	0,156	-0,072	0,108
R-square	0,723	0,094	0,024	0,005	0,012
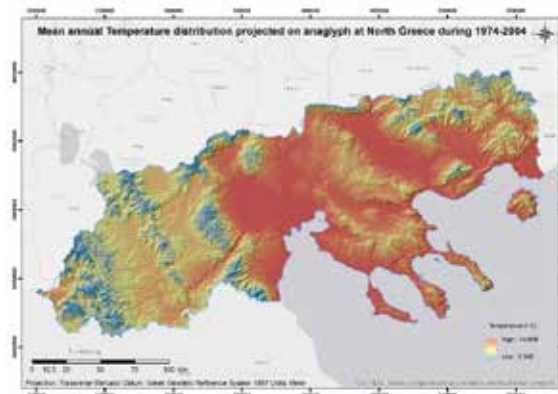
Figure 5. Mean annual temperature distribution at North Greece derived from 20 meteorological – climatological stations during period 1974-2004, projected on anaglyph.
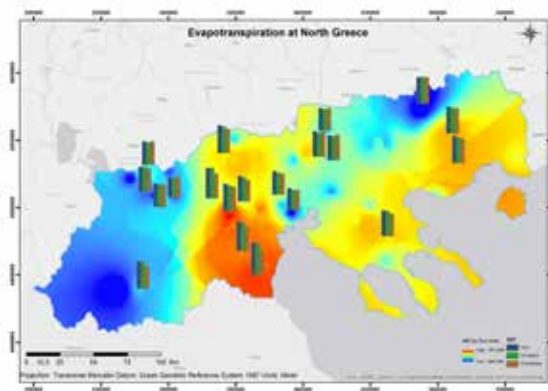
Figure 6. Thematic map of AET by all methods and with IDW by Turc nethod, cell size of 750m.

Actual evapotranspiration was calculated with Turc, Coutagne and Thornthwaite methods for each month at each one of the 20 MCS (Figure 2). AET by Turc method is higher than Thornthwaite method at all stations and in 19 of 20 stations it is higher than Coutagne method, while Coutagne is higher than Thornthwaite method at 15 of 20 stations. On the other hand, Turc method is the most easily applied method of all, as Coutagne method is not always applicable and Thornthwaite's method uses parameters that differ according to elevation and the spatial distribution of each examined place, which makes it very difficult to apply this method at all stations. No significant correlation between elevation and evapotranspiration was found (Table 2). Lastly, the Thornthwaite method is underestimating evapotranspiration in comparison with the other two methods. All AET are projected at each station, while Turc method with the highest AET is projected using IDW spatial interpolation (Figure 6). As Turc method is the easiest applied method, other researchers can use this method and compare their results with figure 6.

Conclusions

A significant correlation, with R^2 = 0,7364 (chart 1), between Mean annual Temperature and elevation was found and the corresponding equation is **T = - 0,004 * E + 14,908** (T is mean annual temperature and E is elevation). The thematic map projecting the distribution of Mean annual Temperature and the elevation is shown at Figure 5. However, there is a significant gap in the MCS regarding elevation 200-450 m, which was necessary for data consistency. The temperature values were estimated through extrapolation, therefore there is also a limitation for areas with elevation above 700m. A better elevation distribution in MCS is suggested for future work.

The mean annual precipitation at each MCS was estimated, but there was no significant correlation between elevation and Precipitation at Macedonia to create an equation. For future work, better elevation distribution of the MCS is suggested. For the creation of the Precipitation maps, 4 different spatial interpolation techniques were examined (Table 2) and IDW method was applied as it had the lowest Root Mean Square Error (Figures 3 and 4). Highest

spatial distribution of stations at figure 3, with 40 MCS, clearly shows the need of good spatial distribution of MCS, as figure 4 with 20 MCS misses values between 417,0 – 417,3 and 853,8 – 999,8.

The mean annual actual evapotranspiration at each one of the 20 MCS was estimated using Turc, Coutagne and Thornthwaite methods and their values are displayed at figure 6. The thematic map (Figure 6) projecting the evapotranspiration distribution by Turc method at Macedonia was created using the IDW spatial interpolation method. The AET used only the Precipitation at the same 20 stations that Temperature data were available and not from the 40 MCS where the precipitation has higher values 853,8 – 999,8. This means that AET at the rest area of the map could be underestimated.

Lastly the need for high spatial-temporal distribution of MCS is clearly shown, but also a good elevation distribution of MCS is also needed and suggested for better results in the future.

Acknowledgments

References

Belletti, B., Rinaldi, M., Buijse, A.D., Gurnell, A.M. and Mosselman, E (2015) A review of assessment methods for river hydromorphology. Environmental Earth Sciences 73: 2079-2100.

Brierley, G.J.and Fryirs, K.A., 2005. Geomorphology and River management: applications of the River Styles Framework, Blackwell.

Brierley, G.J. and Fryirs, K.A., 2008. River futures: an integrative scientific approach to river repair. Society for Ecological Restoration International, Island Press, Washington, DC 304 pp

Burrough, P.A and McDonnell, R.A., 1998. Principles of geographical information systems. Oxford University Press, New York.

Downs, P.W. and Gregory, K.J., 2004. River channel management. Towards sustainable catchment hydrosystems. Arnold, London, pp 395

Eckstein, B.A., 1989. Evaluation of spline and weighted average interpolation algorithms. Comput Geosci, Vol. 15, p. 79–94.

Grimpylakos I.G. 2020. Contribution of the Hydromorphological - Geological and Climatological parameters to the watershed typology, application in basins of Northern Greece. Ph.D. Thesis, School of Geology, Aristotle University of Thessaloniki, Annex Number of Scientific Annals of the School of Geology No 202, 580 pp

Gilvear, D.J., 1999. Fluvial geomorphology and river engineering: future roles utilizing a fluvial hydrosystems framework. Geomorphology 31:229–245

Hutchinson, M.F. and Gessler, P.E., 1994. Splines-more than just a smooth interpolator. Geoderma, Vol. 62, p. 45–67.

EM-DAT, 2024. The International Disaster Database. Center for Research on Epidemiology of Disasters. Available online: https://www.emdat.be/ (accessed on 02 December 2024).

Kilinc, S.F. and Kay, P., 2018. Determination of the Most Suitable Assessment Methods of River Hydromorphology for Turkey. DOI: 10.31807/tjwsm.322489.

Kondolf, G.M., Montgomery, D.R., Piegay, H. and Schmitt, L., 2003. Geomorphic classification of rivers and streams. In: Kondolf GM, Piegay H, (eds) Tools in fluvial geomorphology. Wiley, Chichester, pp 171–204

Matheron, G., 1970. The theory of regionalized variables and its applications, École Nationale Supérieure des Mine, Les Cahiers du Centre de Morphologie Mathématique de Fontainebleau, Paris, Vol. 5, p. 212.

Meitzen, K.M., Doyle, M.W., Thoms, M.C. and Burns, C.E., 2013. Geomorphology within the interdisciplinary science of environmental flows. Geomorphology 200:143–154

Rinaldi, M., Belletti, B., Van de Bund, W., Bertoldi, W., Gurnell, A., Buijse, T. and Mosselman, E., 2013b. Review on eco-hydromorphological methods. Deliverable 1.1, REFORM (REstoring rivers FOR effective catchment Management), Project funded by the European Commission within the 7th Framework Programme (2007 – 2013), Topic ENV.2011.2.1.2-1 Hydromorphology and ecological objectives of WFD, Grant Agreement 282656.

Sear, D.A., Newson, M.D. and Brookes, A., 1995. Sediment related river maintenance: the role of fluvial geomorphology. Earth Surf Proc Land 20:629–647

Tadaki, M., Brierley, G. and Cullum, C., 2014. River classification: theory, practice, politics. WIREs Water 1:349–367

Water Framework Directive (2000/60/EC). Directive 2000/60/EC of the European Parliament and of the Council of 23 October 2000 establishing a framework for Community action in the field of water policy. Official Journal L 327 , 22/12/2000 P. 0001 – 0073.

Watson, D.F. and Philip, G.M., 1985. A refinement of inverse distance weighted interpolation. Geo-Processing, Vol. 2, p. 315–327.

The Pheneos palaeolake in N. Peloponnese, Greece

Groumpou M.[1], Koukouvelas I.[1], Nikolakopoulos K.[1], Sanjuan J.[2], Papadopoulou P.[1], Iliopoulos G.[1].

(1) Geology Department, Patras, Greece, mgroumpos@gmail.com
(2) Department of Earth and Ocean Dynamics, Barcelona, Spain

Introduction

Pheneos polje, located in northern Peloponnese (Greece) is strongly linked to the homonymous mythical lake. Throughout the past millennia, flooding events in the southern part of this polje have given rise to a lake. The myths associated with the lake revolve mostly around its drainage periods, with local populations suggesting that Hercules himself excavated openings to the ground with his bare hands to rescue the villagers from flooding (Jones, 1988). In reality, the water drains through sinkholes that are part of the region's karstic system (Tsoflias, 1973). In the southernmost part of the polje, distinct step-like scarps on the landscape serve as indicators of past lake levels (Figure 1). These scarps, representing notable geomorphological features, have been documented by Pausanias and other historical travelers (Groumpou, 2024). The primary objective of this study was to verify these features as relict shorelines of the ancient Pheneos lake.

Figure 1. Scarps on the landscape in the southern part of Pheneos polje indicating past lake levels.

Methods

Two distinct datasets, consisting of orthophoto maps and digital surface models (DSMs) were used to identify and map the step-like landforms across the landscape. The first dataset consists of a 50 cm spatial resolution orthophoto map and a 5 m pixel size DSM, whereas the second dataset consists of an orthophoto and a DSM of 4 cm spatial resolution. ArcMap 10.8 was used to display and analyze the two datasets. Subsequently, fieldwork was conducted to examine the characteristic features of the stepped landforms, and 35 surface sediment samples were collected from the different step-like scarps across the southern margins of the polje and processed for micropalaeontological analysis.

Results

The results reveal that the step-like scarps in the landscape consist of alternating coarse-grained gravel material and fine-grained material rich in gravel containing lacustrine taxa, which were deposited in a nearshore environment (Groumpou et al., 2023). A pattern of at least four such alternating sediment deposits has been mapped from the orthophoto maps, corresponding to distinct palaeoshorelines (Figure 2). These deposits contain a micropalaeontological assemblage comprising charophyte remains (gyrogonites and oospores), ostracods and gastropods. The most representative taxa of the identified micropalaeontological assemblage are *Nitellopsis obtusa* (Desvaux) Groves, 1919, *Sphaerochara prolifera* (Ziz. Ex. A. Braun) emend. Soulié-Märsche, 1989, *Chara vulgaris* Linnaeus, 1753, *Ilyocypris bradyi* Sars, 1890, *Ilyocypris inermis* Kaufmann, 1900, and *Candona neglecta* Sars, 1887 (Figure 3). Based on the ecological preferences of these taxa and their geographical distribution along the southern margins of the polje, three distinct lacustrine palaeoenvironments are identified: i) ephemeral lake (possibly annual) dominated by *S. prolifera* which is present up to an altitude of 710 m ii) cold and oligotrophic lake environment characterized by

the presence of *N. obtusa* and *I. inermis*, observed up to an altitude of 729 m and iii) warmer and mesotrophic lake, extending to altitudes of up to 744 m.
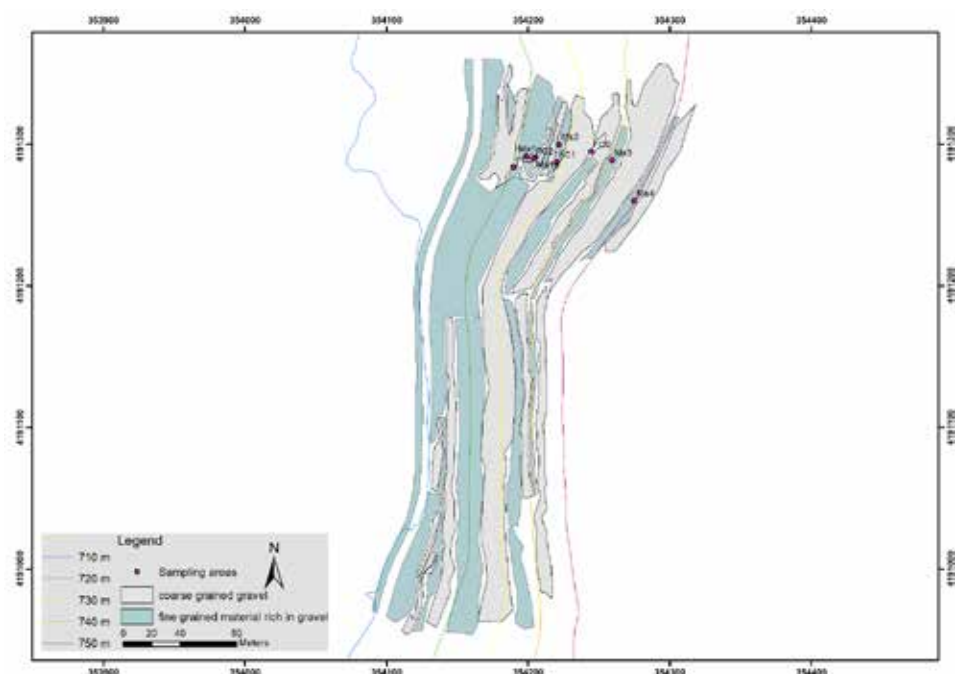

Figure 2. The mapped alternations of the studied sediment material, highlighting distinct palaeoshorelines on the southeastern part of Pheneos polje.
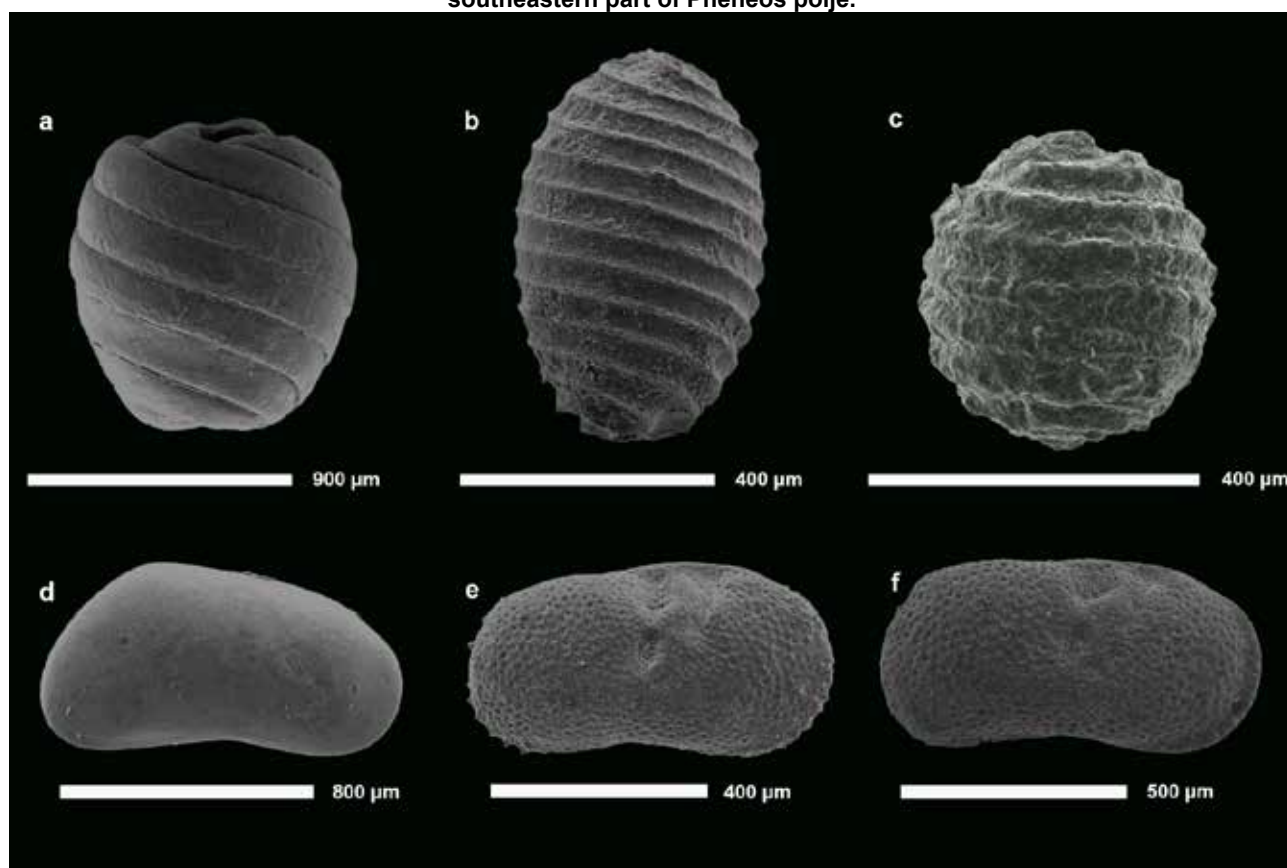

Figure 3. The most representative taxa of the identified micropalaeontological assemblage: a) *Nitellopsis obtusa***, b)** *Chara vulgaris***, c)** *Sphaerochara prolifera***, d)** *Candona neglecta* **e)** *Ilyocypris bradyi* **and f)** *Ilyocypris inermis***.**

Conclusions

The analysis of the stepped landscape in the southern margins of Pheneos polje revealed a sequence of at least four alternating sedimentary deposits, enriched with lacustrine taxa and which are indicative of near-shore depositional environments. The possible boundaries of Pheneos palaeolake are mapped and three distinct lacustrine palaeoenvironments were recognized based on the ecological preferences of the respective taxa (Groumpou et al., 2023). These findings provide insights into the Holocene dynamics and depositional history of the Pheneos polje.

Acknowledgements

References

Jones, W. H.S., 1988. Pausanias, Description of Greece, Books VIII.22-X (translated by W. H.S. Jones). Harvard University Press, Cambridge MA.

Tsoflias, P., 1973. Geology and Geomorphology of mount Helmos and in the area of Loussi of Kalavrita county (Northern Peloponissos). (in Greek) Digital Library "Theofrastos", Aristoteleion University of Thessaloniki, Department of Geology. 23-25 p.

Groumpou, M., 2024. Tectonic geomorphology and palaeoenvironments of north Peloponnese, Greece: the Pheneos polje case study. Ph.D. Thesis, University of Patras, Patras, 171 p.

Groumpou, M., Sanjuan, J., Koukouvelas, I., Nikolakopoulos, K., Iliopoulos, G., 2023. Review of Palaeobotany and Palynology 318, 104973.

Estimation of soil vulnerability index in the metropolitan area of Thessaloniki (Greece)

Grylionaki M.[1], Theodoulidis N.[2], Panou A.[1], Chatzidimitriou P.[1]
(1) Department of Geophysics, Department of Geology, Aristotle University Thessaloniki, Thessaloniki, Greece
mariagrilionaki@gmail.com
(2) Institute of Engineering Seismology and Earthquake Engineering (ITSAK), Thessaloniki, Greece

This paper presents an effort to assess the liquefaction potential across the Thessaloniki metropolitan area by calculating the Soil Vulnerability Index (SVI or Kg) for the surface geological formations and comparing the results with those of previous research. The SVI is associated with shear strain (γ) imposed on surface geological layers and has been effectively correlated with building damage and soil failures, such as liquefaction. To determine the dynamic properties of surface formations, including fundamental frequency (fo) and corresponding amplitude (Ao), the Horizontal-to-Vertical Spectral Ratio (HVSR) method of microtremor measurements was used. A total of 190 microtremor measurements were analyzed, revealing a good correlation between the SVI and liquefaction potential based on previous studies. High SVI values, indicative of increased liquefaction potential, are linked to low fundamental frequencies, high amplitudes, and are predominantly found in areas near the coast, where thick coastal soft deposits and riverbeds are prevalent. Additionally, strain (γ) values, which are related to SVI, were calculated for various peak ground acceleration scenarios and seismic basement velocities (Vb) specific to Thessaloniki. The results, represented in spatially interpolated maps generated via Geographic Information System (QGIS), align quite well with previous liquefaction potential studies conducted throughout the city using different estimation methods. This agreement encourages the use of microtremor measurements, directly linking them to liquefaction potential by employing the methodology utilized in the current study, in other regions as well.

17th INTERNATIONAL CONGRESS of the Geological Society of Greece

Seismotectonics of the NE Aegean region: The Lesvos Island and the Gulf of Edremit

Levent Gülen

Sakarya University, Serdivan, Sakarya, Türkiye,   lgulen@sakarya.edu.tr

Introduction:

Active tectonics of the Aegean is mainly influenced by the interactions of the North Anatolian Fault (NAF) branches, that extend into the Aegean Sea, the counter clockwise rotation and westward extrusion of the Anatolian block, the Hellenic Trench retreat, and the left-lateral strike-slip Pliny-Strabo Shear Zone (PSSZ), that extends towards the Isparta Angle (IA), (Dewey & Şengör, 1979; Taymaz et.al., 1991; Yılmaz & Gürer, 2013). The right-lateral strike-slip NAF gradually gains an additional normal component to the west of 31° E and its branches form the North Aegean Trough (NAT) and Skyros-Edremit Trough (SET) in the North Aegean Sea (Figure-1).
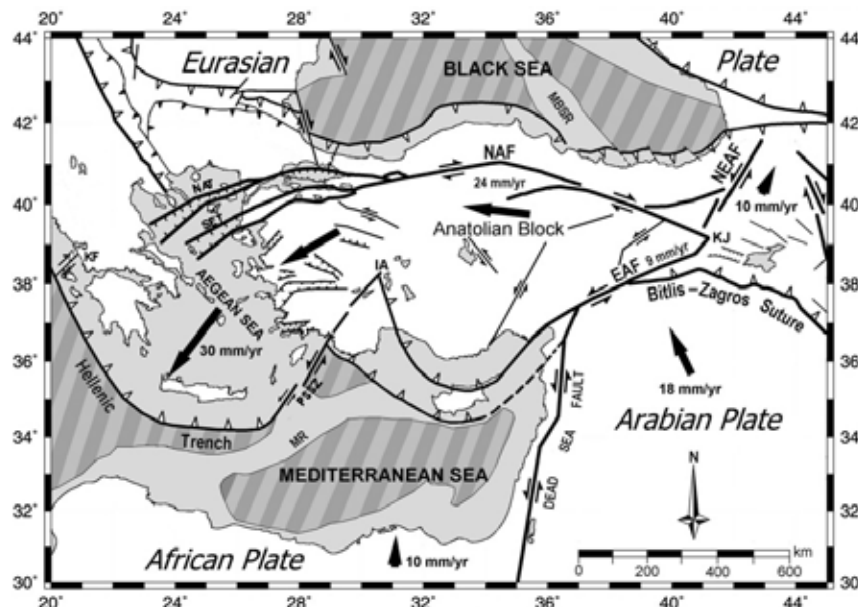
Figure 1. Simplified tectonic map of Turkey and surrounding regions (modified after Gülen et al, 2002).

The Aegean region is one of the rapidly deforming and seismically most active regions of the world as evidenced by historical and instrumental period earthquakes. More than 16 earthquakes with M > 6.5 have occurred since the mid-19th century in the North Aegean Region (Papadopoulos et al., 2002; Ganas et al., 2014). More than 32 major historical earthquakes have occurred just in the Lesvos Island and the Gulf of Edremit area and 22 of them occurred in 1800's (Ambraseys & Jackson, 2000; Ambraseys, 2002; Ambraseys, 2009). The historical earthquakes define an elongate zone extending in NW-SE direction that is parallel to the NE coastline of the Lesvos Island, which may indicate the presence of an unmapped major fault that is orthogonal to the Aghia Paraskevi Fault that traverses the island in NE-SW direction (Figures-2 & 3). The magnitudes of historical Lesvos earthquakes of 1739, 1809, and 1867 were determined as 6.8, 6.6, and 7.0, respectively (Karakaisis et al., 2010). The 1867 Lesvos earthquake was the most destructive among the historical earthquakes. The Oct. 26, 1889 earthquake was also a major earthquake that occurred in the western part of the Gulf of Edremit. This earthquake did not only totally ruin many towns in Lesvos, but also felt strongly as far as Çanakkale in the north and the Rhodes Island in the south (Ambraseys, 2009).

The instrumental period, 6 October, 1944 Gulf of Edremit Earthquake with M_w=6.7 occurred on the Edremit Fault Zone with a normal fault mechanism solution. This earthquake created a minor tsunami with a maximum inundation distance of 170 m. in the town of Ayvalık, on the Turkish coast (Altınok et al., 2012-a; Altınok et al., 2012-b; Sözbilir et al., 2016; Figure-2). Recently the 8 January, 2013 Lemnos Earthquake with M_w=5.7 (Kiratzi & Svigkas, 2013; Kürçer

et. al., 2013; Ganas et al., 2014); the 6 February-20 March, 2017 Gülpınar Earthquake Sequence (Gülen & Yalçın, 2017; Poyraz et al., 2017, Utkucu et al., 2017; Özden et al., 2017; Sözbilir et al., 2018; Ganas et al., 2018; Bekler et al., 2019; Koçyiğit & Gürboğa, 2021), and the 12 June, 2017 Lesvos - Karaburun Earthquake with M_w=6.3 (Kiratzi, 2018; Papadimitriou et al., 2018; Chousianitis & Konca, 2018; Utkucu et al., 2021) occurred in this region (Figure-3). The centroid moment tensor solutions indicate that 2017 Gülpınar, and 2017 Lesvos Earthquakes were caused by normal faulting, whereas the 2013 Lemnos Earthquake was caused by strike-slip faulting (Figure-3). More recently another earthquake sequence had started on 7 January, 2023 with an earthquake of M_w = 5.0 and continued with an earthquake of M_w=5 on 10 January, 2023, both located next to each other on the north coast of the Lesvos Island (Figures-3 and 6).

Figure 2. Seismicity map of the Lesvos Island and vicinity until 2017 (modified after Sözbilir et al., 2016).
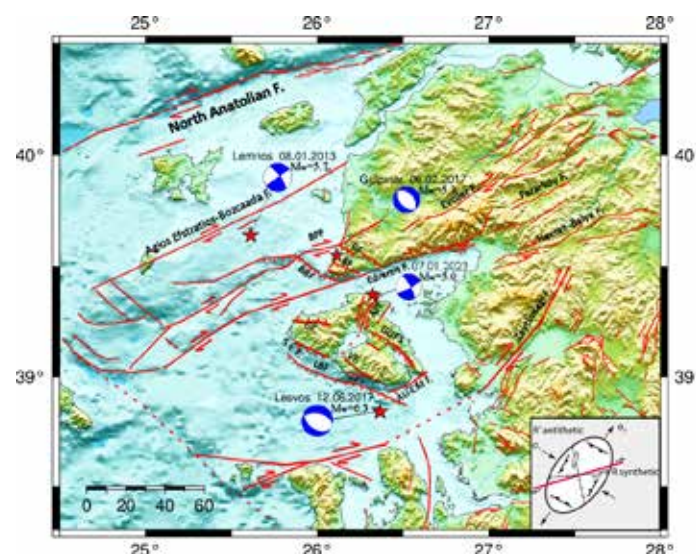
Figure-3. Map of recent earthquakes with $M_w \geq 5.0$ that occurred in the Lesvos Island and the Gulf of Edremit region.

**The 6 February-24 March 2017 Gülpınar (Ayvacık, Çanakkale) Earthquake Sequence**

An earthquake with moderate magnitude M_w=5.3 occurred on 6 Feb., 2017, at 03:51 (UTC) in the Gülpınar (Ayvacık, Çanakkale) region at a depth of 6 km (Poyraz et al., 2017). A second event with M_w=5.1 on the same day at 10:58; a third event with M_w=5.3 on 7 Feb., 2017, at 2:24; and a fourth event with Mw=5.2 on Feb., 12, 2017 at 13:48 were occurred. 26 aftershocks with M_w=4-5, and more than 2000 aftershocks with M≥2.0 occurred in this region between February 6 – March 24, 2017. These earthquakes occurred where there is a normal fault system (Gülpınar-Tuzla, Balabanlı, and Babakale Faults), which have been mapped by field studies (Yılmaz and Karacık, 2001; Sözbilir et al., 2018; Koçyiğit & Gürboğa, 2021). A panoramic photo taken looking in the NW direction shows the textbook example of stair steps like normal fault system in the Gülpınar-Tuzla area (Figure-4). Epicenters of these earthquakes plot in an elongate zone that strikes in the NW-SE direction (Figure-5). The moment tensor solutions of the main shock and a great majority of the aftershocks indicate normal faulting mechanism with NW-SE fault strike (Poyraz et al, 2017; Gülen & Yalçın, 2017; Bekler et al, 2019). The hypocenter depths of the aftershocks are in the range of 5-20 km and the distribution of aftershock hypocenters define normal faulting with a listric fault geometry that dips to SW (Figure-6).

Figure-4. A panoramic photo showing the normal faults in the Gülpınar-Tuzla area (looking towards the NW direction).
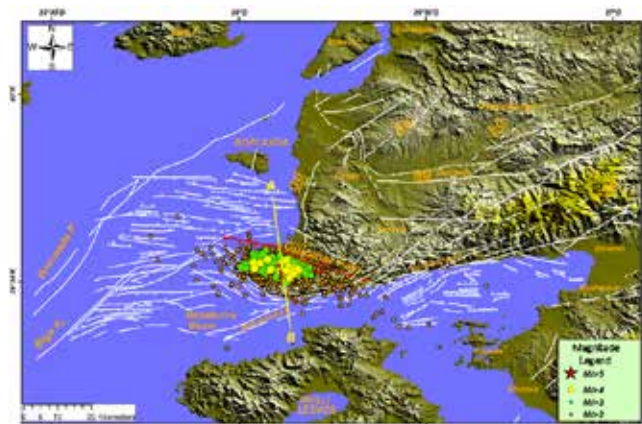
Figure-5.Seismic activity map of the the 6.02-24.3, 2017 Gülpınar Earthquake sequence (modified after Yaltırak et al., 2012).
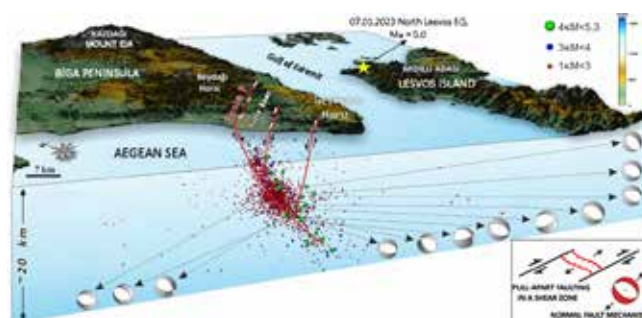
Figure-6. Block diagram of the 6 February- 2017 Gülpınar Earthquake sequence activity (modified after Sözbilir et al, 2018).

The January 7-10, 2023 North Lesvos Earthquake Sequence

An earthquake of moderate magnitude M_w=5.0 occurred on January 7, 2023, at 01:52:57 (GMT) at a depth of 6 km. along the northern coast of the Lesvos Island (Kartal and Kadirioğlu, 2023). The location of this earthquake is shown with a yellow star in Figure-6. On the same day an aftershock of M_w=4.7 occurred at 06:39:30. As of January 7, 2023, nearly one thousand earthquakes with magnitudes; varying between 0.8-5.0 have been recorded by the Disaster and Emergency Management Presidency of Türkiye. On January 10, 2023 another M_w=5 earthquake occurred in the same area. The aftershocks occurred at a depth range of 5-20 km with almost vertical geometry. The epicentral distribution of the aftershocks define an elongate zone extending in the NE-SW direction. Thus, centroid moment tensor solutions of 7 events with $M_w \geq 4.0$ indicate that these earthquakes were caused by a right-lateral strike-slip fault with an average strike of N60°E. The right-lateral strike-slip Aghia Paraskevi Fault is the most prominent tectonic feature on the Lesvos Island and it cuts the central part of the island coast to coast and it was the source fault of the historical 1867 destructive earthquake (Chatzipetros, et al., 2013).. The Aghia Paraskevi Fault has 5 fault segments and the southern 4 of these segments have NNE-SSW strikes (Chatzipetros, et al., 2013). Only the northernmost Sykamia segment has NE-SW strike and the January 7-10, 2023 earthquakes may be associated with the Sykamia segment of the Aghia Paraskevi Fault (Kartal and Kadirioğlu, 2023).

Conclusions

The active tectonics of the NE Aegean region can be explained by the mega-horse-tail geometry of the right-lateral strike-slip North Anatolian Fault's branches and other faults that extend with NE-SW strikes from the mainland Türkiye into the Aegean Sea. The historical and instrumental period seismicity, bathymetry, seismic reflection profiles, field studies, GPS measurements clearly corroborate this conclusion. The insets given in Figures 3 and 6 provide the simplest explanation for the active tectonics of the northern Aegean, which exhibits a NE-SW extensional tectonic regime. In the inset of Figure-3 the strain ellipsoid for a right-lateral strike-slip fault is shown with the positions of σ_1 and σ_3 principle stress axis', as well as the R and R' orientations. Similarly, the inset of Figure-5 also shows how extension takes place in a right-lateral strike-slip shear zone. The fault map given in Figure-5 shows the development of NW-SE trending normal faulting within a NE-SW trending right-lateral strike-slip shear zone that is perfectly consistent with the simple strain ellipsoid and pull-apart faulting explanations.

The fundamental cause of the overall Aegean extensional tectonic regime needs an explanation as well. The subduction transform edge propagator faults (STEP faults or simply tear faults) of the Kefalonia and the Pliny-Strabo Shear zones on both sides of the Hellenic Trench (Özbakır et al., 2023; 2020), as well as the North Anatolian Fault facilitates the Aegean continental lithosphere thrust over the subducting slab (remnant of the Neo-Tethys) causing trench retreat. The trench retreat and the associated mantle flow in that direction causes stretching of the ductile lower crust, which in turn creates an extensional tectonic regime in the brittle upper crust, thus thinning and expanding the surface area of the Aegean continental crust (Gülen, 1990). Supporting evidences for these conclusions were obtained by mantle seismic anisotrophy and seismic tomography studies recently (Jolivet, et al., 2009; Rappisi et al, 2024). In summary, the fundamental cause of the Aegean extension is the drag forces exerted by mantle flow to the Aegean continental lithosphere (Gülen, 1989; 1990).

Acknowledgements

References

Altınok, Y., Alpar, B., Yaltırak, C., and Özer, N., 2012-a. Macroseismic evaluation of the Gulf of Edremit-Ayvacık earthquake, 6 October 1944, İstanbul Yerbilimleri Dergisi, 25, 41-53. **[Journal Article]**

Altınok, Y., Alpar, B., Yaltırak, C., Pınar, A., and Özer, N., 2012-b. The earthquakes and related tsunamis of October 6, 1944 and March 7, 1867; NE Aegean Sea, Nat. Hazards, 60, 3–25. https://doi.org/10.1007/s11069-011-9949-7 **[Journal Article]**

Ambraseys, N., 2002. The seismic activity of the Marmara Sea Region over the last 2000 years. Bull. Seism. Soc. Am., 92,

1-18. **[Journal Article]**

Ambraseys, N., 2009. Earthquakes in the Mediterranean and Middle East: A multidisciplinary study of seismicity up to 1900. Cambridge Univ. Press, 947p. **[Book]**

Ambraseys, N., & Jackson, J., 1998. Faulting associated with historical and recent earthquakes in the Eastern Mediterranean region, Geophys, J. Int. 133, 390–406. **[Journal Article]**

Bekler, T., Demirci, A., and Özden, S., 2019. Biga yarımadası güncel depremleri ve faylanma karakterleri ve sismotektonik değerlendirmesi, 5th International Conference on Earthquake Engineering & Seismology, 8-11 October, 2019, METU, Ankara, Türkiye. **[Conference Proceedings]**

Chatzipetros, A., Kiratzi, A., Sboras, S., Zouros, N., Pavlides, S., 2013. Active faulting in the north-eastern Aegean Sea Islands. Tectonophysics. Vol. 597-598, P.106-122. http://dx.doi.org/10.1016/j.tecto.2012.11.026 **[Journal Article]**

Chousianitis, A. and Konca, A.Ö., 2018. Coseismic slip distribution of the 12 June 2017 Mw = 6.3 Lesvos earthquake and imparted static stress changes to the neighboring crust. Journal of Geophysical Research: Solid Earth, 123, 8926–8936. https://doi.org/10.1029/2018JB015950 **[Journal Article]**

Dewey, J.F.and Sengör, A.M.C., 1979. Aegean and surrounding regions: complex multiple and continuum tectonics in a convergent zone, Geol. Soc. Am. Bull., 90, 84–92. **[Journal Article]**

Emre, Ö., Duman, T. Y., Özalp, S., Elmacı, H., Olgun, Ş., & Şaroğlu, F., 2013. Active fault map of Turkey with explanatory text. Ankara: General Directorate of Mineral Research and Exploration, Special Publication Series-30. **[Book]**

Ganas A., Oikonomou,I.A., and Tsimi, C., 2013. NOAFAULTS: A Digital database for active faults in Greece, Bulletin of the Geological Society of Greece, vol. XLVII, Proceedings of the 13th International Congress, Chania, Sept.2013. **[Conference Proceedings]**

Ganas, A., Roumelioti, Z., Karastathis, V., Chousianitis, K., Moshou, A., and Mouzakiotis, E., 2014. The Lemnos 8 January 2013 (Mw=5.7) earthquake: fault slip, aftershock properties and static stress transfer modeling in the north Aegean Sea, J. Seismol., https://doi.org/10.1007/s10950-014-9418-3 **[Journal Article]**

Ganas, A., Kourkouli, P., Briole, P., Moshou, A., Elias, P., and Parcharidis, I., 2018. Coseismic Displacements from Moderate-Size Earthquakes Mapped by Sentinel-1 Differential Interferometry: The Case of February 2017 Gulpinar Earthquake Sequence (Biga Peninsula, Turkey), Remote Sens., 10, 1089, https://doi.org/10.3390/rs10071089 **[Journal Article]**

Gülen, L., 1989. From plate tectonics to global domain tectonics, in Crust/Mantle Recycling at Convergence Zones, S. R. Hart and L. Gülen (Editors), NATO ASI Series, C258, Kluwer Academic Publishers, Boston, 173–179. **[Book]**

Gülen, L., 1990. Isotopic characterization of Aegean magmatism and geodynamic evolution of the Aegean subduction, in Proc. Int. Earth Sci. Cong. on Aegean Regions, M.Y. Savaşcın & A.H. Eronat (Editors), Vol. 2, 143–166. **[Conference Proceedings]**

Gülen, L., Pınar, A., Kalafat, D., Özel, N., Horasan, G., Yılmazer, M., & Işıkara, A.M., 2002. Surface fault breaks, aftershock distribution, and rupture process of the 17 August 1999 İzmit, Turkey earthquake, Bull. Seism. Soc. Am. 92**,** 230–244. **[Journal Article]**

Gülen, L., and Yalçın, H., 2017. February 2017 Ayvacık, Çanakkale Earthquake Swarm:Seismotectonic and morphotectonic constraints, 4. Uluslararası Deprem Mühendisliği ve Sismoloji Konferansı, 11-13 Ekim 2017, Anadolu Üniversitesi, Eskişehir, Türkiye. **[Conference Proceedings]**

Jolivet, L., Faccenna, C., and Piromallo, C., 2009. From mantle to crust: Stretching the Mediterranean, Earth & Planet. Sci. Lett., 285, 198–209. https://doi.org/10.1016/j.epsl.2009.06.017 **[Journal Article]**

Karakaisis, G.F., Papazachos, C.B. and Scordilis, E.M., 2010. Seismic sources and main seismic faults in the Aegean and surrounding area, Proceedings of the 12th International Congress, Patras, May, 2010, Bull. Seism. Soc. Greece. **[Conference Proceedings]**

Kartal, R.F. and Kadirioğlu, F.T., 2023. January 2023 Mytilene Island (North Aegean Sea) Earthquake Activity and Its Relationship with the Tectonics of the region, Proceedings of the 75th Geological Congress of Turkey, April 10-14, 2023, Ankara, Turkey. **[Conference Proceedings]**

Kiratzi, A., 2018. The 12 June 2017 Mw 6.3 Lesvos Island (Aegean Sea) earthquake: Slip model and directivity estimated with finite-fault inversion, Tectonophysics 724–725, 1–10, https://doi.org/10.1016/j.tecto.2018.01.003 **[Journal Article]**

Kiratzi, A. and Svigkas, N., 2013. A study of the 8 January 2013 Mw5.8 earthquake sequence (Lemnos Island, East Aegean Sea), Tectonophysics 608, 452–460. http://dx.doi.org/10.1016/j.tecto.2013.09.002 **[Journal Article]**

Koçyiğit, A. and Gürboğa, Ş., 2021. Active tectonics of Gülpınar-Tuzla area (Biga Peninsula, NW Turkey): the source of 6 February-24 March 2017 earthquake cluster, Bull. Min. Res. Exp. (2021) 166: 85-112. **[Journal Article]**

Kürçer, A., Yalçın, H., Gülen, L., Kalafat, D., 2014. 8 January 2013 Mw = 5.7 North Aegean Sea earthquake and its seismotectonic significance, Geodinamica Acta, https://doi.org/10.1080/09853111.2014.957503 **[Journal Article]**

McClusky, S., et al., 2000. Global Positioning System constraints on plate kinematics and dynamics in the eastern Mediterranean and Caucasus, J. Geophys. Res., 105, 5695– 5719. **[Journal Article]**

Meade B.J., Hager B.H., McClusky, C., Reilinger R.E., et al., 2002. Estimates of seismic potential in the Marmara region from block models of secular deformation constrained by GPS measurements, Bull. Seismol. Soc. Am., 92, 208–215. **[Journal Article]**

Özbakır, A.D., Şengör, A.M.C., Wortel, M.J.R., and Govers, R., 2013. The Pliny–Strabo trench region: A large shear zone resulting from slab tearing, Earth & Planet. Sci. Lett. 375, 188–195. http://dx.doi.org/10.1016/j.epsl.2013.05.025 **[Journal Article]**

Özbakır, A.D., Govers, R., and Fichtner, A., 2020. The Kefalonia Transform Fault: A STEP fault in the making, Tectonophysics, 787, 228471. http://creativecommons.org/licenses/BY/4.0/ **[Journal Article]**

Özden, S., Över, S., Poyraz, S.A., Yavuz Güneş, Y., Pınar, A., 2017. Tectonic implications of the 2017 Ayvacık (Çanakkale) earthquakes, Biga Peninsula, NW Turkey, J. Asian Earth Sci., https://doi.org/10.1016/j.jseaes.2017.12.021 **[Journal Article]**

Papadimitriou, P., Kassaras, I., Kaviris, G., Tselentis, A., Voulgaris, N., Lekkas, E., et al., 2018. The 12th June 2017 Mw=6.3 Lesvos earthquake from detailed seismological observations, Journal of Geodynamics, https://doi.org/10.1016/j.jog.2018.01.009 **[Journal Article]**

Papadopoulos G, Ganas A, Plessa A (2002) The Skyros earthquake (Mw6.5) of 26 July 2001 and precursory seismicity patterns in the North Aegean Sea. Bull Seismol Soc Am 92(30):1141–1145. **[Journal Article]**

Poyraz, S.A., Pınar, A., Kekovalı, K., Güneş, Y., Kalafat, D., et al., 2017. 2017 yılı Ayvacık, Çanakkale deprem aktivitesinin sismotektonik özellikleri, 4. Uluslararası Deprem Mühendisliği ve Sismoloji Konferansı, 11-13 Ekim 2017, Anadolu Üniversitesi, Eskişehir, Türkiye. **[Conference Proceedings]**

Rappisi, F., Bue, R.L., VanderBeek, Confal, J.M., Erman, C., et al., 2024. 3-D Mantle Flow and Structure of the Mediterranean from Combined P-wave and Splitting Intensity Anisotropic Tomography,
https://essopenarchive.org/doi/full/10.22541/essoar.173499076.65970186/v1 **[Journal Article]**

Sözbilir, H., Uzel, B., Sümer, Ö., Eski, S., Softa, M., Tepe, Ç., Özkaymak, Ç., Baba, A., 2018. Çanakkale-Ayvacık deprem fırtınasının (14 Ocak – 20 Mart 2017) sismik kaynakları, Anadolu Üniversitesi Bilim ve Teknoloji Dergisi – B Teorik Bilimler, **6**:1-17. **[Journal Article]**

Sözbilir, H., Sümer, Ö., Özkaymak, Ç., Uzel, B., Güler, T., and Eski, S., 2016. Kinematic analysis and palaeoseismology of the Edremit Fault Zone: evidence for past earthquakes in the southern branch of the North Anatolian Fault Zone, Biga Peninsula, NW Turkey, Geodinamica Acta, 28:4, 273-294, https://doi.org/10.1080/09853111.2016.1175294 **[Journal Article]**

Straub, C., Kahle, H.G., and Schindler, C., 1997. GPS and geologic estimates of the tectonic activity in the Marmara Sea region, J. Geophys. Res., 102, 27587-27601. **[Journal Article]**

Taymaz T., Jackson J. and McKenzie D. 1991. Active tectonics of the north and central Aegean Sea, Geophys. J. Int., 106, 433-490. **[Journal Article]**

Utkucu, M., Budakoğlu, E., Kızılboğa, S., and Yalçın, H., 2017. Şubat 2017 Ayvacık deprem silsilesi geri plan depremsellik analizi, 4. Uluslararası Deprem Mühendisliği ve Sismoloji Konferansı, 11-13 Ekim 2017, Anadolu Üniversitesi, Eskişehir, Türkiye. **[Conference Proceedings]**

Utkucu, M., Nalbant, S.S., Pınar, A., McCloskey, J., Nicbhloscaidh, M., et al., 2021. The June 12, 2017 M6.3 Karaburun-Lesvos earthquake of the Northern Aegean Sea: Aftershock forecasting and stress transfer, Tectonophysics, https://doi.org/10.1016/j.tecto.2021.228945 **[Journal Article]**

Yaltırak, C., İşler, E.B., Aksu, A.E., and Hiscott, R.N., 2012. Evolution of the Bababurnu Basin and shelf of the Biga Peninsula: Western extension of the middle strand of the North Anatolian Fault Zone, Northeast Aegean Sea, Turkey, Journal of Asian Earth Sciences, 57, 103–119. http://dx.doi.org/10.1016/j.jseaes.2012.06.016 **[Journal Article]**

Yılmaz, Y. and Gürer, Ö.F., 2023. Tectonic development of western Anatolian extensional province, International Geology Review, https://doi.org/10.1080/00206814.2023.2209865 **[Journal Article]**

Yılmaz, Y. and Karacık, Z., 2001. Geology of the northern side of the Gulf of Edremit and its tectonic significance for the development of the Aegean grabens, Geodinamica Acta 14, 31- 43. **[Journal Article]**

The rocks connect us: Volcanic geoheritage of Lesvos Geopark (Greece) and Ida Madra Geopark (Türkiye)

Erdal Gumus[1], Nikolas Zouros[2]
(1) Balikesir University, Balikesir, Türkiye, erdalgumus08@gmail.com, (2) Aegean University, Mytilene, Greece

Introduction

Both Lesvos UNESCO Global Geopark, (Greece) and Ida Madra Geopark (Türkiye) include a variety of geological heritage sites of international significance and are characterized by rich geodiversity. The majority of the geological heritage sites present in the respective territories are related to volcanism, with the 72% of the geosites in Lesvos Geopark and 62% of the geosites in Ida Madra Geopark found on igneous rocks. Highlighting the shared and complementary geohistorical context of neighboring geoparks can enhance the interpretation, conservation, and promotion of geoheritage in a holistic manner and cooperation between territories.

The Aegean region is among the most tectonically active regions on Earth due to the subduction of the African plate beneath the Eurasian plate and the westward extension of the Anatolian microplate. Consequently, the region saw extensive extrusive and intrusive volcanism during the Miocene period (Bozkurt et al. 2005, Innocenti et al. 2009). The vigorous volcanic activity created complex volcanic formations. The geosites of Lesvos Geopark (Greece) and Ida Madra Geopark (Türkiye) are closely associated with Miocene volcanism and tectonics.

A Geopark might be likened to a chapter in a novel; it may be coherent independently but remains incomplete without the additional chapters that contribute to the overarching narrative. In this regard, the coinciding and complementary geosites of the Lesvos Geopark and Ida Madra Geopark may offer a more comprehensive perspective for both. Both Geoparks belong geologically to the Sakarya - Pelagonia massif (Figure 1).
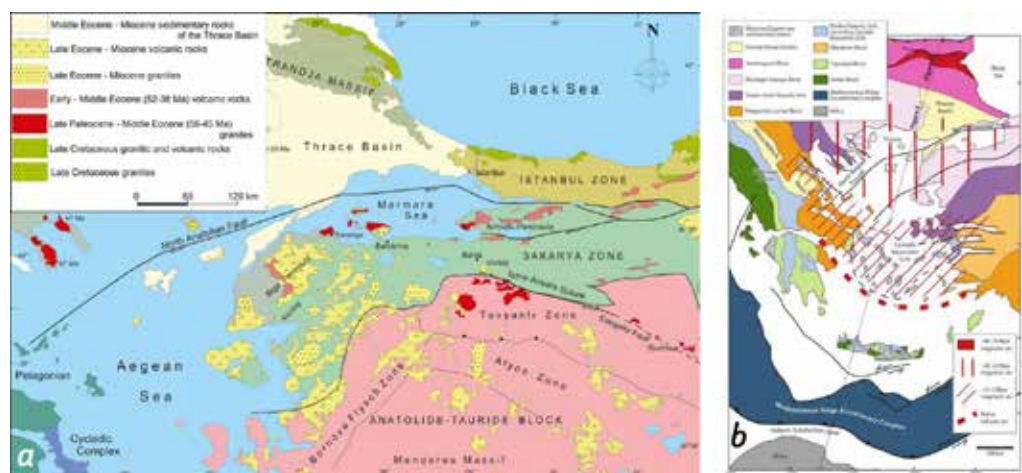
Figure 1. Simplified tectonic map of the North Aegean (a) (Okay et al., 2022) Aegean region (b), (Vouduris, 2018)

The Lesvos Geopark was founded in 2000 as one of the four primary partners of the European Geoparks Network. It is founding member of the Global Geoparks Network since 2004 and recognized as a UNESCO Global Geoparks in 2015. The Lesvos Geopark is distinguished by its exceptional abundance of fossilized trees and volcanic terrains. (Zouros *et al.*, 2003, 2004, 2009, 2010)

The Ida Madra Geopark was established in 2019 and designated as a UNESCO candidate in 2022 (Gumus et al., 2021). The Ida Madra Geopark features the prominent Mt. Ida, composed of metamorphic rocks, alongside Mt. Madra, recognized for its Kozak granitoid (Gumus, 2022).

The two nearby geoparks are close enough to share a common geotectonic setting (Figure 2).

Figure 2. Location map of the Lesvos Geopark (Greece and the Ida Madra Geopark (Türkiye)

Objectives

This study intends to demonstrate how rocks and their geohistorical background can play an important role in bringing together neighboring and geologically interconnected territories. Their geological background can be the basis for the development of common research, educational and geo-touristic activities and provide a stable bridge for collaboration, common activities and cultural exchange.

This study is based on the classification, comparison, and interpretation of the volcanic geosites of the neighboring Lesvos Geopark and Ida Madra Geopark in a comprehensive manner.

Findings

Both Lesvos and the Ida Madra Geopark are significantly influenced by volcanism and associated landscapes, with 72% of geosites in Lesvos Geopark and 62% in Ida Madra Geopark located on igneous lithology (Figure 3).

The geosites of volcanic origin exhibit unique features, including diverse volcanic landscapes, intrusions, domes, columnar lava formations, lava flows, pyroclastics, hot springs, waterfalls, fossils, caves, and canyons.
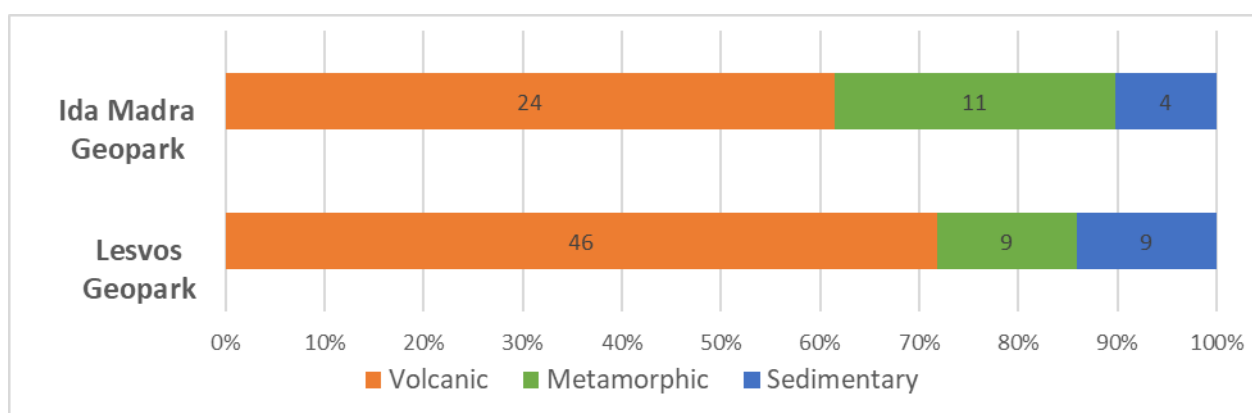
Figure 3. Geosite lithology comparison of Lesvos Geopark and Ida Madra Geopark

The variety of volcanic geosites of both Geopark facilitate a more thorough spatiotemporal interpretation of volcanism in the region. In certain instances, analogous geological processes resulted in comparable

formations, whereas in other cases, they produced distinctly unique appearances. For instance, both geoparks feature characteristic spheroidal exfoliation forms that are nearly identical in size and shape (Figure 4).

Figure 4. Spheroidal exfoliation geosites: Tatlısu geosite /Ida Madra Geopark (a), Vatousa geosite /Lesvos Geopark (b)

The westward extension of the Anatolian microplate dominates the active tectonics that governs both Geoparks. As a result, Miocene volcanics have been affected by major active faults creating impressive fault scarps during Quaternary (Figure 5).

Furthermore, the scientific importance of these geosites is highlighted by their extensive use in geo-education and in enhancing public awareness regarding natural disasters.

Figure 5. Aghia Paraskevi fault scarp geosite/ Lesvos Geopark (a), Pelitköy fault scarp geosite, / Ida Madra Geopark (b)

Conversely, analogous lithologies give rise to entirely distinct geosites and landscapes. For example, the differential weathering of thick ignimbrite deposits along vertical fractures resulted in finger-like columns in Lesvos Geopark, whereas the same lithology, when subjected to a spheroidal fracture pattern, revealed a turtle back-like landscape in Ida Madra Geopark (Figure 6).

Figure 6. Aslanalan geosite/Ida Madra Geopark (a), Candles geosite/Lesvos Geopark (b)

Intrusive volcanics significantly contribute to the geological features of both geoparks. The western section of the Lesvos Geopark features prominent volcanic formations, including the Ipsilou dome, Eressos dome, Mesotopos dome, and Mythimna dome. In contrast, the Ida Madra Geopark is distinguished by its granitic intrusions, exemplified by Mt. Çataldağ and Mt. Madra (Figure 7).

Figure 7. Ipsilou volcanic dome geosite/ Lesvos Geopark (a), Çataldağ granite slab geosite /Ida Madra Geopark (b)

Results and Conclusion

The Miocene volcanism which has significantly shaped both Lesvos Island and the Ida Madra Geopark area, may serve as a geological reference framework frame for cooperation in conservation, education, and research.

This geological continuum hosts inherently related yet fully distinct geosites within both Geoparks. Tracking the geological links between Lesvos Island and Ida Madra Geopark could help to provide a more thorough understanding and interpretation of the region's and Earth's overall geological evolution.

In the last decade, there has been a growing trend in reciprocal visits between Lesvos Island and Balikesir Metropolitan Area, evidenced by the traditional connections between Mytilene and Ayvalik as well as the establishment of new ferry routes and destinations connecting the two territories.

This fact presents significant potential for development of collaborative educational initiatives, including field excursions and Erasmus Exchange programs, as well as geotourism activities like offering inter-geopark tour packages.

References

E. Bozkurt and S. K. Mittwede (2005). Introduction: Evolution of Continental Extensional Tectonics of Western Turkey. Geodinamica Acta 18/3-4: 153–165.

Gumus, E, Soykan, A, Helvacı C, Ulusoy ,İ., (2021) Aspiring Ida Madra Geopark-2021 UNESCO Geoparks Candidate of Turkey. Proceedings of the Digital 9th International Conference on UNESCO Global Geoparks. Juju, South Korea

Gumus, E (2022). Aspiring Ida Madra Geopark. UNESCO Application Dossier

Voudouris, Panagiotis. "A Field Guide on the Geology and Mineralogy of Lavrion, Attica, Greece." (2018).

Innocenti, F., Agostini, S., Tokcaer, M., and Savaşcın, M.E. (2009). Volcanic Rocks from Foça-Karaburun and Ayvalık-Lesvos Grabens (Western Anatolia) and Their Petrogenic-Geodynamic Significance. Turkish Journal of Earth Sciences (Turkish J. Earth Sci.), Vol, 19.

Okay, A. I., Topuz, G., Kylander-Clark, A. R., Sherlock, S., & Zattin, M. (2022). Late Paleocene–Middle Eocene magmatic flare-up in western Anatolia. Lithos, 428, 106816.

Zouros, N., Martini, G., (2003) Introduction to the European Geoparks network. In NHM of Petrified Forest. Proceedings of 2nd International Symposium of Natural Monuments and Geological Heritage, Lesvos (pp. 17-21)

Zouros, N., Fassoulas, Ch., Velitzelos, E., Mountrakis, D., Soulakellis, N., (2005) Monuments geotopes in the aegean islands – Contribution to the protection and promotion of Geological heritage in Greece. 50 Proceedings of the 4th European Geopark's Meeting, 2-5 October

Zouros, N., (2004) European Geoparks Network: geoconservation, promotion, education and local development. Proceedings of the 5th International Symposium on Eastern Mediterranean Geology. Thessaloniki 14-19 April 2004 p. 441-444

Zouros, N., (2009) The petrified forest of Lesvos – a unique natural monument. In: N. Evelpidou, T. De Figueiredo, F. Mauro, V. Tecim, A. Vasilopoulos, (ed.) Natural Heritage monuments – Europe from West to East. Springer Verlag Berlin Heidelberg 2010 p. 15-26

Zouros, N., (2010) Lesvos Petrified Forest Geopark, Greece: geoconservation, geotourism, and local development. In The George Wright Forum Journal (Vol. 27, No. 1, pp. 19-28)

Assessing Climate Change Impacts on Troodos Mountain (Troodos UNESCO Global Geopark area) Through Methodological Approaches and Community Engagement in the ClimEmpower Project

Petros Hadjicostas [1], Evi Kazamia [1], Georgios Xekalakis [2], Christos Anastasiou [2], Petros Christou [2, 3]

[1] Troodos Development Company LTD, Troodos, Cyprus
[2] Department of Civil Engineering, School of Engineering, Frederick University, 1036 Nicosia, Cyprus
[3] Faculty of Civil Engineering and Architecture, Kaunas University of Technology, 44249 Kaunas, Lithuania
*Correspondence: info@anetroodos.com

Abstract

The Troodos Mountain region, including the Troodos UNESCO Global Geopark, is increasingly vulnerable to the impacts of climate change, facing both environmental degradation and socio-political challenges. Within the ClimEmpower project, we apply an integrated methodological framework combining climate modeling, geospatial analysis, and community engagement to assess these effects. Climate projections are based on downscaled outputs from the EURO-CORDEX initiative (RCMs under RCP4.5 and RCP8.5 scenarios), while trends in temperature and precipitation are quantified using 25 years of daily data from local meteorological stations. Geospatial analysis utilizes shapefiles of the study area and climate-related indicators to produce climate risk maps. These maps integrate environmental datasets with socio-economic vulnerability information gathered through Community of Practice (CoP) meetings. The CoP sessions also offer critical insights into local experiences, resource management challenges, and governance gaps faced by residents. Preliminary results indicate rising temperatures and declining precipitation patterns, correlating with increased drought stress, wildfire risks, and biodiversity shifts within the region. This participatory, data-driven approach underscores the need for adaptive and inclusive governance strategies tailored to the specific vulnerabilities of mountain communities. Our findings contribute to evidence-based policymaking aimed at enhancing regional resilience to climate change.

Acknowledgements

References

Georgios Xekalakis, Lopez, P.M., Ruiz, M.A., Tötzer, T., Kaleta, P., Konstantinos Karystinakis, Moumtzidou, A., Forjan, R., Christou, P., Anastasiou, C., Pavone, V., Gigliola D'Angelo, Cobos, F.S., Bügelmayer-Blaschek, M., Socrates Boutsis, Marija Vurnek, Murano, I., Prete, P.D., Kutschera, P. and Dimitrios Leonidis (2024). User-Driven Climate Resilience Across Southern European Regions. Climate, [online] 13(1), pp.2–2. doi: https://doi.org/10.3390/cli13010002.

Xekalakis, G., Anastasiou, C., Bügelmayer-Blaschek, M., Molina López, P., Gamallo-Paz, I., Tötzer, T., Pavone, V., Kazamia, E., Christou, P., & Havlik, D. (2025). BUILDING CLIMATE RESILIENCE IN MOUNTAIN REGIONS. Eleventh International Conference on Remote Sensing and Geoinformation of Environment (RSCy25), Paphos, Cyprus. Eleventh International Conference on Remote Sensing and Geoinformation of Environment. https://doi.org/10.5281/zenodo.15058105

Climempower.eu. ABOUT—ClimEMPOWER. 2023. Available online: https://climempower.eu/about/ (accessed on 9 January 2025).

Tötzer, T., Bügelmayer-Blaschek, M., Hochebner, A., Kozlowska, A., Schneider, M., Chatzichristaki, C., Molina Lopez, P., Murano, I., Xekalakis, G., and Havlik, D.: Climate change resilience in South-European regions: data, services, indicators and gaps, EGU General Assembly 2025, Vienna, Austria, 27 Apr–2 May 2025, EGU25-9170, https://doi.org/10.5194/egusphere-egu25-9170, 2025.

Geoconservation in Portugal: an overview

Henriques M.H.[1], Custódio S.[1], Carvalho I.S.[1,2]

(1) Geosciences Centre, Department of Earth Sciences, Faculty of Sciences and Technology, University of Coimbra (Polo II), Rua Sílvio Lima 3030-790, Coimbra, Portugal, hhenriq@dct.uc.pt (2) Department of Geology, Federal University of Rio de Janeiro, Cidade Universitária - Ilha do Fundão, CCMN/IGEO 21.949-900, Rio de Janeiro, Brazil

Introduction

Geoheritage and geotourism help to promote inclusive and sustainable economic growth, full and productive employment and decent work for all, in line with the Sustainable Development Goals of the 2030 Agenda (Gill, 2017). This is a particularly important issue for peri-Mediterranean countries, whose economy is heavily dependent on tourism, mostly seasonal and concentrated on beaches. Tourism in Portugal reached historic highs last year and contributed to around half of the real growth in Gross Domestic Product (GDP), generating a direct and indirect contribution of 33.8 billion euros to GDP in 2023, which corresponds to 12.7% (INE, 2023). Diversifying the tourism offer and creating products in low-density territories represents a challenge for consolidating the country's tourism industry and making it compatible with sustainable development goals.

Protecting and valuing the geological heritage of Portugal is an important asset in promoting sustainable, non-seasonal tourism which is reflected in the well-being of the residents. It is up to the political authorities to implement public policies that guarantee the effective geoconservation of these territories, and for other sectors of society to become more involved in safeguarding their geoheritage.

There is no specific legislation on geoconservation in Portugal. The national law to protect natural areas (Decree-Law nº19/93 of 23rd July) defines several different categories created mainly for biological purposes with only one category remaining to include sites of geological interest that deserve to have their physical integrity safeguarded (Henriques, 2004). As so, the geological heritage of Portugal is protected at national level through Natural Monuments, which are part of the National Network of Protected Areas (Table 1). These are defined as natural occurrences containing one or more aspects which, due to their uniqueness, rarity or representativeness in ecological, aesthetic, scientific and cultural terms, require their conservation and the maintenance of their integrity (ICNF, 2025).

Table 1. Natural Monuments of Portugal that are part of the National Network of Protected Areas.

Name	Characterization	Classification date	Level
Pegadas de Dinossáurios de Ourém/Torres Novas	The largest Middle Jurassic (Bajocian-Bathonian) sauropod trackside (147 meters long) known in the world.	1996	National
Carenque	One of the largest and earliest (Lower Cretaceous) known continuous dinosaur tracks (127 meters long) produced by two herbivorous quadrupeds and possibly bipedal carnivores.	1997	National
Lagosteiros	High quality Upper Jurassic dinosaur tracks.	1997	National
Pedra da Mua	Trails of Tithonian age that record the first evidence of gregarious behavior among sauropods recognized in Europe.	1997	National
Pedreira do Avelino	The prints of the smallest sauropod known in Europe of Kimmeridgian age.	1997	National
Cabo Mondego	Jurassic record including the Bajocian GSSP and the Bathonian ASSP.	2007	National
Portas do Ródão	An imposing gorge carved out by the River Tagus in the quartzite ridges of the Perdigão mountain range, with a 45 meters wide bottleneck.	2009	National
Canhão Cársico de Ota	One of the most interesting "canyon" valleys in the Portuguese karst regions, with almost vertical escarpments carved into the Upper Jurassic limestones.	2019	Local
Livraria do Mondego	Sequence of subverticalized Armorican quartzites, in thick layers with well-defined stratification surfaces, which resemble the arrangement of a set of books on a shelf, and which refers to the name given to the site.	2024	Local

The first classified geological sites in Portugal date back to 1996 and 1997 and refer exclusively to dinosaur tracks, which reflects how dinosaurs captivate humans and are a charismatic component of our contemporary human existence (Yates and Peacock, 2023). The following decade saw the classification of the last two national Natural Monuments, which no longer refer to geological heritage of the paleontological type like the previous ones but can be included in the stratigraphic type (Habibi *et al.*, 2018). Among them is the Cabo Mondego Natural Monument, located on the west coast of the country, with a particularly significant record of the Middle and Upper Jurassic (Fig. 1), and which is part of the territory related to the ongoing "Atlantic Geopark Project", aimed at a future application to the Global Geoparks Network (Custódio et al., 2024, 2025 this volume).

Figure 1. The extraordinary Middle Jurassic stratigraphic record of Cabo Mondego Natural Monument, where the Bajocian GSSP (A and B) and the Bathonian ASSP (C) were defined. The Upper Jurassic record includes dinosaur footprints on the surface bedding plane (D and E), as well as convoluting bedding and soft sediment injection structures (E) interpreted as dinoturbation structures (Carvalho *et al.*, 2022).

Natural Monuments of national rank are managed by a national, centralized entity, the Institute for Nature Conservation and Forests (ICNF), which belongs to the Ministry of Environment and Energy. The same Ministry runs a database of geological sites located in national territory intended for scientific, technical, and educational purposes, to support nature conservation and land use policies, with free access and constant updates with the collaboration of the geological community (Fig. 2). It includes nearly four hundred geological sites distributed by 26 thematic categories following a methodology adapted to national-level inventories originally defined by ProGEO (the European Association for the Conservation of Geological Heritage) and IUGS (the International Union of Geological Sciences) (Brilha et al., 2005; LNEG, 2025). But the first national inventory of geological heritage, which brings together the main sites in Portugal where elements of geodiversity (minerals, fossils, rocks, geoforms) with high scientific value occur, was the result of a research project that took place between 2007 and 2010 at University of Minho and is available through the ICNF website (Fig. 3; Geossítios, 2025). The two inventories are currently being merged in a strategy to promote geoconservation in Portugal more effectively (Aires et al., 2023).

Despite being classified and formally protected, the Natural Monuments of national rank have not been the subject of valuation and monitoring interventions, procedures that are required in effective geoconservation practices (Henriques *et al.*, 2011). The classification of a natural monument aims to protect natural values, namely notable

occurrences of geological heritage, in the integrity of their characteristics and in the immediate surrounding areas, and the adoption of measures compatible with the objectives of their classification (ICNF, 2025), i.e., the promotion of scientific research, geoeducation and geotourism. The current conditions of the Portuguese Natural Monuments of national rank are a long way from such goals and the communities that occupy the territories are completely oblivious to the geological heritage that surrounds them.

Figure 2. The official website of the National Inventory of Geological Heritage at the Laboratório Nacional de Energia e Geologia (LNEG, 2025).

Figure 3. The official website of the National Inventory of Geological Heritage at the Instituto da Conservação da Natureza e das Florestas (Geossítios, 2025).

This top-down nature conservation strategy has proved to be totally inappropriate and has not contributed to harmonious integration between communities and nature. In parallel with the Portuguese state's disinvestment in the conservation of the country's geodiversity, a number of local initiatives have sprung up for this purpose. Among them are projects aimed at integrating territories into the UNESCO World Geoparks Network.

The bottom-up approach

The first Portuguese Geopark to join the UNESCO World Geoparks Network was Naturtejo in 2006, followed by Arouca, the Azores, Terras de Cavaleiros, Estrela and Oeste (CNU, 2025; Fig. 4; Table 2). Rather than emerging from

a nationwide political decision, UNESCO Global Geoparks (UGGp) are established through a bottom-up process involving all relevant local and regional stakeholders and authorities in the area, deeply committed to the exploration, development and celebration of the links between the geological heritage and all other aspects of the area's natural, cultural and intangible heritage (UNESCO, 2025).

Figure 4. UNESCO Global and Aspiring Geoparks in Portugal (modified after AG, 2025).

UGGp proved to be a sustainable strategy for protecting the geological heritage of Portugal. This may have inspired the Portuguese political authorities to change the legislation on the protection of geological heritage, allowing the creation of Local Natural Monuments. Proposals for their creation come from the local authority, as well as their management, once the classification has been approved by the national authority. The last two Natural Monuments to be classified by the Portuguese State have this status (Table 1).

Table 2. UNESCO Global Geoparks in Portugal.

Name	Official Website	Designation date
Naturtejo	https://www.naturtejo.com/	2006
Arouca	https://aroucageopark.pt/	2009
Azores	https://www.azoresgeopark.com/	2013
Terras de Cavaleiros	https://geoparkterrasdecavaleiros.pt/p/en/	2014
Estrela	https://www.geoparkestrela.pt/	2020
Oeste	https://www.geoparqueoeste.com/	2024

The relevance of community involvement in geoconservation

Nature conservation in Portugal was initially governed by top-down approaches, based on centralized classification initiatives that resulted in difficulties in the management of protected areas. The geological heritage classified as Natural Monuments covers around 1500 ha, of which around 1000 ha correspond to the Portas do Ródão Natural

Monument (ICNF, 2025), a territory included in the Naturtejo Geopark and therefore subject to the geoconservation requirements of UNESCO's Global Geoparks Network (GGN, 2025). But the rest of the area, although classified, has not been valued and, in some cases, is at risk of destruction due to lack of monitoring. The potential for using these sites of recognized scientific and educational interest is practically nil, since they lack the infrastructure to support visitors and the information to understand how the site record contributes to understanding the history of the Earth. The Natural Monuments are briefly described on the official ICNF website, which is the only information available to anyone wishing to visit them.

The creation of geoparks, which emerge from local initiatives, with extensive community involvement in all stages of geoconservation, has proved to be the most effective way of guaranteeing the integrity of geological objects with heritage value, as well as their enjoyment by society. They demonstrated to be a viable approach to the development of areas with remarkable geological heritage which can be adapted to various social and economic contexts as well as cultural ones (Henriques and Brilha, 2017).

Portuguese authorities recognized the relevance of community involvement, and the last two Natural Monuments to be classified in Portugal are already local in scope, and their geoconservation is expected to be more effective. Moreover, the organization of nature protection at state level was altered to integrate the National Network of Protected Areas (a government initiative and responsibility) with classified areas with alternative management systems like those integrated into the Natura 2000 Network and other areas classified under international commitments assumed by the Portuguese State, such as RAMSAR Sites, Geoparks and Biosphere Reserves (SNAC, 2025). However, the maintenance of national natural monuments without improvements that allow them to be used for educational and/or geotourism purposes is a waste of an economic, social and environmental asset.

Conclusions

With regard to geoconservation in Portugal, there is a state entity that aggregates information on the inventory of the country's geological heritage, in close collaboration with the academic community – the Laboratório Nacional de Energia e Geologia, which is a state laboratory of the Ministry of the Environment and Energy (LNEG, 2025). Within the same Ministry, the ICNF oversees the National Network of Protected Areas, which aims to ensure the protection of the geological heritage and the integrity of its characteristics, in the territorial context in which they are located (ICNF, 2025). In this sense, it is possible to say that the country's geological heritage is reasonably well known and inventoried. But geoconservation refers to more than the inventory of a territory's geological heritage. In Portugal, all the other steps that make it possible to guarantee the physical integrity of geological sites (classification, monitoring), as well as their enjoyment for educational and geotourism purposes (valuation) has been assumed fundamentally by local and/or private initiative. It is essential to provide the ICNF with the necessary means to ensure the monitoring and valuation of the protected areas for which it is responsible, i.e., the National Natural Monuments.

Acknowledgements

References

AG, 2025. Algarvensis Geoparque. https://geoparquealgarvensis.pt/unesco/rede-portuguesa-dos-geoparques-mundiais (retrieved 26.2.2025).

Aires R., Machado, S., Pereira, P., Matos, J.X. & Brilha, J., 2023. A unificação dos inventários de geossítios como estratégia para a geoconservação em Portugal. Resumos do XI CNG 2023, Coimbra, 621-622.

Brilha, J., Andrade, C., Azerêdo, A., Barriga, F.J.A.S., Cachão, M., Couto, H., Cunha, P.P., Crispim, J.A., Dantas, P., Duarte, L.V., Freitas, M.C., Granja, M.H., Henriques, M.H., Henriques, P., Lopes, L., Madeira, J., Matos, J.M.X., Noronha, F., Pais, J., Piçarra, J., Ramalho, M.M., Relvas, J.M.R.S., Ribeiro, A., Santos, A., Santos, V. & Terrinha, P., 2005. Definition of the Portuguese frameworks with international relevance as an input for the European geological heritage characterization. Episodes, 28(3), 177-186. https://doi.org/10.18814/epiiugs/2005/v28i3/004

Carvalho, I.S., Cunha, P.P., Figueiredo, S. D., 2022. Dinoturbation in Upper Jurassic siliciclastic levels at Cabo Mondego (Lusitanian Basin, Portugal): evidences in a fluvial-dominated deltaic succession. Palaeoworld 31(3), 455-477. https://doi.org/10.1016/j.palwor.2021.09.001

CNU, 2025. Geoparques Mundiais da UNESCO. Comissão Nacional da UNESCO. https://unescoportugal.mne.gov.pt/pt/redes-unesco/geoparques-mundiais-da-unesco (retrieved 26.2.2025).

Custódio, S.C., Henriques, M.H., Rosado-González, E.M., Vaz, N.M. & Sá, A.A., 2024. Selected Geoheritage Resources of

"Atlantic Geopark" Project (Central Portugal). Geosciences, 14(3), 81. https://doi.org/10.3390/geosciences14030081

Geossítios, 2025. Inventário Nacional do Património Geológico. https://geossitios.progeo.pt/index.php/about (retrieved 26.2.2025).

GGN, 2025. Global Geoparks Network. https://www.globalgeoparksnetwork.org/ (retrieved 26.2.2025).

Gill, J.C., 2017. Geology and the Sustainable Development Goals. Episodes 40(1), 70-76. http://dx.doi.org/10.18814/epiiugs/2017/v40i1/017010

Habibi, T., A. Ponedelnik, A.A., Yashalova, N.N., Ruban, D.A., 2018. Urban geoheritage complexity: Evidence of a unique natural resource from Shiraz city in Iran. Resources Policy 59:85–94. https://doi.org/10.1016/j.resourpol.2018.06.002

Henriques, M.H., 2004. Jurassic heritage of Portugal: state of the art and open problems. Rivista Italiana di Paleontologia e Stratigrafia 110(1), 389-392. DOI: https://doi.org/10.13130/2039-4942/6317

Henriques, M.H., Brilha, J., 2017. UNESCO Global Geoparks: a strategy towards global understanding and sustainability. Episodes 40(4), 349-355. DOI: 10.18814/epiiugs/2017/v40i4/017036

Henriques, M.H., Pena dos Reis, R., Brilha, J., Mota, T., 2011. Geoconservation as an Emerging Geoscience. Geoheritage 3:117–128. DOI: 10.1007/s12371-011-0039-8

ICNF, 2025. Instituto da Conservação da Natureza e das Florestas. https://www.icnf.pt/conservacao/ordenamentoegestao/snac (retrieved 11.2.2025).

INE, 2023. Estatísticas do Turismo – 2023. Instituto Nacional de Estatística. file:///C:/Users/M%C2%AA.%20Helena%20Henriques/Downloads/ETurismo_2023.pdf (retrieved 13.12.2024).

LNEG (2025). Geoportal Energia e Geologia. National Inventory of Geological Heritage. https://geoportal.lneg.pt/en/databases/geosites/#!/ (retrieved 26.2.2025)

SNAC, 2025. Sistema Nacional de Áreas Classificadas. https://www.icnf.pt/conservacao/ordenamentoegestao/snac (retrieved 11.2.2025)

UNESCO, 2025. UNESCO Global Geoparks. https://www.unesco.org/en/iggp/geoparks/about (retrieved 27.2.2025).

Yates, D., Peacock, E., 2023. T. rex is Fierce, T. rex is Charismatic, T. rex is Litigious: Disruptive Objects in Affective Desirescapes. International Journal of Cultural Property 30(4):396-418. DOI:10.1017/S0940739124000055

Beach retreat due to sea level rise induced by climate change: The case of the Korasida, Heromylos and Limnionas beaches in southeastern Evia facing the Aegean Sea

Iatrou[1] A., Karakostas[1] D., Markozanes[1] F., Karditsa[2] A., Poulos[1] S.

(1) Laboratory of Physical Geography, Section of Geography and Climatology, Department of Geology and Geoenvironment, Panepistimioupolis-Zografou 15784, Attiki, Greece.

(2) Department of Port Management and Shipping, National and Kapodistrian University of Athens, Psahcna, Evia, Greece

Introduction

The processes that govern the formation and evolution of beach zones include marine and terrestrial processes; the former, in the case of an essentially tideless environment, refer to the incoming waves, their transformation and breaking conditions that induce nearshore currents and sediment transport, while the latter to the delivery of terrestrial sediment (i.e. cliff erosion, river inputs). These processes acting in different times (from seconds to decades) and spatial (for a few meters to km) scales, are subjected also to the various human (direct or indirect) interventions. Such an indirect anthropogenic intervention is climate change which among other impacts causes the rise of sea level; the latter has a significant impact on beach zone evolution with undesirable consequences to coastal ecosystem services with coastal tourism being among them.

The purpose of the present study is to provide an estimate of shoreline retreat associated with the sea level rise (SLR) for the year 2100, according to the latest IPCC 2021 report (Masson-Delmotte et al., 2021), in the case of three beaches in Evia facing the Aegean Sea (Figure 1). The three beaches are (from north to south) Korasida, Heromylos and Limnionas, selected based on their size in both width and length, together with their direct exposure to incoming waves from the NE, E and SE directions (open Aegean Sea), making them highly relevant for assessing the impact of sea-level rise on coastal retreat. The first two beaches have been formed in front of schist formations while the third one in front of marbles, with both formations belonging to the Styra Nappe of the Cycladic Blueschist Unit (Xypolias et al., 2003).
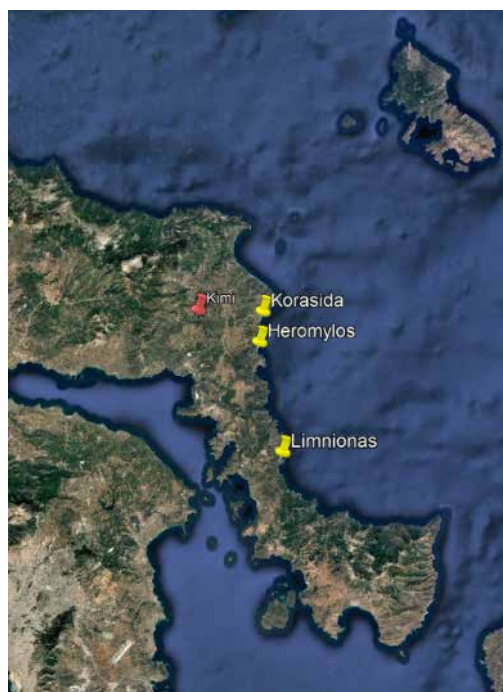

Figure 1. The location of the beaches under investigation.

Methods

Shore-normal profiles were measured with the use of a Leica Distance Meter (subaerial part) and a Portable Handy Depth Sounder Hondex PS-7 (subaqueous part). For the geographical position of profile, a Topcon GPS was used. Reanalysis of hourly wave data, regarding the neighbouring area of Kimi (shown in Figure 1), were obtained from the Copernicus platform, covering a period of 20 years (1/1/2002 - 31/12/2021).

For the purpose of the present study the highest (1%) of the wave characteristics (height (H) and period (T)) have been identified for each of the three predominant directions. For the estimation of shoreline retreat the most common method, the Bruun's rule (Bruun, 1962), has been used (Figure 2), which is based on the change of the beach's morphometric characteristics due to the rise of the sea level, assuming a shoreline retreat retaining unchanged beach profile, with the eroded sediment deposited on the shoreface, retaining depth unchanged. Therefore, the calculated estimates could be considered as indicative.
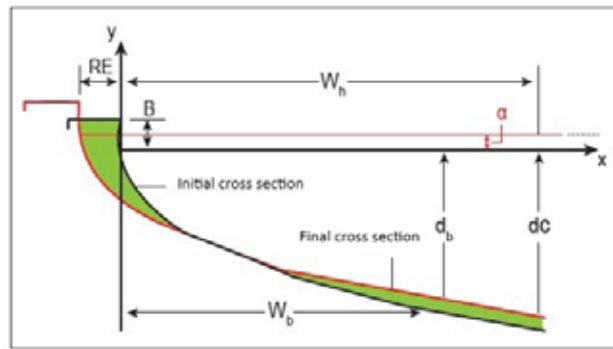
Figure 2: Illustration of Bruun's rule (from Poulos and Karditsa, 2020).

The retreat (RE: retreat) of the beach boundary is given by Brunn's (1962) relationship (equation 1):

$$wE = \frac{W_C \; a}{d_c + B} \qquad (1)$$

Where, (α): the sea level rise; (dc): the maximum depth of bottom sediment mobilization given by Hallermeier (1981) (equation 2); (W_c): the horizontal distance of dc from the shoreline; and (B): is the berm height.

$$dc = 2.28\, H_e - 68.5\, (H_e^2 / g T_e^2) \qquad (2)$$

where, (e: extreme) values (with a yearly exceedance of 0.137%) of wave height (H) and Period (T) and (g) earth's gravity.

The retreat of all beaches was calculated for the various Shared Socio-economic Pathways (SSP) scenarios provided by IPCC (Masson-Delmotte et al., 2021), which are: SLR = 0.28 m (SSP1a-1); SLR = 0.60 m (SSP2-4.5); SLR = 1.01 m (SSP4-8.5).

Results

The basic morphometric and wave characteristics of the three beaches are presented in Table 1. The wave characteristics refer to the wave height (H_e), period (T_e), direction, closure depth (d_c) and its distance from the shore (W_c) for the extreme values of H and T. Limnionas beach is the widest beach (39 m), followed by Heromylos (28 m) and Korasida (22 m). All three locations have similar beach heights (< 3 m), while Korasida has the steepest subaerial slope. Heromylos and Korasida have higher significant wave heights compared to Limnionas. Finally, Heromylos has the greatest depth of closure, followed by Korasida and Limnionas.

Table 1. The basic morphometric and hydrodynamic characteristics of the 3 beaches.

	Morphometric characteristics			Hydrodynamic characteristics				
	Beach Width (W) (m)	Beach Height (B) (m)	Shoreface slope (β_f)	Wave Direction	H_e (m)	T_e (s)	d_c (m)	W_c (m)
Heromylos	28	2.8	0.045	NE	5.1	8.3	11.3	250.5
Korasida	22	2.6	0.090	SE	5.2	8.9	11.7	129.7
Limnionas	39	2.7	0.060	E	3.7	8.9	7.6	128.2

The estimated retreat for the three SSP sea level rise scenarios is shown in Table 2. For all sites, both the absolute retreat (Re in meters) and the retreat relative to the beach width (Re in %) increase significantly with increasing expected sea level rise (0.28 m from SSP1 to 1.01 m SSP4).

Heromylos is the most vulnerable of the three sites, even under moderate sea level rise (SSP2-4.5), and shows the highest retreat values (Re=18.8 m (67.1%) under the worse scenario SSP4-8.5. Korasida shows moderate retreat values, while under the SSP4-8.5 scenario Re is 9.6 m (43.5%). Limnionas is the least affected but still shows significant impacts. For example, under SSP4-8.5 the overtopping reaches 12.2 m (31.3%), which is the lowest of the three sites.

Table 2. The estimated retreat (RE) for the three beaches with respect to the sea level rise ("α" in equation 1) related to the weak (SSP1a), moderate (SSP2-4.5) and worse (SSP4-8.5) case scenarios due to climate change.

Sea Level Rise Scenarios		Heromylos	Korasida	Limnionas
SSP1a–1: 0.28 m	Re (m)	5.2	2.7	3.4
	Re (%)	18.6	12.1	8.7
SSP2-4.5: 0.60 m	Re (m)	11.2	5.7	7.2
	Re (%)	39.8	25.9	18.6
SSP4-8.5: 1.01 m	Re (m)	18.8	9.6	12.2
	Re (%)	67.1	43.5	31.3

Discussion and Conclusions

The three beaches exposed to the open Aegean Sea are expected to retreat by 2.7-5.2 m for the SSP1a-1 scenario, by 5.7-11.2 m for the moderate SSP2-4.5 scenario and by 9.6-18.8 m for the worse SSP4-8.5 scenario by 2100. The differences between the retreat values are due to their different morphodynamic and hydrodynamic characteristics, as shown in Table 1. Heromylos experiences the highest retreat under all scenarios, reaching 18.8 m (67.1%) under SSP5-8.5. Korasida and Limnionas show lower but still significant retreat values, with Korasida reaching 9.6 m (43.5%) and Limnionas 12.2 m (31.3%). The vulnerability of Heromylos and Korasida beaches is also related to the fact that they are exposed to the highest wave heights (5.1-5.2 m). On the other hand, they show the most dramatic retreat. Limnionas beach is exposed to the lowest wave heights (3.7 m). The relatively lower retreat values under all climate scenarios may also be related to the higher beach elevation or better natural resilience to sea level rise.

Given the economic, ecological, and social importance of these beaches, proactive measures need to be considered to mitigate the effects of rising sea levels and associated coastal hazards. Implementing a combination of continuous monitoring to predict beach response and adaptive strategies (eg. nature based solutions and interventions) will support preserving the value and function of these coastal areas in the face of climate change.

References

Bruun, P., 1962. "Sea-level rise as a cause of shore erosion." Journal of the Waterways and Harbors division 88(1), 117-130.

Hallermeier, R. J., 1981. "A profile Zonation for Seasonal Sand Beaches from Wave Climate". Coastal Engineering, 4, 253 - 277.

Masson-Delmotte, V. P., Zhai, P., Pirani, S. L., Connors, C., Péan, S., Berger, N., ... & Scheel Monteiro, P. M., 2021. IPCC, 2021: Summary for policymakers. *In:* Climate change 2021: The Physical Science Basis. Contribution of Working Group I to the Sixth Assessment Report of the Intergovernmental Panel on Climate Change.

Poulos, S., and, Karditsa, A., 2020. Applied and Environmental Oceanography -An Introduction to coastal zone management, DISIGMA publisher, Thessaloniki

Xypolias, P., Kokkalas, S., & Skourlis, K., 2003. Upward extrusion and subsequent transpression as a possible mechanism for the exhumation of HP/LT rocks in Evia Island (Aegean Sea, Greece). Journal of Geodynamics, 35(3), 303-332.

Contribution to the stratigraphic study of the pyroclastic Formations of the Lesvos Petrified Forest, Lesvos Island, Greece.

Iliopoulos, G.[1], Papadopoulou P.[1], Valiakos, I.,[2], Zouros, N.[2,3]

(1) Department of Geology, University of Patras, Patras, Greece, iliopoulosg@upatras.gr (2) Natural History Museum of the Lesvos Petrified Forest, Sigri, Greece (3) Department of Geography, University of the Aegean, Mytilene, Greece

Introduction / Background

Lesvos Petrified Forest represents one of the most important monuments for the geological heritage of Greece. It is located on the western peninsula of Lesvos Island and has been recognized as a Natural Monument since 1985, covering an area of 15.000 hectares. Silicified tree trunks, both lying and in upright position, as well as fossil leaves of lower Miocene age are found enclosed in pyroclastic and volcaniclastic material deriving from a nearby stratovolcano chain (Zouros et al., 2015). The protected area of the Lesvos Petrified Forest became one of the 4 first European Geoparks in 2000 and global geopark in 2004. In 2015 Lesvos Island became a UNESCO Global Geopark with the petrified forest as the main geological heritage area of international significance. Recognized as one of the first 100 IUGS geological heritage sites, the Petrified Forest is a locus for research, education, and sustainable tourism.

Recently, the construction of the new Kalloni-Sigri road brought to light new fossiliferous localities (Zouros at al., 2015, 2022). Construction works with extensive new roadcuts, exposed several artificial sections along the road, which on the one hand brought to light numerous fossilized trees and leaves, and on the other hand enabled the stratigraphic research of the volcanoclastic rocks at Akroheiras Hill (within the protected area of the Lesvos petrified forest) which contain them (Fig. 1A), and allowed the detailed stratigraphic analysis of the Sigri Pyroclastic Formation (Pe-Piper et al. 2019b).
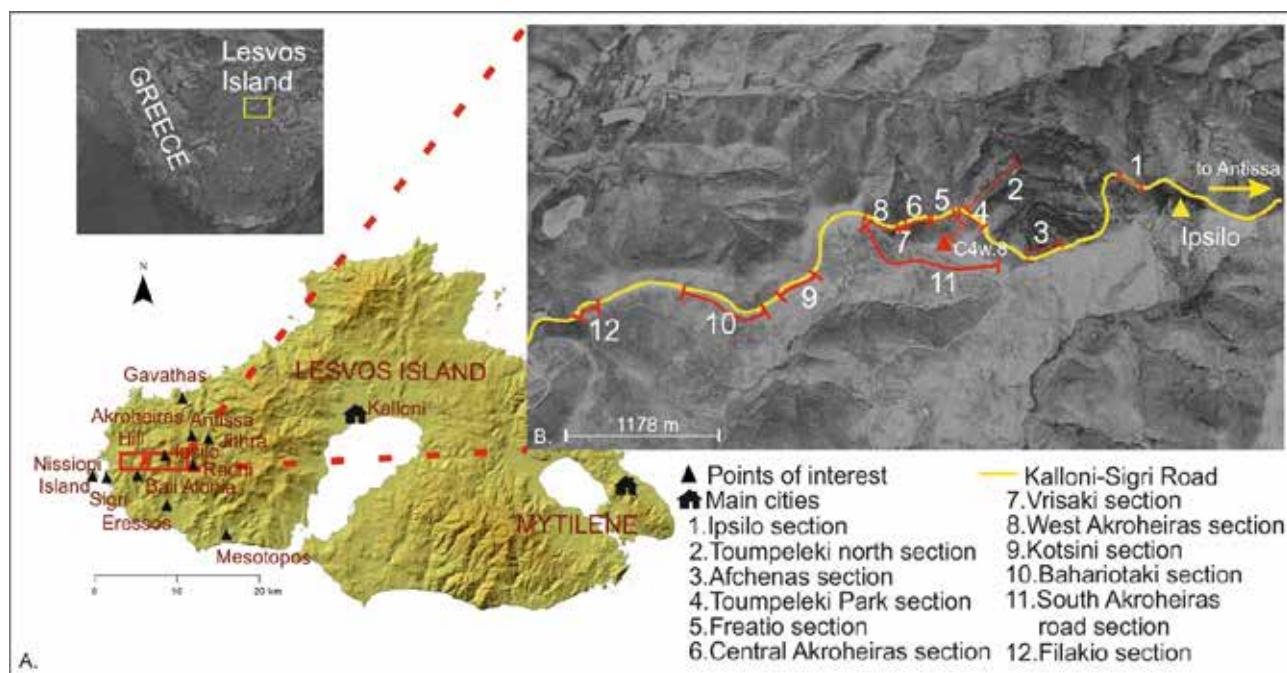
Fig. 1: A. DEM image of Lesvos Island. Main cities, villages and main points of interest are noted. The study area is noted with the red rectangle. B. Satellite image of the study area, where the 12 studied sections (red lines) are highlighted.

Twelve different sections located along the new road that cuts across Akroheiras Hill (Fig. 1B), were stratigraphically recorded and are presented herein, while a new stratigraphic scheme for the pyroclastic deposits of Lesvos is proposed.

Geological setting

During the last fifty years the volcanic rocks of Lesvos have been extensively studied and mapped (Hecht, 1974a, b, c; Pe-Piper, 1978; 1980; Pe-Piper et al., 2019b), and the overall stratigraphic structure of the volcanic formations of the Island has been provided (Pe-Piper & Piper, 1993; Pe-Piper et al., 2019a, b). Pyroclastic and volcaniclastic rocks of several

hundred meters extend at the western part of the Island and are known until now as the Sigri Pyroclastic Formation (Pe-Piper 1980; Pe-Piper et al., 2019b), lying above Permian schists and marbles (Katsikatsos et al., 1982). Sigri pyroclastics are mostly tuffs containing exceptionally preserved silicified trunks and fossilized leaves (Velitzelos & Zouros, 1997; Zouros et al., 2007; Zouros, 2021; Liapi et al., 2022; Tsitsou et al., 2022; Liapi et al., 2024). The age of Sigri pyroclastics has been estimated between 21.5 and 18.0 Ma (Pe-Piper et al., 2019b). The stratovolcano chain follows the dominating NNE-SSW dextral strike-slip tectonic regime of the Aegean-Anatolian microplate (Yilmaz et al., 2000). In Lesvos Island three successive neotectonic stages have been reported since the Miocene: a) the earliest one is of Upper Miocene age, based on its relation to synchronous volcanism and associated rocks, and formed strike–slip faults of E–W to ENE–WSW strike b) the second one took place in the Pliocene and formed normal faults of NW–SE strike, as well as strike–slip faults of NNE–SSW strike c) finally, the active stage since the Pleistocene forms E–W trending normal faults (Chatzipetros et al., 2013)

Material and Methods
Detailed stratigraphic logging was conducted in twelve sections along the new road cuttings from Moni Ipsilou Hill to Fylakio (Fig. 1A). Stratigraphic logging was performed in many places of each site as the lateral continuity of the layers was interrupted by faults, and lateral changes of the pyroclastic material occurred. The lithological characterisation of the pyroclastic rocks follows Fisher & Schmincke (1984) and Francis & Oppenheimer (2003). The presence of the most prominent fallen or standing tree trunks was noted, as well as the respective fossil leaf horizons. Basic sedimentary structures were also recorded. Rough stratigraphic cross sections containing the most important features of each section (characteristic horizons, major faults etc) were recorded and photos of each section were taken. Identification of the stratigraphic discontinuities took place (particularly erosional unconformities which mostly correspond to palaeosoil horizons). These discontinuities as well as some fine tuff layers, which present obvious and recordable lateral continuity, were used for the correlation of the different stratigraphic columns in each section, and subsequently for the correlation of the different sections.
The different formations were distinguished using criteria of the International Commission on Stratigraphy (Murphy and Salvador, 1999), as well as using physical characteristics of the rocks. Subdivision of formations in members took place when possible, taking into account erosional unconformities or/and palaeosoil development. In addition, palaeosoil horizons were also used to distinguish the different eruption phases.

Results
The prevailing lithology of pyroclastic rocks from the study area are tuff layers (fine to lapilli tuffs), with thicknesses ranging from a few millimeters to several meters characterized by sharp contacts. Grading is common (normal, reverse or normal to reverse), and pumice and lithic lapilli are often present. Pyroclastic rocks are often intercalated with volcaniclastic layers namely channeled or layered tuffaceous conglomerates and sandstones. The recorded palaeosoil horizons present thicknesses from a few millimeters to around ten centimeters or more and are easily traced by their black, green or/and red color. Neither their color nor their thickness appears stable laterally. They often evolve to thin horizons of fine tuff or even they disappear leaving only a discontinuity, many times difficult to observe. Their coloring is attributed to alteration due to the circulation of hydrothermal fluids (Pe-Piper et al., 2019a). The layers are dipping with a general NE-SW orientation and low angles (3-16˚). Some differentiations were noticed as NE-SW (sections 4, 12) and NW-SE (sections 10, 12) orientations also occur, which are attributed to the described above tectonic regime.
Several high angled (60-90˚) faults, deforming the studied sections have been observed. Most of them are sinistral strike slip faults with NE-SW or NNE-SSW directions (sections 1, 3, 4, 5, 7, 8, 9, 10, 11, 12). N-S directed faults were also noticed (sections 1, 4, 5, 10, 11). Additionally, E-W or WSW-ENE directed sinistral strike slip faults (sections 3, 6, 7, 10, 11) and a few NW-SE normal faults (sections 1, 10) were also recorded. The lateral continuity of the sections is interrupted by Quaternary channels. Their position is controlled by faults as it has been also implied for the older channels (Lamera et al., 2004), which are uplifting the western blocks.
Twelve sections were lithostratigraphically recorded in detail namely Ipsilo section, Toumpeleki north section, Afchenas section, Toumpeleki section (east and west part), Freatio section, Central Akrocheiras section, Vrisaki section, West Akrocheiras section, Kotsini/Bachariotaki sections, South Akroheiras road cut section and Filakio section (Fig.1B).
Ipsilo section stretches for 250 m at the foot of Ipsilo Hill (Fig.1B, Section 1) and has a recorded thickness ranging between 4 and 20m. It presents pyroclastic tuffs with high pumice content at its base, while at higher levels locally developed palaeosoil horizons were recorded. The stratigraphy of **Toumpeleki north section** was recorded along a narrow natural section across a stream valley north of the road (Fig.1B, Section 2). A total of 65 m of pyroclastic material was recorded. Brown volcanic material was recorded at the base of this section. Upwards the sequence is composed of both coarse and lapilli tuffs with a characteristically high percentage of pumice at the lower part. Further upwards lapilli tuff layers exist for at least 55 m. **Afchenas section (**Fig.1B, Section 3) consists of thick (around 60m) reddish chaotic (poorly sorted) polymictic,

mostly clast supported volcaniclastic deposits with substandard stratification and angular clasts. Wedged laterally secondary fine grained layers with high pumice content can be seen. **Toumpeleki Park section (east part)** (Fig.1B, section 4, Fig. 2) consists mostly of coarse and lapilli tuffs and some volcaniclastic layers, often containing transported trunks and branches (with thickness 16m). Seven palaeosoil horizons were recorded from bottom to top. Standing fossil trunks implying the presence of a respective forest were recorded on six of the palaeosoil horizons. Fossil leaves were recorded on at least three stratigraphic horizons. **Toumpeleki Park section (west part)** presents 90m of pyroclastic rocks. The lower 37 m consist mostly of both coarse and lapilli tuffs with intercalations of palaeosoil horizons and volcaniclastic layers, often containing transported trunks and branches. In total, eight palaeosoil horizons and two disconformities were recorded from bottom to top. Standing fossil trunks were recorded in four palaeosoil horizons and fossil leaves were recorded just in one case. At the upper stratigraphic levels (from 37 to 90 m column height) of this section a concise stratigraphic recording was conducted (due to vegetation cover) revealing a more coarse grained stratigraphic sequence. **Freatio section** (Fig.1B, Section 5) is a very unique and important site because of the exceptionally high number of transported fossilized trunks that have been excavated and are preserved on site. The section has a length of more than 100m and is delimited in both sides and on top of the west end by Quaternary channels. It consists mostly of fine and coarse tuff layers and volcaniclastic sediments with a total thickness of around 14m. Four palaeosoil horizons were recorded. Standing trunks were recorded on three horizons. At its lower part a thick (4.60 m) lahar which turns into a mud flow deposit at the top exists. A large number of transported trunks were excavated lying in different orientations. This accumulation is interpreted as a log jam. **Central Akroheiras section** (Fig. 1B, Section 6) is lying west from Freatio section. It stretches for more than 290m and the thickness of the pyroclastic sequence is more than 40m. It consists mostly of coarse and lapilli tuffs and some very characteristic volcaniclastic sediments that have been deposited in small rivers. The upper stratigraphic levels present an overall more coarse-grained lithology and thicker layers. Nine palaeosoil horizons and a disconformity were recorded. Standing fossil trunks were recorded on three palaeosoil horizons. Fossil leaves were recorded at several stratigraphic levels. **Vrisaki section** (Fig. 1B, section 7) is a small section consisting mostly of tuffs (coarse /lapilli tuffs and tuff breccia) and volcaniclastic sediments with a total thickness of 20m. Seven paleosoil horizons were recorded between the volcaniclastic layers. This section presents lateral continuity with **West Akroheiras section** which lies immediately westwards. It consists of coarse tuffs, lapilli tuffs and less of tuff breccia layers. Volcaniclastic layers also exist. The total thickness of the pyroclastic layers of this section is 22m. Seven palaeosoil horizons were recorded in this section. Standing fossil trunks were recorded in three palaosoil horizons. Fossil leaves were recorded in great numbers in many locations throughout this section. The upper stratigraphic levels show an overall different lithology. Most of the layers are thick and coarse grained and bear a lighter color. **Kotsini-Bachariotaki sections** (Fig. 1B, sections 9 & 10 respectively), stretch for more than 870 m along the road. The total thickness of the pyroclastic layers that were recorded is 21m. A characteristic palaeosoil horizon with multiple standing trunks can be noticed in both sections. Fossilized leaf litter was noticed in the lower part. Its upper part appears thicker and coarser grained with transported volcanic bombs. **South Akroheiras road section** (Fig.1B, section 11) stretches for 1424 m along the road that leads to Bali Alonia Petrified Forest Park. A variety of layers from volcaniclastic layers to tuff breccia with varying thicknesses (from 2 cm to approx. 30 m) were recorded. Palaeosoil horizons, fossil trunks and fossil leaves were also recorded in some places. The stratigraphic sequence is disrupted by faults and thus the correlation with the other sections was difficult. However, the existence of common very thick (1-30m) tuff breccia layers and the decreased frequency of palaeosoil horizons must be noted.
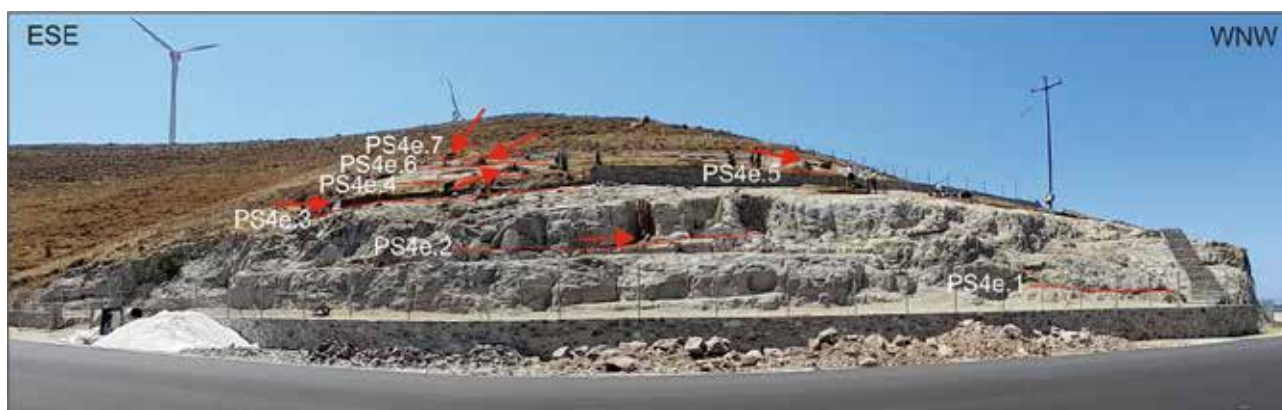

Fig. 2: Panoramic view of east Toubeleki park section (section 4). Toubeleki park section (east) consists a characteristic section where seven palaeosoil horizons (PS4e.1-7) can be seen (red lines). The red arrows indicate the position of standing fossil trunks.

Filakio section (Fig.1B, section 12) stretches for 140 m along the new Kalloni-Sigri road towards Sigri. It is the western of the studied sections, but it is one of the most important since a large number of both standing and fallen trunks were excavated. It is composed of relatively thick lapilli tuffs, tuff breccia, discontinuous thin palaeosoil horizons and conglomerate lenses at its lower part (road level) and thinner tuffs and volcaniclastic layers with intercalations of palaeosoil horizons upwards (Filakio Park level). The total thickness of this sequence is 12.5 m. Five palaeosoil horizons were recorded and standing fossil trunks were recorded in three of them. The lower part of the section shows volcaniclastic characteristics with thin intermittent palaeosoil horizons.

Discussion

The studied sections provide a detailed stratigraphic record of the broader Akroheiras Hill pyroclastics. The lateral continuity of the layers is often interrupted by post deposition Quaternary erosional surfaces, the road construction works and the severe faulting. The recorded faults have vertical displacements from a few centimeters up to 10m (i.e. Freatio section). Thus, the different characteristic horizons (palaeosoils and disconformities) from each section were correlated. The correlation of the different sections revealed that many palaeosoil horizons bear trunks in upright position recorded in at least one of the studied sections (Fig.3).
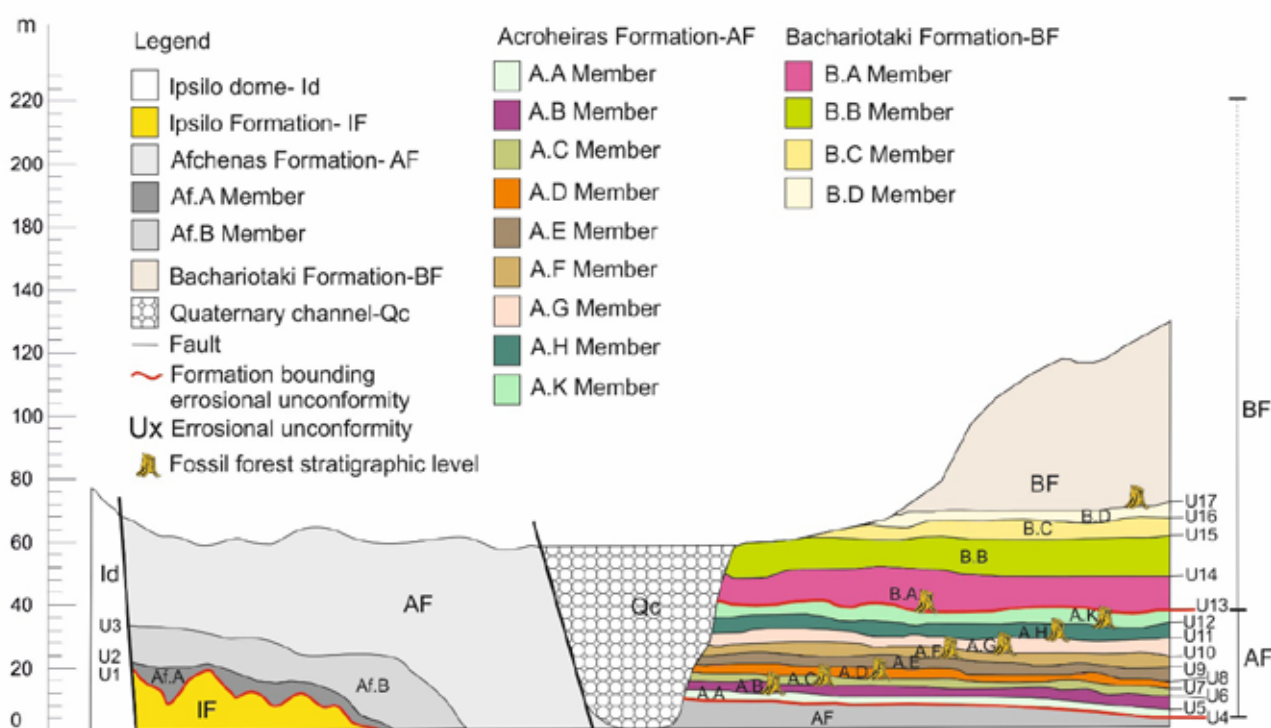
Fig. 3: Simplified synthetic section of Akroheiras Hill presenting the relative position of the described in the text Formations, Members and disconformities/palaeosoils (Us).

Moreover, four new Formations have been established namely Ipsilo Fm, Afchenas Fm, Akroheiras Fm, and Bachariotaki Fm (Fig. 3), replacing Sigri Pyroclastics Fm, which from now on will be considered as the Sigri Pyroclastics Group.

Ipsilo Formation: The pyroclastic rocks of this formation consist coarse and lapilli tuffs with characteristically high percentage of pumice (vitric tuffs) (up to around 50%). Secondary channels also exist. Fossilized wood is scarce in this formation and no trunks in upright position exist. Its lower limit was detected in Toumpeleki North section, where it comes in contact with brown ignimbrite (0-3m). The nature of their contact could not be evaluated due to limited exposure. Its upper limit is a distinct disconformity which can be seen in several sites along the road (U1). In places a weak palaeosoil horizon can be noticed. The total visible thickness of Ipsilo Formation pyroclastic rocks is five m but increases eastwards and may reach up to 20m.

Afchenas Formation: Thick (around 60m) reddish chaotic (poorly sorted) polymictic, mostly clast supported volcaniclastic material with substandard stratification and angular clasts can be seen along the road. Secondary channels can also be noticed. Its upper stratigraphic levels can be seen in the lower part of Freatio section and the lower part of Filakio section. In this part thin intermittent palaeosoil horizons and conglomerate lenses are detected. No or limited fossilized wood can be found in this

formation except its upper limit, where also trunks in upright position were noticed. The material is probably of fluvial origin and may represent hyperconcentrated or gravelly debris flows (Pe-Piper et al., 2019b) carrying mostly andesitic blocks and has been deposited close to the source. This formation outcrops also at Rachi area as mentioned in Pe-Piper et al. (2019b). The total thickness of this Formation is at least 58m. The lower part of this Formation can be divided in two Members, Af.A and Af.B.

Akroheiras Formation: the pyroclastic rocks of this formation are made of relatively thin (0.5 cm to 7m) fine grained secondary pyroclastic layers (predominantly lithic, fine or/and coarse tuffs and minor lapilli tuffs) intercalated by repeated palaeosoil horizons. Standing and fallen fossilized trunks as well as fossilized leaves are found in great numbers in this formation. The different layers are the result of pyroclastic avalanches (lahars, debris and mud flows) as well as river flows with limited lateral continuity. This formation comes in contact with the underlying Afchenas Formation through the disconformity/palaeosoil horizon U5 (Fig.3), while its upper limit is set to the disconformity signified by palaeosoil horizon U14 (Fig.3). Its total thickness is approximately 30m. Parts of the pyroclastics of this formation are exposed in several of the studied sections (Toumpeleki east, Toumpeleki west, Freatio, Central Akroheiras, Vrisaki, West Akroheiras and Filakio). Nine members are distinguished (Members A.A-A.K) separated by 9 palaeosoil horizons respectively (palaeosoils U6-U14, Fig. 3).

Bachariotaki Formation: The pyroclastic layers of this formation appear thicker (up to 30 m in Bali Alonia Section) and overall, more coarse grained than the other formations. They consist mostly of lapilli tuffs and tuff breccia with transported blocks and volcanic bombs. Volcaniclastic layers are also present. The stratigraphy of this part of the sequence appears complicated due to the multiple thick lobes that can be noticed and intense tectonism. Moreover, there are no adequate sections to record the stratigraphy in detail due to the high vegetation cover of the Akroheiras Hill slopes. Based on the total thickness of the recorded layers in the upper part of Akroheiras Fm and in South Akroheiras road section, the total thickness of this formation is estimated as 200m up to the hilltop of Akroheiras Hill. Both transported and standing trunks exist in this formation too although their frequency is reduced. Its upper limit is unknown due to erosion and vegetation cover (on top of Akroheiras Hill). In the lower Bachariotaki Fm, which is exposed in Toumpeleki Park west, Central Akroheiras, Vrisaki and West Akroheiras, four Members have been established (Members B.A, B.B, B.C, BD) bounded by the relative erosional unconformities/palaeosoils (U15-U19). Pyroclastic layers of this formation are also exposed in Kotsini/Bachariotaki sections as also in South Akroheiras road sections, but the existence of multiple faults does not allow the correlation of these layers and thus no other members are established for this formation for the time being.

The high pumice content of Ipsilo Formation may imply pyroclastic deposits deriving from ignimbrite or deposited during the same ignimbrite-forming eruption (Fisher and Heiken, 1982). As implied by Piper et al. (2019b) the location of the main source of Sigri pyroclastics was most likely in the wider Mesotopos area. It is possible that Ipsilo Formation was coeval with an ignimbrite forming eruption happening in Mesotopos prior to Eressos dome intrusion/extrusion as this could account for the high percentage of pumice and the low lithic content of this formation. The presence of the ignimbrite in Toumpeleki north section may contribute to this. On the contrary, due to the high lithic content of Afchenas Formation it may have derived from an Eressos Fm dome that had already been extruded during the formation of this sequence. In both formations a low time gap between the volcanic phases is implied by the reduced number of palaeosoil horizons that were formed or/and preserved. Ipsilo and Afchenas Formations bear little or no fossilized wood, nevertheless, they serve as the base of the fossiliferous Sigri pyroclastics.

Akroheiras Fm shows a high number of palaeosoil horizons and units. Each unit was formed when pyroclastic material deriving from neighboring volcanoes lying eastwards (Kouli and Seymour, 2006) was remobilized, enriched with water and flowed down the pre-existing alluvial system. These secondary pyroclastic flows reached the plain area lying further to the west carrying also fallen trunks and leaves. Each palaeosoil horizon is marking the cessation of the volcanic activity for a certain period of time. Therefore, the recorded palaeosoil horizons can serve as markers for distinguishing between different eruptions as has also been mentioned by Piper et al., (2019b) for the recorded palaeosoil horizons of Central Akroheiras area. At least 9 eruptive phases are evidenced in this part of the sequence corresponding to the establishment of the respective members.

When there was enough time between the previous and the next eruption, forests were developing on the formed soils. Thus, in Akroheiras Fm, nine (9) successive forest forming periods were recorded. The forests were buried later on under water saturated with cold pyroclastic material. Because the flows were not hot enough to burn the trees and because there was water in them the tree trunks and the leaves that were buried under anoxic conditions (otherwise the wood would have been decomposed) were preserved and then had the opportunity to get fossilised.

Within the lower part of Bachariotaki Fm at least four more eruptive phases are assured with one more forest developing period. In total, in Akroheiras and the lower part of Bachariotaki Fms 13 eruptive phases which correspond to the 13 defined members of the formations are mentioned herein. Moreover, at least 10 successive forest forming periods are witnessed by the different stratigraphic levels of the standing trunks.

Conclusions
- A new stratigraphic model is hereby proposed based on the lithology of the layers and the major stratigraphic hiatuses for the previously called Sigri Pyroclastic Formation (Pe-Piper, 1980; Pe-Piper & Piper, 1993; Pe-Piper et al., 2019b), and

which herein is revised as the Sigri Pyroclastic Group.

• Four pyroclastic formations are introduced for the Sigri pyroclastic rocks, Ipsilo Fm, Afchenas Fm, Akroheiras Fm and Bachariotaki Fm, bounded by erosional unconformities.

• Akroheiras Fm is further divided in Members A.A to A.K., as is also the case for the lower part of Afchenas Fm (Members Af.A and Af.B) and the lower part of Bachariotaki Fm (Members B.A to BD). The different Members are also bounded by palaeosoils and respective disconformities that correspond to different volcanic eruptions.

• Thus, at least 13 eruptive phases are identified. The cessation of each eruption was followed by the formation of a palaeosoil and the subsequent development of a forest on it.

• At least 10 successive forest developing periods have been recorded until now in the Akroheiras Hill pyroclastic sequences. It is certain that more forest forming events are hidden below the dense vegetation in the wider area of the Sigri pyroclastics.

References

Chatzipetros, A., Kiratzi, A., Sboras, S., Zouros, N., & Pavlides, S., 2013. Active faulting in the north-eastern Aegean Sea Islands. Tectonophysics, 597–598, 106–122. https://doi.org/10.1016/j.tecto.2012.11.026

Fisher, R.V. and Heiken, G., 1982. Mt. Pelee, Martinique: May 8 and 20, pyroclastic flows and surges. J. Volcanol. Geotherm. Res., 13:339-371

Fisher, R., Schmincke, H.U., 1984. Pyroclastic Rocks, Springer-Verlag Berlin Heidelberg.

Francis, P., Oppenheimer, C., 2003. Volcanoes. Oxford University Press.

Hecht, J., 1974a: Geological map Mithimna sheet. 1:50000. IGME, Athens

Hecht, J., 1974b: Geological map Polychnitos sheet. 1:50000. IGME, Athens.

Hecht, J., 1974c: Geological map Eresos sheet. 1:50000. IGME, Athens.

Katsikatsos, G., Mataragas, D., Migiros, G., Triandafillou, E., 1982. Geological study of Lesbos Island, Special Report, IGME, Athens.

Kouli, M., Seymour, K., 2006. Contribution of remote sensing techniques to the identification and characterization of Miocene calderas, Lesvos Island, Aegean Sea, Hellas. Geomorphology 77, 1-16.

Lamera, S., Kouli, M., Vamvoukakis, C., Seymour, K. St., 2004. Volcanic Stratigraphy, Sources and Mesothermal Au-Ag Deposit in Polychnitos Ignimbrite, Lesvos. Abstract in proceedings 10th International Congress. Bulletin of the Geological Society of Greece. April 2004, Thessaloniki.

Liapi, E., Zidianakis, G., Tsitsou, E., Iliopoulos, G., Zouros, N., 2022. New floristic data of the Early Miocene Lesvos Petrified Forest − Part A: Non-vascular plants, ferns and monocots from the West Akrocheiras outcrop. Bulletin of Geological Society of Greece Sp. Publ. 10, pp. 395–396.

Liapi, E., Iliopoulos, G., Zouros, N., 2024. Documenting the leaf flora of a new fossiliferous locality from the Lesvos Petrified Forest. Folia Musei rerum naturalium Bohemiae occidentalis - Geologica et Paleobiologica 58 (1), pp. 29–33.

Murphy, M., Salvador, A., 1999. International Subcommission on Stratigraphic Classification of IUGS, International Commission on Stratigraphy, International Stratigraphic Guide— An abridged version. Episodes 22 (4).

Pe-Piper, G., 1978. The Cenozoic volcanic rocks of Lesbos (Greece), unpublished readership thesis, University of Patras.

Pe-Piper, G., 1980. The Cenozoic Volcanic Sequence of Lesvos, Greece. Z. dt. geol. Ges., 131, 889- 901.

Pe-Piper, G., Piper, D.J.W., 1993. Revised stratigraphy of the Miocene volcanic rocks of Lesbos, Greece. Neues Jahrbuch für Geologie und Palaeontologie Monatshefte, 1993 (2),97–110.

Pe-Piper, G., Imperial, A.M., Piper, D.J.W., Zouros, N.C., Anastasakis, G., 2019a. Nature of the hydrothermal alteration of the Miocene Sigri Petrified Forest and host pyroclastic rocks, western Lesbos, Greece. Journal of Volcanology and Geothermal Research, 369,172–187.

Pe-Piper, G., Piper, J.W.D., Zouros, N., Anastasakis, G., 2019b. Age, stratigraphy, sedimentology and tectonic setting of the Sigri Pyroclastic Formation and its fossil forests, Early Miocene, Lesbos, Greece. Basin Research 2019, DOI: 10.1111/bre.12365.

Tsitsou, E., Zidianakis, G., Liapi, E., Iliopoulos, G., Zouros, N., 2022. New floristic data of the Early Miocene Lesvos Petrified Forest − Part B: Dicotyledon taxa from the West Akrocheiras outcrop Bulletin of Geological Society of Greece Sp. Publ. 10, pp. 398–399.

Velitzelos, E., Zouros, N., 1997. The petrified forest of Lesvos–Protected natural monument. Proc. Internat. Sympos. On Engineering Geology and the Environment, Athens, 3037-304.

Yılmaz, Y., Genç, Ş. C., Gürer, F., Bozcu, M., Yılmaz, K., Karacik, Z., … Elmas, A., 2000. When did the western Anatolian grabens begin to develop? Geological Society, London, Special Publication, 173, 353–384.

Zouros, N., Velitzelos, E., Valiakos, I., & Labaki, O., 2007. The Plaka Petrified forest park in Western Lesvos -Greece. Bulletin of the Geological Society of Greece, 40, 1880–1891.

Zouros, N.,Valiakos, I., Gribilakos, G., Plougarlis, A., Mpentana, K., Rozakis, V., Agiasoti, M., Tsalkitzi, O., 2015. New fossil findings in the Petrified Forest of Lesvos along the new Kaloni-Sigri road. The forest under the road a new traveling exhibition of the Lesvos Geopark. 13ᵗʰ European Geoparks Conference, Rokua, Finland.

Zouros, N.C., 2021. The Miocene petrified forest of Lesvos, Greece: Research and geoconservation activities. Geoconservation Research. 4(2), 635–649.

Zouros, N., Soulakellis, N.,Valiakos, I., Bentana, K., Theodorou, E., Zgournios, E.,Antonakis, E. and Lamprakopoulos, A. 2022. Enhancement and promotion of the new fossiliferous sites along the new Kalloni Sigri road.-An example of good practice in geoconservation in Lesvos Isl. UNESCO Global Geopark Greece. Bulletin of Geological Society of Greece Sp. Publ. 10, pp. 849-850.

17th **INTERNATIONAL CONGRESS** of the Geological Society of Greece

Geological study of the basement structure in the wider area of Filiro (Circum-Rhodope Belt, Central Macedonia, Greece)

D. Ioannidis, E. Katrivanos, A. Chatzipetros

School of Geology, Department of Structural, Historical and Applied Geology, Aristotle University of Thessaloniki, Greece, dioannif@geo.auth.gr

Abstract

The western border of the Serbo-Macedonian massif with Circum-Rhodope belt has been a subject of discussion in the past. Several questions have been raised about the geological structure of the study area (NE part of Thessaloniki, Pefka, Filiro, Asvestochori), based on variations in structural and lithological characteristics. Field – structural and lithological data were initially collected and then the geological structure and the tectonostratigraphy of the study area were visualised. In the area of interest there are characteristic rocks of both continental and oceanic crust in contact, as a result of past tectonic events (D1-D6 deformation events). Older tectonic events of compressive ductile stress regime (D1-D2) are correlated with the tectonic emplacement of ophiolites and the general terrane accretion, whine newer ones of brittle stress regime (D4-D5) are related with the thrusting and the creation of tectonic slices, as well as the inversion of the whole series. The lithological units of the area have been inverted by these tectonic events (D4-D5). As a result, the older rocks are placed tectonically on top of the younger ones. Compression forces have created a fold-and-thrust belt with a sense of movement to-the-SW. A lithological unit belonging to the Serbo-Macedonian massif is tectonically intercalated between the lithological units of Circum-Rhodope belt. The pre-alpine basement in the study area is of Serbo-Macedonian origin and the tectonic movement of the tectonic slices was accomplished on this basement.

Geological setting

The study area is geologically located mainly within the Circum-Rhodope Belt, which is part of the Internal Hellenides. The Circum-Rhodope Belt is traditionally divided into three units (from north-east to south-west):Deve Coran - Dubya, Melissochori - Cholomontas, Aspri Vrisi - Chortiati (Mountrakis 2010).

The Circum-Rhodope Belt was characterised palaeogeographically as the continental slope of the Greek hinterland during Jurassic. The presence of the oceanic crust of the Axios Zone at its eastern boundary, the turbiditic character of its rocks and the origin of its sediments from the Serbo-Macedonian Massif as described in Meinhold and Kostopoulos (2013) are indications consistent with this model. Structural and lithological features of Circum-Rhodope Belt show many variations. Thus, several questions have been raised about the geological structure of the study area.

The Serbo-Macedonian Massif starts from the Greek-Bulgarian border and extends in a northwest-southeast direction to the coast of Sithonia and Mount Athos peninsulas. Its western boundary is the contact with the Circum-Rhodope Belt , while its eastern boundary is in the basin of the Strimonas river, where it meets the Rhodope Massif. The similarities that appear in the rocks of the Serbo-Macedonian are many, however the massif has been divided into two units, namely Kerdyllia and Vertiskos. Palaeogeographically, the Serbo-Macedonian Massif, together with the Rhodope Massif, expresses the Greek hinterland. Its rocks represent a continental crust with evidence of orogenies older than the Alpine (Papanikolaou 2015). There are views that consider the Serbo-Macedonian Massif to be part of the Eurasian plate and views that place it within the Cimmerian blocks that were attached to Eurasia. What is important, however, is that the Serbo-Macedonian Massif was not part of Gondwana at the start of the Alpine cycle, but was already in Eurasia undergoing the effects of the Ercynian orogeny (Papanikolaou 2015).

In this paper we present new field and structural data from the study area to investigate the shallow structural configuration and the geological structure of the basement, as well as the deformation phases and geotectonic evolution in general.

Methodology

The identification and differentiation of the cartographic units was the first step in a traditional field-work way (Figure 1). Then, based on field-structural data we decipher the deformation events (Table 1) that affected the units and we construct the tectonostratigraphic column (Figure 2). The final stage is to produce the geological cross-sections (Figure 3). All the field structural data were measured and verified using a geological compass. The points chosen for measurement were the contacts between two cartographic units, the foliation of the rocks, the folds (limbs and b-axis) and the mirror surfaces of the faults. Many structural features (foliation, lineation, folds, faults, kinematic markers, slip lines) were identified, measured and helped to distinguish the tectonic events (Table1), providing information on the stress field of the epoch in which they acted and on the kinematics of deformation. The analysis of the tectonic structures (folds, faults, tectonic contacts and lineation) was carried out in order to distinguish the tectonic events find the temporal succession of the deformation events with the final result being the understanding of the geological history of the area. The tectonic structures studied belong to the macroscopic scale.
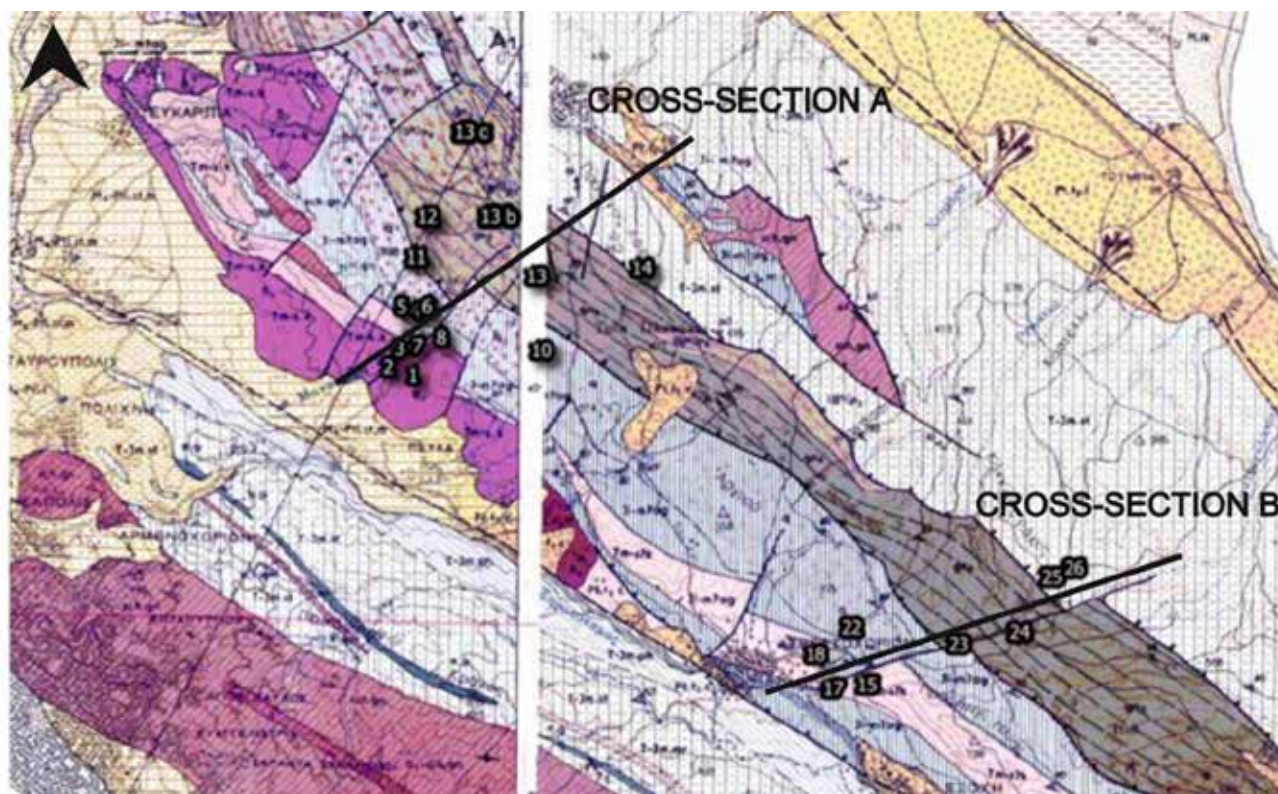
Figure 1.Geological map of the study area with field measurement points and location of geological sections. According to the geological mapping (Kockel et al.1970a Thermi sheet, Kockel et al.1970b Thessaloniki sheet).
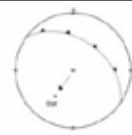
Results

The data analysed showed that the geological structure that exists today was not created by a single tectonic episode, but is the result of a series of deformation events. The newer events overprinted the older ones, making it more difficult to identify them. The distinction macroof the deformation events was based on the geometric characteristics of the tectonic structures (orientation, position, shape) and their kinematic analysis. The tectonic structures formed by compressive forces are due to the convergence of the African plate with Eurasia, the destruction of the Tethys Ocean and the increase in the thickness of the continental crust. Extensional structures followed the compressive ones, first with the collapse of the compressive structure and later with back arc extension.

We distinguished six main deformation events (D1-D6) in the study area (Table 1) which is coherent to similar studies in the broader area (Kilias et al. 2010, Katrivanos et al. 2013, 2016, Kilias 2024), revealing that the Internal Hellenides underwent complex deformation and metamorphism during the Alpine orogeny. The rocks appear to be inverted, with the older rocks tectonically superimposed on the newer ones. The degree of metamorphism increases to the northeast, i.e. towards the upper tectonostratigraphic horizons. The tectonic contacts between the formations are due to the action of reverse faults. Parts of the Serbo-Macedonian Massif were trapped between the units of the Circum-Rhodope Belt (Aspris Vrysi - Chortiati, Melissochori - Cholomonta). In this way, continental crustal rocks came into contact with rocks characteristic of the oceanic crust and deep-sea sediments. The sense of movement was from north-east to south-west. The geological structure of the tectonostratigraphic column (Figure 2) and of the two geological sections(Figure 3) prove that they belong to the same geotectonic zone (Circum-Rhodope Belt), have been affected by common deformation events and consist of the same formations.

However, there are some differences between the two areas: In the Asvestochori area, no occurrences of microgneiss and augen gneiss have been found. Thus, the Serbo-Macedonian Massif in the area consists only of greenschist. The degree of metamorphism of the greenschist is obviously greater than that of the surrounding rocks, but it does not reach the degree of metamorphism of the gneiss rocks of the Pefka-Filiro area. In the area of Asvestochori, the formation of clay shales contains interbeds of graphitic shales. In the Pefka area, graphitic shales are absent or could not be found. Finally, the orientation of the formations in the two areas shows a slight deviation from NW-SE in the Pefka-Filiro area to WNW-ESE in the Asvestochori area.

Table 1. Deformation events based on our field- structural observations and on other similar studies (Kilias et al. 1999,2010,Tranos et al. 1999, Katrivanos et al. 2013,2016, Kilias 2024)

DEFORMATION EVENTS (D)	AGE	STRESS REGIME & DEFORMATION CONDITIONS	STRUCTURES	KINEMATICS	GEODYNAMIC RESULTS
D1	MID-LATE JURASSIC	COMPRESSION DUCTILE	NOT FOUND		Ophiolite obduction and thrusting
D2	LATE JURASSIC-EARLY CRETACEOUS	COMPRESSION DUCTILE	CLOSED FOLDS & SCHISTOSITY CREATION		Thrusting and terrain accretion (photo 1,2)
D3	LATE CRETACEOUS	EXTENSION	NOT FOUND		Basin formation
D4	PALEOCENE-EOCENE	COMPRESSION SEMI-BRITTLE	REVERSE FAULTS – OPEN KNICK FOLDS		Intense imbrication of all units (photo 3,4,5)
D5	OLIGOCENE-MIOCENE	TRANSPRESSION BRITTLE	STRIKE – SLIP to NORMAL FAULTS - REVERSE FAULTS		Boundary effect between ductile extension in Pangaion unit to the east and brittle extension in Paikon unit to the west. Localized event in CRB as a boundary effect
D6a	MIOCENE-PLIOCENE	EXTENSION BRITTLE	HIGH – ANGLE NORMAL FAULTS		General faulting and basin Formation (Mygdonia)
D6b	PLIOCENE-PLEISTOCENE	EXTENSION BRITTLE	HIGH – ANGLE NORMAL FAULTS		General faulting (photo 6)
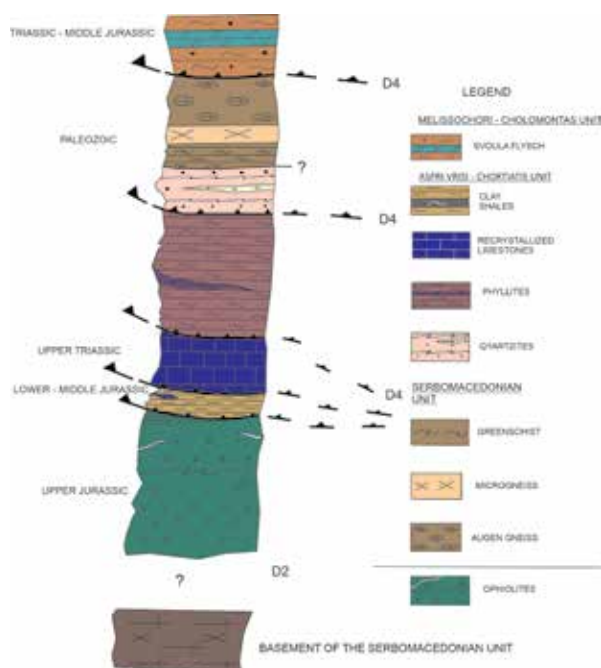
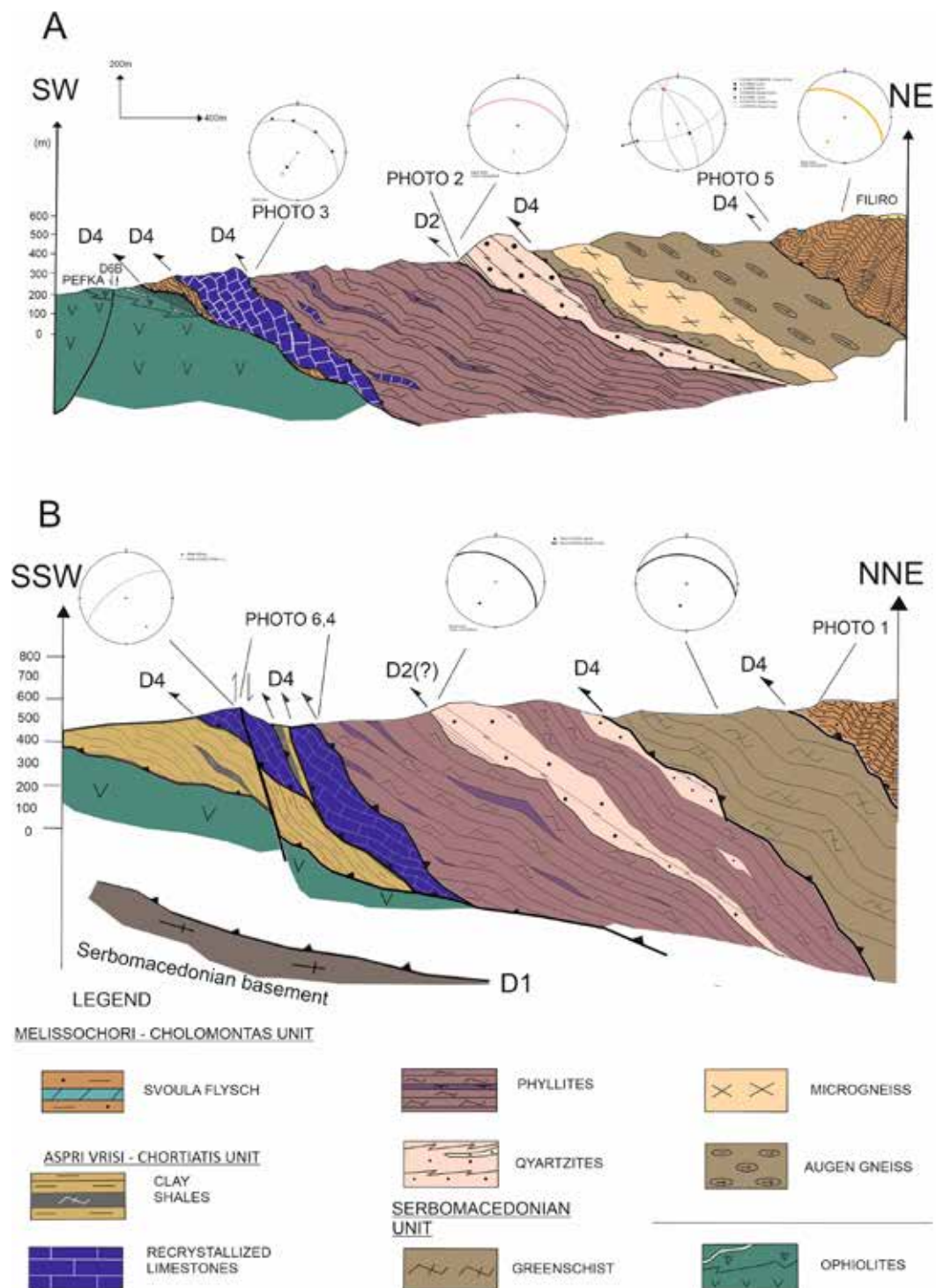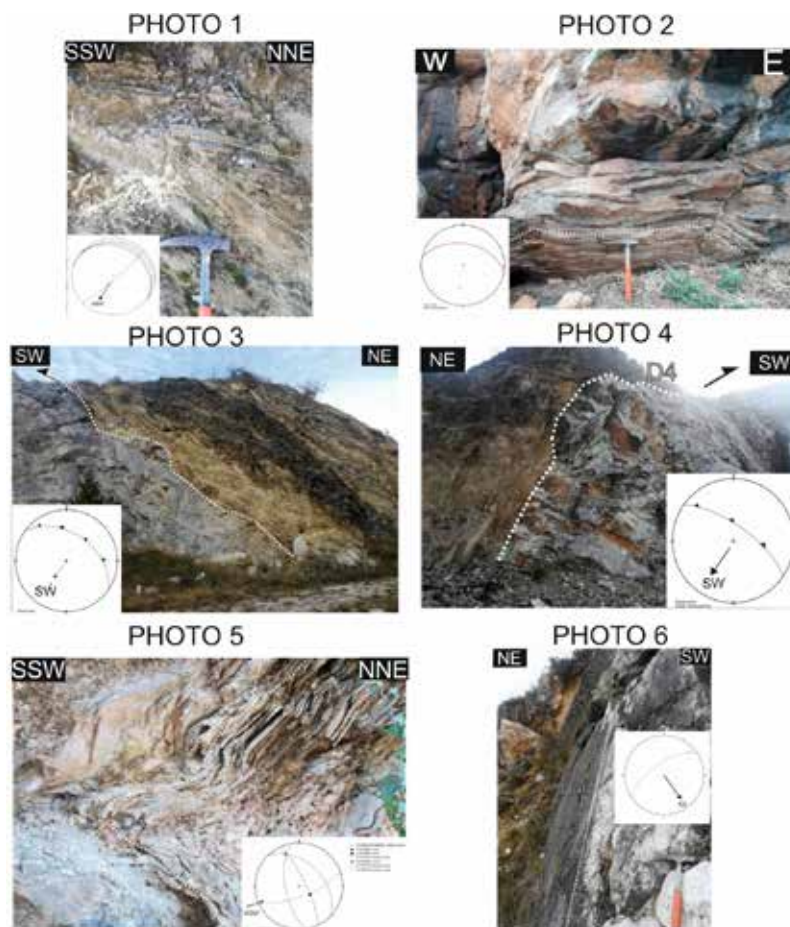**Figure 2. Tectonostratigraphic column of the study area.**

Figure 3.Geological cross - sections in the Pefka - Filiro (A) and Asvestochori (B) study areas (see Figure 1 for location).

Figure 4. (see Figure 3 for reference).
Photo 1 : D2 event , closed to sub-isoclinal fold , submerged and inverted with a direction to SW (Svoula flysch)
Photo 2: D2 event, schistosity (quartzites-phyllites contact)
Photo 3: D4 event, reverse fault, flat – ramp – flat structure (limestones – phyllites contact , Filiro area)
Photo 4: D4 event, reverse fault, flat – ramp – flat structure (limestones – phyllites contact, Asvestochori area)
Photo 5: D4 event ,open fold with a direction to WSW (Svoula flysch)
Photo 6: D6b event, normal fault

Conclusions

- The whole area was affected by a polyphase deformation (D1-D6 events), that started in ductile conditions (D1-D3) and continued with brittle conditions (D4-D6).
- Older tectonic events of compressive ductile stress regime (D1-D2) are associated with the tectonic emplacement of ophiolites and the general terrane accretion, whine newer ones of brittle stress regime (D4-D5) are related to the thrusting and the creation of tectonic slices, as well as the inversion of the whole series.
- During the D4 deformation event, parts of the Serbo-Macedonian Massif were tectonically intercalated within the Circum-Rhodope Belt formations.
- In Oligocene – Miocene, the localized conditions of the stress regime fall into the category of transpression, while in the same age ductile extension prevails to the east (Pangaion unit) and brittle extension prevails to the west (Paiko unit).
- We consider that the pre-alpine basement in the study area is of Serbo-Macedonian origin and the tectonic movement of tectonic slices was accomplished on this basement.

References

Katrivanos E., Kilias A. and Mountrakis D., 2013. Kinematics of deformation and structural evolution of the Paikon Massif (Central Macedonia, Greece): A Pelagonian tectonic window? Neues jahrbuch fuer Mineralogische Abhandlunger, 269, 149-171.

Katrivanos E., Kilias A. and Mountrakis D., 2016. Deformation history and correlation of Paikon and Tzena terranes (Axios zone, Central Macedonia, Greece) E.G.E. 12

Kilias, A. 2024.The Alpine Geological History of the Hellenides from the Triassic to the Present—Compression vs. Extension, a Dynamic Pair for Orogen Structural Configuration: A Synthesis. 72.

Kilias A. 2021. The Hellenides: A multiphase deformed orogenic belt, its structural architecture, kinematics and geotectonic setting during the Alpine orogeny: Comression vs Extension the dynamic peer for the orogen making. A synthesis. Journal of Geology and Geoscience.1-56.

Kilias A., Frisch W., Avgerinas A., Dunkl I., Falalakis G. and Gawlick H.-J. 2010. Alpine architecture and kinematic of deformation of the northern Pelagonian nappe pile in the Hellenides. Austrian Journal of Earth Sciences.

Kilias A., Falalakis G. and Mountrakis D. 1999.Cretaceous±Tertiary structures and kinematics of the Serbomacedonian metamorphic rocks and their relation to the exhumation of the Hellenic hinterland (Macedonia, Greece).

Kockel, Mollat, Antoniadis P. 1970a Geological map of Greece 1:50.000, Thermi sheet, Institute of Geological and Mineral Exploration, Athens

Kockel, Antoniadis P., Ioannidis K.1970b Geological map of Greece 1:50.000, Thessaloniki sheet, Institute of Geological and Mineral Exploration, Athens

Meinhold G., Kostopoulos D. K. 2013. The Circum-Rhodope Belt, northern Greece: Age, provenance, and tectonic setting.

Mountrakis D. 2010. Geology and geotectonic evolution of Greece. Thessaloniki. :University studio press. 321 p.

Papanikolaou D. 2015. Geology of Greece. Athens: Pataki publication.433 p.

Tranos M., Kilias A. and Mountrakis D., 1999. Geometry and kinematics of the Tertiary post metamorphic Circum- Rhodope Belt Thrust System (CRBTS), Northern Greece.